CIVIL ENGINEERING JOURNAL

číslo 3/2025

Obsah:

Article no. 21

THE CIVIL ENGINEERING JOURNAL 3-2025

RESEARCH ON INTELLIGENT SYNCHRONOUS TENSION MONITORING OF SUSPENDER OF THROUGH ARCH BRIDGE

Lin Wang, Quansheng Sun, Shengqi Yang and Yuxiang Guan

Department of Civil Engineering, Northeast Forestry University, Harbin， 150040, China; email: sunquansheng@nefu.edu.cn

Received: *24.04.2024*
Received in revised form: *20.06.2024*
Accepted: *30.08.2025*

ABSTRACT

Suspender tension and cable adjustment are important construction procedures in the construction of through arch bridges. The traditional suspender tension method is asynchronous tension. Because it is tensioned in batches and manually reads, it will cause errors in the control of suspender tension, which often fails to reach the tension accuracy. Therefore, it is necessary to determine whether secondary cable force adjustment is needed according to the site conditions, which may increase the construction period, management cost and construction cost. In this paper, the overall intelligent synchronous tensioning technology is applied to a through arch bridge. By monitoring the measured suspender cable force, structural deformation and structural stress in the synchronous tensioning process and comparing them with the theoretical values, the traditional asynchronous tensioning technology and intelligent synchronous tensioning technology are compared based on the finite element software. The influence of the error caused by asynchronous tensioning on the structure is analyzed and compared with the suspender cable force, structural stress and structural deformation in the synchronous tensioning process. The results show that the bridge is relatively sensitive to the tension cable force, so it is necessary to accurately control the construction cable force. The overall intelligent synchronous tensioning technology can control the error of the suspender cable force within 3% during the bridge completion process, the geometric shape error of the whole bridge is controlled within 4mm, and the stress error is within 7MPa, avoiding the secondary cable force adjustment. It not only reduces the structural stress generated during the construction of the suspender, but also saves the construction period and construction cost, and ensures the safety of the construction process.

KEYWORDS

Through arch bridge, Synchronous tensioning, Suspender, Cable adjustment

INTRODUCTION

The through arch bridge is a combination of beam and arch bridge with light structure, beautiful line shape and strong spanning ability. It combines the advantages of both and has low cost [1]. It is widely used in the construction of urban and highway bridges in China. But its structure itself is a multiple statically indeterminate structure system [2-3]; arch rib and suspender are the main load-bearing components of through arch bridge, and the size of suspender cable force will directly affect the geometric shape and internal force distribution of the bridge and then affect the overall working state of the whole bridge [4]. Therefore, the installation and tension of the suspender is an important part of the whole construction. Improper tension control of the suspender will not only cause excessive stress to the main beam and arch rib, but also affect the geometric shape of the whole bridge, affect the normal operation of the bridge, and bring safety hazards to the construction [5], and the tension sequence will also have a greater impact on the geometric shape and stress state of the bridge [6].

The traditional suspender tension adopts the method of asynchronous tension, that is, the suspender tension and tension sequence are determined before the suspender tension, and the oil pressure jack is used to tension the suspender in batches according to the order set in advance and read the data. The construction monitoring party uses the vibration method [7-8] to measure the suspender cable force after tension. In the construction process, the post-tensioned suspender will play a role in loading or unloading the pre-tensioned suspender, which may cause the loss of over-tension or tension cable force [9]. Therefore, according to the actual situation of the construction site, it is decided whether secondary cable force adjustment is needed [10]. And in the construction process, it is impossible to control the cable force as a whole. In the adjustment of the cable force, it is necessary to repeatedly try different cable force combinations to achieve the design of the bridge cable force. The efficiency is low and the adjustment accuracy is not high [11]. Therefore, a new suspender tensioning method, namely the overall intelligent synchronous tensioning technology, is proposed.

The overall intelligent synchronous tensioning technology [12] was invented in 2015.Its working principle is based on the tension as the control index and the suspender elongation as the auxiliary control parameter. When the bridge is working, the control center sends out tensioning instructions to control the operation of each jack, and ' synchronously ' tensioning all the suspenders of the bridge. At the same time, it can also control the operation of a single or local jack, and perform ' asynchronous ' tension and boom force adjustment on the local suspenders of the bridge.

The overall synchronous tensioning system of suspender is mainly composed of control cabinet, intelligent jack, signal acquisition and transmission system and hydraulic oil circuit system. Intelligent equipment system control tension instead of manual construction operation, can improve the construction conditions, improve the construction accuracy, quality and reliability.

Connect the control center to multiple intelligent pump stations, with each intelligent pump station capable of connecting to 10 jacks. Each jack is connected to the pump station via separate oil inlet and return lines. At the pump station, each jack's oil inlet and return ports are equipped with a frequency converter and solenoid valve. The pump station's PLC adjusts the oil inlet and return rates of each jack based on the displacement and tension signals transmitted by the data acquisition box of each jack, in conjunction with instructions from the computer control center. By controlling the switch frequency of the solenoid valve, different tension rates for each jack are achieved.

All suspenders of the whole bridge are tensioned synchronously to avoid the influence of adjacency between suspenders. There is no need for iterative calculation and cyclic tension, which can shorten the construction period, avoid the installation and disassembly of jacks back and forth, and avoid safety risks. And all the suspenders of the whole bridge are slowly stretched in place, which is more in line with the design and calculation process of the bridge, and ensures that the construction quality of the bridge accurately meets the design indicators.

The tension process is automatically completed by the program. The tension force is used as the control index, the suspender elongation is used as the auxiliary control parameter. The loading pause point and the holding load are accurately controlled, and the force value and displacement are visualized without manual operation of the oil pump. The intelligent tension of the suspender and the adjustment of the boom force are displayed in real time during tension. The tension value can also be checked by the pressure value of the hydraulic oil meter, and the cable force monitoring can be realized at the same time of tension. The control accuracy of the force value reaches ±1%. The construction and monitoring are synchronized to reduce the alternating approach time and further shorten the construction period.

Engineering situation

In a certain bridge alignment, the angle between the normal to the centerline of the route and the centerline of the navigational channel is approximately 27.5°. The river channel at the crossing point is straight, with a water surface width of about 150m along the axis direction of the route. The main bridge is a double-layer simply supported steel truss steel arch bridge with a span of 150m and a total length of 153m. The main beam adopts fully welded double-layer trusses, with the main truss varying in height from 10.394 to 11.0792m and a main truss spacing of 37.3m. The arch ribs are set with a secondary parabolic curve, with a rise of 37.5m (measured from the centerline of the lower span system). Both the upper and lower bridge decks have a 2% cross slope in both directions.

The entire bridge has a total of 44 suspenders, with 22 each set on the north and south sides, designed as double suspenders. The spacing of the suspenders in the longitudinal direction of the bridge is 10.6m, and in the transverse direction, it is 1.2m. Each suspender is made of high-strength parallel steel wires with a diameter of 91*Φ7, with a tensile strength not less than 1670MPa.

Fig. 1 – Bridge real picture

Measuring point arrangement

1. Geometric shape monitoring points

Set up two monitoring sections at the front and rear ends of the main girder and set coordinate observation points at the top center positions of the monitoring sections on the top and bottom chord of bridge girders. The main arch observation point is located at the lifting lug installation, as shown in Figure 2. The geometric shape monitoring uses a high precision leveling instrument to measure the elevation of the monitoring point after each construction stage. The high precision leveling instrument has an error within 2mm/km, ensuring high accuracy of the measurement data.

DOI 10.14311/CEJ.2025.03.0021

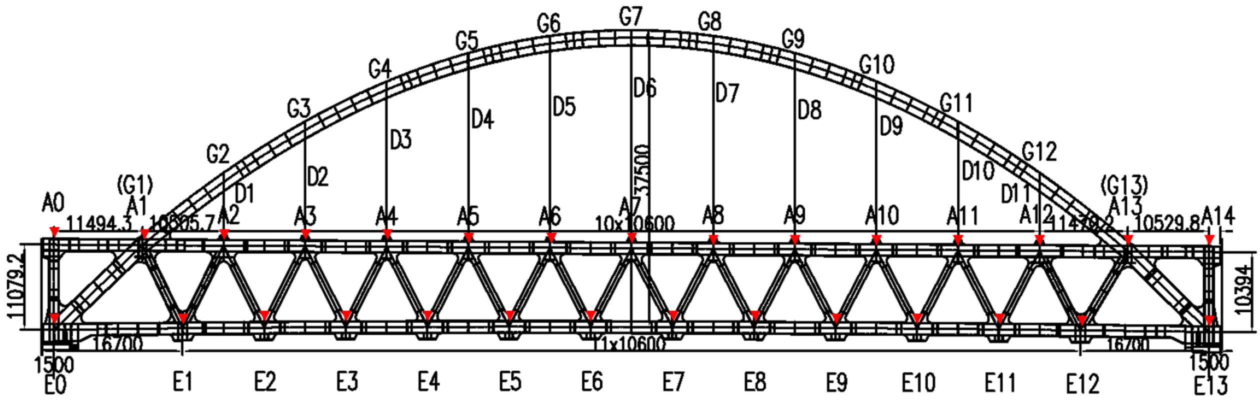

Fig. 2 – Bridge geometry monitoring points (mm)

2. Strain monitoring points

In order to better ensure the accuracy of the stress test results of the structure, on the basis of a large number of research on the commonly used strain sensors, the vibrating wire strain sensor is selected for monitoring. The error of the vibrating wire strain gauge sensor is within ±1.5% of the full scale.

The quarter cross section and the mid-span section of the steel truss girder are selected as the strain monitoring sections. Four strain monitoring points are set in the mid-span, and two strain monitoring points are set in the quarter cross section. The main truss has a total of 32 vibrating wire surface strain gauges. The layout of the monitoring section sensors is shown in Figure 3.

According to the results of structural analysis, and taking into account the symmetry of the two transverse arch ribs and the comparability of the data, the key sections of the bridge are arch foot section, quarter cross section and vault section. The monitoring section and the layout of the section sensor are shown in Figure 4, a total of 28 vibrating wire surface strain gauges.

DOI 10.14311/CEJ.2025.03.0021

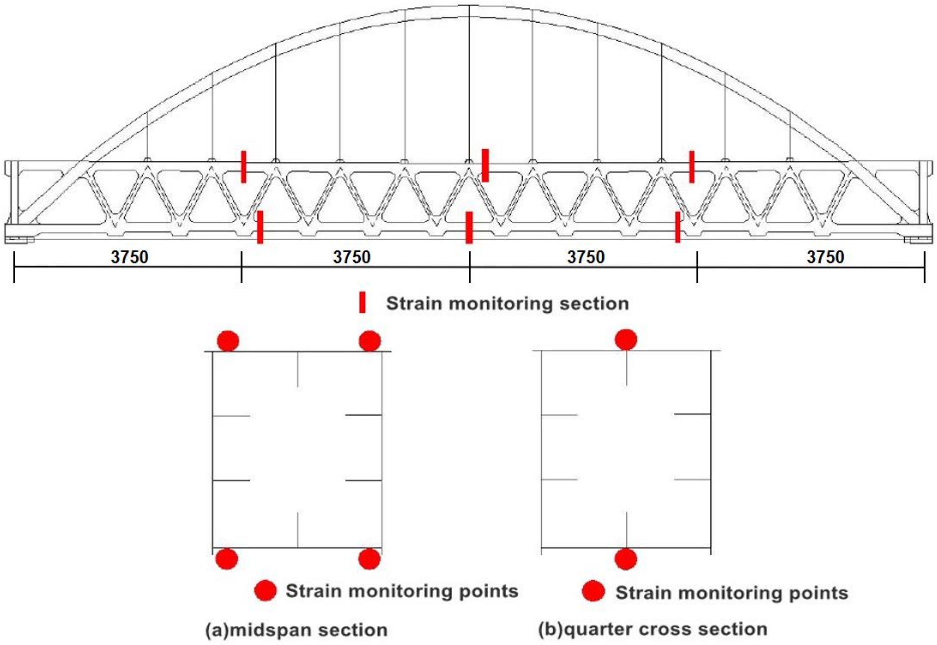

Fig. 3 – Strain monitoring point of main truss (unit : cm)

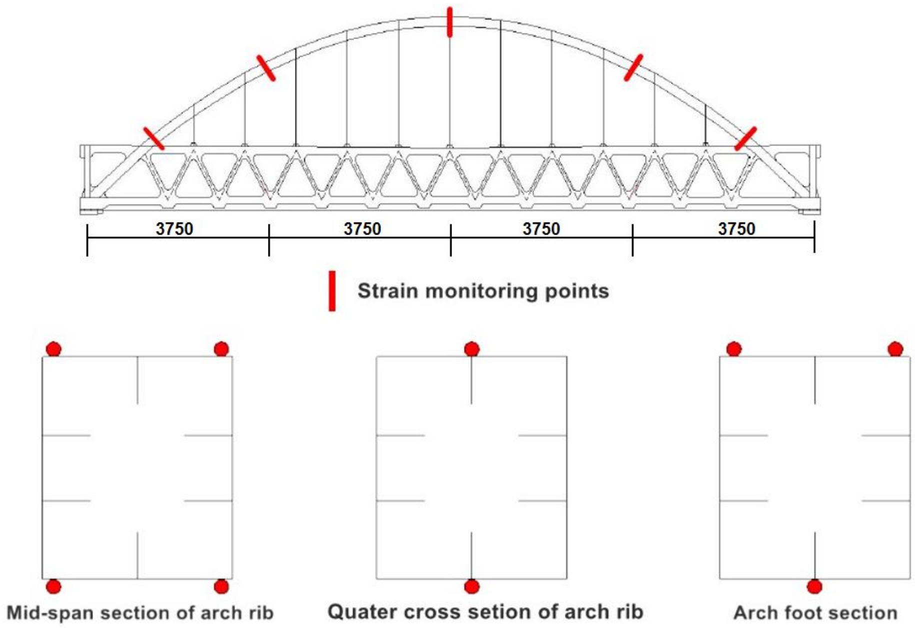

Fig. 4 – Arch rib strain monitoring point (unit : cm)

3. Cable force monitoring of suspender

In the construction control, based on the supervision of the measurement results of the jack of the construction unit, the environmental random vibration method (spectrum analysis method) is used to monitor the cable force. This method utilizes highly sensitive sensors temporarily attached to the suspenders to pick up the pulsating signals of the cables under environmental excitation.

In the process of suspender tensioning, the reading of the intelligent jack is used as the actual tensioning tonnage, and the vibration frequency method is used to monitor the cable force of each suspender during the tensioning construction process.

Fig. 5 – Application of integral intelligent synchronous tensioning technology in this bridge

Fig. 6 – Cable force measurement

4. Tension of suspender

During the construction process, due to the subsequent need to remove the lower support and other construction processes, the initial tension cable force of the boom is designed to be the bridge cable force through the forward iteration [13]. All suspenders of the entire bridge are tensioned in stages as a whole, with tensioning carried out in five steps, that is, pre-tension (total cable force 10%) → pre-tension unloading force → 30% (The first level tension) → 65% (The second level tension) → 100% (The third level tension). After the tension is completed, according to the cable force value displayed by the overall intelligent synchronous tension system and the cable force value measured by the construction monitoring, if the individual cable force does not meet the specification, the local single suspender cable force adjustment is carried out to make the final cable force meet the design and specification requirements.

Build finite element model

The spatial finite element model of the bridge is established by MIDAS Civil finite element software, as shown in Figure 7. Among them, the arch rib, main truss and main beam are simulated by beam element, and the suspender is simulated by truss element. The whole bridge is divided into 1617 nodes and 2896 elements, including 2874 beam elements and 22 truss elements. The diaphragm of the main bridge is simulated by a custom material without bulk density but with elastic modulus, and its weight is supplemented by the uniform load of the unit to simulate its role in the transverse connection of the bridge. Strictly follow the construction process set by the construction site to divide the construction stage of the model and fully consider the temporary load of each construction stage. There are four bearings at the end of the bridge, including one fixed bearing, two unidirectional movable bearings and one bidirectional movable bearing. The construction temporary support uses only compressive support to simulate the support effect of the support on the truss.

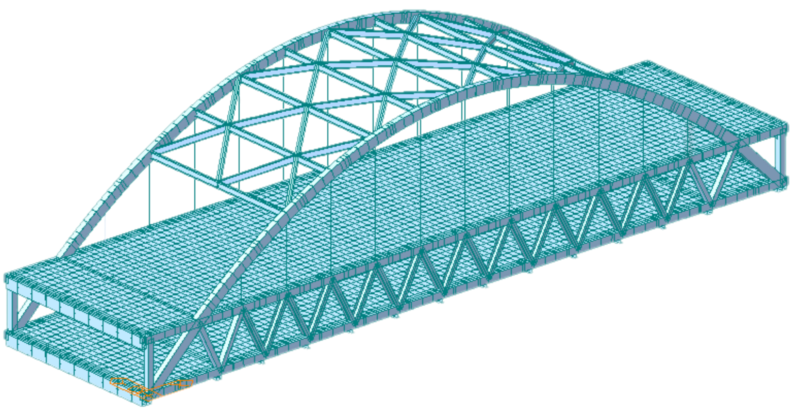

Fig. 7 – Bridge finite element model

Comparison of overall intelligent synchronous tensioning technology and asynchronous tensioning scheme

1. Comparison of initial cable force

In the original design scheme, the bridge adopted a symmetrical tensioning method from the crown to the arch feet at both ends as the suspender tensioning scheme, that is, D6 → D5 →... → D1 ; D6 → D7 →... → D11. However, in the end, due to the tight construction period of the project and the need for one-step tensioning in place, the overall intelligent synchronous tensioning technology is selected. The comparison between the initial tension cable force of the suspender and the overall intelligent synchronous tension cable force is shown in Figure 8.

DOI 10.14311/CEJ.2025.03.0021

From the comparison, it can be seen that the cable force value of the asynchronous tension and the cable force distribution of the suspender present a ' W ' shape, which is evenly distributed on both sides of the synchronous tension cable force. The difference between the maximum cable force of the asynchronous tension and the maximum cable force of the synchronous tension is 253kN. The cable force of the bridge is basically symmetrical along the middle line of the bridge.

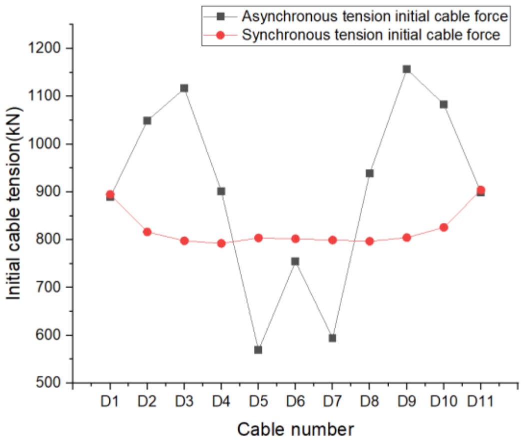

Fig. 8 – Comparison of initial cable force

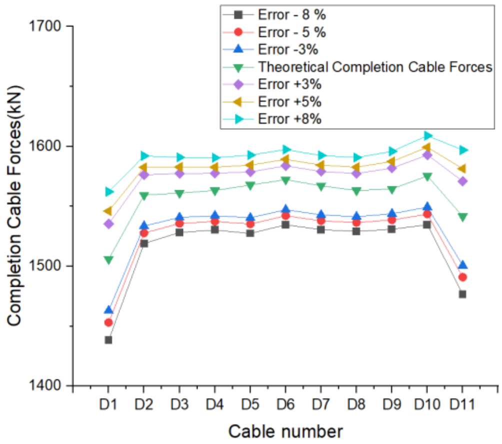

Fig. 9 – Comparison of Completion Cable Forces

If the asynchronous tensioning scheme is adopted, the difference between the maximum and minimum values of the initial tension cable force is 588kN, and after the synchronous tensioning scheme is adopted, the difference between the maximum and minimum values of the initial tension cable force is 111.5kN. Therefore, the difference between the maximum and minimum values of the initial tension cable force of the boom using the synchronous tensioning scheme is smaller than the difference between the maximum and minimum values of the initial tension cable force of the boom using the asynchronous tensioning scheme.

Therefore, it can be considered that the interaction between the suspenders of the bridge is more obvious, and the synchronous tensioning scheme can largely ignore the interaction between the suspenders, so that the initial tension cable force distribution is more average, the cable force distribution is relatively reasonable, and the local stress in the tensioning process is reduced, which is more conducive to the construction. However, the asynchronous tensioning scheme is adopted, and the difference of some cable force values is too large, which will lead to the excessive local stress in the tensioning construction process, which is relatively unfavourable to the construction process.

2. Comparison of Completion Cable Forces

Because the asynchronous tensioning adopts the method of manual batch tensioning, it is inevitable to produce the error of the tension cable force of the suspender. In this paper, the error values of the six asynchronous tensioning initial tension cable forces with error values of ±3%, ±5%, ±8% are used. The finite element software is used to calculate the Completion Cable Forces under the condition of error, and the synchronous tensioning Completion Cable Forces are compared, as shown in Figure 9.

Through the comparison in the figure, it can be seen that with the increase or decrease of the overall initial tension cable force error, the increase and decrease of the Completion Cable Forces of a single suspender are nonlinear. The reason for this situation is that the subsequent support removal and bridge deck pavement construction steps will cause the suspender cable force to be redistributed. However, on the whole, the distribution trend of Completion Cable Forces is basically the same. With the increase of error, the error of Completion Cable Forces also increases. When the maximum error of the initial tension cable force is ±8%, the maximum error of the Completion

Cable Forces will be-4.49% ~ +3.73%, but the cable force error is the error when all the suspenders increase by 8% or decrease by 8%. Since the initial tension cable force of the asynchronous tension is the cable force after the forward iteration optimization, the interaction between the suspenders has been considered in the iteration process, and the actual tension on site should be a random error. The error range of the actual Completion Cable Forces will be larger than the theoretical simulation value. Therefore, if the traditional asynchronous tension is actually used, the secondary cable force adjustment is required.

3. Geometric shape comparison

Because the stiffness of the main beam of the bridge is much larger than that of the arch rib, the displacement of each node of the main truss in the finite element model is basically the same during the simulation of tension, and the two sides of the bridge are symmetrical. Therefore, only the actual displacement of the unilateral arch rib node is compared, as shown in Fig.10.

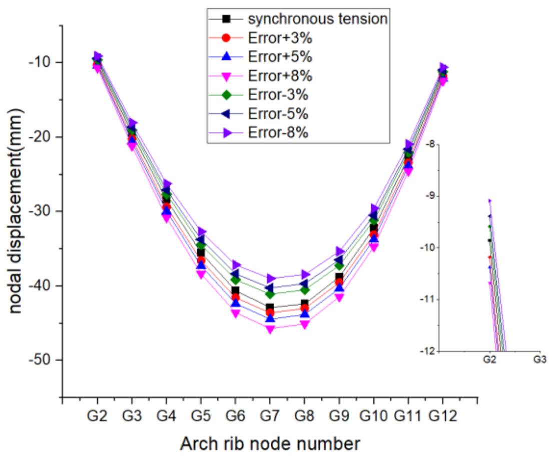

Fig. 10 – Arch rib node displacement comparison

Tab. 1 - Displacement error table of arch rib node caused by cable force error(unit:mm)

node number	Error +3%	Error +5%	Error +8%	Error -3%	Error -5%	Error -8%
G2	-0.3	-0.5	-0.8	0.3	0.5	0.8
G3	-0.7	-1.1	-1.7	0.5	0.9	1.5
G4	-1.0	-1.5	-2.4	0.8	1.3	2.2
G5	-1.0	-1.8	-2.8	1.1	1.8	2.8
G6	-0.9	-1.7	-3.0	1.5	2.3	3.5
G7	-0.7	-1.6	-2.8	1.8	2.7	3.9
G8	-0.6	-1.4	-2.7	1.9	2.7	4.0
G9	-0.8	-1.5	-2.7	1.5	2.3	3.4
G10	-0.9	-1.5	-2.5	0.8	1.3	2.5
G11	-0.7	-1.2	-1.9	0.6	1.1	1.8
G12	-0.4	-0.6	-1.0	0.3	0.5	0.9

As shown in the figure, as the error value increases, the overall arch rib node displacement will also increase, and vice versa. However, combined with the data in Table 1, it can be seen that taking the error of the suspender cable force as ±3% as an example, when the suspender cable force increases by 3% synchronously, the error value of the displacement at the arch foot is greater than the error value when the suspender cable force decreases by 3% synchronously. That is, the change of G2G3G4 node and symmetrical G10G11G12 node when the cable force increases by a fixed percentage is greater than that when the cable force decreases by a fixed percentage. In the middle of the arch rib span, the error of the suspender cable force is still ±3%. When the suspender cable

DOI 10.14311/CEJ.2025.03.0021

force is reduced by 3% synchronously, the error value of the displacement in the middle of the arch rib span is greater than the error value when the suspender cable force is increased by 3% synchronously. That is, the change of G6G7G8 node when the cable force decreases by a fixed percentage is greater than that when the cable force increases by a fixed percentage. This trend can also be clearly seen in Figure 10.

4. Stress comparison

Because the construction steps of asynchronous tensioning are inconsistent with the construction steps of synchronous tensioning, the stress distribution of each section after tensioning is selected as a comparison. The stress changes of the upper and lower edges at the measurement points are basically the same. This paper analyzes the variation of stress on the upper edge, as shown in Figures 11 and 12.

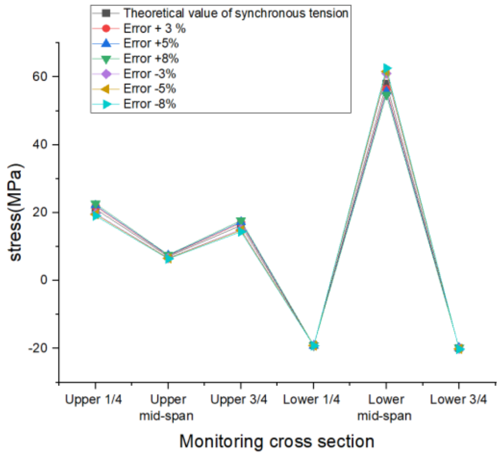

Fig. 11 – Main truss monitoring section stress comparison

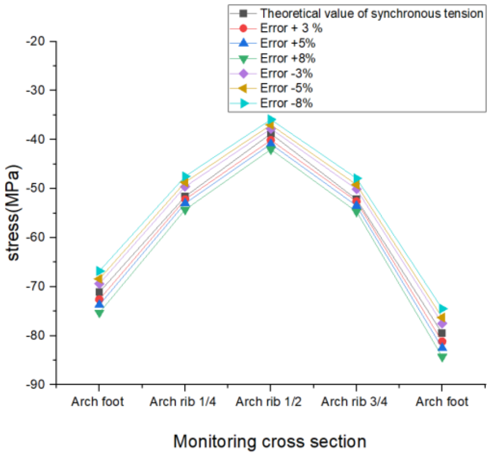

Fig. 12 – Arch rib monitoring section stress comparison

It can be seen from the comparison in the figure that with the increase of the suspender cable force error, the stress of the upper layer of the truss and the arch rib increases as a whole, and the stress of the lower layer decreases as a whole. This is because the increase of the cable force value of the suspender makes the arch rib and the upper truss share the load originally borne by the lower truss, which leads to the increase of the overall stress, which is consistent with the theoretical expectation. In the figure, the maximum stress error caused by the cable force is-5Mpa, and the position is the arch foot when the error is 8%. When the corresponding error is-8%, the stress error at the arch foot is 4.3Mpa, and the reason for the geometric shape trend of Section 3 is that when the overall suspender cable force error increases, the increase of the arch foot stress of the bridge is greater than the decrease of the overall suspender cable force error. When the overall suspender cable force error decreases, the change of the arch rib quarter cross section position and the mid-span position of the bridge is greater than the change at the arch foot position, which leads to the trend of the geometric shape of the bridge due to the cable force error.

Monitoring Numerical Analysis

1. Monitoring analysis of suspender cable force

Due to the symmetry of the arch ribs and main trusses on the left and right sides of the bridge, only the data of the cable force of the single-side suspenders and the suspenders after the completion of the bridge are listed, as shown in Table 2

From the comparison between the monitoring results of the suspender cable force and the theoretical calculation values, it can be seen that when the intelligent overall synchronous tension technology is applied to the bridge, the suspender tension cable force is distributed around 1560kN, and the suspender tension cable force is relatively average. The overall situation of the cable force of the suspender after multi-stage tension and completion of the bridge is close to the theoretical value; after the completion of the bridge, the deviation between all the suspender cable forces of the whole bridge and the theoretical bridge cable forces is within 3%, so it can be considered that the synchronous tension monitoring results meet the design requirements.

Tab. 2 - Suspender cable force monitoring value and theoretical value comparison

	The first level tension			The second level tension		
Suspender number	theoretical value (kN)	monitoring value (kN)	error%	theoretical value (kN)	monitoring value (kN)	error%
D1	268	294	9.7%	582	620	6.6%
D2	245	241	-1.6%	531	516	-2.8%
D3	239	221	-7.7%	519	496	-4.4%
D4	238	221	-7.0%	515	477	-7.4%
D5	241	236	-2.1%	523	526	0.6%
D6	241	231	-4.1%	521	514	-1.4%
D7	240	223	-7.1%	520	475	-8.6%
D8	239	230	-3.7%	518	493	-4.9%
D9	241	254	5.4%	523	548	4.8%
D10	248	245	-1.0%	537	556	3.5%
D11	271	275	1.4%	588	579	-1.5%
	The third level tension			Bridge completed		
Suspender number	theoretical value (kN)	monitoring value (kN)	error%	theoretical value (kN)	monitoring value (kN)	error%
D1	895	930	3.9%	1506	1540	2.3%
D2	816	791	-3.1%	1559	1537	-1.4%
D3	798	772	-3.3%	1561	1538	-1.5%
D4	792	777	-2.0%	1563	1551	-0.8%
D5	804	821	2.1%	1568	1588	1.3%
D6	802	817	1.9%	1572	1591	1.2%
D7	799	760	-4.9%	1567	1532	-2.3%
D8	797	752	-5.6%	1563	1522	-2.6%
D9	804	846	5.2%	1565	1609	2.9%
D10	826	856	3.6%	1575	1608	2.1%
D11	904	924	2.2%	1542	1564	1.5%

2. Geometric shape monitoring analysis

Because the bridge is constructed with full support, and the stiffness of the main truss of the bridge is much larger than that of the arch rib, it is a rigid beam flexible arch system. For the rigid beam flexible arch system, the tension of the suspender is mainly to adjust the internal force of the arch rib, and it does not have the function of adjusting the geometric shape of the main beam [14]. Therefore, the geometric shape of the main truss is compared with the displacement before and after the complete tension, as shown in Figures13 ~ 15.

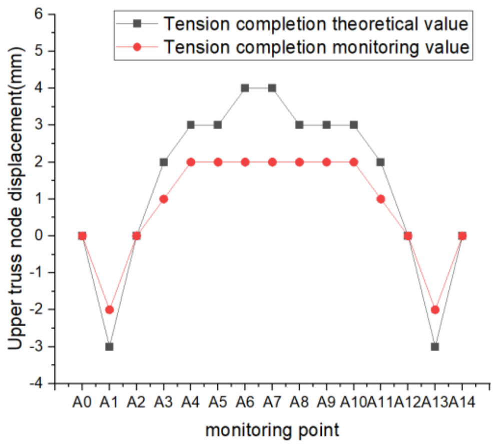

Fig. 13 – Displacement comparison of upper truss joints before and after tension

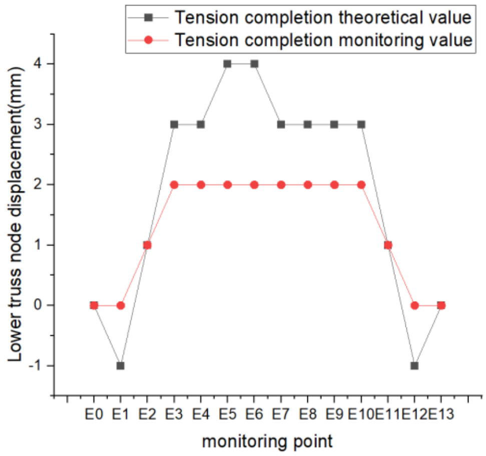

Fig. 14 – Displacement comparison of lower truss joints before and after tension

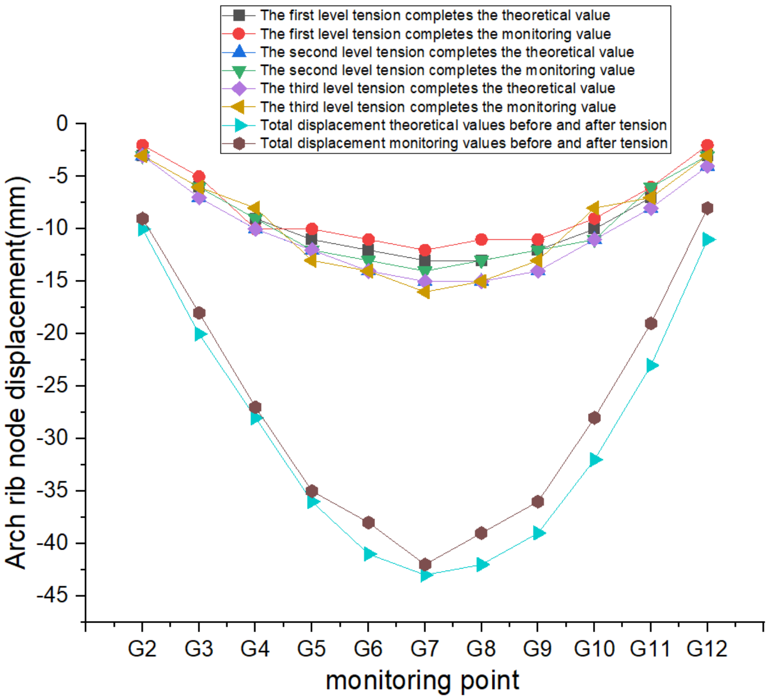

Fig. 15 – Arch rib displacement comparison

By comparing the displacement values of each node of the main truss and arch rib before and after tensioning, it can be seen that during the tensioning process, the maximum displacement of the upper and lower main girder trusses occurs in the middle of the span, and the maximum displacement after tensioning is 3mm. The displacement of the arch rib increases with the tension of the suspender. The maximum displacement occurs at the mid-span position after tension, and the maximum value is 43 mm. The displacement error of the whole bridge is controlled within 4 mm. From the comparison of the maximum displacement value of the arch rib and the main beam truss, it can be concluded that the overall stiffness of the main beam of the bridge is indeed much larger than the overall stiffness of the arch rib. In Figures 13 ~ 15, it can be seen that there is an obvious bulge in the displacement change of the theoretical value of the main girder truss at the A6A7 and E5E6 positions. This is because the bridge needs to meet the navigation requirements during the construction process, so there is no bracket at the navigation position of the river. In the theoretical model, in order to simulate the mid-span cantilever assembly, the boundary is not added in the mid-span. Therefore, in the tensioning stage, the cantilever assembly position will produce a large upward displacement relative to other positions of the main girder truss. During the monitoring process of the bridge, some measuring points have large deviations. The causes of the errors are personnel factors and environmental factors during the measurement, as well as the factors of the simulation accuracy of the full-bridge stiffness by the rod calculation model. However, on the whole, the overall change trend of the geometric shape monitoring value of the whole bridge is in good agreement with the theoretical calculation value.

3. Stress monitoring analysis

The bridge undergoes three-stage suspender synchronous tension during the construction process, and its stress state changes continuously with the construction. The stress monitoring data of the left truss and arch rib monitoring section of the bridge at each construction stage are listed below. Figures 16 and 17 are the comparison curves of the corrected stress data and theoretical analysis values of each monitoring section.

By comparing the stress monitoring values and theoretical calculation values of each section, it can be seen that the actual stress value and change trend of the whole bridge are in good agreement with the theoretical calculation values. The stiffness of the main girder of the bridge is large, so the stress change of the main girder section is relatively small during the tension process. The section with the largest change in stress is the mid-span position of the lower truss. The change value before and after tension is −27.44MPa, and the degree of stress change is close to the theoretical expected value of −31.27MPa. During the monitoring process, the difference between the monitoring value and the theoretical value of the 3/4 section at the arch rib is 7MPa, and the deviation is within the allowable range. The maximum stress is smaller than the material yield limit value specified in the specification, and the structure is in a safe state.

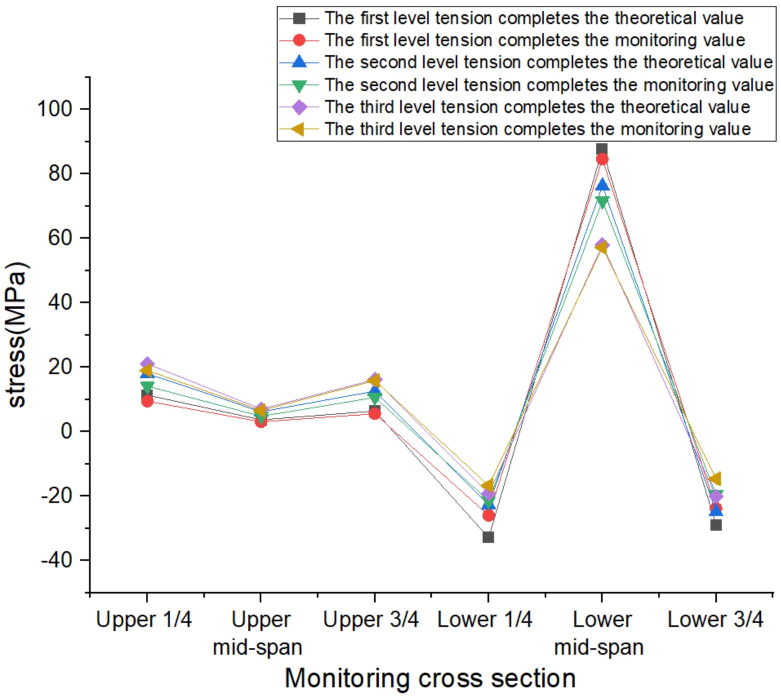

Fig. 16 – Main truss monitoring section stress comparison

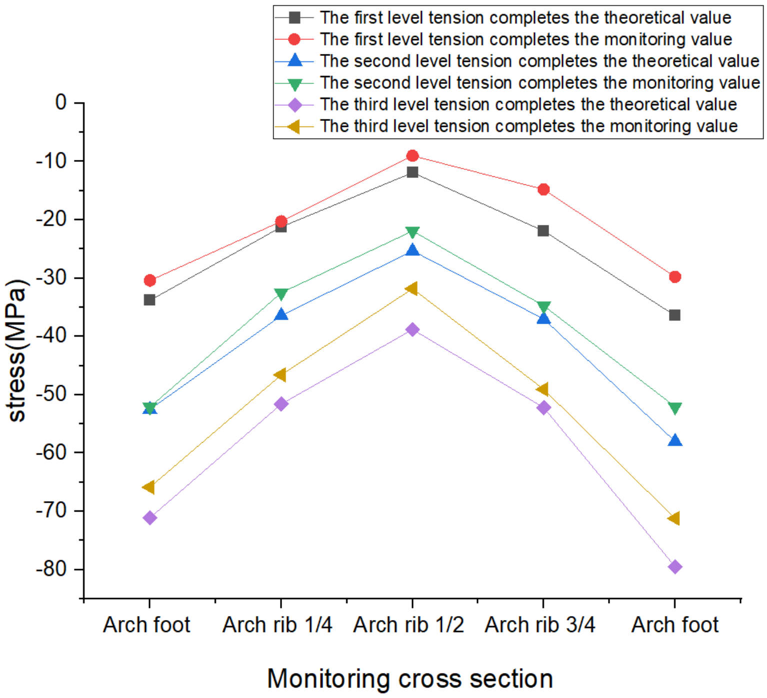

Fig. 17 – Arch rib monitoring section stress comparison

CONCLUSION

In this paper, based on the application of the overall intelligent synchronous tensioning in this project, and combined with the finite element software MIDAS Civil, the traditional tensioning method and the overall intelligent synchronous tensioning are compared and analyzed, and the conclusions are as follows.

(1) When the overall cable force of the suspender is greater than the design cable force, the increase of the force at the arch foot is greater than that at the mid-span of the arch rib, resulting in greater stress concentration at the arch foot. On the contrary, greater stress concentration will occur at the mid-span of the arch rib. Therefore, during the construction of the structural bridge, the cable force should be accurately controlled to prevent the construction safety problems caused by stress concentration.

(2) In the suspender tension construction process of the through arch bridge, the application of the overall intelligent synchronous tension technology can control the suspender cable force error within 3% during the bridge completion process. Compared with the traditional asynchronous tension method, the cable force control during the tension process is more accurate. It can control the local stress error of the bridge within 7MPa, prevent local large stress concentration and excessive local deformation during the tension process, and meet the design requirements.

(3) In the process of synchronous tensioning, because the whole bridge jack can be controlled at the same time, it is not necessary to move the jack with the traditional asynchronous tensioning, and the suspender can be tensioned in place at one time, which can avoid multiple iterative calculations, measurement and adjustment of cable force.

REFERENCES

[1] Y.K. Yi, 2007. Research on Key Issues in the Design Theory of Beam Arch Composite System. Tongji University.

[2] J.Y. Luo, 2004. Research on Construction Control of Long Span Steel Tube Concrete Arch Bridge. Guangxi University

[3] Y. L. Wu, M. W. Qiu, S. K. Ma, X. L. Gao, Y. H. Han, 2022. Research on Hanger Force and Main Arch Stability of Long-Span Concrete-Filled Steel Tube Arch Bridge. Geofluids, vol. 2022, 3541528.

[4] J. P. Zhang, A. R. Liu, Z. J. Ma, H. Y. Huang, L. B. Mei, Y. H. Li, 2013. Behavior of Self-Anchored Suspension Bridges in the Structural System Transformation. Journal of Bridge Engineering, vol. 18(8), 712-721.

[5] A.B. Gu, 2000. Bridge Engineering-Volume 2. China People's Communications Publishing House, 73-74.

[6] H. K. Kim, M. J. Lee, S. P. Chang, 2006. Ination of hanger installation procedure for a self-anchored suspension bridge. Engineering Structures, vol. 28(7), 959-976.

[7] Y. L. Deng, L. M. Deng, 2021. Suspender Replacement Method for Long-Span Concrete-Filled Steel Tubular Arch Bridges and Cable Force Measurement Based on Frequency Method. Advances in Civil Engineering, vol. 2021, 7308816.

[8] B Xu, D Dan, Y Zou, 2019. Accurate identification method and practical formula of suspender tension based on tri-segment suspender dynamic model. Engineering Structures, 109710.

[9] Q. Qi, R.L. Zhang, R.P. Hu, C. Wang, 2017. Experimental study on the variation law of cable force during the construction process of tied arch bridges. Journal of Railway Science and Engineering, Vol. 14(09), 1893-1898.

[10] D. Liang, J. Ma, Z. Liu, Y. Wang, 2016. A Cable Adjustment Method for Arch, Curved Beam and Cable Composite Bridge in Completion State. Journal of Highway and Transportation Research and Development, vol. 33(8).

[11] S.S. Fu, 2003. Determination and adjustment of cable force for highway cable-stayed bridges. Dalian University of Technology.

[12] W. Su, H. Di, Y. Gao, H.H. Liao. D.K. Liu, 2022. A construction system and method for synchronous tensioning and suspension force adjustment of railway bridges. Tianjin.

[13] Q. Li, Z.G. Zhao, J. Liu, H. Peng, 2015. The Application of Formal Iteration Method in the Construction Control of Suspension Rods in Through Tied Arch Bridges. Sino foreign highways, Vol. 35(03), 192-195.

[14] C.F. Lu, 2015. Bridge engineering. China Railway Publishing House, 41.

CIVIL ENGINEERING JOURNAL

Article no. 22

THE CIVIL ENGINEERING JOURNAL 3-2025

STUDY ON THE MECHANICAL PROPERTIES OF LARGE DIAMETER AND LONG DISTANCE REINFORCED CONCRETE PIPE JACKING IN WEAK STRATUM

Haijun Lu, Xuhui Cui ,Yanhe Zhang, Lei Yang and Rui Yang

CCCC Second Harbour Engineering Company Ltd., Wuhan, China, email: luhaijun1163@163.com

Received: 18.12.2023
Received in revised form: 23.09.2024
Accepted: 13.08.2025

ABSTRACT

In order to study the mechanical properties of large diameter and long distance reinforced concrete pipe jacking process in weak stratum, based on the Tangxun Lake sewage pipe jacking project in Wuhan, the jacking force, contact pressure, slurry pressure and pipeline strain were monitored on site, and their changes in the jacking process were analyzed, which provided reference significance for the similar projects in the future. The results showed that during the jacking process, the axial stress of the pipe was mainly compressive stress, and there are some areas of stress concentration. As the jacking distance increases, the axial stress of the pipe first increases and then remains relatively stable. The hoop strain of pipe is mainly compressive strain, which is mainly affected by earth pressure and axis deviation. Under the slurry pressure, the hoop strain at the top and bottom of the pipe increases, while the left and right sides decrease. The bottom of the pipe is in contact with the soil, and the contact pressure is the largest, while the left and right sides are in full or partial contact with the slurry. The crown of the pipe is in contact with the slurry and the contact pressure is affected by the mud pressure. In addition, the contact pressure is not directly related to the jacking distance.

KEYWORDS

Weak stratum, Large diameter reinforced concrete pipe jacking, Mechanical properties, Field testing

INTRODUCTION

As urbanization progresses towards a high-quality and sustainable stage, higher demands are being placed on urban underground space construction technology. Exploring construction technologies with low environmental impact, high efficiency, and low cost has become a common goal. The emergence of pipe jacking technology is a beneficial attempt, and now it has been widely used in underground engineering. The safety of pipe structure is a key factor to ensure the smooth progress of pipe jacking engineering.

In terms of field testing, Milligan and Norris [1-2] conducted tests on the angle deviation and stress distribution, longitudinal strain, axial strain, shear stress, and contact pressure between the pipeline contact surface and soil layer at the pipe connection through monitoring instruments arranged at the pipe jacking construction site. Zhang Peng [3-6] and others combined with the arch-shaped curtain jacking project in Gongbei Tunnel to conduct on-site monitoring of the axial and hoop strains and contact pressure of the pipe by installing monitoring instruments on the pipe, studying the distribution and variation of axial, hoop, and contact pressure of pipe jacking under deep burial conditions during the construction process. Zhang Yunlong [7] and others studied the change law of the pressure around the rectangular box and the contact state of the box-soil-lubricant through the field detection of Suzhou rectangular box pipe jacking project. Through the in-situ monitoring and direct shear test, Liu Kaixin[8] and others found that in the severe pipe sticking, the hoop strain of the pipe in contact with the blockages showed the tensile state, while the pipe in contact with the slurry or groundwater exhibited compressive strain. Based on the field monitoring of Hubei comprehensive pipe jacking project, Feng Xin [9] and others analyzed the change rules of contact pressure, mud pressure and pipe strain. Wei Gang [10] and others combined with a sewage interception project to investigate the compression size and state of the pipe by installing strain instruments on the inner and outer layers of the pipe jacking skeleton. Feng Jinyong [11] and others found through on-site monitoring that the hoop stress of the pipe was initially under compression and later turned to tension, and the longitudinal strain change was controlled by the deviation of the pipeline axis. Ji et al. [12] proposed a method to predict the jacking force of the pipe jacking through the particle model. By calibrating the microscopic parameters of the sand, the particle model can reproduce the macroscopic material behavior of the sand, so as to derive the contact pressure around the pipe. Then the interface friction coefficient is used to evaluate the friction resistance of the pipe jacking. Sheil[13] proposed a probabilistic observational approach for predicting microtunneling jacking forces.

In terms of numerical simulation, Zhou [14] analyzed the influence of different mechanical parameters of gaskets and different loads on the stress of pipes by using numerical simulation software,and found that pipeline deviation is an important reason for pipe tension and local compression, which can be improved by increasing prestressing belts. Zeng Qin [15] also used simulation methods to study the changes in internal forces, pipe-soil contact pressure, and pipe-soil contact resistance of rectangular pipe jacking during construction. Liu Xian [16] and others established a numerical model of longitudinal force changes with jacking distance in tunnel sections and verified it theoretically with the pipe jacking tunnel project at Jing'an Temple Station of Shanghai Metro Line 14. Yen et al. [17] used ABAQUS software to establish the jacking force of pipe jacking models under different contact areas and different slurry additives lubrication conditions,and obtained the effects of contact area and slurry additives on the jacking force of pipe jacking. Wen et al. [18] conducted a numerical and theoretical study on jacking force prediction in slurry pipe jacking traversing frozen ground.

In summary, existing research mainly focuses on the internal forces of pipes and the combined contact pressure, but there is little research on ultra-long distance and large diameter reinforced concrete pipe jacking in soft soil layers. Therefore, this paper combines the Tangxunhu sewage treatment plant tailwater drainage pipe jacking construction project in Wuhan City to conduct corresponding monitoring of the pipeline, study the stress characteristics during pipe jacking construction, and explore its distribution and variation rules, providing a reference for the safe design and construction of pipelines.

PROJECT PROFILE

The starting point of the Tailwater Discharge Project of Tangxun Lake Wastewater Treatment Plant is the Tangxun Lake Wastewater Treatment Plant, and the end point is Donggang, with a total length of about 10.8km. The pipeline is mainly divided into land and lake sections, and the pipeline construction is mainly carried out by the method of pipe jacking, with a small amount of open-cut sections in the land section. The land section adopts double-row DN1240×20mm welded steel pipes for jacking, with a total length of about 7.06km; the lake section adopts D4000 reinforced concrete pipes for jacking, with a total length of about 3.77km. The lake section includes three jacking sections, which are 1#~2# shaft, 3#~2# shaft, and 4#~3# shaft, and the general layout of the project is shown in Figure 1.

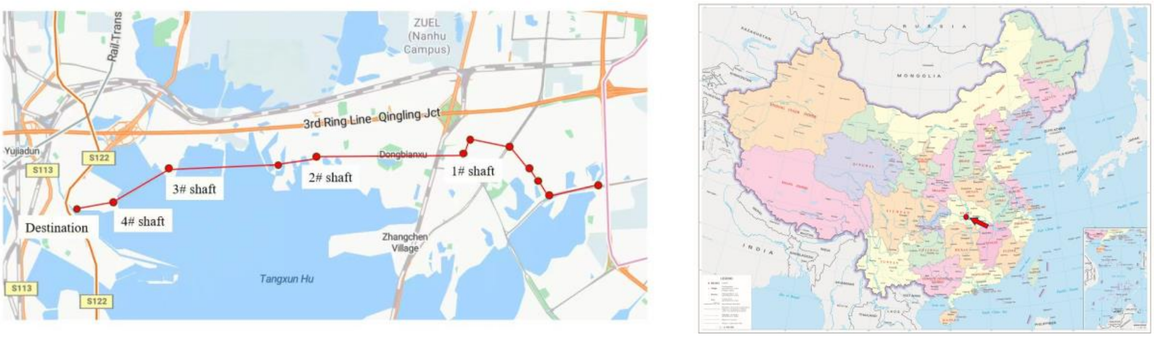

（a） （b）

Fig.1 - The general layout of the project

The on-site test was carried out on the 3#~2# shaft jacking section, which is about 1556.8m in total length. The geological profile of the construction area is shown in Figure 2, and the geological layers of this section are very complex, including loose fill, silt, clay, silt-clayey-fine sandy soil, fine sandy soil, fine sandy soil interbedded with silt-clay, clayey-medium sand with high plasticity, highly weathered mudstone, and moderately weathered mudstone from top to bottom, with the soil properties shown in Table 1. The jacking mainly passes through silt-clayey-fine sandy soil, fine sandy soil, clay, fine sandy soil interbedded with silt-clay, and highly weathered mudstone. Among them, silt-clayey-fine sandy soil is in a soft plastic to flowing state, with low strength, high compressibility, and high difficulty and risk in jacking construction.

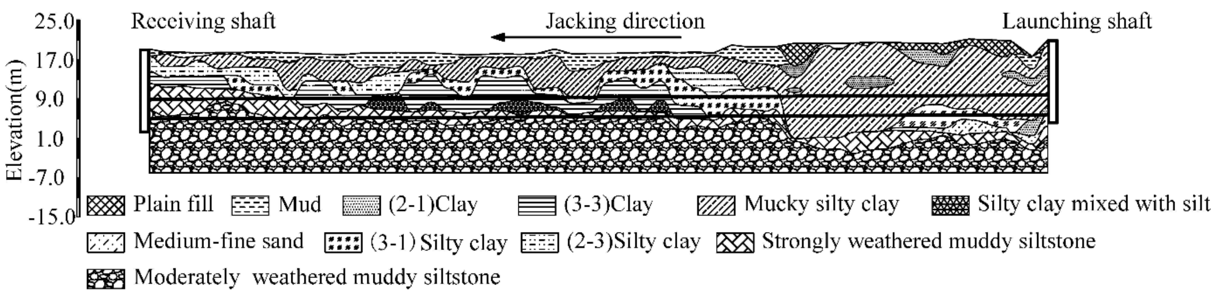

Fig.2 - Geological profile of pipe jacking

Tab. 1 - Summary of soil properties

Soil	Density (g/cm3)	Internal friction angle (°)	Cohesion (kPa)	Elastic Modulus （MPa）	Poisson's ratio
Plain fill	1.85	8	10	8	0.3
Silt	1.67	4	9	6	0.35
Clay	1.76	6	16	10	0.32
Muddy silty clay	1.78	5	11	10	0.41
Silty clay	1.91	11	27	20	0.3
Silty clay with silt	1.97	10	20	24	0.28
Strongly weathered argillaceous siltstone	2.05	17	48	120	0.25
Moderately weathered argillaceous siltstone	2.16	22	70	210	0.22

MONITORING SCHEMES

During on-site testing, the contact pressure around the pipe, mud pressure, and steel bar strain were mainly monitored, and were measured using earth pressure cell, pore water pressure gauge, and steel bar strain gauge respectively. The 36th, 77th, 155th, 204th, 291st, 355th, 462nd, and 519th pipes were selected as test sections, among which the 36th, 291st, and 519th pipes were equipped with 4 earth pressure cells, 4 pore water pressure gauges, 4 hoop strain gauges, and 4 axial strain gauges, as shown in Figure 3. The remaining pipes were only equipped with 4 hoop strain gauges and 4 axial strain gauges. The technical parameters of the sensors used are shown in Table 2. The acquisition frequency was 1 time/10 minutes.

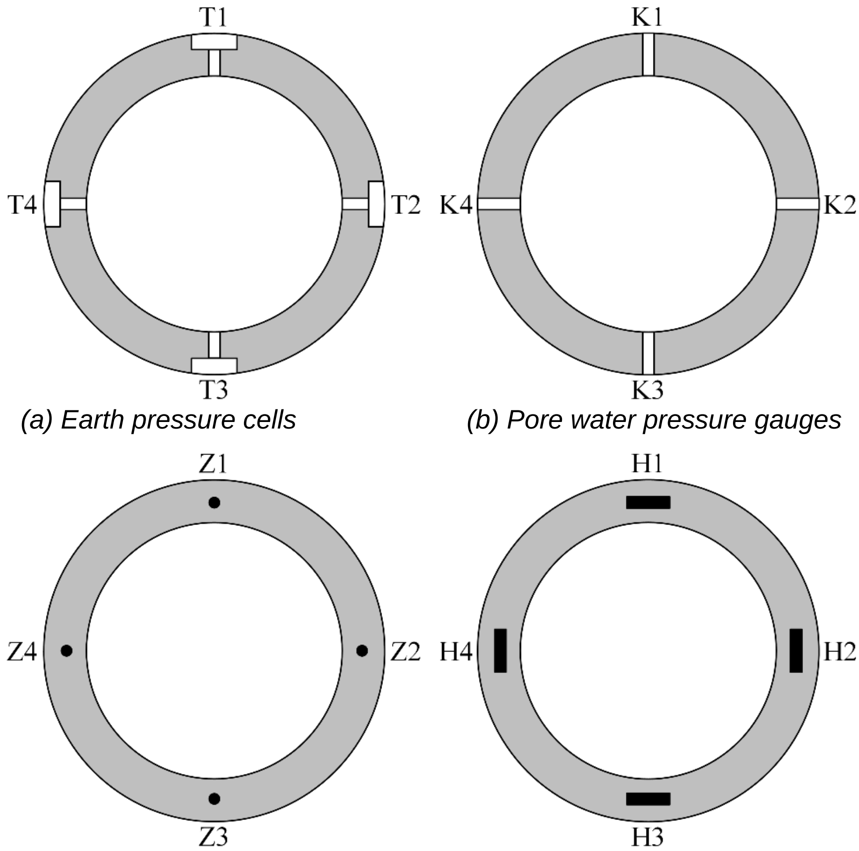

(a) Earth pressure cells *(b) Pore water pressure gauges*

(c) Axial stress gauges *(d) Hoop stress gauges*

Fig.3 - Schematic diagram for locations of monitoring points

Tab. 2 - Sensor Technical Parameters

sensor type	model	Range	precision
earth pressure gauge	JTM-V2000B	0~1MPa	2kPa
Pore water pressure gauge	JTM-V3000F	0~1MPa	2kPa
Rebar Strain Gauge	JMZX-416HAT	±1500με	1με

DOI 10.14311/CEJ.2025.03.0025

ANALYSIS OF MONITORING RESULTS

（1） Jacking force analysis

The variation curve of jacking force in the 3#~2# working well jacking section is shown in Fig.4. The jacking force generally increases with the increase of jacking distance, showing a stepwise rise, with a maximum of up to 26,000kN. However, there are irregular fluctuations in the rising trajectory. According to the changes in the geological layers, the variation of jacking force can be divided into three stages. When entering the fine sandy soil and clay layers from the silt-clayey-fine sandy soil layer, the jacking force increased significantly and then stabilized; when entering the highly weathered mudstone layer from the fine sandy soil and clay layers, the jacking force also increased significantly. Combined with the actual situation on site, the sharp rise and fall around 500m is due to the occurrence of floating phenomenon in the jacking trajectory, and the sudden increase in resistance in some pipes leads to the increase of jacking force. Then, the measure of activating relay station No.3 was taken to effectively alleviate the problem of abnormal increase of jacking force, resulting in the decrease of jacking force. At 670m, when the relay station was stopped, the frictional resistance increased and the jacking force rebounded; from 800m to 1200m, when the machine head entered the fine sandy clay layer, the frictional resistance was relatively small, and the jacking force fluctuated within a certain range. At 1300m, the jacking force reached its maximum value, because the synchronous grouting pressure decreased with the increase of distance, resulting in poor lubrication effect of the pipe outer wall and continuous increase of frictional resistance. After increasing the slurry injection pump, the external grouting of the pipe outer wall was strengthened, the frictional resistance of the pipe outer wall decreased, and the jacking force decreased and fluctuated within a certain range. The formula of the mud is shown in Table 3.

Tab. 3 - The formulation of the mud

Type of mud	Formulation of mud
Synchronous grouting mud	Bentonite : Na2CO3 : CMC = 8% : 0.4% : 0.1%~0.2% (The ratio of all the above formulation is the mass ratio to water)
Secondary grouting mud	Bentonite : Na2CO3 : CMC = 6% : 0.3% : 0.1%~0.2% (The ratio of all the above formulation is the mass ratio to water)

Note: CMC is a kind of additive, which can improve the viscosity of mud.

In the early stage of jacking, due to the initial lubrication grouting, the pipe circumference did not form a complete mud jacket, and the unit frictional resistance around the pipe was relatively high, about 26kPa. From 0m to 30m of jacking, the unit frictional resistance decreases linearly. From 30m to 300m of jacking, the rate of decrease in unit frictional resistance gradually slows down. After 300m, the unit frictional resistance basically stabilizes at around 1.2kPa. According to relevant engineering specifications and engineering cases, controlling the unit frictional resistance at around 1.2kPa in such geological layers is already a relatively low level, indicating that the grouting lubrication has achieved good results.

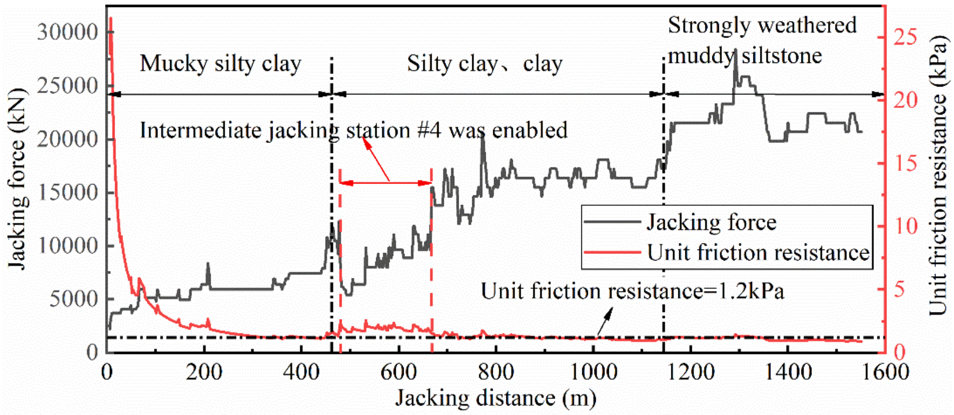

Fig.4 - Jacking force and unit frictional resistance

（2） Analysis of pipe circumference contact pressure and mud pressure

The test data of the 36th pipe at the jacking distance of 280~285m was selected for analysis, and the contact pressure around the pipe is shown in Figure 5. The contact pressure around the pipe is in the range of 160~270kPa, and the order of magnitude is bottom contact pressure > left and right contact pressure > top contact pressure. The reason may be that the gravity of the pipe is greater than the buoyancy, and the pipeline is in full contact with the soil. The gravity and the top soil pressure of the pipeline all act on the bottom soil, resulting in a larger bottom foundation reaction force and a larger contact pressure around the bottom pipe; while the strata where the left and right pipes are located are the same, the magnitude and direction of the strata soil pressure on the pipe are equal and opposite, and the pore water pressure also has basically the same effect on the pipe. Therefore, the contact pressure around the pipe on both sides is basically the same. For the contact pressure received at the top, it indicates that there is no annular clearance at the top, and it is also in a full contact state, but because the top only receives the vertical soil pressure of the overlying soil, the contact pressure is relatively small. At the same time, it can be seen that the contact pressure fluctuations of the four parts of the pipe during the jacking process are small overall, and the influence of jacking on the contact pressure around the pipe is relatively small.

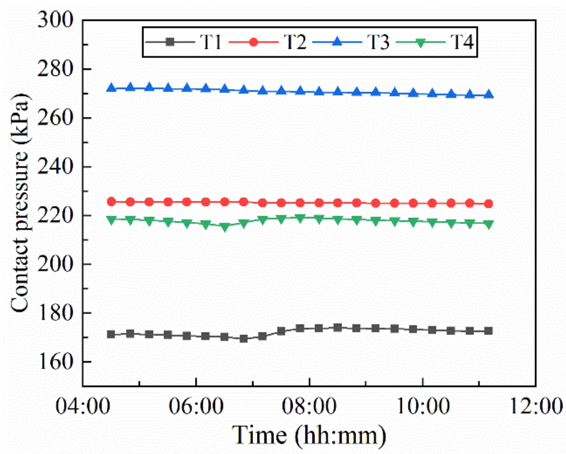

Fig.5 - No. 36 pipe contact pressure

During the on-site testing process, it was found that the pore water pressure gauge had poor testing results and did not reflect the actual grouting situation. The reason for this may be that the top hole of the pore water pressure gauge was filled with soil, preventing the slurry from entering. Therefore, the analysis of slurry pressure was no longer conducted.

To explore the effect of grouting on the contact pressure around the pipe, the changes in contact pressure of the 36th pipe during a certain grouting process were analyzed as an example. As shown in Figure 6, after opening the grouting valve, the bottom contact pressure around the pipe did not change significantly, while the other three areas rapidly increased and maintained stable contact pressure under the action of grouting pressure. The phenomenon of small changes in bottom pressure is firstly related to the arrangement of the grouting system inside the pipe. In order to make room for the drainage system and power system wiring inside the joint, and also facilitate personnel access, no grouting holes were arranged at the bottom, so the bottom was not directly affected by grouting pressure. Secondly, due to the close contact between the bottom of the pipe and the soil, it is difficult for the slurry injected from both sides to penetrate into the bottom, ultimately resulting in no change in the contact pressure around the bottom of the pipe with the change of grouting pressure. However, in the top, right, and left areas, after opening the grouting valve, the slurry invaded the outside of the pipe. Due to the formation of stable mud skin, it prevented the rapid dissipation of grouting pressure and acted on the pipe outer wall, increasing the contact pressure around the pipe. Further analysis of the changes in contact pressure showed that the top increased by 26 kPa, the right increased by 22 kPa, and the left increased by 28 kPa. The output pressure of the grouting pump was 250 kPa, indicating that the slurry pressure loss was significant during transportation and injection into the outer wall of the pipe. The slurry pressure actually acting on the pipe outer wall was about 1/10 of the output pressure of the grouting pump. After closing the grouting valve, the contact pressure around the top, left and right sides of the pipe rapidly decreased in a few minutes, and the slurry pressure rapidly dissipated outside the pipe, causing the contact pressure around the pipe to return to the level before grouting.

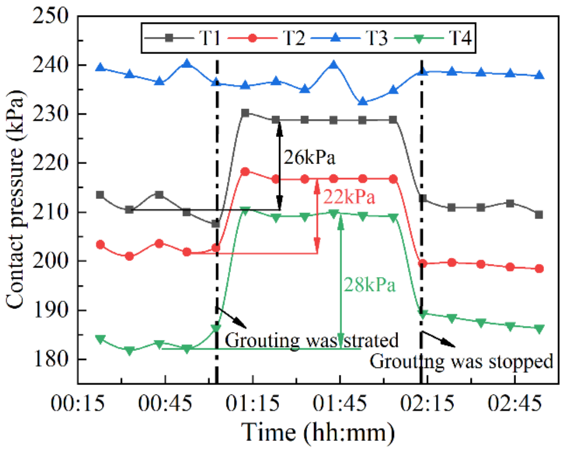

Fig.6 - Contact pressure of pipe No. 36 during grouting

During the stoppage of jacking, the contact pressure of the 36th pipe is shown in Figure 7. Since the bottom contact pressure is less affected by slurry pressure and the actual changes are relatively insignificant, only the pressure changes in the other three areas are studied. After the completion of jacking, the contact pressure gradually decreased overall. Stage I lasted for 9 hours and showed rapid decline, while Stage II lasted for 6 hours, with a gradually slowing decline rate, tending towards a stable state. This is because after the completion of jacking, the initial pressure of Stage I slurry was relatively high, so the slurry pressure dissipated quickly. At the same time, the soil was squeezed during the jacking process, and the release of deformation caused the contact pressure acting on the pipe to rapidly decrease after the stoppage of work. In Stage II, the rebound force of the soil basically dissipated, and the slurry pressure dissipated slowly, causing the contact pressure acting on the pipe to slowly decrease and reach a stable state at around 17 hours.

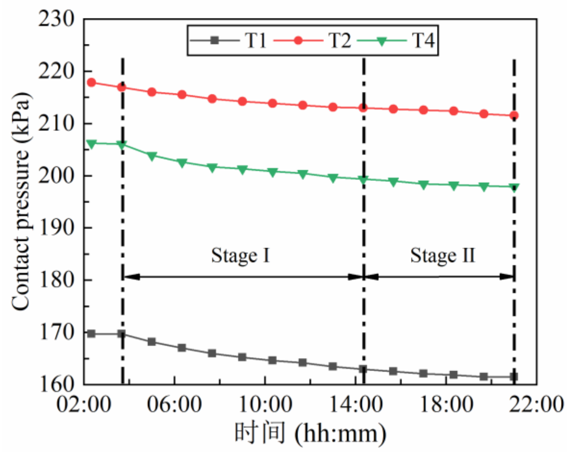

Fig.7 - Contact pressure of No. 36 pipe during jacking stop

（3） Axial strain analysis

Effect of construction stoppage on axial strain

At the jacking distance of 270-275m, the axial strain of the 36th pipe is shown in Figure 8. Throughout the monitoring period, the strains at the four positions, Z1 (top), Z2 (right), Z3 (bottom), and Z4 (left), were negative, indicating that the main stress on the pipe in the jacking process was compressive stress. During the jacking process, the strains of each part of the pipe remained stable. The strains on the left and right sides of the pipe were much greater than those at the bottom and top. The strain on the right side was greater than that on the left side, and the strains at the bottom and top remained basically the same. This indicates that the axial pressure received by the monitoring pipe was unevenly distributed during this jacking distance, mainly concentrated on the left and right sides, with relatively small pressure on the top and bottom. The right side was under greater stress than the left side, possibly due to a slight rightward tilt of the pipe, leading to more concentrated stress on the right side. After the stoppage of work, the strains on both sides decreased sharply, and except for the right side, the strains at other positions were basically the same, remaining within a certain range. This indicates that after the jack was unloaded, the axial stress of the pipe decreased, but a certain amount of strain was maintained, indicating that under the action of frictional resistance, the pipe maintained a certain amount of deformation. The axial stress of the pipe continued to be compressive, and the transmission of the jacking force was mainly completed by the left and right parts, with little change at the bottom and top. During the jacking process of the sections of the pipe at 270-272.5m and 272.5-275m, the strains remained basically unchanged, indicating that the increase in axial stress near the pipe was relatively small.

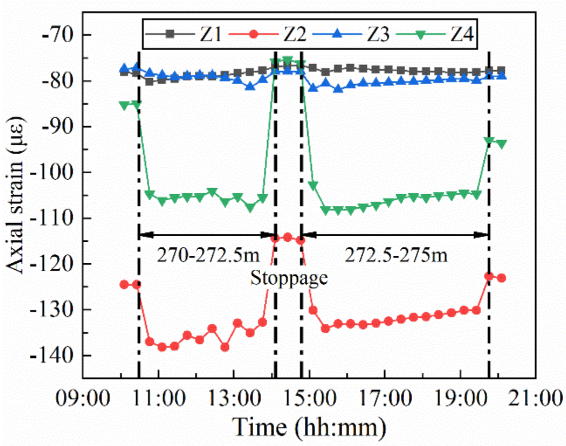

Fig.8 - Axial strain of No. 36 pipe when construction stops

Relationship between axial strain and jacking distance

To study the variation and distribution law of axial stress at the same pipe under different jacking distances, the 36th monitoring pipe was selected as the research object. The average strain values during the jacking process and stoppage period of the pipe at 270-272.5m, 762.5-765m, and 1482.5-1485m were selected as the research objects, as shown in Figure 9.

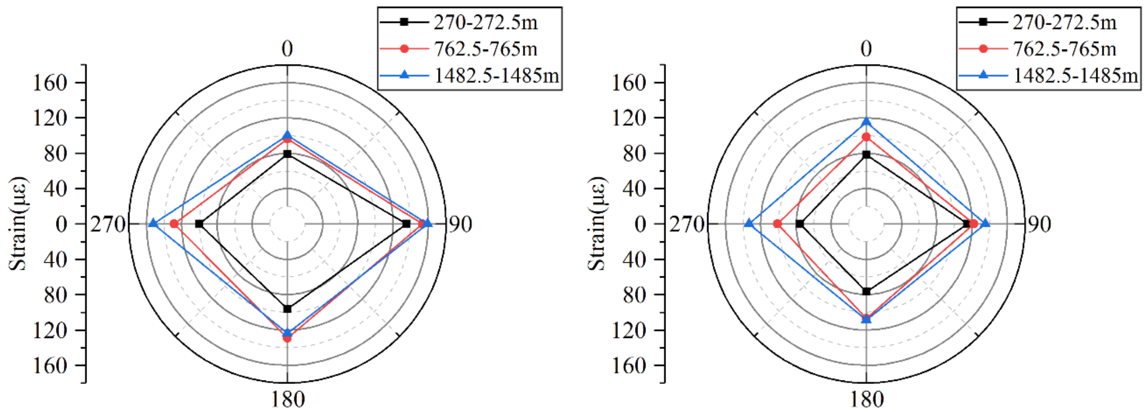

(a) During the jacking process *(b) Shutdown phase*

Fig.9 - Axial strain comparison diagram of No. 36 pipe with different jacking distances

Comparing the axial strain values of the three different jacking distances, it can be seen that the overall strain values of each part of the pipe in the last two jacking distances are slightly larger than that of the first jacking distance, and the strain changes of each part are relatively small, indicating that the axial strain of the pipe remains basically unchanged with the increase of jacking distance. At the same time, it can be observed that the strains on the left and right sides of the pipe are larger, and the strains at the bottom and top are smaller in all three jacking distances, indicating that the overall stress state of the pipe remains basically unchanged. With the increase of jacking distance, the stress on the left and right sides becomes more concentrated, and the transmission of the jacking force is mainly completed by the left and right sides. As shown in Figure 9(b), during the stoppage period, the axial strain of each part of the pipe gradually increases with the increase of jacking distance, indicating that the axial stress of the pipe in the stable state gradually increases after the jack is unloaded. The reason is that with the increase of jacking distance, the contact area between the pipe and the stratum continuously increases, resulting in an increase in frictional resistance. Under the action of frictional resistance, the rebound of the pipe gradually decreases, leading to an increase in axial stress in the stable state. At the same time, it can also be observed that with the increase of jacking distance, the distribution range of axial stress of the pipe during the stoppage period remains basically unchanged.

Effect of pipe deflection on axial strain

During the construction process of large-diameter reinforced concrete pipe jacking, after the relay station is activated, the maximum stroke inconsistency caused by the installation error of the relay station cylinder leads to non-uniform pushing in the pushing process, resulting in a large torque on the pipe and causing deviation of the pipe behind the relay station.

According to on-site records, after the 3rd relay station was activated, the pipe was deviated to a certain extent. The 77th pipe was just behind the 3rd relay station. In order to explore the influence of pipe deviation on the distribution law of axial stress, the axial stress monitoring data of the 77th pipe from April 4th to April 12th were selected as the research object, mainly studying the changes of axial stress under pushing state. As shown in Fig.10, the strain on both sides of the pipe remained basically between -100με and -200με during the entire monitoring period, while the strain at the bottom of the pipe gradually increased from -100με on April 5th to -500με. At the same time, the strain at the top decreased from -400με to around -200με, and then alternated between increase and decrease. It can be seen that the deviation of the pipe changes the distribution of axial stress, resulting in a negative correlation between the axial strain distribution of the top and bottom regions of this pipe. At the same time, it can also be seen that the left and right sides of the pipe do not show significant changes in stress. Based on the above analysis, the size of axial stress in the symmetrical part of the pipe shows a clear negative correlation.

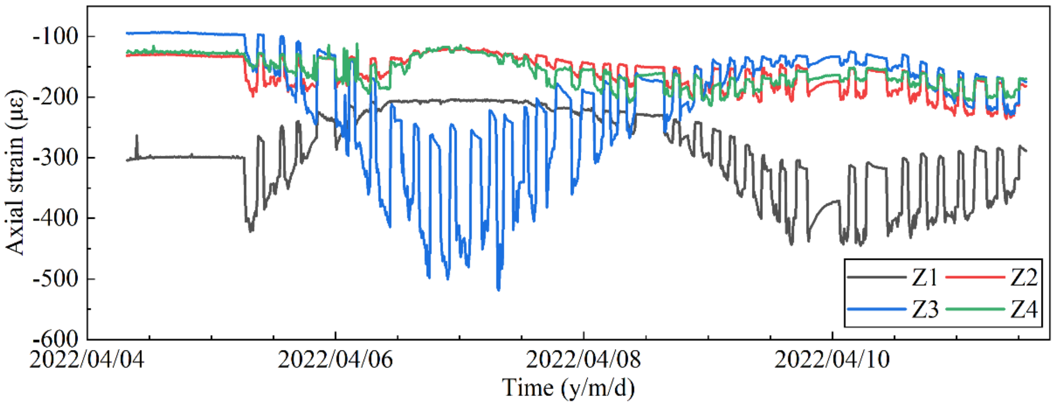

Fig.10 - Axial strain of pipe No. 77

Axial strain analysis of pipes at different positions

To study the variation law of axial stress at different positions of the pipe during the jacking process at the same time period, three consecutive axial strain monitoring sections arranged after the 3rd relay station (to avoid the influence of the relay station on axial stress) were selected as the research objects, namely the 77th, 122nd, and 155th pipes. Due to serious uplift in the later stage of jacking, an earlier jacking period was selected to avoid the influence of uplift. According to data comparison, axial stress of the pipe was mainly concentrated at the top and bottom during this period, with small changes on both sides. The variation law of the top and bottom was basically the same. Therefore, the variation law of axial stress was studied by focusing on the top of each pipe.

As shown in Figure11, the axial strain variation law of the three pipes was basically consistent during the jacking process, with the strain of the 155th pipe > the strain of the 122nd pipe > the strain of the 77th pipe. This is because as the jacking distance increases, the frictional resistance borne by the entire jacking pipe becomes greater, and the applied jacking force also increases accordingly. The pipe closer to the back end bears greater axial force, resulting in greater strain. During the stoppage period, after the unloading of the cylinder, the strain of the pipe decreased sharply, and the strain of the three pipes was basically the same, with the same axial stress borne.

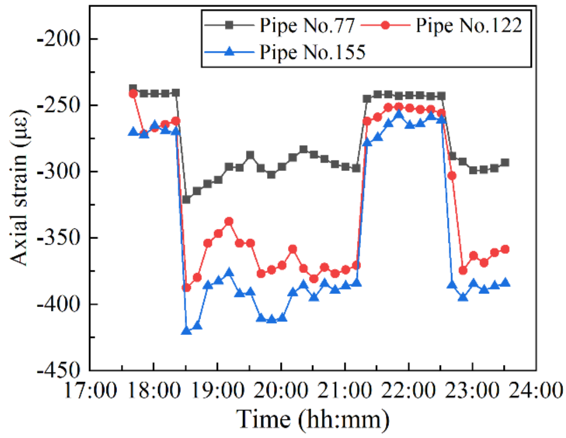

Fig.11 - Axial strain of different pipes in the same period

（4） Hoop strain analysis

Effect of jacking distance on hoop strain

During the jacking process at 285-300m, 859-874m, and 1514-1529m, the hoop strain of the 36th pipe is shown in Figure 12. The hoop strain of each part of the 36th pipe is relatively stable, with a fluctuation range of no more than 20με. From the comparison of strain magnitude, the strain at the bottom > the strain at the top > the strain on the left > the strain on the right, and the overall strain is compressive, indicating that the entire pipe has been under compressive stress as the jacking distance increases. At the same time, as the jacking distance increases, the magnitude relationship of hoop stress at each part of the pipe remains consistent, indicating that the hoop stress state of the pipe has not undergone significant changes. Under the interference of the external environment, the hoop stress is relatively stable as a whole, fluctuating within a small range, indicating that a complete mud jacket has been formed outside the pipe outer wall and the pipeline is evenly stressed in the hoop direction.

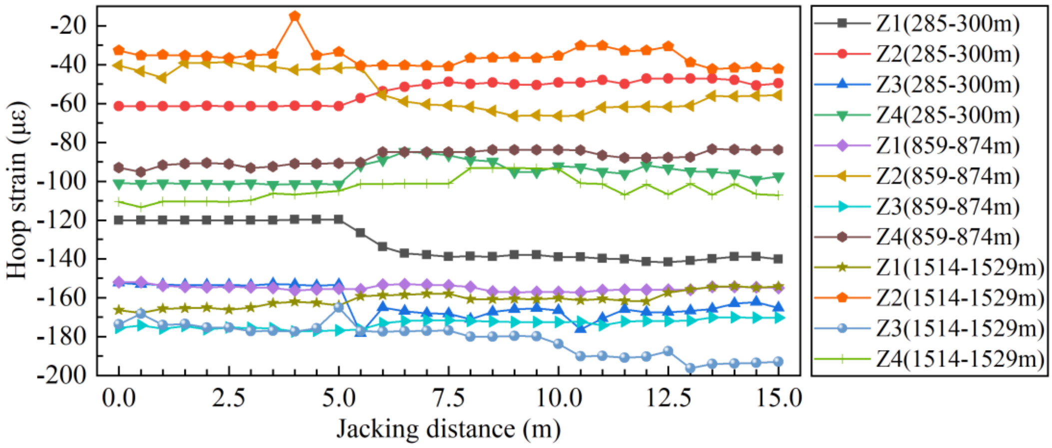

Fig.12 - Hoop strain of No. 36 pipe

Effect of grouting on hoop strain

During a grouting process, the hoop strain of the 36th pipe is shown in Figure 13. Before grouting, the hoop strain of the pipe was basically kept within a relatively stable range, with the strain at the bottom > the strain at the top > the strain on the left > the strain on the right, and the overall strain was compressive, indicating that the pipe was under compressive stress in the hoop direction during the jacking process. However, due to the influence of factors such as the deviation of the pipeline axis caused by the soil pressure of the formation, the distribution of hoop stress of the pipe was uneven, with the stress at the bottom and top much greater than the compressive stress on both sides. After grouting, the hoop strain at the four parts of the pipe fluctuated under the action of grouting pressure, but the overall magnitude relationship of strain did not change. The hoop strain at the top and bottom increased, while the hoop strain on both sides decreased. The reason for this may be that in the annular clearance on both sides, the mud pressure exerted a greater force on the pipe outer wall, squeezing the pipe outer wall on both sides and increasing the hoop stress at the top and bottom of the pipe, while releasing the hoop pressure on both sides of the pipe, resulting in an increase in hoop stress at the bottom and top, and a decrease in hoop stress on both sides.

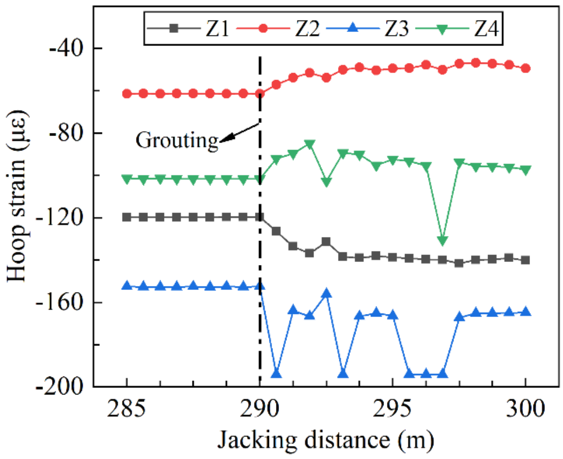

Fig.13 - Hoop strain of pipe No. 36 during grouting

CONCLUSION

This article studies the mechanical performance of large-diameter long-distance reinforced concrete pipe jacking construction in a weak stratum through on-site experiments. Based on monitoring data, the following conclusions were mainly obtained:

(1) The jacking force increases with the increase of the jacking distance, and the overall rise is stepped. The unit friction resistance around the pipe decreases linearly at the initial stage of jacking, and then the reduction rate gradually slows down until the unit friction resistance around the pipe tends to be stable. This is because the lubrication grouting is just started, and the complete mud sleeve is not formed around the pipe. The unit friction resistance around the pipe is large. After the complete mud sleeve is formed around the pipe, the unit friction resistance is reduced to 1.2 kPa, which is a lower level in this kind of stratum.

(2) During the jacking process, the axial compressive stress of the pipe is mainly compressive stress, and the distribution of compressive stress is not uniform. The compressive stress at the top and bottom of the pipe is relatively small, the compressive stress on the left and right sides is relatively large, and the compressive stress on the right side is greater than that on the left side. It is speculated that the pipe is slightly skewed to the right during the jacking process, resulting in a more concentrated stress on the right side; with the increase of the jacking distance, the axial stress of the pipeline increases first and then remains relatively stable. After the shutdown, the axial pressure of the pipe dissipates rapidly, but the overall performance is still in the axial compression state. This is because after the jack is unloaded, the friction resistance around the pipe makes the pipe unable to completely rebound, and a certain compressive strain is maintained in the axial direction, so the whole pipe is in the axial compression state. Under the influence of the deflection of the pipe, the axial stress of the symmetrical part of the pipe shows a significant negative correlation.

(3) During the jacking process, there is a full contact state between the pipe and the stratum, and the contact pressure around the pipe changes little, and the overall performance is the contact pressure around the bottom of the pipe > the contact pressure around the left of the pipe ≈ the contact pressure around the right of the pipe > the contact pressure around the top of the pipe. After grouting, the contact pressure at the top, left and right sides of the pipe increases rapidly, while the change of the contact pressure at the bottom is not obvious. This is because the bottom of the pipe is not placed with the grouting hole and the bottom of the pipe is in close contact with the soil. The mud injected on the left and right sides is difficult to penetrate to the bottom of the pipe, resulting in no significant change in the contact pressure at the bottom of the pipe after grouting.

(4) During the normal jacking process, the hoop strain of the pipe is mainly compressive strain. And the hoop strain of the pipe is relatively stable, basically fluctuating in a small range. This is because a complete mud sleeve is formed outside the pipe, and the pipe is evenly stressed in the hoop direction, so the hoop strain of the pipe does not change much; However, after grouting, the hoop strain at the top and bottom of the pipe increases, and the hoop strain on the left and right sides decreases. The reason may be that in the annular gap, the mud pressure on the left and right sides of the pipe is large, and the left and right sides of the pipe is squeezed, so that the hoop stress at the top and bottom of the pipe increases. At the same time, the hoop pressure on the left and right sides of the pipe is released, so that the hoop stress at the bottom and top of the pipe increases, and the hoop stress on the left and right sides decreases.

(5) Based on the study of the mechanical properties of large-diameter long-distance reinforced concrete pipe jacking construction in weak strata, this paper provides the basis for the setting of construction parameters for the subsequent pipe jacking project in the weak strata, which is of great significance for ensuring construction safety.

REFERENCES

[1] Milligan G W E, Norris P. Site-based research in pipe jacking—objectives, procedures and a case history[J]. Tunnelling and Underground Space Technology, 1996, 11: 3-24. https://doi.org/10.1016/0886-7798(95)00041-0.

[2] Milligan G W E, Norris P. Pipe–soil interaction during pipe jacking[J]. Proceedings of the Institution of Civil Engineers-Geotechnical Engineering, 1999, 137(1): 27-44. https://doi.org/10.1680/gt.1999.370104.

[3] Zhang P, Feng X, Zeng C, et al. Field performance of steel pipes during curve jacking in Gongbei tunnel[J]. Tunnelling and Underground Space Technology, 2022, 128: 104585. https://doi.org/10.1016/j.tust.2022.104585

[4] Zhang P, Zhang Y, Ariaratnam S T, et al. Field monitoring and analysis of soil deformation of curved steel pipe jacking in Gongbei tunnel[J]. Tunnelling and Underground Space Technology, 2023, 138: 105153. https://doi.org/10.1016/j.tust.2023.105153

[5] Zhang P, Ma BS, Zeng C, et al. On-site monitoring test and analysis of contact pressure of deeply buried curved steel pipe jacking[J]. Journal of Huazhong University of Science and Technology (Natural Science Edition), 2016, 44(5): 93-97. https://doi.org/10.13245/j.hust.160517.

[6] Zhang P, Wang XY , Zeng C, et al. On-site monitoring test research on mechanical characteristics of deep buried curved steel pipe jacking[J]. Journal of Geotechnical Engineering, 2016, 38(10): 1842-1848. https://doi.org/10.11779/CJGE201610013

[7] Zhang YL, Feng X, Zhou H, Zhang P, Ma BS, Tan LX, Wang JF (2022). Pressure characteristics of rectangular box jacking considering box-soil-lubricant interaction. Tunn Undergr Space Technol 126:104569. https://doi.org/10.1016/j.tust.2022.104569.

[8] Liu K, Xiao A, Zhang P, et al. Study on mechanical response of steel pipe jacking considering the effect of pipe sticking[J]. Tunnelling and Underground Space Technology, 2022, 127: 104617. https://doi.org/10.1016/j.tust.2022.104617.

[9] Feng X, Zhang P, Chen X, et al. Field mechanical properties of large section concrete pipes during jacking in fractured moderately weathered siltstone[J]. Tunnelling and Underground Space Technology, 2023, 131: 104818. https://doi.org/10.1016/j.tust.2022.104818

[10] Wei G, Xu RQ, Yu JY, et al. Field test research on mechanical performance of pipelines in pipe jacking construction[J]. Rock and Soil Mechanics, 2005(8): 1273-1277. https://doi.org/10.16285/j.rsm.2005.08.019.

[11] Feng JY, Jiang K, Pan W, et al. Mechanical characteristics of large-diameter curved pipe-jacking tunnels in soft ground [J]. Science Technology and Engineering, 2021, 21(6): 2420-2426.
[12] Ji X, Ni P, Barla M. Analysis of jacking forces during pipe jacking in granular materials using particle methods[J]. Underground Space, 2019, 4(4): 277-288.
[13] Sheil B. Prediction of microtunnelling jacking forces using a probabilistic observational approach[J]. Tunnelling and Underground Space Technology, 2021, 109: 103749.
[14] Zhou J Q. Numerical analysis and laboratory test of concrete jacking pipes[D]. Oxford: University of Oxford, 1998.
[15] Zeng Q. Research on Load Characteristics and Construction Mechanics Behavior of Quasi-Rectangular Pipe Jacking Tunnel[D]. Chengdu: Southwest Jiaotong University, 2018.
[16] Liu X, Jiao BC, Pan WQ, et al. Research on Time-varying Law of Longitudinal Force of Pipe Jacking in Large Section Steel Structure[J]. Journal of Geotechnical Engineering, 2022, 44(10): 1810-1816. https://doi.org/10.11779/CJGE202210006.
[17] Yen J.; Shou K. Numerical simulation for the estimation the jacking force of pipe jacking[J]. Tunnelling and Underground Space Technology, 2015, 49: 218-229.
[18] Wen K.; Zeng W.; Shimada H.; et al. Numerical and theoretical study on the jacking force prediction of slurry pipe jacking traversing frozen ground[J]. Tunnelling and Underground Space Technology, 2021, 115:104076.

Article no. 23

THE CIVIL ENGINEERING JOURNAL 3-2025

HIGH-PERFORMANCE CONCRETE WITH RECYCLED CONCRETE AGGREGATES: EFFECTS OF PRODUCTION TECHNOLOGY ON MECHANICAL PROPERTIES AND SHRINKAGE

Bohdan Sousedík, Vlastimil Bílek and Oldřich Sucharda

VSB - Technical University of Ostrava, Faculty of Civil Engineering, Department of Building Materials and Diagnostics of Structures, Ostrava-Poruba, Ludvíka Podéště 1875/17, 70800, Czech Republic; bohdan.sousedik@vsb.cz, vlastimil.bilek@vsb.cz, oldrich.sucharda@vsb.cz

Received: 04.06.2024
Received in revised form: 18.03.2025
Accepted: 30.08.2025

ABSTRACT

This research project explores the potential of incorporating fine recycled concrete aggregates (RCA) into high-performance concrete (HPC). The primary objective of this study is to assess the mechanical properties, shrinkage behaviour, and production methodologies, with a particular emphasis on the approach to water dosing. A secondary objective is to assess the potential of internal curing using RCA. The experimental program encompasses concrete mixtures with varying proportions of recycled material and water content. The compressive and bending strength values of the samples were measured, and all samples were monitored for shrinkage over a period of 1 - 28 days. Contrary to the prevailing assumption that the replacement of natural aggregates with recycled ones results in a reduction in strength, this study proposes an alternative conclusion. Specifically, the study indicates that mixtures containing 15% natural aggregate, when substituted with RCA, demonstrate higher strength than those composed exclusively of natural aggregates.

KEYWORDS

High Performance Concrete, Recycled Concrete Aggregates (RCA), Shrinkage, Mechanical properties, Production technology

INTRODUCTION

In the contemporary field of materials engineering for construction, there is a growing emphasis on the use of high-strength and high-performance concrete (HPC) [1, 2]. This trend is driven by the recognition of the numerous advantages offered by HPC, including superior mechanical properties, excellent durability, and extended service life. Moreover, the use of HPC aligns with the increasing demand for innovative technological solutions in construction [3, 4].

A key criterion for the sustainable development of the construction industry is the reduction of energy consumption and the efficient use of available raw materials [5, 6]. Given the limited availability of natural resources, the incorporation of recycled materials plays a vital role in promoting sustainability. It is particularly relevant in the construction industry, which is a major producer of waste, especially construction and demolition waste.

The utilisation of recycled concrete aggregates (RCA) represents an important component of the circular economy and the sustainable development of concrete and concrete structures [7]. The need to preserve natural aggregate resources is becoming increasingly urgent, a concern that is also addressed through life cycle assessment (LCA) analyses [8].

RCA can serve as a partial replacement for natural aggregates; however, several challenges must be carefully considered [9, 10]. The quality of RCA is generally lower than that of high-grade natural aggregates, particularly in terms of mechanical performance. Additionally, RCA typically exhibits a higher water absorption capacity.

According to established standards [11, 12], it is generally acceptable to replace a portion of coarse natural aggregates with coarse RCA. However, the use of fine RCA fractions—such as the 0/4 mm size range—poses particular challenges [13, 14]. These fine particles tend to have high water absorption, irregular grain shapes, and rough surface textures, which often lead to reduced workability in fresh concrete.

Nevertheless, this high absorption capacity can also be leveraged in concrete mixtures, for example, to support internal curing.

As noted by Aïtcin [15], referring to the earlier work of Powers [16], water interacts with Portland cement through two distinct mechanisms:

- Chemically, by reacting with cement compounds to form calcium silicate hydrate (C-S-H) gel, portlandite, and other hydration products.
- Physically, by becoming incorporated as "gel water"—water molecules that are physically bound within the hydration products, yet do not participate in chemical reactions.

Furthermore, a reduction in the volume of hardened cement paste is observed during the hydration process. This volume contraction has been shown to result in an approximate 8% decrease relative to the initial paste volume. The phenomenon is accompanied by an increase in concrete porosity, characterised by the formation of numerous capillary pores.

It has been established that, if the water-to-cement ratio (w/c) is equal to or greater than 0.42, as referenced in [15], then concrete will contain sufficient water to facilitate hydration and the saturation of fine capillaries with water. The phenomenon of volume contraction is characterised by its diminutive scale. However, in the event of the water-to-cement ratio being less than 0.42, the stress exerted by the menisci in fine capillaries is known to induce the shrinkage of hardened cement paste [15-18].

High-performance concrete has a water-to-cement ratio (w/c) of less than 0.42, which results in a significant effect of self-desiccation. In certain cases, the use of internal curing has been employed as a solution to this problem [19, 20, 21]. The process entails the incorporation of porous aggregates that have been saturated with water into the concrete mixture. During the process of self-desiccation, water is consumed and subsequently replaced by water from porous aggregates. Water-saturated expanded clays are typically employed in the self-curing of concrete. However, the utilisation of RCA is a potential avenue for exploration. The strength values of RCA can exceed those of expanded clay, and RCA exhibits a high level of absorption. The use of a minute proportion of RCA can be regarded as a highly advanced method of employing waste and problematic materials.

METHODOLOGY FOR THE EXPERIMENTAL PROGRAM

This article presents three different methods of incorporating recycled concrete aggregates (RCA) into high-performance concrete (HPC) [22] and [23]:

Dry method

RCA has been used to replace a proportion of the natural aggregates in the mixture. This has been achieved by adding RCA to the dry mixture, without the need for water or an increase in the quantity of water used during the mixing process. It is evident that the water absorption capacity of porous aggregates will result in an effective w/c that is lower than that of concrete that does not incorporate porous aggregates. This is due to the fact that the water absorption capacity of the aggregates is greater than that of the natural sand. What will be the effect? Firstly, it is important to note that the workability of the mixture could be suboptimal. The strength values of HPC can be elevated (lower w/c), but the presence of inadequate water content within HPC can have harmful effects on hydration, resulting in shrinkage and the formation of cracks. Furthermore, the strength values of RCA could be lower than those of concrete with natural aggregates, which would also affect the resulting strength values. What will be the result?

Water method

In this approach, RCA is incorporated alongside an increased quantity of mixing water to achieve a workability comparable to that of a reference mixture composed solely of natural aggregates. During mixing, only a portion of the additional water is absorbed by the RCA, resulting in a higher effective water-to-cement ratio (w/c). Consequently, the degree of cement hydration is enhanced. This method of water addition is regarded as the most practical and convenient for application in real-world concrete production.

Pre-soaked method

Prior to incorporation into the concrete mixture, RCA was soaked in water for 24 hours. Although this method is regarded as the most precise in controlling the aggregate moisture content, it can pose practical challenges in implementation.

The objective of this study is to compare the aforementioned methods of incorporating RCA regarding their effects on both flexural and compressive strength values, as well as concrete shrinkage.

MATERIALS

Recycled concrete aggregates (RCA)

Recycled concrete aggregates (RCA) with a fraction size of 0/4 mm, produced by DESTRO company and illustrated in Figure 1, were employed as a replacement for natural sand. The RCA was characterised in accordance with the requirements of ČSN EN 12620+A1 (Aggregates for concrete) [12]. The performed tests included sieve analysis, bulk density determination, and water absorption capacity measurement. Prior to use, the RCA samples were oven-dried at a temperature of (105 ± 5) °C. Density and absorption capacity were measured using the pycnometric method [24]. Concrete samples were produced using both dried RCA and RCA pre-soaked in mixing water for 24 hours.

Fig. 1 – Fraction 0/4 RCA delivered by DESTRO.

A sieve analysis of the recycled concrete aggregates was conducted in accordance with the standard ČSN EN 933-1 (Determination of particle size — sieve analysis of aggregates) [25]. The results are presented as a grading curve in Figure 2.

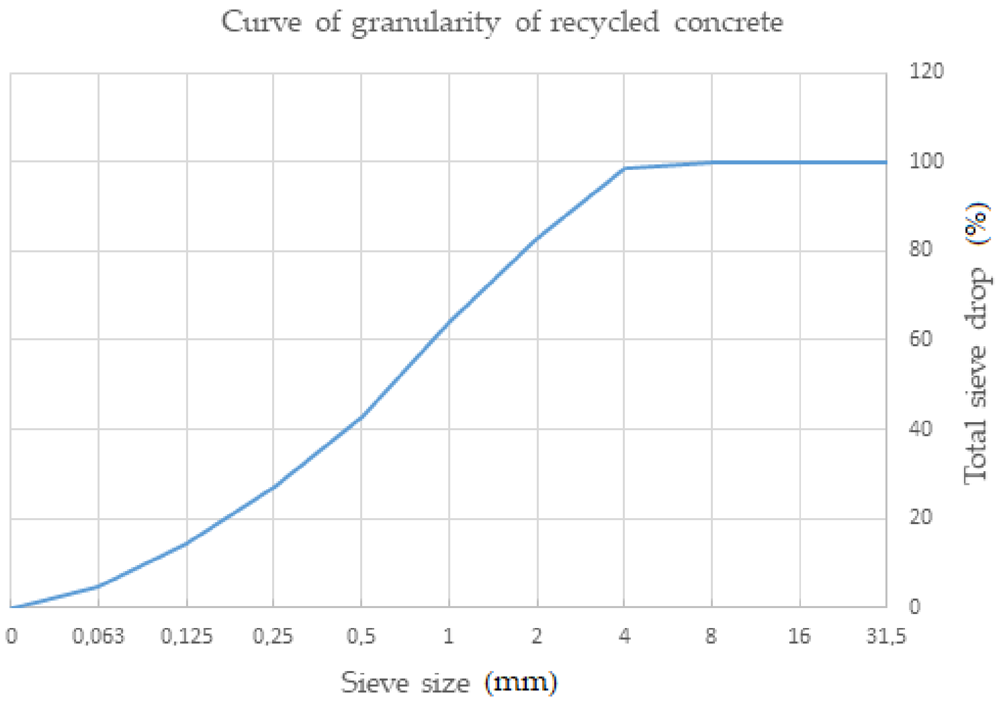

Fig. 2 – Grading curve of recycled concrete aggregates (RCA)

Basic raw materials for concrete production

The concrete was composed of fine natural aggregates, specifically sand 0/4 mm, sourced from the Polešovice gravel plant. This sand meets the requirements for use in concrete and mortar applications [24-25]. Prior to use, the aggregate was oven-dried at (105 ± 5) °C to achieve near-zero moisture content. The absorption rate of this sand was determined to be 1.5%.

Ordinary Portland cement CEM I 42.5 R, manufactured at the Cement Hranice cement factory, was employed in the concrete production.

Potable water from the municipal water supply was used as the mixing water.

Superplasticiser BASF MasterGlenium ACE 300, based on polycarboxylate ethers, was employed to improve the workability of the concrete.

Metakaolin Metaver I (NEWCHEM) was incorporated as a pozzolanic admixture, while finely ground limestone was serving as a second admixture.

Composition of concrete mixes

Eight high-performance concrete mixtures were carefully designed and prepared. Two reference mixtures were produced: one using oven-dried natural sand and the other employing natural sand pre-soaked in water. The use of RCA in both dried and soaked forms address concerns related to its potential deterioration.

A series of alternative mixtures were formulated by partially replacing natural sand with RCA at replacement levels of 10% and 15%. Initially, the dry method was applied, where RCA was added without additional water. Subsequently, two mixtures containing the same proportions of RCA were prepared with increased mixing water to achieve workability similar to the reference mixes. In the final set of mixtures, natural sand was replaced by RCA at 10% and 15%, respectively, with the RCA having been soaked in water for 24 hours prior to mixing.

The compositions of these concretes are shown in Table 1.

Tab. 1 - Composition of high-performance concretes

1 m³	Designation of mixes			
	Reference	10% Recycled	10% Recycled + water	10% Soaked recycled + water
Sand Polešovice 0–4 [kg]	960	864	864	864
Cement CEM I 42.5 R [kg]	650	650	650	650
Metakaolin [kg]	75	75	75	75
Limestone [kg]	60	60	60	60
Recycled concrete 0–4 [kg]	0	96	96	96
Water [kg]	165	165	175	175
Plasticizer Glenium 300[kg]	8	8	8	8

1 m³	Designation of mixes			
	Sand	15% Recycled	15% Recycled + water	15% Soaked recyclated + water
Sand Polešovice 0–4 [kg]	960	816	816	816
Cement CEM I 42.5 R [kg]	650	650	650	650
Metakaolin [kg]	75	75	75	75
Limestone [kg]	60	60	60	60
Recycled concrete 0–4 [kg]	0	144	144	144
Water [kg]	180	165	180	180
Plasticizer Glenium 300 [kg]	8	8	8	8

Testing procedure

Following the mixing process, the concrete was cast into steel moulds measuring 40 × 40 × 160 mm. The moulds were compacted, and a glass plate was placed on top to ensure a flat surface. Subsequently, the specimens were cured for 24 hours in a climate chamber maintained at a temperature with relative humidity exceeding 95%. After demoulding, the specimens were wrapped in polyethylene (PE) foil. To verify the absence of water evaporation during curing, the specimens were weighed both before wrapping and after removal of the aluminium foil at the end of the curing period.

The evaluation of volume alterations was conducted utilising the FORMTEST Mituloyo apparatus, as depicted in Figure 3. In this device, the deformation of the joists is measured on steel spikes that are concreted into the joist during the casting process. The use of steel spikes as measuring bases within the forms during the casting process facilitates the measurement of deformations from the initial day of mixing, thereby providing a reference point for comparison with previous values. Subsequent measurements were conducted on the same days as for ordinary concrete, i.e. at the ages of 2, 3, 4, 7, 11, 18, 25 and 28 days. The measurement was therefore carried out on beams with dimensions of 40x40x160 mm3, with the measurement being taken on three specimens in each case. The measurement of each specimen was conducted in both directions, i.e. twice. The instrument's sensitivity, as evidenced by its capacity to detect a deformation of one micrometer, necessitated meticulous calibration with a wooden standard following each measurement to ensure accuracy and reliability. During the entirety of the measurements, the temperature and humidity levels in the laboratory environment were meticulously regulated. However, these parameters exhibited minimal fluctuations throughout the measurement process, with all values being recorded at a temperature of (23 ± 2) °C and a humidity level of (50 ± 5) %.

Fig. 3. – FORM+TEST strain gauge.

RESULTS

Consistency of high-performance concrete

The consistency values of the concretes are shown in Table 2. Mixtures without additional water tend to exhibit reduced workability, as seen in mixtures A, B, D, and F. This reflects a real-world scenario where the water absorption capacity of recycled concrete aggregate (RCA) is not properly accounted for. In addition to absorption, the coarser surface texture of RCA compared to sand further contributes to the decline in workability. The issue was addressed by adding water to achieve a consistency comparable to the reference mixture (see mixtures A, C, E, and F). However, due to the rougher surface of RCA, more water had to be added than the amount indicated by laboratory-determined absorption. While the measured absorption of RCA was 10%, the effective water addition corresponded to 20%. Concrete made with pre-saturated RCA also showed inferior workability compared to the reference mix F, likely due to the angular shape and rough surface of RCA particles.

DOI 10.14311/CEJ.2025.03.0023

Tab. 2 - Workability of high-performance concretes

	Cone flow [mm]		Mean value [mm]
(A) Reference	250	250	250
(B) 10% Recycled	160	170	165
(C) 10% Recycled + water	250	250	250
(D) 15% Recycled	120	130	125
(E) 15% recycled + water	230	250	240
(F) Reference to soaked	250	250	250
(G) 10% Recycled + water soaked	170	170	170
(H) 15% Recycled + water soaked	180	190	185

Strength of high-value concretes

Table 3 presents the average bending and compressive strength values of the concretes, which are graphically illustrated in Figure 4.

Tab. 3 - Strengths of high-performance concretes

	[MPa]		[kg/m³]
	Bending strength	Compressive strength	Volume density
(A) Reference	10.7	102.4	2373
(B) 10% Recycled	10.6	93.6	2364
(C) 10% Recycled + water	10.4	99.3	2385
(D) 15% Recycled	10.7	88.8	2402
(E) 15% recycled + water	10.1	95.7	2385
(F) Reference to soaked	10.9	99.3	2294
(G) 10% Recycled + water soaked	10.2	94.5	2325
(H) 15% Recycled + water soaked	9.9	96.4	2320

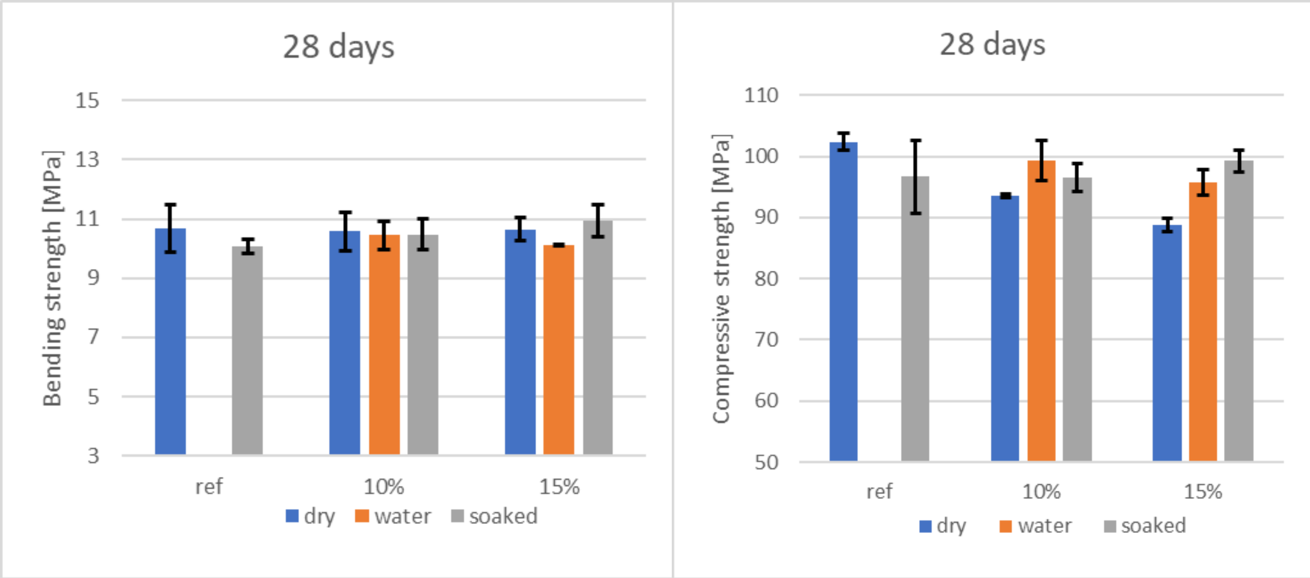

Fig. 4 – Bending and compressive strength values of prepared fine-grained high-performance concretes with error bars representing standard deviation.

The bending strength values are similar regardless of the method used to dose RCA, which is an interesting observation. This may be attributed to the high-water absorption capacity of RCA. Consequently, there is no significant difference between dosing with pre-soaked RCA and adding water to dry RCA. Furthermore, bending strength values remain nearly constant across different RCA dosages. This suggests that the intrinsic strength of RCA likely does not play a significant role in bending strength. Instead, the self-curing ability of RCA may be more influential. A similar trend is observed for compressive strength. While dry RCA reduces compressive strength as its dosage increases, concretes with RCA and added water, as well as those with pre-soaked RCA, exhibit comparable compressive strengths. This may be interpreted as a positive effect of RCA's self-curing properties.

The compressive strength of concrete without added mixing water is slightly lower than that of the reference mix A. This is likely due to the lower strength of the RCA combined with poorer compaction caused by the reduced consistency. Concrete with a higher amount of mixing water shows increased strength, suggesting that the extra water is absorbed by the RCA and does not affect the effective water-to-cement ratio. Similarly, concretes with pre-soaked RCA exhibit strength values comparable to the reference concrete F.

Shrinkage of high-performance concrete with RCA

The results of relative deformation for the individual mixtures are presented in Figures 5 and 6. The graphs are divided according to the recycled material content, with each including a comparison to the reference mixture.

As shown in the graphs, the addition of RCA did not significantly reduce shrinkage, with the smallest shrinkage observed in the reference mix. This outcome may be influenced by several factors: (1) a substantial portion of shrinkage likely occurs during the first day of curing, which was not captured by the measurements; (2) the shrinkage primarily involves changes in absolute volume, while macroscopic dimensional changes are less pronounced; and (3) differences in the water-to-cement ratio (w/c) due to added water are insufficient to cause notable variations in shrinkage.

The shrinkage of concretes containing pre-soaked RCA is presented in Figure 7. The values are nearly identical to those observed in the previous cases of concretes without additional water or with increased mixing water. The concrete with 15% pre-soaked RCA exhibited slightly higher initial shrinkage; however, at 28 days, the shrinkage was slightly lower than that of the reference concrete.

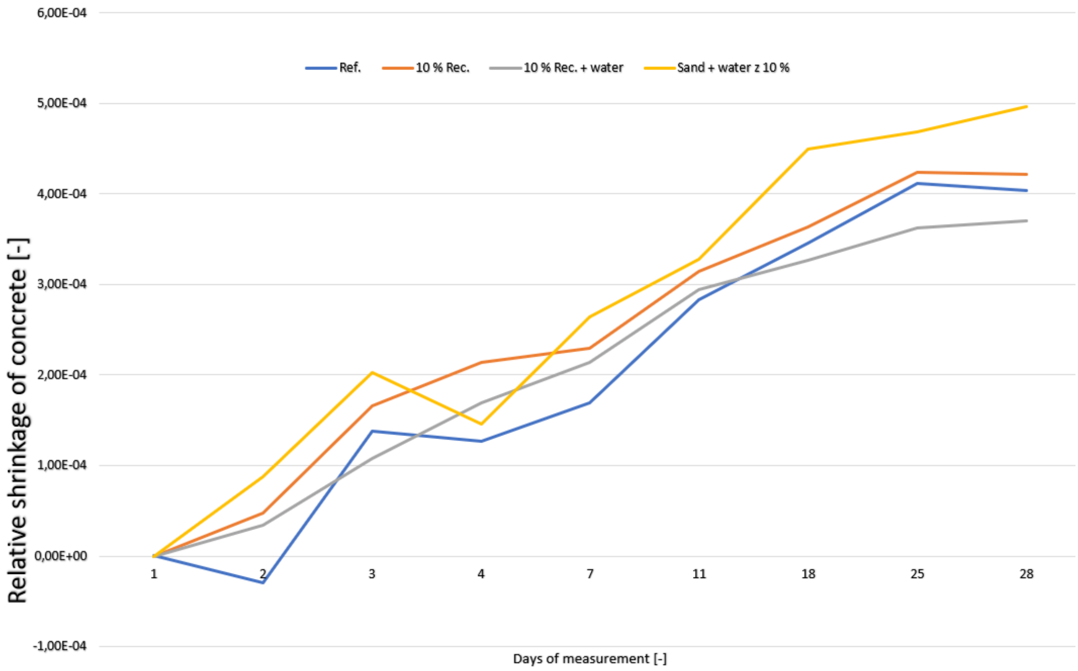

Fig. 5 – Relative shrinkage of concretes with 10% RCA.

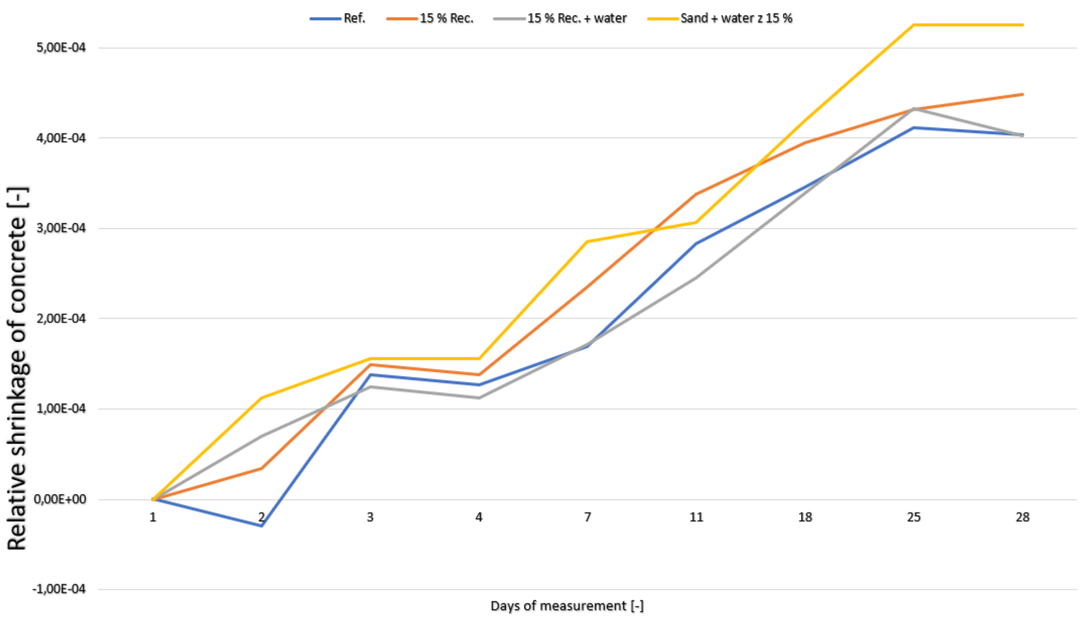

Fig. 6 – Relative shrinkage of concrete with 15% RCA

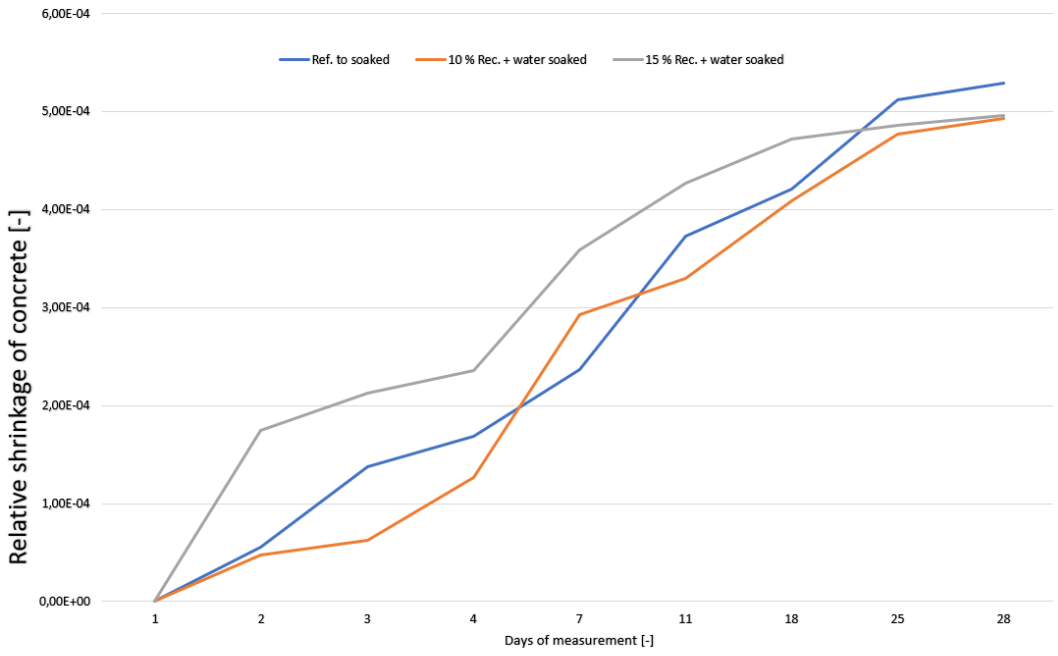

Fig. 7 – Relative shrinkage of concrete with soaked RCA.

CONCLUSION

The aim of this work was to determine whether the addition of recycled concrete to high-performance concrete, as a partial replacement for natural aggregate, affects concrete shrinkage as well as its flexural and compressive strength.

The results of the analysis of the 0/4 fraction of recycled concrete showed that its use in interior applications has no significant effect on shrinkage, regardless of the method of water dosing. Surprisingly, the influence remains very small even when RCA is used in a saturated state or with excess water of up to 21%. It should be noted that shrinkage was not measured during the first day of curing. The results may vary considerably depending on the volume change that occurs during this early stage.

The effect of replacing 10% and 15% of natural aggregates with RCA on compressive and flexural strength is not significant. The dependence of strength on the method and amount of added water is unexpectedly low.

The properties of RCA, particularly its fine fractions, can vary considerably. However, it is not appropriate to automatically consider fine RCA fractions (maximum aggregate size < 4 mm) as poor-quality material unsuitable for use in concrete, especially high-performance concrete, as suggested in ČSN EN 206+A2, Annex E [26].

Further research will focus primarily on measuring shrinkage during the first day of curing and on assessing the impact of RCA on concrete durability. It is also necessary to use and compare a range of different RCA sources.

ACKNOWLEDGEMENTS

This article has been achieved with the financial support of the Ministry of Education, specifically by the Student Research Grant Competition of the Technical University of Ostrava under identification number SP2025/094. This paper was created also as part of the project No. CZ.02.01.01/00/22_008/0004631. Materials and technologies for sustainable development within the Jan Amos Komensky Operational Program financed by the European Union and from the state budget of the Czech Republic.

REFERENCES

[1] Aitcin, P.C. High Performance Concrete; CRC Press: Boca Raton, FL, USA, 2018; ISBN 978036786598.

[2] Moravcik, M.; Bujnakova, P.; Bahleda, F. Failure and damage of a first-generation precast prestressed bridge in Slovakia. Struct. Concr. 2020, 21, 2353–2362.

[3] Fiala, C.; Hejl, J.; Tomalová, V.; Bílek, V.; Pavlů, T.; Vlach, T.; Volf, M.; Novotná, M.; Hajek, P. Structural Design and Experimental Verification of Precast Columns from High Performance Concrete. Adv. Mater. Res. 2015, 1106, 110–113.

[4] Mateckova, P.; Bilek, V.; Sucharda, O. Comparative Study of High-Performance Concrete Characteristics and Loading Test of Pretensioned Experimental Beams. Crystals 2021, 11, 427

[5] Kashino, N., Ohama, Y., RILEM International Symposium Environmental Conscious Materials and Systems for Sustainable Develop-ment, pp.179-186, 2004Schokker A., J., et. al., The Sustainable Concrete Guide Applications, US GREEN CONCRETE COUNCIL, page 183, 2010. ISBN: 978-0-87031-401-8

[6] Schokker A., J., et. al., The Sustainable Concrete Guide Applications, US GREEN CONCRETE COUNCIL, page 183, 2010. ISBN: 978-0-87031-401-8

[7] Xiao, J. Zh., Li, JB, Zhang, Ch., On relationship between the mechanical properties of recycled aggregate concrete: On over-view, Materials and Structures, 39, pp. 655-664, 2006.

[8] Finnveden G., Hauschild MZ, Ekvall T., Guinée J., Heijungs R., Hellweg S., Koehler A., Pennington D., Suh S. Recent devel-opments in Life Cycle Assessment. Journal of Environmental Management, 91 (1), pp. 1 - 21, 2009. DOI: 10.1016/j.jenvman.2009.06.018

[9] Collepardi, M, The New Concrete, Grafiche Tintoretto, p. 436. 2010. ISBN 8890377720.

[10] Aïtcin, P.-C.; Mindess, S. Sustainability of Concrete. Spon Press: New York, NY, USA, 2011.

[11] Pavlů, T., Kočí, V., Hájek, P. Environmental Assessment of Two cycles of Recycled Aggregate Concrete, Sustainability 2019, 11, 6185, doi: 10.3390/su11216185.

[12] ČSN EN 12620+A1. Aggregate for concrete. Prague: Czech Standardization Institute, 2008

[13] Florea, M.V.A., Browers, H.J.H. Properties of Various Size Fraction of Crushed Concrete Related to Process Conditions and Re-USE, Cem. Concr, Res. 2013, 52, 11-21, doi:10.1016/j.cemconcres.2013.05.005

[14] Fan, C.-C, Huang, R., Hwang, H., Chao, S.-J. The Effect of Different Fine Recycled Concrete Aggregates on the Properties of Mortar, Materials 2015, 8, 2658-2672, doi:10.3390/ma8052658.

[15] Aïtcin, P.-C., The Problems with High Strengths and Low w/c Ratio Concretes, Cement-Wapno-Beton, 2/2014, pp.127-137

[16] Powers, T.C. The properties of fresh concrete, John Wiley and Sons, New York 1968, 664p

[17] Jensen, O.M., Hansen, P.E., Water-entrained cement-based materials I. Principles and theoretical background, Cement and Concrete Research 31, 2001 pp.647-654

[18] Tazawa, E. Autogenous shrinkage of concrete, F FN Spon, London, 1998, 406p

[19] Aïtcin, P.-C. Internal Curing, Proceedings of 3rd Int.Symposium Non.Traditional Cement Concrete, Bilek and Kersner (eds) 2008, Brno (Czech Republic) ISBN 978-80-214-3642-8

[20] Mahmoodi,S., Sadeghian,P. Self-Healing Concrete: A Review of Recent Research Developments and Existing Research Gaps, 7th International Conference on Engineering Mechanics and Materials, CSCE Annual Conference, 2019, Laval, QC, Canada, MA11-1 – MA11-10

[21] Al Saffar, D.M., Al Saad, A.J.K., Tayeh, B.A. Effect of internal curing on behavior of high performance concrete: An overview, Case Studies in Construction Materials 10, 2019. doi./10.1016/j.cscm.2019.e0022

[22] Experimental program (https://zenodo.org/) doi:10.5281/zenodo.11475054

[23] Soudedik, B. A possibility of internal curing of HPC using recycled concrete or bricks, diploma thesis, VSB - Technical University of Ostrava, 2018

[24] EN 1097-6 Tests for mechanical and physical properties of aggregates, Part 6: Determination of particle density and water absorption, Prague, Czech Standardization Institute, 2014

[25] EN 933-1. Testing of geometric properties of aggregates - Part 1: determination of grain size - mesh analysis. Prague: Czech Standardization Institute, 2012.

[26] CSN EN 206+A2, Concrete - Specifications, properties, production and compliance. Prague: Czech Standardization Institute 2021.

CIVIL ENGINEERING JOURNAL

Article no. 24

THE CIVIL ENGINEERING JOURNAL 3-2025

MULTI-INDEX EVALUATION METHOD FOR GROUTING REPAIR EFFECT OF DISEASES IN EXPRESSWAYS BASED ON COMBINED WEIGHTING METHOD - CLOUD MODEL

Changyou Wang[1,2], Shuning Zhao[3], Wenliang Zhang[2,4], Kun Dong[3], Peng Li[3] and Junjie Wang[3]

1. *Shandong Hi-speed Group Co.LTD. Shandong High-speed Building, No. 8 Longao North Road, Lixia District, Jinan City, Shandong Province,China; sdglwz@163.com*
2. *Shandong Key Laboratory of Highway Technology and Safety Assessment. Shandong University, Block A, Shandong High-speed Engineering Technology Center, No. 12550, 2nd Ring East Road, Jinan City,China*
3. *Ocean University of China. College of Engineering. 238 Songling Road, Laoshan District, Qingdao,China; shuning9919@163.com, dongkun@ouc.edu.cn, lp@ouc.edu.cn, wjj9@sohu.com*
4. *Shandong Hi-speed Group Co.LTD Innovation Research Institute. Floor 11, Block A1, Haier Green City Olympic Village Central Plaza, Longding Avenue, Lixia District, Jinan City, Shandong Province,China; wenliangzhang@cumt.edu.cn*

Received: 09.05.2024
Received in revised form: 25.07.2025
Accepted: 30.08.2025

ABSTRACT

As a highly practical technique, grouting repair technology is widely used in the practical repair of highway diseases. Existing single indicator detection methods can well reflect certain characteristic indicators of roads, such as compaction and strength. However, the road performance after grouting often needs to be comprehensively evaluated from multiple perspectives, which is difficult to achieve through a single detection method. Therefore, this paper proposes a multi-index evaluation method that comprehensively considers the mechanical properties, uniformity, and compactness of the road after grouting repair. This method combines hierarchical analysis and entropy weight method, integrating subjective evaluation with objective reality, to assign weights to each evaluation index and obtain the weight ranking of relevant influencing factors in the evaluation index system. Based on these indexes and the combined assign weight method, a comprehensive evaluation model for asphalt pavement is constructed and demonstrated by cloud model step by step. Taking the reconstruction and expansion project of two actual expressway to do the case studies, the grouting effect for different road defects is evaluated by the proposed model. After that, the actual excavation situation of the expressway show that the evaluation results are closer to the actual performance. The transition from qualitative and empirical evaluation of grouting repair effect to scientific and semi-quantitative evaluation has been initially achieved. The evaluation model for grouting effect based on the combined weighting method-cloud model can accurately and effectively evaluate the performance of the expressway after grouting repair.

KEYWORDS

Expressway, Asphalt pavement, Grouting effect, Combined weighting method, Comprehensive evaluation model

INTRODUCTION

With the continuous improvement of the transportation network, some roads have begun to exhibit various diseases such as voids and cracks due to the combined effect of traffic volume, operational loads, and construction quality. These issues have seriously affected the driving comfort, service life of highways, and the personal safety of citizens. To address this problem, grouting repair technology has emerged as an ideal non-excavation precision repair method due to its advantages of simple operation, low cost, and minimal impact on traffic. During the grouting process, lots of cementitious material is injected into the interior of the road, for the purpose of filling voids or enhancing intensity [2, 3]. However, as to its concealment characteristics, the detection and evaluation of the grouting repair effect of highway diseases lags behind in practical applications, and the repair effect cannot be fully and accurately verified. Inaccurate or even wrong evaluation of the grouting effect may lead to serious safety accidents. Therefore, it is very important and necessary to effectively evaluate the grouting effect.

A single-index detection method can effectively reflect a certain characteristic of a road, such as strength, stiffness, cracks, porosity and so on. Zhao et al. [2] conducted detections on the thickness, strength, and damage status of various structural layers of cement concrete pavement using Falling Weight Deflectometer (FWD) and Ground Penetrating Radar (GPR), and proposed a method to calculate the fatigue stress of cement concrete pavement. J.N.Karadelis [3] established a finite element model based on FWD to analyze the multi-layer pavement system with different material and geometric characteristics, linking layer stiffness with surface deflection of the pavement system. Liu [4] proposed a method for detecting internal cracks in asphalt pavement based on GPR images by combining the DeepAugment strategy with target detection, which made the crack area features in GPR images more prominent. Pei et al. [5] used GPR to establish a permittivity-void fraction model that can quickly and accurately detect the porosity and uniformity of asphalt mixtures. However, for the performance evaluation of roads, it often needs to be comprehensively evaluated from multiple perspectives, and it is difficult to achieve this goal with a single-index detection method. For this purpose, multiple technical indicators detection are suggested for asphalt pavement performance evaluation, including not limited to pavement damage, uniformity, porosity, compaction, and structural strength.

Similarly, for the grouting repair effects of highway diseases, a multi-indicator comprehensive evaluation model is a relatively reasonable and effective evaluation method. In order to ensure that the road performance evaluation results could objectively reflect the actual road conditions, various analysis theories have been applied to establish many grouting effect evaluation models, evolving from a single-indicator evaluation method to a multi-indicator evaluation method. Based on fuzzy comprehensive evaluation and D-AHP. Using artificial neural networks (ANN) and regression models, Fan et al. [6] proposed a mixed fuzzy evaluation method for curtain grouting efficiency evaluation, and then used it to evaluate the curtain grouting efficiency of a hydropower project in China. Mansour Fakhri et al. [7] proposed a practical road evaluation scheme that established the relationship between deflection and two pavement performance indicators, namely the International Roughness Index (IRI) and Pavement Assessment and Serviceability Evaluation Rating (PASER). This model has been successfully applied to the evaluation of grouting effects on road diseases. Li et al. [8] explored the method for selecting pavement performance evaluation indicators using BP neural networks, where an artificial neural network method was introduced for evaluating pavement performance after grouting based on five indicators: International Roughness Index, damage rate, structural strength index, side friction coefficient, and texture depth. Wang et al. [9] established an evaluation index system for road performance, and the fuzzy consistency theory was used to determine the weight value of each indicator. After that, a comprehensive evaluation of the pavement was achieved through the gray clustering function. Sang et al. [10] took the performance of asphalt pavement, deflection basin parameters, and structural damage as evaluation indicators. Factor analysis method was used to extract common factors of each indicator, and the weights were determined by the contribution rate. This approach provided a comprehensive evaluation of the condition of the pavement structure, making the evaluation results more fair. Li et al. [11] established a new comprehensive evaluation model for asphalt pavement through the TOPSIS method, introducing information entropy to determine weights. This model took into account the objectivity and practicality of the indicators, avoided the interference of subjective factors. Li et al. [12] proposed a comprehensive evaluation method based on Analytic Hierarchy Process (AHP) and Fuzzy Comprehensive Evaluation (FCE) to evaluate the performance of asphalt mixture pavement from different perspectives. Deng et al. [13] proposed an evaluation framework for engineering geological suitability, based on the Analytic Hierarchy Process and Cloud Model. Though many comprehensive evaluation methods mentioned above are proposed, none of those is specially designed for the performance evaluation of grouting repair effect in highway engineering.

According to the comprehensive research status, there is still a lack of a comprehensive evaluation model that combines subjective and objective methods for evaluating the grouting repair effect of internal diseases in highways. Furthermore, to avoid the fuzziness and uncertainty in determining the weights of indicators in expert scoring, a comprehensive evaluation model for the grouting repair effect of internal diseases in highways is proposed in this paper based on the cloud model. The model utilizes Analytic Hierarchy Process (AHP) to determine subjective weights and entropy weight method to determine objective weights. It also introduces the idea of narrowing the subjective-objective deviation from Game Theory to calculate the optimal combined weights. Finally, taking two highway reconstruction and expansion projects in China as examples, the rationality and effectiveness of the evaluation model are analyzed.

EVALUATION MODEL FOR GROUTING EFFECT

The construction process of the grouting repair and its effect evaluation is shown in Figure 1.

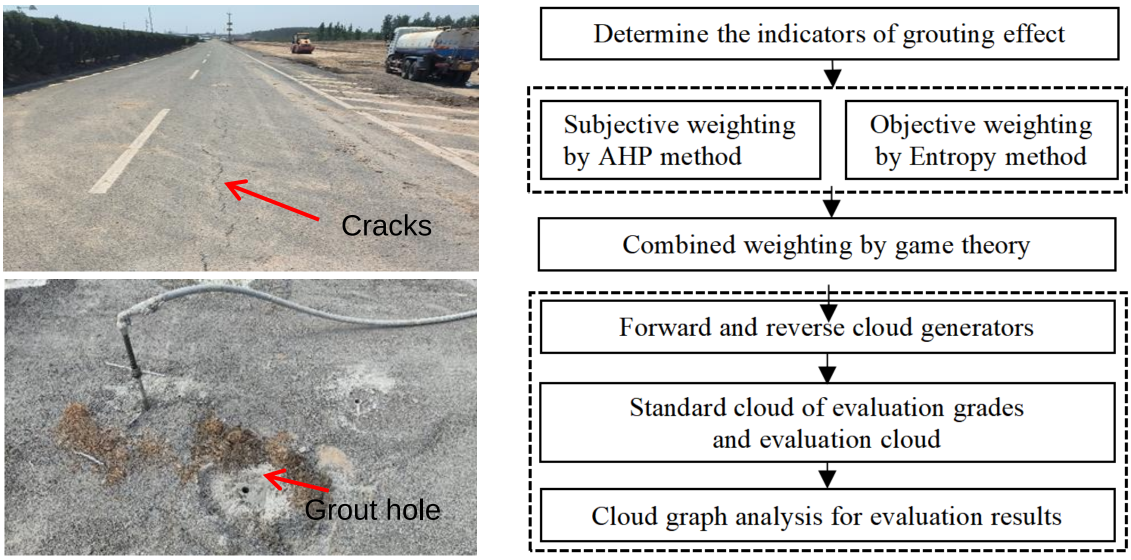

(1) Grouting repair *(2) Repair effect evaluation*

Fig. 1 – Construction process of the grouting repair and its effect evaluation

AHP subjective weight method

(1) AHP Structural Model

The model composed of evaluation objective, evaluation criteria, and indicators is known as the Analytic Hierarchy Process Structural Model [12, 13]. As shown in Figure 2, the AHP structural model is divided into three layers: the objective layer, the criterion layer, and the index layer [14]. The evaluation objective, grouting effectiveness U, is categorized, and summarized to form evaluation criteria, including mechanical performance U_1, density and uniformity U_2. The two criteria constitute the criterion layer. Subsequently, three indicators for each criterion are determined to form the index layer. For the index layer of mechanical performance criterion, there are Pavement Structure Strength Index U_{11} Soil Subgrade Modulus U_{12}, and Deflection Ratio Before and After grouting U_{13}. The index layer of density and uniformity contains Compaction Degree of the Base Layer U_{21}, Void Ratio of the Surface Layer U_{22} and GPR Image Recognition U_{23}.

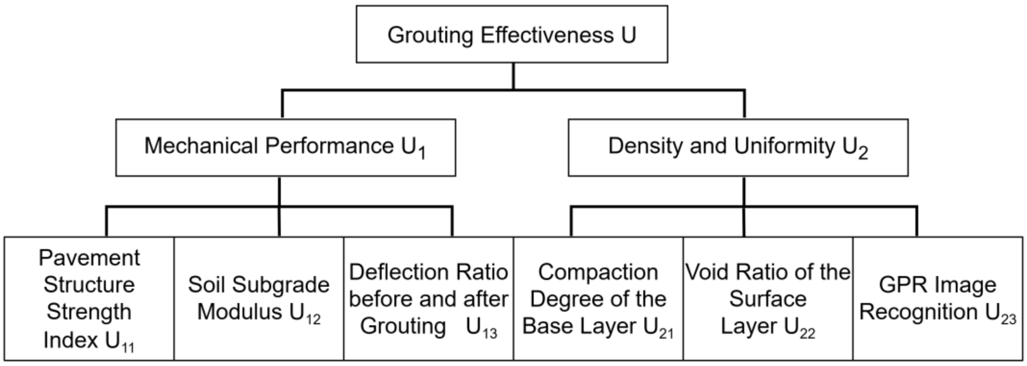

Fig. 2 –Structure Model for Analytic Hierarchy Process

(2) Judgment Matrix

The judgment matrix is the result of comparisons made by multiple experts on the importance of different criterions or indicators. By using the 1-9 scale method to compare the importance of each pair of criterions or indicators within the same level, the comparison results are arranged to form a judgment matrix. The final matrix obtained by organizing these comparison results is the one we refer to. and its general form is as follows:

$$A = \begin{bmatrix} a_{11} & a_{12} & \cdots & a_{1j} \\ a_{21} & a_{22} & \cdots & a_{2j} \\ \vdots & \vdots & \cdots & \vdots \\ a_{i1} & a_{i2} & \cdots & a_{ij} \end{bmatrix} \tag{1}$$

where, a_{ij} represents the degree of importance of u_i relative to u_j when comparing the two criterions or indicators u_i and u_j, and n is the number of criterions or indicators in each matrix. It should be noted that if the degree of importance of u_i to u_j is equal to a_{ij}, then the degree of importance of u_j to u_i could be marked as $1/a_{ij}$. For the AHP structural model using in the evaluation of grouting effect, there are a total of three judgment matrices, one second-order matrix for the criterion layer, and two third-order matrices for the index layer.

DOI 10.14311/CEJ.2025.03.0024

Tab. 1 - 1-9 Scale Method

Scaling	Meaning	Describe
1	same	u_i to u_j equally important.
3	a bit	$u_i$to u_j is a bit important
5	obvious	u_i to u_j is clearly important
7	strong	u_i to u_j is strongly important
9	absolute	$u_i$to u_j is absolutely important
2，4，6，8	between scales	u_i to u_j between scales

(3) Determine the weight vector of criterions and indicators.

Calculate the geometric mean of elements in each row of the judgment matrix

$$m_i = \sqrt[n]{\prod_{j=1}^{n} a_{ij}} \tag{2}$$

By normalizing using formula (3), (4), we obtain the eigenvector W , where w_i represents the obtained weight coefficient. In other words, the eigenvector W is just the weight vector for the criterions or indicators in a judgment matrix.

$$w_i = \frac{m_i}{\sum m_i} \tag{3}$$

$$\mathrm{W} = (w_1, w_2, \cdots, w_n)^T \tag{4}$$

Corresponding to the three judgment matrices, it also has three weight vectors in the AHP subjective weight method.

(4) Consistency Test

The calculated weight vector must pass consistency testing before it can be applied. Using the Consistency Index (CI) to measure the degree of consistency, it can be expressed as follow

$$\mathrm{CI} = {\lambda_{max} - n}/{n - 1} \tag{5}$$

Where λ_{max} is the maximum eigenvalue of the judgment matrix, and it can be calculated by the Equation 6

$$\lambda_{max} = \sum_{i=1}^{n} \frac{\sum_{j=1}^{n} a_{ij} w_j}{n w_i} \tag{6}$$

Due to people's subjective understanding of objective matters, it is insufficient to solely rely on the value of CI to determine whether a matrix is consistent. Therefore, the average random consistency index (RI) is adopted to correct the CI value. When the consistency ratio (CR) calculated form Equation 7 is less than or equal to 0.1, the judgment matrix is considered to have acceptable consistency. Otherwise, adjustments need to be made to obtain a judgment matrix that passes the consistency test.

$$\mathrm{CR} = \frac{\mathrm{CI}}{\mathrm{RI}} \tag{7}$$

In the equation, RI represents the average random consistency index, and its value varies with n, as listed in Table 2.

Tab.2 - The relationship between RI and the order n of the judgment matrix

n	1	2	3	4	5	6	7	8
RI	0	0	0.58	0.90	1.12	1.24	1.32	1.41

Entropy objective weight method

(1) Establishing an initial evaluation matrix

The first step in the Entropy objective weight method [15] is to construct a multi-indicator matrix. Assuming there are m evaluation objectives and n evaluation indicators, x_{ij} is defined as the j-th evaluation indicator of the i-th evaluation objective. This allows us to obtain the raw data matrix: $X = \left(x_{ij}\right)_{m*n}$, where $i = 1,2,\dots,m; j = 1,2,\dots,n$

$$X = \begin{bmatrix} x_{11} & x_{12} & \cdots & x_{1n} \\ x_{21} & x_{22} & \cdots & x_{2n} \\ \vdots & \vdots & \cdots & \vdots \\ x_{m1} & x_{m2} & \cdots & x_{mn} \end{bmatrix} \tag{8}$$

During the Entropy objective weight method for grouting effect, the Index U_{11} , $U_{12}, U_{13,}U_{21,}U_{22}$ and U_{23} in Figure 2 are directly regarded as the evaluation indicators, while the different measurement points after grouting repair were adopted as the evaluation objectives. Therefore, the element x_{ij} in matrix X represent the raw data from different measurement points

(2) Data Normalization Processing

Due to the significant impact of different types of indicators on the results, it is necessary to eliminate the influence of dimensionality during the calculation process and standardize the data accordingly. The processing steps are as follows:

For positive indicators,

$$\overline{x_{ij}} = \frac{x_{ij} - \min(x_{1j}, x_{2j,\dots,} x_{mj})}{\max(x_{1j}, x_{2j,\dots,} x_{mj}) - \min(x_{1j}, x_{2j,\dots,} x_{mj})} \tag{9}$$

For negative indicators，

$$\overline{x_{ij}} = \frac{\max(x_{1j}, x_{2j,\dots,} x_{mj})}{\max(x_{1j}, x_{2j,\dots,} x_{mj}) - \min(x_{1j}, x_{2j,\dots,} x_{mj})} \tag{10}$$

For moderateness indicators，

$$\overline{x_{ij}} = 1 - \frac{|x_{ij} - x_{best,j}|}{max|x_{ij} - x_{best,j}|} \tag{11}$$

Where $x_{best,j}$,j represents the optimum value for a given moderateness indicator. Besides, to ensure the effectiveness of numerical values, an effective value of 0.0001 is added to each value after dimensionless normalization.

(3) Calculate the proportion P of each indicator under different objectives

$$p_{ij} = \overline{x_{ij}} / \sum_{i=1}^{m} \overline{x_{ij}} \tag{12}$$

(4) Calculate the entropy value of the j th evaluation indicator

$$e_j = -\frac{1}{\ln(m)} \sum_{i=1}^{m} p_{ij} \ln(p_{ij}) \tag{13}$$

(5) Calculate the information redundancy.

To calculate the information redundancy of the jth indicator, the following equation is taken:

$$d_j = 1 - e_j \tag{14}$$

(6) Calculate the weight of the indicator

Using the calculated information redundancy, the objective weight could be obtained easily for the jth indicator as

$$w_j = d_j / \sum_{j=1}^{m} d_j \tag{15}$$

Combined Weighting in Game Theory

(1) Construct a weight vector set

In the aspect of multi-level indicator evaluation, assuming that g types of subjective and objective weighting methods are adopted, g types of weights can be obtained. Based on these weight data, the basic weight vector set uk can be derived for each method [16].

$$u_k = \left(u_{k1}, u_{k2}, \cdots u_{kj}\right), k = 1,2, \cdots g \tag{16}$$

where u_{kj} represents the weight set for the indicators in the j-th level under the k-th weight method.

Then, the linear combination of g types of weight vectors at the j-th level is a possible set of weights up

$$u_j = \sum_{k=1}^{g} a_k\, u_{kj}^T, a_k > 0 \tag{17}$$

where represents the linear combination coefficient, and u_j is a comprehensive weight vector for the j-th level indicators.

(2) Constructing an Optimal Game Model

The game model in game theory aims to find a consistent compromise model among the weights obtained through the g methods, based on the coordination objectives of Nash equilibrium. The ultimate goal is to minimize the deviation among the various weights, thereby achieving the optimal "benefits" of the game.

The process of finding the optimal weight vector can be simplified into seeking the linear combination factors a_k for the optimal weighted set. The objective is to minimize the deviation between $u_j$and each u_k to the greatest extent possible.

$$\min\left\|u_j - u_{ij}\right\|_2, (i = 1,2, \cdots, g) \tag{18}$$

Starting from the differential properties of matrices, it is straightforward to derive the first-order optimal derivative for each indicator level as:

$$\sum_{k=1}^{g} a_k u_{ij} u_{kj}^T = u_{ij} u_{kj}^T, (i = 1,2, \cdots g) \tag{19}$$

The corresponding linear equation system is:

$$\begin{bmatrix} u_{1j}u_{1j}^T & u_{2j}u_{2j}^T & \cdots & u_{1j}u_{gj}^T \\ u_{2j}u_{1j}^T & u_{2j}u_{2j}^T & \cdots & u_{2j}u_{gj}^T \\ \vdots & \vdots & \cdots & \vdots \\ u_{gj}u_{1j}^T & u_{gj}u_{2j}^T & \cdots & u_{gj}u_{gj}^T \end{bmatrix} \begin{bmatrix} a_1 \\ a_2 \\ \vdots \\ a_g \end{bmatrix} = \begin{bmatrix} u_{1j}u_{1j}^T \\ u_{2j}u_{2j}^T \\ \vdots \\ u_{gj}u_{gj}^T \end{bmatrix} \tag{20}$$

According to formula (20), the linear combination factors can be obtained, and then by normalization it yeilds the linear coefficient.

$$a^* = a_k / \sum_{k=1}^{g} a_k \tag{21}$$

Finally, the ultimate combined weight is calculated as:

$$u_j^* = \sum_{k=1}^{g} a^* u_{kj}^T = \left(u_{j1}^*, u_{j2}^*, \cdots, u_{jn}^*\right) \tag{22}$$

where u_{jn}^* represents the weight value for the n-th indicator in the j-th level.

When the combined weight vector for indicators in the third level are determined, the combined weights for indicators in the other levels could be calculated by the superposition of weight value in the lower level.

Evaluation by Cloud Model Theory

Definition and Numeric Characteristics of the Cloud

The cloud model is an uncertain transformation model for processing qualitative concepts and quantitative descriptions. It is based on probability theory and fuzzy mathematics, aiming to address issues of randomness and fuzziness in uncertainty research [17]. The definition of the cloud model could be described as follows.

Let R be a quantitative domain represented by precise numerical values, and C be a qualitative concept on R. If x is a quantitative value in R and a random realization of the qualitative concept C, then the membership degree$\mu(x)$of x to C is a random number with a stable tendency. The distribution of $\mu(x)$follows the following pattern as $\mu: R \to [0,1], \forall x \in R, x \to \mu(x)$.Then each x represents a cloud droplet, and the distribution of x in the domain R is called a cloud.

The cloud model proposed in this study serves as a theoretical framework for addressing uncertainty in qualitative-quantitative conversion, rooted in probability theory and fuzzy mathematics [17]. Unlike the "point cloud model" used in laser scanning—where dense clusters of 3D points reconstruct physical objects—this model characterizes evaluation concepts excellent grouting effect as probabilistic distributions rather than rigid numerical thresholds.

The numerical characteristics of the cloud are represented by the expected value Ex, entropy En, and hyper-entropy He, which reflect the quantitative characteristics of the qualitative concept. The expected value Ex is the point in the domain space that best represents the qualitative concept C. In this study, Ex is used to represent the "evaluation value of grouting repair for internal defects in highways". The entropy En is used to comprehensively measure the fuzziness and probability of the qualitative concept, reflecting the reliability of the qualitative concept C. In this article, it represents the reliability of the "evaluation value of grouting repair for internal defects in highways". A larger En indicates a lower credibility of the grouting effect evaluation results. The hyper-entropy He is a measure of the uncertainty of entropy, reflecting the cohesion of all points in the numerical domain space that represent the linguistic value. At the same time, hyper-entropy He also reflects the dispersion and thickness of the cloud. If the hyper-entropy value is larger, the randomness of the grouting effect evaluation results is greater, and the "thickness" of the cloud is also greater, resulting in less accurate evaluation results.

Determination of Cloud Evaluation Criteria

Establishment of the comment set

Based on the research on the evaluation of grouting effects, an evaluation indicator set U is established, including three levels as mentioned above in Section 2.3. A combination of expert survey method and on-site data survey method is adopted to accurately assess the rationality of the grouting repair. Ultimately, the evaluation grades of grouting repair are divided into four categories: excellent, good, qualified, and unqualified. For each indicator, a comment set V is formulated with scoring ranges of [8,10], [4,8], [2,4], and [0,2], respectively corresponding to the four evaluation grades. It should be noted that adhering to the principles of scientificity, rationality, and a combination of quantitative and qualitative methods, the grade classification for each evaluation indicator in the third level is provided simultaneously, as detailed in Table 3. The grade classification establishes a relationship between indicator values and comment set V.

Tab. 3 - Indicator Grade Classification

Indicator	Indicator Grade Classification			
	Excellent [8,10]	Good [4,8]	Qualified [2,4]	Unqualified [0,2]
U_{11}	> 90	80~90	70~80	< 70
U_{12}	> 95 (MPa)	75~95(MPa)	60~75(MPa)	< 60(MPa)
U_{13}	≥2	1.5~2	1.2~1.5	≤1.2
U_{21}	> 98%	97%~98%	96%~97%	< 96%
U_{22}	3%~4%	4%~5%	5%~6%	> 6%， < 3%
U_{23}	Dense	Slightly dense	Moderately Loose	Severely Loose

Construction of the standard cloud evaluation feature parameters V_{max} represent the maximum boundary of a comment set，V_{min} represent the minimum boundary of a comment set. According to the upper and lower bounds $[V_{max}, V_{min}]$, the standard cloud evaluation feature parameters (Exk, Enk, and Hek) are calculated as follows for each comment set.

$$\begin{cases} Ex_k = (V_{max} + V_{min})/2 \\ En_k = (V_{max} - V_{min})/6 \\ He_k = k \end{cases} \tag{23}$$

Among them, k is a constant, and typically the value of super-entropy He is set to 0.1. Table 4 and Figure 3 indicate the cloud evaluation standards and cloud evaluation grades calculated by Equation 23 at different levels. It should be noted that the standard evaluation cloud, as shown in Figure 3, reflects only the evaluation grades, independent with the tested data.

Tab. 4 - Parameters of Cloud Model for Each Evaluation Grade

Evaluation Grade	interval	Exk, Enk, Hek
Excellent	[8,10]	(9, 0.333, 0.1)
Good	[4,8]	(6, 0.667, 0.1)
Qualified	[2,4]	(3, 0.333, 0.1)
Unqualified	[0,2]	(1, 0.333, 0.1)

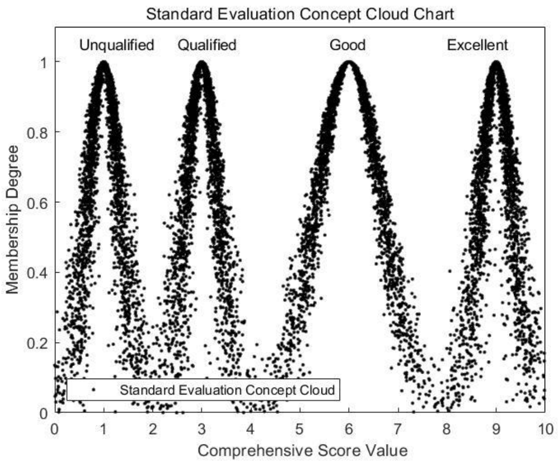

Fig. 3 –Cloud Evaluation Standards for Grouting Effect

Calculating the cloud parameters for individual indicators

After the measured values of the evaluation indicators are obtained, the corresponding evaluation grades are determined according to the guidelines in Table 3. Thereafter, experts in relevant fields are invited to assign detailed score $x_i$to each indicator within its scoring interval. The three cloud parameters (Ex, En, He) of each indicator can be then calculated based on the scoring results.

$$\begin{cases} \mathrm{Ex} = \overline{X} = \frac{1}{n}\sum_{i=1}^{n}(x_i) \\ \mathrm{En} = \sqrt{\frac{\pi}{2}} \times \frac{1}{n}\sum_{i=1}^{n}(x_i - E_x) \\ \mathrm{He} = \sqrt{|s^2 - E_n^2|} \end{cases} \tag{24}$$

In the above formula, x_i represents the scoring result for a given indicator of the i-th evaluation objective. s^2represents the the variance of the samples for the series of x_i, and can be calculated as follows in Equation 25.

$$s^2 = \frac{1}{n-1}\sum_{i=1}^{n}(x_i - \overline{X})^2 \tag{25}$$

Integrating Evaluation Cloud Parameters considering combined weight

During the evaluation indicators in the presented evaluation model for grouting effect, the indicators in the third level are calculated first by Equation 26. By using the combined weights, the cloud parameters for the upper-level indicators are calculated. The calculation formula is as follows:

$$\begin{cases} \mathrm{Ex}_{j-1} = \sum_{i=1}^{n} u_{ji}^{*} Ex_{i,j} \,/\, \sum_{i=1}^{n} u_{ji}^{*} \\ \mathrm{En}_{j-1} = \sum_{i=1}^{n}(u_{ji}^{*2} En_{i,j})^2 \,/\, \sum_{i=1}^{n} u_{ji}^{*2} \\ \mathrm{He}_{j-1} = \sum_{i=1}^{n}\left(u_{ji}^{*2} He_{i,j}\right) \,/\, \sum_{i=1}^{n} u_{ji}^{*2} \end{cases} \tag{26}$$

where the parameters represent the cloud parameters for the i-th indicators in the j-th level.

Determination of evaluation grade

By comparing the individual cloud chart with the cloud evaluation standards in Figure 3, the region with the maximum matching degree is identified to determine the grade of the evaluation objective.

Taking the following set of data in Table 5 as an example, in which the different scores of five road sections (S1~S5) are preset. Based on the data, we obtained Ex, En and He according to Formulas 24 and 25. En measures the fuzziness of qualitative concepts, while He characterizes the uncertainty of entropy. From the cloud diagrams of the following three sets of data, it can be clearly seen in Figure 4 that the greater the dispersion degree of the original data, the larger the En. As En increases from 0.041 to 0.401 and then to 1.604, the distribution of cloud droplets becomes more scattered, and the cloud diagram becomes wider, changing from a tight cluster to a widespread dispersion. The larger the He, the more cloud droplets far away from the center appear at the edge of the cloud diagram.

Tab. 5 -Cloud image example data

Date	S1	S2	S3	S4	S5	Ex	En	He
Date1(red)	7.9	8	8	8	8	7.98	0.041	0.020
Date2(blue)	8	8	7	8	8	7.80	0.401	0.198
Date3(green)	8	4	8	8	8	7.20	1.604	0.791

DOI 10.14311/CEJ.2025.03.0024

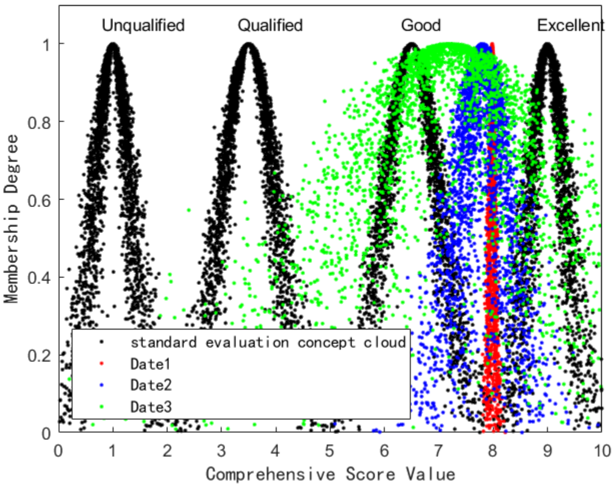

Fig. 4 –Cloud image example

CASE STUDY ANALYSIS - EXPRESSWAY FROM SHANDONG

Project Overview

A certain expressway in Shandong Province of China is selected to do the case study for the method verification. The traffic volume of this expressway has increased rapidly, especially for heavy-duty vehicles. Under the combined effects of vehicle loads and natural environmental factors, pavement diseases have rapidly developed, mainly including longitudinal cracks, void formation and loosening. These diseases have reduced the usability and driving comfort of the pavement. Therefore, polymer grouting repair technology was used to restore and improve the pavement service level.

After repair, six series of measurement data for the third level indicators were obtained from different repair sections (S1~S6) through corresponding on-site testing methods. The main testing methods and devices are shown in Table 6, and the relevant indicator data are shown in Table 7.

The weight calculation process and the comprehensive cloud evaluation result is shown in the following section. It should be noted that the data of U_{23} were given by the five experts according to the GPR image recognition, which represented the uniformity of pavement structure.

Tab. 6 - On site inspection content

Detection Items	Main Equipment Invested	Equipment Model
Pavement Structure Strength Index U_{11}	Laser Dynamic Deflection Measurement System	JILSFWD
Soil Subgrade Modulus U_{12}	FWD Falling Weight Deflectometer	JILSFWD
Deflection Ratio Before and After Grouting U_{13}	FWD Falling Weight Deflectometer	JILSFWD
Compaction Degree of the Base Layer U_{21}	Boring Core Drilling Machine	/
Void Ratio of the Surface Layer U_{22}	Nuclear-free Density Gauge	2701-B
GPR Image Recognition U_{23}	3D Ground Penetrating Radar (GPR)	GeoScope

Tab. 7 - Sample Data from the Expressway in Field

Indicator	S1	S2	S3	S4	S5	S6
U_{11}	99.39	99.38	99.78	99.72	99.46	99.40
U_{12}	344(MPa)	255(MPa)	363(MPa)	659(MPa)	509(MPa)	588(MPa)
U_{13}	1.3	1.5	1.6	2	1.8	2.3
U_{21}	98%	97%	98%	98%	97%	97%
U_{22}	5%	5%	5%	4%	3%	5%
U_{23}	97	92	95	94	96	98

Determination of Indicator Weights

As mentioned in Section 2.1 and 2.4, three levels are defined to classify the evaluation indicators. There is only one indicator in the first level, grouting effectiveness U, which is also the final evaluation objective. The second-level indicators include mchanical performanceU_1, density and uniformity U_2. For the lower level below U_1, there are Pavement Structure Strength Index U_{11}, Soil Subgrade Modulus U_{12}, and Deflection Ratio Before and After Grouting U_{13}. For the lower level below U_2, it contains Compaction Degree of the Base Layer U_{21}, Void Ratio of the Surface Layer U_{22} and GPR Image Recognition U_{23}. Therefore, the following indicator set can be obtained.

$$\begin{cases} U = \{U_1, U_2\} \\ U_1 = \{U_{11}, U_{12}, U_{13}\} \\ U_2 = \{U_{21}, U_{22}, U_{23}\} \end{cases} \tag{27}$$

Subjective weight

When determining subjective weights, this study invited ten experts and scholars with diverse professional backgrounds. Four of them are from universities, three from research institutes, and three from engineering testing companies. Each expert was required to have at least five years of experience in highway engineering and have either led or participated in at least three expressway grouting repair projects. These qualifications guarantee that the experts possess in-depth practical knowledge and expertise, enabling them to provide reliable and valuable opinions for our research on post - grouting repair performance evaluation. Then, the subjective weight could be determined with AHP subjective weight method in Section 2.1.

Determining the pairwise weight ratio between elements U_1 and U_2 to form the judgment matrix A_U;

$$A_U = \begin{bmatrix} 1 & 1/2 \\ 2 & 1 \end{bmatrix} \tag{28}$$

The maximum eigenvalue$\lambda_{max}$of the judgment matrix A_U is 2, and the corresponding eigenvector is $W_{\mathrm{U}} = [0.3333\ \ 0.6667]^T$.

Determine the weight ratio of elements U_{11}, U_{12} and U_{13} and form the judgment matrix A_{U1}.

$$A_{U1} = \begin{bmatrix} 1 & 2 & 2 \\ 1/2 & 1 & 1/2 \\ 1/2 & 2 & 1 \end{bmatrix} \tag{29}$$

The maximum eigenvalue λ_{max} of the judgment matrix A_{U1}. is 3.054, and the corresponding eigenvector is $W_{U1} = [0.4934\ 0.1958\ 0.3108]^T$.

Determine the weight ratio of elements U_{21}, U_{22} and U_{23} and form the judgment matrix A_{U2}.

$$A_{U2} = \begin{bmatrix} 1 & 3 & 1/3 \\ 1/3 & 1 & 1/5 \\ 3 & 5 & 1 \end{bmatrix} \tag{30}$$

The maximum eigenvalue λ_{max} of the judgment matrix A_{U2} is 3.039, and the corresponding eigenvector is $W_{U2} = [0.2583\ 0.1047\ 0.6370]^T$.

The consistency ratio of A_U, A_{U1}, A_{U2} is 0, 0.027, and 0.019, respectively. All the consistency ratios are lower than 0.1, which satisfy the consistency requirement.

By comprehensively calculating the two levels of weights, the subjective weights for the grouting repair effect of internal diseases in expressways is obtained, as shown in Table 8. The overall weight is calculated by multiplying the two levels of weight, aiming to show the weight related to the first level indicator, grouting effectiveness U.

Tab. 8 - Subjective Weight Statistics Table

Second-level Indicators	weight	Third-level Indicators	weight	Overall Weight
U_1	0.3333	U_{11}	0.4934	0.1644
		U_{12}	0.1985	0.0653
		U_{13}	0.3108	0.1036
U_2	0.6667	U_{21}	0.2583	0.1722
		U_{22}	0.1047	0.0698
		U_{23}	0.6370	0.4247

Objective Weight

Objective weights are assigned to different indicators using the entropy weight method. The data and indicator values, as shown in Table 7, come from on-site detection after grouting repair. By Equations 9 - 11, the standardized data matrix could be obtained as follows.

$$X = \begin{bmatrix} 0.0250 & 0.0000 & 1.0000 & 0.8500 & 0.2000 & 0.0500 \\ 0.2203 & 0.0000 & 0.2673 & 1.0000 & 0.6287 & 0.8243 \\ 0.0000 & 0.2000 & 0.3000 & 0.7000 & 0.5000 & 1.0000 \\ 1.0000 & 0.0000 & 1.0000 & 1.0000 & 0.0000 & 0.0000 \\ 0.5000 & 0.5000 & 0.5000 & 0.0000 & 0.5000 & 0.5000 \\ 0.8333 & 0.0000 & 0.5000 & 0.3333 & 0.6667 & 1.0000 \end{bmatrix} \tag{31}$$

The entropy value, objective weight, and information redundancy are calculated using the formula (12)-(15). The specific results are shown in Table 9:

Tab. 9 - Objective Weight Statistics Table

Second-level Indicators	weight	Third-level Indicators	e_j	d_j	Overall Weight
U_1	0.5476	U_{11}	0.6051	0.3949	0.2852
		U_{12}	0.8178	0.1822	0.1316
		U_{13}	0.8188	0.1812	0.1308
U_2	0.4524	U_{21}	0.6132	0.3868	0.2793
		U_{22}	0.8983	0.1017	0.0735
		U_{23}	0.8620	0.1380	0.0996

Determination of Combined Weights

The weight vector set for the third-level indicators and the two weight methods is established as follows:

$$\{u_{13}, u_{23}\} = \begin{Bmatrix} (0.1644,0.0653,0.1036,0.1722,0.0698,0.4247), \\ (0.2852,0.1316,0.1308,0.2793,0.0735,0.0996 \end{Bmatrix} \tag{32}$$

The corresponding linear equations are derived by Equation 20:

$$\begin{bmatrix}0.25692 & 0.17263\\0.17263 & 0.21324\end{bmatrix}\begin{bmatrix}a_{12}\\a_{22}\end{bmatrix}=\begin{bmatrix}0.25692\\0.21324\end{bmatrix} \tag{33}$$

Solve Equation 33 and normalize the results, the linear combination factors are obtained.

$$\begin{bmatrix}a_{12}\\a_{22}\end{bmatrix}=\begin{bmatrix}0.63269\\0.36731\end{bmatrix} \tag{34}$$

Using the Equation 22, we can obtain the combined weights for each indicator in the third level based on game theory. The combined weights for indicators in the second levels could be calculated by the superposition of weight value in the third level. Table 10 summarizes the weights obtained from the three methods.

Tab.10 - Combined Weight Assignment Table

Indicators	AHP Method	Entropy Method	Combined Method	Indicators	AHP Method	Entropy Method	Combined Method
U_1	0.3333	0.5476	0.413	U_{11}	0.1644	0.2852	0.2094
				U_{12}	0.0653	0.1316	0.0899
				U_{13}	0.1036	0.1308	0.1137
U_2	0.6667	0.4524	0.587	U_{21}	0.1722	0.2793	0.2121
				U_{22}	0.0698	0.0735	0.0712
				U_{23}	0.4247	0.0996	0.3037

Application of Cloud Evaluation Method

Subsequently, these experts analyzed the measured expressway sample data in Table 7. Based on their professional knowledge in architectural engineering and the classification of indicator levels in Table 3, they determined the scores of the evaluation indicators for the six road sections (S1~S6), as shown in Table 11.

Tab.11 - Indicator Evaluation Values for Each Road Section

Indicator	S1	S2	S3	S4	S5	S6
U_{11}	9.4	9.4	9.6	9.6	9.5	9.5
U_{12}	10	10	10	10	10	10
U_{13}	3	4	4.8	8	7	8.1
U_{21}	8	7	8	8	7	7
U_{22}	8	8	8	7	8.5	8
U_{23}	9.7	9.2	9.5	9.4	9.6	9.8

Substituting the evaluation values in Table 11 into the formula (24), the cloud parameters (Ex, En, He) for each third-level indicator are obtained. Using the cloud parameters of the third-level indicators, the evaluation cloud parameters for other second-level indicators can be derived. Similarly, the evaluation cloud parameters for the first-level indicators can be derived. All the cloud parameters for the three level are shown in Table 12.

Tab.12 - Cloud Parameters for all the Indicators

indicator	Cloud Parameters	indicator	Cloud Parameters	indicator	Cloud Parameters
U_{11}	(9.5, 0.501, 0.493)	U_{21}	(7.5, 0.752, 0.515)	U_1	(8.595, 0.904, 0.695)
U_{12}	(10, 0, 0)	U_{22}	(7.917, 0.460, 0.175)	U_2	(8.608, 0.414, 0.250)
U_{13}	(5.817, 2.832, 1.815)	U_{23}	(9.533, 0.251, 0.127)	U	(8.602, 0.297, 0.205)

The comprehensive cloud and the standard cloud can be plotted in the same coordinate system to obtain a comparison chart of the comprehensive cloud and the standard cloud. This evaluation method not only provides the final fuzzy comprehensive evaluation result, but also includes the intermediate results, that is for the second and third level. The intermediate calculation results are shown in Table12, and the final evaluation result for the first level, grouting effect, is shown in Figure 5.

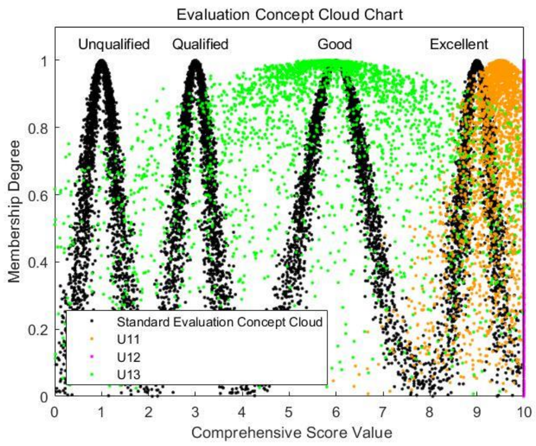

(1) Third-Level Indicators 1

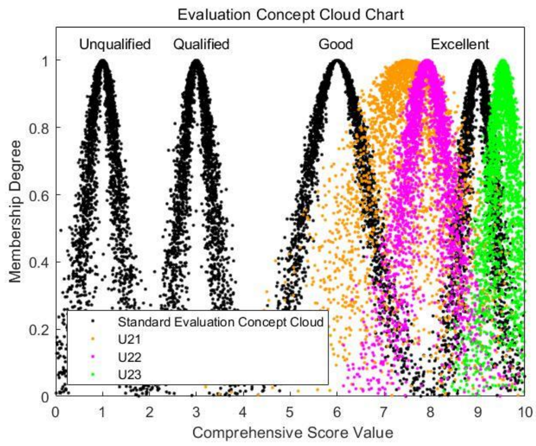

(2) Third-Level Indicators 2

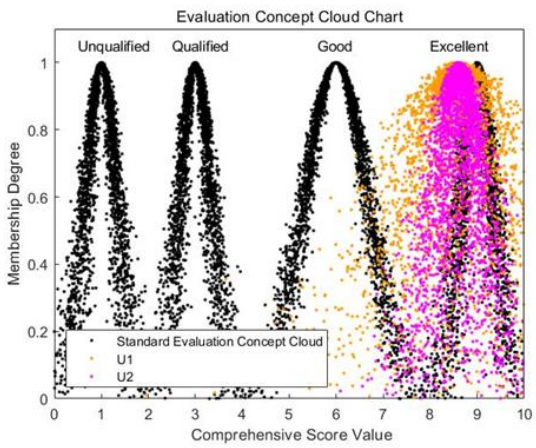

(3) Second-Level Indicators

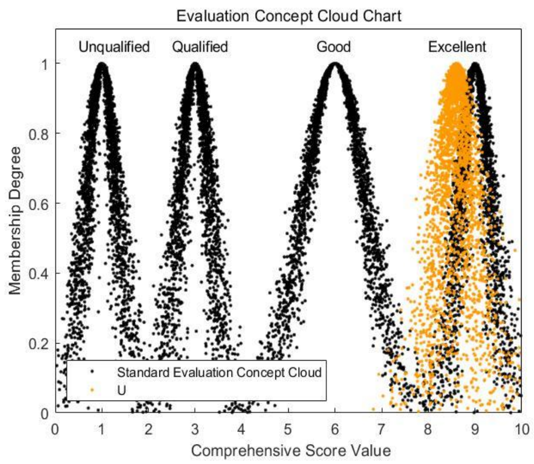

(4) First-Level Indicators

Fig. 5 –Comparison Chart for Indicators

Obviously, all indicators of the expressway after grouting repair have reached or beyond the grade of good. From Figure 5, the dynamic modulus indicator of the soil base (U_{12}) has reached the excellent level across the board. The grouting-before-and-after deflection ratio indicator (U_{13}) is slightly less stable compared to other indicators. The reasons for this are as follows: although the average road deflection values are all smaller than those before grouting, and the decrease is significant, the existence time of the disease varies. In areas with more severe damage, the deflection values before grouting reach 300μm to 500μm, or even greater than 500μm. However, in areas with less severe damage, the deflection values before grouting are mostly less than 200μm. Therefore, the larger the deflection value before grouting, the greater the improvement after grouting, resulting in larger fluctuations in this indicator.

As can be seen from Figure 5, the comprehensive cloud of grouting effect is between "good" and "excellent," and is closer to the "excellent" level. Therefore, it can be determined that the final result of the grouting effect evaluation is "excellent". Overall, the evaluation results obtained above are consistent with the actual construction status, indicating that the constructed evaluation model has strong practicality in evaluating the effect of grouting repair on expressways.

CASE STUDY ANALYSIS - EXPRESSWAY FROM LIAONING

Project Overview

Another expressway in Liaoning Province of China is selected to do further case study for the method verification. The expressway selected for grouting repair was initially constructed at the beginning of this century and has been open to traffic for 19 years. Under the impact of traffic loads, it has developed numerous transverse and longitudinal pavement cracks, as well as vehicle bumps at bridgeheads, which have compromised the safety and comfort of driving. Therefore, road maintenance and reinforcement are urgently needed.

To comprehensively evaluate the actual effectiveness of grouting repair for this road, grouting repairs were carried out separately for three typical defects: longitudinal pavement crack, transverse pavement crack, and roadbed settlement. Systematic inspections were conducted on different repaired road sections, and six series of measurement data covering three-level indicators were obtained for six road sections of each defect (S1~S6, S7~S12, S13~S18),. The main inspection contents are detailed in Table 6, while specific data for each relevant indicator can be referred to in Tables 13.

Tab. 13 - Sample data after grouting repair

Detect Type	Indicator	S1	S2	S3	S4	S5	S6
longitudinal crack	U_{11}	80.42	81.51	84.13	80.44	81.53	83.41
	U_{12}	70(MPa)	74(MPa)	83(MPa)	71(MPa)	74(MPa)	80(MPa)
	U_{13}	1.06	1.32	1.31	1.39	1.57	1.32
	U_{21}	98%	97%	99%	98%	99%	98%
	U_{22}	3%	4%	3.5%	4%	3.5%	4%
	U_{23}	91	92	93	90	95	92
Detect Type	Indicator	S7	S8	S9	S10	S11	S12
transverse crack	U_{11}	92.71	88.42	86.37	92.48	94.16	90.85
	U_{12}	120(MPa)	94(MPa)	86(MPa)	119(MPa)	137(MPa)	106(MPa)
	U_{13}	1.38	1.55	1.19	1.26	1.32	1.33
	U_{21}	97%	98%	98%	99%	98%	98%
	U_{22}	3.5%	3%	4%	4%	4%	3.5%
	U_{23}	96	98	97	96	96	94
Detect Type	Indicator	S13	S14	S15	S16	S17	S18
Roadbed settlement	U_{11}	82.51	81.72	84.56	81.33	87.82	79.31
	U_{12}	76(MPa)	74(MPa)	85(MPa)	73 (MPa)	103(MPa)	67(MPa)
	U_{13}	1.35	1.44	1.26	1.21	1.20	1.26
	U_{21}	97%	98%	97%	98%	98%	98%
	U_{22}	4%	4%	4%	3.5%	4.5%	3.5%
	U_{23}	92	93	94	94	93	91

Determination of Indicator Weights

Since the evaluation indicators are the same, the same subjective weights as in Section 3.1 are used here, while the objective weights for different indicators are assigned using the entropy weight method. The indicator values are obtained from on-site inspections after grouting repair, as shown in Table 13. The standardised data matrix can be obtained using Equations 9 to 11. Entropy values, information redundancy, and target weights are calculated using Equations 12 to 15. Finally, using the game theory formula (16) to (22), the combined weights for each third-level indicator are obtained. The combined weights for the second-level indicators can be calculated by summing the third-level weight values. Table 14 shows the combined weights in grouting repair evaluation, respectively for longitudinal cracks, transverse cracks, and roadbed settlement defects.

Tab.14 - Combined weight of indicators in grouting repair for different detects

Detect Type	Indicator	AHP Method	Entropy Method	Combined Method	Indicator	AHP Method	Entropy Method	Combined Method
longitudinal crack	U_1	0.3333	0.4767	0.388	U_{11}	0.1644	0.2127	0.1828
					U_{12}	0.0653	0.1740	0.1067
					U_{13}	0.1036	0.0900	0.0984
	U_2	0.6667	0.5233	0.612	U_{21}	0.1722	0.0970	0.1435
					U_{22}	0.0698	0.3010	0.1579
					U_{23}	0.4247	0.1253	0.3106
Detect Type	Indicators	AHP Method	Entropy Method	Combined Method	Indicators	AHP Method	Entropy Method	Combined Method
transverse crack	U_1	0.3333	0.5662	0.374	U_{11}	0.1644	0.1625	0.1641
					U_{12}	0.0653	0.1997	0.0885
					U_{13}	0.1036	0.2039	0.1209
	U_2	0.6667	0.4338	0.626	U_{21}	0.1722	0.1454	0.1676
					U_{22}	0.0698	0.1457	0.0829
					U_{23}	0.4247	0.1427	0.3759
Detect Type	Indicators	AHP Method	Entropy Method	Combined Method	Indicators	AHP Method	Entropy Method	Combined Method
Roadbed settlement	U_1	0.3333	0.5587	0.403	U_{11}	0.1644	0.1459	0.1587
					U_{12}	0.0653	0.1890	0.1033
					U_{13}	0.1036	0.2238	0.1405
	U_2	0.6667	0.4413	0.597	U_{21}	0.1722	0.1272	0.1584
					U_{22}	0.0698	0.2048	0.1112
					U_{23}	0.4247	0.1093	0.3279

Application of Cloud Evaluation Method

Based on their expertise in road engineering, the experts used the indicator classification in Table 3 to grade and score the indicator sample data for each section of the Liaoning Province expressway presented in Table 13, as shown in Table 15.

Tab. 15 - Evaluation values of indicators for each road section

Detect Type	Indicator	S1	S2	S3	S4	S5	S6
longitudinal crack	U_{11}	4.2	4.6	5.6	4.2	4.6	5.3
	U_{12}	3.3	3.8	5.6	3.5	3.8	5.0
	U_{13}	1	2.8	2.7	3.3	4.5	2.8
	U_{21}	8	4	9	8	9	8
	U_{22}	8	8	10	8	10	8
	U_{23}	9.1	9.2	9.3	9.0	9.5	9.2
Detect Type	Indicator	S7	S8	S9	S10	S11	S12
transverse crack	U_{11}	8.5	7.4	6.6	8.1	8.1	8.0
	U_{12}	10	8.8	7.2	10	10	10
	U_{13}	3.2	4	2.9	2.4	2.8	2.8

	U_{21}	4	8	8	9	8	8
	U_{22}	10	8	8	8	8	10
	U_{23}	9.6	9.8	9.7	9.6	9.6	9.4
Detect Type	Indicator	S13	S14	S15	S16	S17	S18
roadbed settlement	U_{11}	4.1	4.1	4.2	4.1	4.0	3.9
	U_{12}	4	3.9	6.0	3.8	10	3.0
	U_{13}	3	3.6	2.4	2	2	2.4
	U_{21}	4	8	4	8	8	8
	U_{22}	8	8	8	10	6	10
	U_{23}	9.2	9.3	9.4	9.4	9.3	9.1

Substituting the scoring results in Table 15 into the formula (24), the cloud parameters (Ex, En, He) of third-level indicators for each defect are obtained. Substituting the cloud parameters of the third-level indicators into the formula (26), the evaluation cloud parameters for second-level and first-level indicators can be derived. All the cloud parameters for the three levels are shown in Table 16.

Tab.16 - Cloud parameters of longitudinal crack evaluation indicators

Detect Type	indicator	Cloud Parameters	indicator	Cloud Parameters	indicator	Cloud Parameters
longitudinal crack	U_{11}	(4.750,0.585,0.084)	U_{21}	(7.667,1.532,1.058)	U_1	(4.108,0.713,0.227)
	U_{12}	(4.167,0.947,0.232)	U_{22}	(8.667,1.114,0.418)	U_2	(5.236,1.220,1.035)
	U_{13}	(2.850,0.877,0.711)	U_{23}	(9.217,0.153,0.079)	U	(4.798,0.564,0.422)
indicator	indicator	Cloud Parameters	indicator	Cloud Parameters	indicator	Cloud Parameters
transverse crack	U_{11}	(7.783,0.655,0.182)	U_{21}	(7.500,1.462,0.981)	U_1	(6.608,0.678,0.217)
	U_{12}	(9.333,1.114,0.286)	U_{22}	(8.667,1.114,0.418)	U_2	(6.493,1.126,0.781)
	U_{13}	(3.017,0.487,0.245)	U_{23}	(9.617,0.111,0.072)	U	(6.536,0.537,0.337)
indicator	indicator	Cloud Parameters	indicator	Cloud Parameters	indicator	Cloud Parameters
roadbed settlement	U_{11}	(4.067,0.097,0.034)	U_{21}	(6.667,2.228,0.835)	U_1	(3.813,0.724,0.242)
	U_{12}	(5.117,2.409,0.954)	U_{22}	(8.333,1.393,0.572)	U_2	(4.836,1.688,0.749)
	U_{13}	(2.567,0.613,0.123)	U_{23}	(9.283,0.111,0.035)	U	(4.424,0.720,0.307)

By plotting the comprehensive evaluation cloud and standard cloud on the same coordinate system, a clear comparison can be observed and the evaluation conclusion can be easily made. This evaluation method not only provides the final fuzzy comprehensive evaluation results, but also includes the evaluation results of the second-level and third-level indicators. The final evaluation results of the grouting effect, including the first-level and second-level evaluation results, are shown in Figure 6.

From the comprehensive cloud map of grouting repair effects, it is clear that grouting repair technology in these road sections exhibits significant differences in repair effectiveness across various types of defects. The repair effectiveness, ranked from best to worst, is as follows: transverse cracks (Good), longitudinal cracks (Qualified), and roadbed settlement (Qualified), with the most significant repair effectiveness observed for transverse cracks.

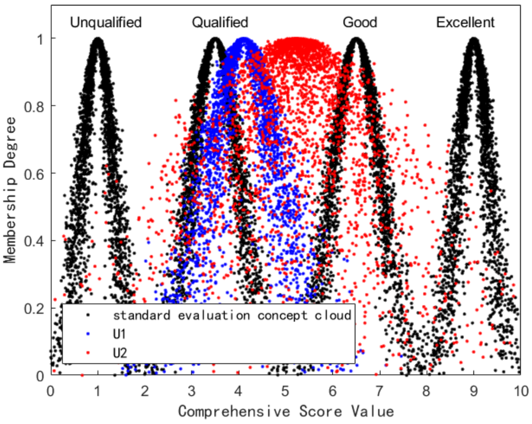

(1) Second-Level for longitudinal crack

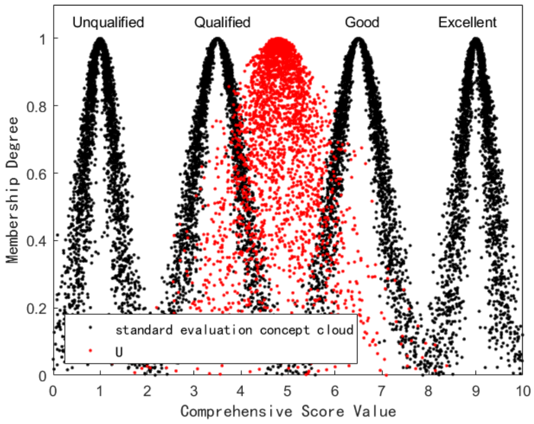

(2) First-Level for longitudinal crack

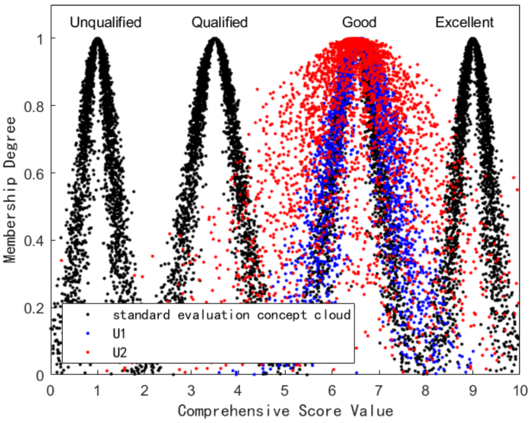

(3) Second-Level for transverse crack

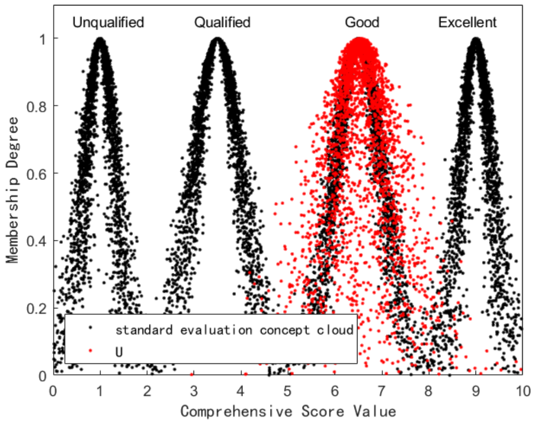

(4) First-Level for transverse crack

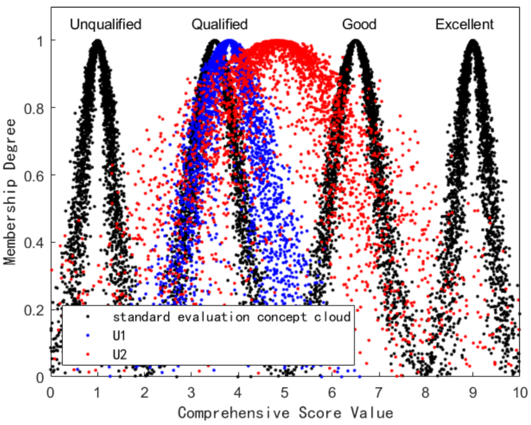

(5) Second-Level for roadbed settlement

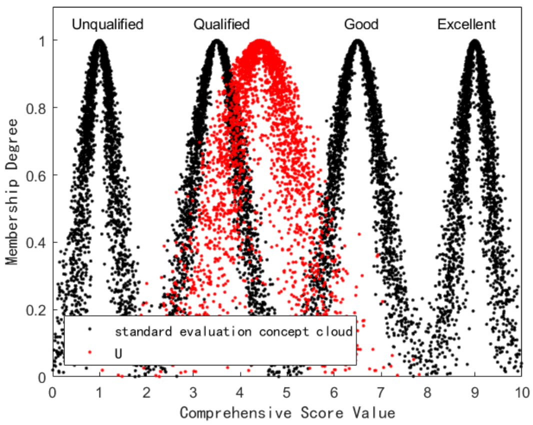

(6) First-Level for roadbed settlement

Fig. 6–Comparison Chart for two levels of Indicators

In terms of both the improvement and the stability, the repaired results of density and uniformity are superior to those of mechanical performance. A detailed analysis reveals that the mechanical performance repair effects are relatively poor, primarily due to the close correlation between the deflection ratio before and after grouting repair. Specifically, if the deflection value of the road section before grouting repair is already small, the change in deflection value after grouting repair is limited, resulting in minimal fluctuations in the deflection ratio before and after repair. This, to some extent, affects the evaluation results of mechanical performance repair effects.

The conclusion in this section not only clarifies the performance differences of grouting repair technology in addressing various defects and performance indicators but also provides important basis for optimising grouting repair schemes in the future. To address the issue of relatively insufficient mechanical performance restoration effects, future efforts could consider combining the initial deflection values of road sections to establish more targeted grouting parameters (such as grouting pressure and grouting material ratios) to enhance mechanical performance repair effects. Additionally, this conclusion validates again the effectiveness of the evaluation method presented in this paper and the effectiveness of evaluation indicators in reflecting actual repair conditions, providing a reference for effect assessments in similar projects.

CONCLUSION

In order to find an effective method to evaluate the grouting repair effect of internal diseases in expressways, this paper proposes a new comprehensive evaluation system that combines cloud model theory with combined weighting methods, comprehensively considering the fuzziness and randomness of the model. This method can maximize the rationalization of evaluation results. It has been verified through a highway repair project in China. The main conclusions are as follows:

(1) The Analytic Hierarchy Process (AHP) and Entropy Weight Method are used to subjectively and objectively assign weights to the indicators in the evaluation of grouting repair effects for internal diseases in asphalt pavement of expressways, respectively. Game theory is then employed to do the assignment of weights and form comprehensive weights. This method not only compensates for the excessive subjectivity of AHP but also combines it with the objective data of the Entropy Weight Method, making the evaluation model more accurate and scientific.

(2) An evaluation model for grouting repair effects is established using cloud model theory, which can effectively address the fuzziness and randomness inherent in decision-making problems. It achieves the conversion between qualitative expressions and quantitative data in the evaluation of grouting repair effects, making the evaluation results more scientific and reasonable.

(3) Two case studies including three different types of road defects are conducted by combining the combined weighting method with the cloud model, which is applied on two highways, respectively in Shandong and Liaoning Province of China. Similarity analysis is performed between the obtained comprehensive evaluation cloud charts and the standard cloud chart, determining the the evaluation grades of the grouting repair effect for different defects in the two engineering projects. The evaluation results are consistent with the actual engineering situation, indicating that the model has a good practicality and could provide a scientific method for evaluating the grouting repair effect.

ACKNOWLEDGEMENTS

This study was funded by Innovation Research Institute of Shandong High-speed Group Co., Ltd. (grant number SDGS-2022-0455-09).

REFERENCES

[1] Tao X, Xiao H., 2012. Investigation into causes of in-place rutting in asphalt pavement. Construction and Building Materials,vol. 28: 525-530 (https://doi.org/10.1016/j.conbuildmat.2011.09.007)

[2] Weitian Zh. et al., 2022. Structural condition assessment and fatigue stress analysis of cement concrete pavement based on the GPR and FWD. Construction and Building Materials, vol. 328: 127044 （https://doi.org/10.1016/j.conbuildmat.2022.127044）

[3] Karadelis J N.,2000. A numerical model for the computation of concrete pavement moduli: a non-destructive testing and assessment method. NDT & E International, vol. 33: 77-84 (https://doi.org/10.1016/S0963-8695(99)00034-1)
[4] Zhen L.et al.,2022.GPR-based detection of internal cracks in asphalt pavement: A combination method of DeepAugment data and object detection. Measurement, vol.197:111281. (https://doi.org/10.1016/j.measurement.2022.111281)
[5] Yunfeng P, Yinchuan G, Aiqin S, et al.,2023. Uniformity evaluation of asphalt pavements in hot and humid areas based on ground-penetrating radar. Construction and Building Materials, vol.384: 131432.
[6] Guichao F.et al.,2016.A hybrid fuzzy evaluation method for curtain grouting efficiency assessment based on an AHP method extended by D numbers. Expert Systems with Applications, vol.44: 289–303. (https://doi.org/10.1016/j.conbuildmat.2023.131432)
[7] Mansour F, Shahni Dezfoulian R.,2019.Pavement structural evaluation based on roughness and surface distress survey using neural network model. Construction and Building Materials, vol.204: 768–780. (https://doi.org/10.1016/j.conbuildmat.2019.01.142)
[8] Ming L, Chao L.et al.,2009. Review of the Back-Propagation Neural Network Method as a Basis for Pavement Performance Assessment. American Society of Civil Engineers, vol.2012: 1–8. （https://doi.org/10.1061/41047(354)
[9] Guanhu W, Liangcai C.et al.,2009. Comprehensive Evaluation Model of Grey Fixed Weight Clustering for Airport Pavement Service Performance. American Society of Civil Engineers, vol.2012: 984–989.（https://doi.org/10.1061/41039(345)163）
[10] Fan S.et al.,2023. Factor analysis evaluation of asphalt pavement performance considering structural strength and hidden cracks. Construction and Building Materials, vol.408: 133651. （ https://doi.org/10.1016/j.conbuildmat.2023.133651）
[11] Yan L, Jiupeng Z.et al., 2023.Suitability evaluation method for preventive maintenance of asphalt pavement based on interval-entropy weight-TOPSIS. Construction and Building Materials, vol.409: 134098. （https://doi.org/10.1016/j.conbuildmat.2023.134098）
[12] Xian L, Jiancun F.et al.,2024. Laboratory investigation for the bridge deck pavement performance of conventional asphalt mixtures based on fuzzy comprehensive evaluation method. Case Studies in Construction Materials, vol.20: e02784.（https://doi.org/10.1016/j.cscm.2023.e02784）
[13] Fei D,Jian P.et al.,2023. 3D geological suitability evaluation for underground space based on the AHP-cloud model[J]. Underground Space, vol.8: 109–122.（https://doi.org/10.1016/j.undsp.2022.03.006）
[14] Ouma Y, Opudo J, Nyambenya S.2015. Comparison of Fuzzy AHP and Fuzzy TOPSIS for Road Pavement Maintenance Prioritization: Methodological Exposition and Case Study. Advances in Civil Engineering, vol.2015.（https://doi.org/10.1155/2015/140189）
[15] Zhihong Z, Yi Y, Jingnan S. 2006.Entropy method for determination of weight of evaluating indicators in fuzzy synthetic evaluation for water quality assessment. Journal of Environmental Sciences, vol.18: 1020–1023.（https://doi.org/10.1016/S1001-0742(06)60032-6）
[16] Wanying L.et al.,2023. Evaluation of provincial power supply reliability with high penetration of renewable energy based on combination weighting of game theory-TOPSIS method. Sustainable Energy, Grids and Networks, vol.35: 101092.（https://doi.org/10.1016/j.segan.2023.101092）
[17] Xinfan M.et al.,2022. Comprehensive evaluation of 5G+ smart distribution network based on combined weighting method-cloud model. Global Energy Interconnection, vol.5: 675–691. （https://doi.org/10.1016/j.gloei.2022.12.009）

Article no. 25

THE CIVIL ENGINEERING JOURNAL 3-2025

APPLICATION OF THE OPTIMIZED REGRESSION TO VOLUME EXPANSION EVALUATION OF CEMENT PASTE WITH FLY ASH AND MGO EXPANSIVE ADDITIVE

Yishuo Wang, Ziyu Liu and Cheng Wang

Xi'an University of Science and Technology, Xi'an710600, Shaanxi, China; 22403050108@stu.xust.edu.cn

Received: 21.10.2024
Received in revised form: 13.02.2025
Accepted: 01.09.2025

ABSTRACT

The synergistic effects of fly ash (FA) and magnesium oxide (MgO) expansive addition (MEA) on the expansion behavior and mechanical qualities of cement paste are validated by studies that manipulate dose and curing temperature as factors. Few studies have been conducted on the use of machine learning (ML) techniques to predict the volume expansion (V_e) of cement paste when FA and MEA are present. Utilizing a set of data that contained 170 experimental results that were obtained from previous research, the purpose of this study was to develop and evaluate ML algorithms for the assessment of V_e. To achieve this, the Extra tree regression (ETR) was created. The technique uses FA, Portland cement (PC), MEA, and sample age (Age) as input parameters. The Red-Tailed Hawk Algorithm (RTHA) and the Electric Eel Foraging Algorithm (EEFA) establish the hyperparameters of ETR, which greatly affect its effectiveness. The variation percentages of the two models developed for these measures are a minimum of 13%; in some cases, this variation decreases by 53%, illustrating the ETR (R)'s predictive reliability and efficacy. For instance, for the RMSE index, ETR (R) achieved values of 0.0053 and 0.01 during the training and testing phases, which are about 28% and 14% lower than the corresponding values of ETR (E) at 0.0068 and 0.0114, correspondingly. The impact of this research allows practical applications: cement formulation optimization, structural integrity, and enhanced quality control in the building and construction industry. An example could be an exact prediction of volume expansion V_e by the model, which gives very valuable cost reductions by preventing cracks and material performance consistency in cement paste with FA and MgO additives MEA.

KEYWORDS

Cement Paste, Volume Expansion, Fly Ash; Machine Learning, Extra Tree Regression, Optimal models

INTRODUCTION

For large-scale concrete constructions, thermal stresses that can lead to fracturing are a considerable issue, necessitating the performance of temperature control strategies throughout the creation phase. In the case of hydraulic mass cement-based composite constructions, the primary cause of gaps is temperature-induced warping occurring shortly after the completion of creation [1, 2]. The initial fracturing phenomenon observed in cement-based composite primarily arises from the balance between resistance and stress throughout the hardening phase. As cement-based composite matures, its attributes evolve, leading to a gradual growth in resistance, which in turn results in the distribution of high temperatures [3, 4]. The simultaneous effects of hydration heat and the cooling of the surroundings create a temperature gradient within the cement-based composite construction.

Various temperature control techniques, including the application of ice for $\mathrm{pre-cooling}$ aggregates, the installation of cooling water pipes within the construction, and the performance of surface heat retention techniques, have been employed to mitigate the occurrence of temperature-related gaps [5]. Nevertheless, they are not cost-effective, and certain approaches, like pipe cooling, are quite intricate and could significantly impact the construction actions timeline [6].

In both investigation and functional applications, the addition of a suitable amount of magnesium oxide, which has been calcined at elevated temperatures, can be incorporated into the dam's cement-based composite preparation procedure. This inclusion facilitates the expansion of the cement-based composite, effectively counteracting contraction distortion that may occur during a diminish in temperature [7, 8]. The incorporation of magnesium oxide as an enhancer factor in mass concrete, alongside routine auxiliary measures such as surface heat protection, can effectively manage self-induced volume distortion, thereby decreasing and stopping gaps in dam concrete. This approach has the potential to avert gaps in dams and minimize the reliance on conventional cement-based composite temperature management techniques, such as aggregate $\mathrm{pre-cooling}$, ice blending, and the use of embedded refrigerating water conduits [9].

The distribution strategy of magnesium oxide concrete is notably difficult [10]. The hydration procedures of both the cement and the magnesium oxide contribute to endogenous distortion. Additionally, the presence of FA within the cementing matter significantly affects the features of magnesium oxide cement-based composite [11].

The labor-intensive and expensive characteristics of laboratory studies, coupled with the possible negative impacts on the environment, have led to a growing interest in alternative approaches. These include non-linear and advanced regression techniques, tuned models [12], optimized models, and hybrid models [13–16]. It is generally crucial to mathematically model the endogenous volume distortion (distribution) and the corresponding distribution stress during the construction phase.

Numerous engineering actions in China have resulted in the collection of remarkable distortion data [17]. B. Zhu (2002, 2003) [18, 19] proposed the measured quantities for the endogenous volumetric distortion of micro-distribution concrete and founded a computation model of the endogenous volume distortion in light of these variations. According to the engineering test data and pertinent laboratory analyses, G. Yang et al. (2004) [20] proposed that the endogenous volumetric distortion features of magnesium oxide cement-based composite at a fixed temperature align with a $\mathrm{hyperbolic}$ model. G. Zhang et al. (2002, 2005) [21–23] conducted a thorough analysis utilizing imitation methods to examine the effects of the growth of cement-based composite's elastic modulus, the degree of creep over time, and temperature on the distribution of MgO. Liu et al. (2006) [24] developed a numerical model to describe the correlations among the endogenous volume distortion of magnesium oxide cement-based composite, the content of magnesium oxide, the volume of FA, and the $\mathrm{temperature}$. P. Xu and colleagues introduced the equivalent age method to assess the un-planned volume distortion of magnesium oxide cement-based composite in their 2008 study [25]. Moreover, $\mathrm{sub-stitute}$ models have been suggested, including the arctangent curve model developed by C. Chen and associates in 2008 [26].

According to the references [27–29], it is evident that model ETR was developed in 2014, making it a relatively newer model compared to older models like ANN and SVR. In contrast, the optimization algorithms $RTHA$ and $EEFA$ are very recent developments and have not yet been applied in civil engineering and concrete technology. A comprehensive review of the technical literature shows that the optimized models of $ETR + RTHA$ and $ETR + EEFA$ are less used in various fields of civil engineering. These models will be predicted and optimized in future research.

The estimation of cement paste volume expansion (V_e) FA and MEA using ML techniques have not received much attention. The objective of this study was to develop and evaluate ML techniques for assessing V_e via a dataset of 170 test results derived from previously published research. ETR algorithm has been devised to achieve this objective. The approach utilizes input parameters like PC, FA, MEA, and sample age (Age) to produce the layouts. The effectiveness of ETR is considerably influenced by its hyperparameters, which may be enhanced through optimization techniques. The present work used advanced optimizers, namely the EEFA and the RTHA, to achieve this particular target. The efficacy of the established regression analysis is assessed by several metrics, taking into account the values of observed and anticipated V_e. Engineers may reduce the danger of cracking and other expansion-related problems by fine-tuning mixes to obtain desired qualities by forecasting the volume expansion behavior of cement paste. It makes use of sophisticated optimizers such as RTHA and EEFA, which could save time and money in experimental research.

Overall, it was reviewed that recent studies demonstrate the effectiveness of incorporating magnesium oxide in cement-based composites to reduce temperature-induced warping and crack reduction in large-scale concrete structures. Advanced modeling techniques, including the ETR algorithm and optimization methods such as EEFA and RTHA, are used to predict volume expansion in cement pastes and increase the understanding of endogenous volume distortion. The goal of integrating these models is to improve construction practices by minimizing the risk of cracking and optimizing material properties, thereby reducing reliance on traditional temperature control methods.

Previous studies indicated that a limited application of machine learning techniques was employed to forecast the volume expansion parameter of cement paste (V_e). Additionally, the predominant reliance on laboratory experiments proved to be both expensive and time-consuming. Consequently, this research aims to implement advanced machine learning methodologies that offer predictions that are not only more cost-effective but also more precise and efficient.

RESEARCH METHODOLOGY

Dataset Pre-Processing

Different quantitative studies have been conducted to estimate the growth in volume (V_e) of cement paste, and the result is that the precise and correct selection of input parameters when using ML approaches is one of the main agents used to achieve perfect estimation. The initial step for using an ML approach requires the crucial selection of input and outcome parameters and data sets, which directly affects the precision and practicality of soft computing approaches. Therefore, data must be collected from reliable resources to have a positive impact on estimation precision [30]. Following the set criteria for feature selection, a whole of 170 data were collected, which were divided into two parts, training and testing, with quantities of 70% and 30%, respectively. This data-splitting strategy has been adopted using the existing literature [31–34]. The input parameters include four items: FA, PC, extensive addition of MgO (MEA) and example age (age), and the outcome parameter is the volume growth component (V_e) of the cement paste. Regarding the volumetric growth (V_e) of cement paste, it can be said that it is an important agent in understanding the behavior and properties of cement base matters. This parameter refers to the increase in volume of cement paste due to hydration and other chemical reactions that occur when water is added to cement. A higher water/cement proportion can lead to increased volumetric growth, but may negatively affect resistance. Also, it is very essential to predict the performance of concrete and cement-based materials during curing and long-term use. Also, in Table 1, by using commonly used statistical indicators including Minimum, Maximum, Average, Standard Deviation, Skewness and Kurtosis, more features of the related dataset have been divided into two parts. The standard deviation shows the changeability of the data, the skewness shows the disproportion of the data broadcast, for example, the value 0 indicates a symmetrical broadcast, quantities greater than 0 indicate a right-skewed broadcast, and quantities less than 0 indicate a left-skewed broadcast. kurtosis also indicates the dispersion of the broadcast, i.e. the number 0 is normal, the positive value of the broadcast has more outliers, and the negative values of the broadcast have less outliers. For example, in this table, in the training part, the FA ranges from 0 to 40% with an average of 21.68%

and a slight broadcast to the left. Also, in the test part, the parameter V_e declined by an average of 0.046% compared to the value of the same parameter in the training part and has a positive skew, which is similar to the broadcast pattern of the same parameter in the training part. Consequently, this table shows the general insight of the input and outcome parameters for the two mentioned levels and shows the general changes in the amount of data broadcast and their central tendency. This method is very useful for understanding the performance of the model and recognizing its attributes.

In order to understand the data set used deeply, graphic displays are used to understand the attributes of the data. For example, in Figure 1, an example of this graphic display is given to compare the outcome parameter against four input parameters. This chart is a combination of a violin diagram and a box chart that depicts the broadcast of two parameters in front of each other for comparison. For example, part a of Figure 1 shows the two parameters PC and V_e. The left y-axis displays the numbers of the PC parameter, ranging from 55% to 100%. The y-axis on the right side represents V_e, ranging from 0 to 0.18%. The violin chart for the cyan PC variable illustrates the broadcast of quantities in percentage. Its width also shows various density numbers of data dots. The violin chart for the orange parameter V_e also shows the broadcast of the numbers of this parameter. Each violin plot overlaps with the box plot, which forms the line inside the box (middle). This chart effectively shows the broadcast between two parameters and displays their central tendencies, variability, and potential outliers. It is especially useful for comparing the acting of two parameters in relation to each other and also for identifying patterns or trends in the data.

Tab. 1 - Statistics for each variable included in the dataset

Variable	Type	Amount	Unit	Statistics					
				$Min.*$	$Max.$	$Avg.$	$St.D.$	$Skew.$	$Kurt.$
Training phase	Input	PC	%	60	100	78.31933	16.31205	0.155304	-1.49253
	Input	FA	%	0	40	21.68067	16.31205	-0.1553	-1.49253
	Input	MEA	%	0	10	5.042017	3.969199	-0.01496	-1.42207
	Input	Age	$Days$	0.829	91.25	36.93034	30.48136	0.355487	-1.32172
	Target	V_e	%	0	0.166	0.050824	0.044724	1.049979	0.170372
Testing phase	Input	PC	%	60	100	82.7451	15.85207	-0.24905	-1.38556
	Input	FA	%	0	40	17.2549	15.85207	0.249051	-1.38556
	Input	MEA	%	0	10	5	4.315953	0	-1.70516
	Input	Age	$Days$	1.029	91.044	29.69829	29.47453	0.665697	-0.94112
	Target	V_e	%	0	0.166	0.045608	0.049919	1.048993	-0.09609

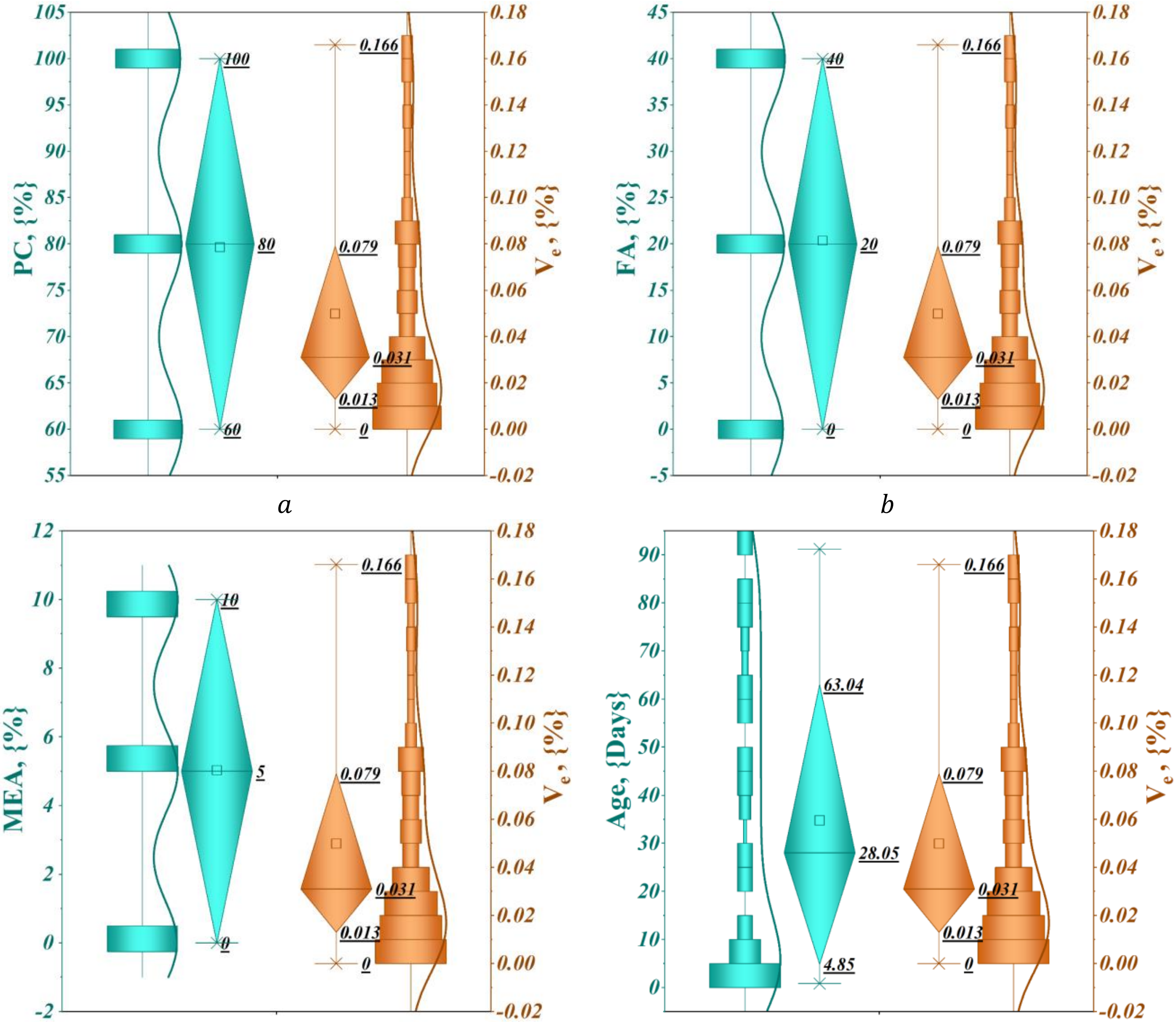

Fig. 1 - Visualization form of the variables versus target

The diagram presented in Figure 2 shows the results of the Morris analysis of the data set, where a method of sensitivity analysis was used to evaluate the importance of the input parameters in the model. Moise analysis examines the effect of changes in input parameters on the outcome parameter. This method actually determines which changes in the input parameter have a great impact on the results of the outcome parameter. For example, part c of Figure 2 shows the input parameters including (PC, FA, MEA, Age) and the corresponding sensibility criterion. The vertical axis of section c shows the sensibility measure (σ), which quantifies the change in the model outcome against changes in each input parameter. PC and FA parameters have the highest sensibility numbers (0.1417), which indicates that they have the most influence on the model result. Bar graphs allow visual comparison of how each parameter contributes to result changeability. This can inform decisions about which parameters to prioritize for further estimation or correction in the model. Morri's analysis, as shown in this chart, is a valuable tool for recognizing important input parameters that significantly affect model outcomes.

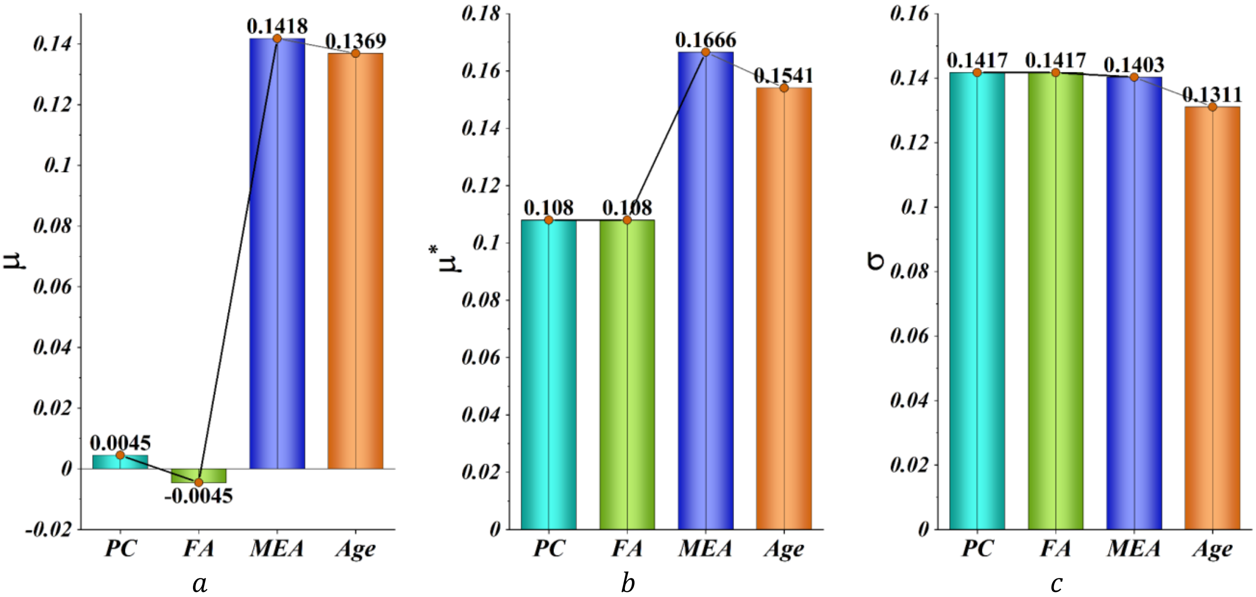

Fig. 2 - Morris analysis for variables' importance evaluation

The chart shown in Figure 3 shows a correlation matrix that shows the Spearman correlation coefficients among different parameters associated with a particular data set. The following explains the main components and concepts of Spearman's correlation: quantities in cells represent Spearman's correlation coefficients, which can range from -1 to 1. A value of 1 indicates a perfect positive correlation (in which a growth in one variable corresponds to a growth in another parameter), while -1 indicates a perfect negative correlation (in which a growth in one parameter leads to a decline in the other). A coefficient of 0 indicates no correlation. Diagonal cells, which reflect the correlation of a variable with itself, show a quantity of 1.0. For instance, the correlation coefficient between the parameters Age and V_e is significantly high at 0.69, which indicates a robust positive correlation. Also, the correlation between MEA parameter and V_e has an acceptable correlation with a quantity of 0.6. Spearman's correlation matrix provides important insights about the connections among various parameters in the data set. It helps identify positive and negative correlations, thereby facilitating further analysis and informed decision-making about matter function. Spearman's correlation is particularly useful in this context, as it evaluates monotonic connections and makes it pliable against the influence of outliers and non-linear associations.

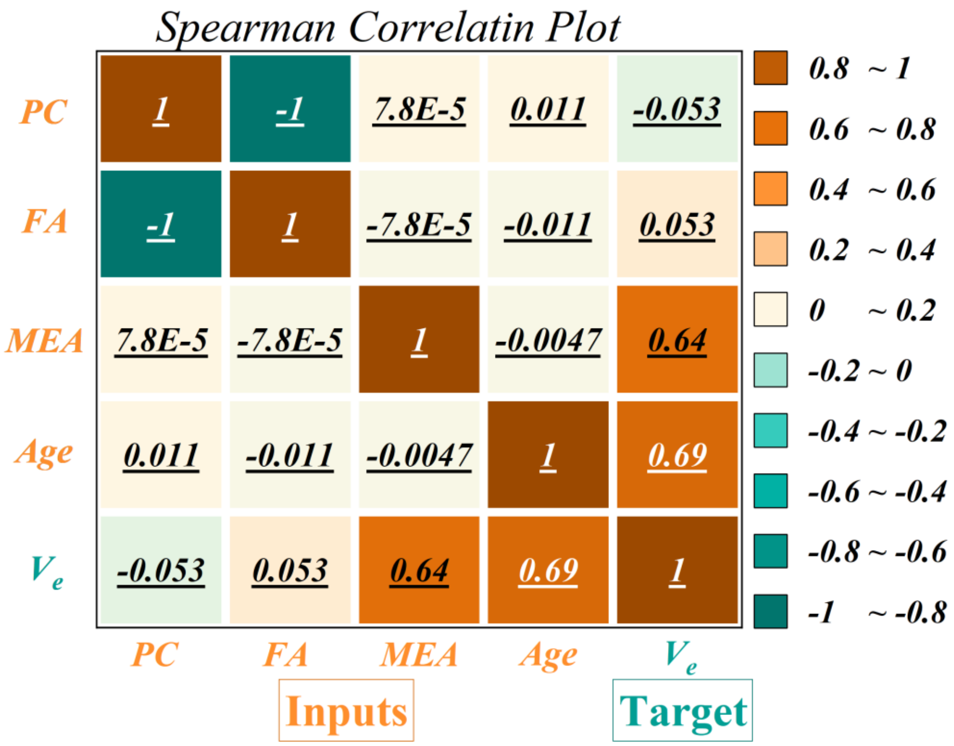

Fig. 3 - Introduced variables correlation matrix values

Electric Eel Foraging Algorithm ($EEFA$)

Electric eels, part of the Gymnotidae family, are deceptive hunters in the animal area, renowned for their terrific capacity to manufacture electric evacuations in freshwater rsurroundings. The phases of utilization and discovery in electric eel foraging optimization are designed based on the social hunt acting observed in electric eels, which encompass their interactions, relaxing tactics, movement strategies, and chasing methods. Statistical models illustrating the searching acting of EEFA optimizations are presented in the following part [27].

Communication Behavior

When eels face a group of fish, they begin to swim together in a coordinated manner, manufacturing a twisting movement. To efficiently capture numerous small fish gathered at the center of this organization, the eels initiate a motion into a large, electrified circle [27]. The interaction indicates that every eel utilizes its situation to communicate with others efficiently. The process of calculating an eel's novel situation involves comparing its location to the center of the crowd and an accidentally selected eel. The distinction between an eel manufactured accidentally within the quest zone and one selected accidentally from the existing crowd is utilized to set the eel's situation. Eels engage with each other through a procedure known as churning, which reflects their erratic motions. This acting is donated by the models shown in the following manner [27].

$$C = n_1 \times B \tag{1}$$

$$n_1 \sim N(0,1) \tag{2}$$

$$B = [b_1, b_2, b_3, \dots, b_k, \dots, b_d] \tag{3}$$

$$b(k) = \begin{cases} 1 & if\ k == g(l) \\ 0 & else \end{cases} \tag{4}$$

$$g = randperm(d) \tag{5}$$

$$l = 1,2,\dots,\left\lceil \frac{T-t}{T} \times r_1 \times (d-2) + 2 \right\rceil \tag{6}$$

T represents the highest value of repetitions allowed.

The concept of inter-active acting was introduced as bellows [27]:

$$\begin{cases} \vartheta_i(t+1) = x_j(t) + C \times \left(\bar{x}(t) - x_i(t)\right), p_1 > 0.5 \\ \vartheta_i(t+1) = x_j(t) + C \times \left(x_r(t) - x_i(t)\right), p_1 \leq 0.5 \end{cases}$$
$$\begin{cases} \vartheta_i(t+1) = x_i(t) + C \times \left(\bar{x}(t) - x_j(t)\right), p_2 > 0.5 \\ \vartheta_i(t+1) = x_i(t) + C \times \left(x_r(t) - x_j(t)\right), p_2 \leq 0.5 \end{cases} \quad (7)$$

$$\bar{x}(t) = \frac{1}{N}\sum_{i=1}^{N} x_i(t) \quad (8)$$

$$x_r = Low + r \times (Up - Low) \quad (9)$$

In this context, p_1 and p_2 represent accidental quantities within the range of $(0, 1)$. The parameter x_j denotes the situation of an accidentally chosen eel from the present crowd, where $j \neq i$. The whole crowd size is indicated by n, while $r_1$is another accidental quantity also within the interval $(0, 1)$. The subordinate $fit(i)$ computes the fitness score for the possible crowd of the ith electric eel. Furthermore, r is an accidentally manufactured vector that falls within the range of $(0, 1)$, and Low and Up define the lowest and highest borders of the quest zone in the same order.

It is essential to note that in the primary two instances of Eq. (7), the relation fits as $fit\left(x_j(t)\right) < fit(x_i(t))$. Conversely, in the latter scenarios of this numerical expression, $fit\left(x_j(t)\right) \geq fit(x_i(t))$ is also observed. Additionally, Eq. (9) illustrates that the interactions among electric eels facilitate their motion toward various situations within the discovery region. This acting can be highly advantageous for studying EEFA throughout the quest region.

Relaxing acting

In the quest zone, the zone where any single dimension of an eel′s situation vector is moved to the central diagonal is defined as the relaxing region. This resting zone can be described by the following attributes [27]:

$$\left\{X \middle| \left|X - Z(t) \leq \alpha_0 \times \left|Z(t) - x_{prey}(t)\right|\right|\right\} \quad (10)$$

$$\alpha_0 = 2.e^{\frac{\mu-1}{T}} \quad (11)$$

$$Z(t) = Low + z(t) \times (Up - Low) \quad (12)$$

$$z(t) = \left(x_{rand(n)}^{rand(d)}(t) - Low^{rand(d)}\right) \quad (13)$$

In this context, α_0 represents the initial scale of the relaxing region while x_{prey} indicates the starting situation vector of the currently identified improved resolution. The parameter r_2 is an accidental quantity manufactured within the interval $(0, 1)$. The expression $\alpha_0 \times \left|Z(t) - x_{prey}(t)\right|$ donates the extent of the relaxing area. Here, z signifies a normalized quantity, and $x_{rand(n)}^{rand(d)}(t)$ refers to a specific situation dimension selected from an accidentally chosen quest factor within the existing crowd.

An eel assumes its relaxing acting within its designated relaxing zone before initiating the relaxing acting described in Equation 14.

$$R_i(t+1) = Z(t) + \alpha \times \left|Z(t) - x_{prey}(t)\right| \quad (14)$$

$$\alpha = \alpha_0 \times sin(2\pi r_3) \quad (15)$$

where r_3 is an accidentally manufactured quantity within the interval $(0, 1)$, and a donates the scale of the relaxing zone.

In its relaxing situation, where this relaxing acting can be replicated, an eel modifies its place as it approaches its relaxing region while maintaining its relaxing place [27]:

$$v_i(t+1) = R_i(t+1) + n_2 \times (R_i(t+1) - round(rand) \times x_i(t)) \tag{16}$$

$$n_2 \sim N(0,1) \tag{17}$$

Application of EEFA

The whole crowd size and the highest value of repetitions are two key control variables that basic EEFA sets up prior to starting the enhancement procedure. An accidentally manufactured set of eels is uniformly dispersed. Each eel employs inter-active acting to manufacture novel applicant resolutions during each repetition when the energy agent $E > 1$. Each eel engages in utilization through relaxing, movement, or chasing, acting with equal probability when the energy agent $E \leq 1$ manufactures fresh applicant resolutions. In every repetition of the loop, the present best resolution is revised following a comparison between the newly found resolution and the available ones. As the procedure continues, the agent E diminishes, compelling each eel to shift from discovery to utilization. The interactive procedure continues until the stopping situation is met. The improved resolution up to that moment is preserved thereafter. A concise overview of EEFA's pseudocode is presented in Algorithm 1, accompanied by its flowchart in Algorithm. (1).

Algorithm 1. A pseudocode highlighting the essential methods of EEFA.
1: Explain the variables n and T 2: Accidentally setting up the crowd $X_i (i = 1,2,\ldots,n)$ and evaluate their fitness score fit_i, while X_{prey} represents the improved resolution discovered up to this point. 3: While (The expiration agent has not been met) do 4: for every eel X_i do 5: Calculate E 6: if $E > 1$, then 7: Execute the inter-active acting using Equation 7 8: Calculate the fitness fit_i 9: else 10: if $rand > 1/3$, then 11: Determine the relaxing zone using Equation 14 12: Execute the relaxing procedure 13: Calculate the fitness fit_i 14: else if $rand > 2/3$, then 15: Execute the movement procedure 16: else 17: Determine the chasing zone 18: Execute the chasing 19: end if 20: end if 21: Adjust the situation of each eel 22: end for 23: Revise the resolution achieved to date, X_{prey} 24: end while 25: Revise the resolution X_{prey}

Red-Tailed Hawk Algorithm ($RTHA$)

The procedure of identifying nasty activity utilizes RTHA for attribute selection. This tactic mimics the chasing acting of this creature [28]. The acting exhibited throughout the chasing procedure is examined and exhibited. The three distinct stages of RTHA include low rising, high rising, and bending and stooping.

Members ascend high into the sky, searching for an ideal situation in terms of power supply accessibility, as illustrated by the numerical modeling in Eq. (18):

$$X(t) = X_{best} + \left(X_{mean} - X(t-1)\right).Levy(dim).TF(t) \quad (18)$$

In Eq. (18), the situation of these creatures at the $\mathrm{t-th}$ repetition is illustrated as $X(t)$. The best position achieved up to that dot is X_{best}, while X_{mean} indicates the mean of the places. The $Levy$ subordinate refers to the Levy flight expansion, and also, the transition agent subordinate is denoted as $TF(t)$.

$$Levy(dim) = s\frac{\mu \times \sigma}{|\vartheta|^{\beta^{-1}}}$$
$$\sigma = \left(\frac{\Gamma(1+\beta).sin\left(\frac{\pi\beta}{2}\right)}{\Gamma\left(\frac{1+\beta}{2}\right).\beta.2^{\left(1-\frac{\beta}{2}\right)}}\right) \quad (19)$$

In scenarios where the issue size is small, β is a collection at a fixed value of 1.5, s is fixed at 0.01, and also u and v represent accidental integers within the range of 0 to 1.

$$TF(t) = 1 + sin\left(2.5 + \left(\frac{t}{T_{max}}\right)\right) \quad (20)$$

T_{max} represents the highest value of repetitions. In the low-rising acting, members spiral downwards towards the aim, flying at a lower height. The numerical representation of this is provided in Equations 21:

$$\begin{gathered} X(t) = X_{best} + \left(x(t) + y(t)\right).StepSize(t) \\ StepSize(t) = X(t) - X_{mean} \end{gathered} \quad (21)$$

In this context, x and y represent the axes of the coordinate system.

$$\begin{cases} x(t) = R(t).sin\left(\theta(t)\right) \\ y(t) = R(t).cos\left(\theta(t)\right) \end{cases} \begin{cases} R(t) = R_0.\left(r - \frac{t}{T_{max}}\right).rand \\ \theta(t) = A.\left(1 - \frac{t}{T_{max}}\right).rand \end{cases} \begin{cases} x(t) = \frac{x(t)}{max|x(t)|} \\ y(t) = \frac{y(t)}{max|y(t)|} \end{cases} \quad (22)$$

In this context, r illustrated a control achievement [1], [2], while the primary quantity, represented as R_0, falls within the interval $[0.5 - 3]$. The parameter A signifies the angle achievement $[515]$, and rand refers to an accidental integer within the interval $[0,1]$. This variable facilitates the hawk's helix motion around the aim.

The hawk quickly descends and strikes its aim from the arbitrary situation while gliding at a low altitude, as illustrated in Equation 23:

$$\begin{gathered} X(t) = \alpha(t).X_{best} + x(t).StepSize1(t) + y(t).StepSize2(t) \\ StepSize1(t) = X(t) - TF(t).X_{mean} \\ StepSize2(t) = G(t).X(t) - TF(t).X_{best} \end{gathered} \quad (23)$$

The agents for acceleration and gravity are donated by α and G, in the same order:

$$\begin{gathered} \alpha(t) = sin^2\left(2.5 - \frac{t}{T_{max}}\right) \\ G(t) = 2.\left(1 - \frac{t}{T_{max}}\right) \end{gathered} \quad (24)$$

In Equation (24), the acceleration α of this creature's growth as time t progresses, improving the convergence proportion. Additionally, the gravitational impact G declines the variety of utilization as the hawk approaches the aim.

Selecting a suitable attribute that assists the sorter in recognizing an example class within the data presents a substantial challenge [35].

In the chosen procedure, improving the function of categorization duties is important, along with the automatic deletion of unfitting attributes once the desired ones have been recognized. The RTHA is utilized to identify the best sub-collection of properties and leverages the sorter to assess the categorization function. A_c represents categorization precision, bs indicates the size of the attribute sub-collection, and D_t refers to the whole quantity of properties in the data collection. The sorter fault can be donated as $1 - A_c$, while the selected sub-collection of properties from the data is expressed as $\frac{d_s}{D_t}$. Thus, the fitness subordinate is defined as below:

$$\downarrow Fitness = \mu.(1 - A_c) + (1 - \mu).\frac{d_s}{D_t} \tag{25}$$

In Equation 25, the weight assigned to the fault categorization is μ, which ranges from 0 to 1.

To gain a clearer insight into the properties of the suggested RTHA and its basics, the concepts related to RTHA are outlined in Algorithm 2.

Algorithm 2. Pseudocode of RTHA.
Setting up: Accidental manufacture within the discovery region While $t < T_{max}$ do Elevated level: for $i = N_{pop}$ do Determine the Levy flight broadcast Determine the movement agent TF Revise situations Finish Decline level: for $i = N_{pop}$ do Determine the directional coordinates Revise situations Finish The phase of bending and gliding: for $i = N_{pop}$ do Determine the acceleration and the gravitational agents Determine the StepSize Revise situations Finish Finish

Extra Tree Regression (ETR)

The ETR introduced by Geurts et al. [36] is a group learning technique that depends on a large quantity of decision trees (DTs). The ETR differs from the random forest method in 2 significant ways: (1) the ETR selects an accidental binary dividing number to divide the nodes of the DT, whereas the random forest method employs an improved dividing factor. (2) The ETR leverages all available data dots to diminish divergence, whereas the random forest method employs the boot-strap tactic, a sampling way that allows for substitution. The ETR offers several benefits, including (1) a direct and impactful node dividing procedure compared to other group learning tactics. (2) The ETR competently addresses the issue of over-fitting due to its considerable unpredictability and leverages the whole data collection to decline divergence.

Workability Indicators

To comprehensively assess ETR models, it is essential to include many performance metrics since each criterion provides distinct insights into the model's precision and dependability.

Performance Index (PI) by Equation 26
Coefficient of Determination (R^2) by Equation 27
Root Mean Square Error ($RMSE$) by Equation 28
Symmetric Mean Absolute Percentage Error ($SMAPE$) by Equation 29
Mean Absolute Scaled Error ($MASE$) by Equation 30
Theil's U Statistic (U) by Equation 31

Willmott's Index of Agreement (WI) by Equation 32
Uncertainty with a 95-coincidence level ($U_{95}\%$) by Equation 33
Scatter index (SI) by Equation 34

$$PI = \frac{1}{\bar{N}} \frac{RMSE}{\sqrt{R^2 + 1}} \tag{26}$$

$$R^2 = \left(\frac{\sum_{i=1}^{n} (N_i - \bar{N})(O_i - \bar{O})}{\sqrt{\left[\sum_{i=1}^{n} (N_i - N)^2\right]\left[\sum_{i=1}^{n} (O_i - \bar{O})^2\right]}} \right) \tag{27}$$

$$RMSE = \sqrt{\frac{1}{n} \sum_{i=1}^{n} (O_i - N_i)^2} \tag{28}$$

$$SMAPE = \frac{1}{n} \sum_{i=1}^{n} \frac{|N_i - O_i|}{\frac{(|N_i| + |O_i|)}{2}} \times 100 \tag{29}$$

$$MASE = \frac{\frac{1}{n} \sum_{i=1}^{n} |N_i - O_i|}{\frac{1}{n-1} \sum_{i=1}^{n} |N_i - N_{i-1}|} \tag{30}$$

$$U = \frac{\sqrt{\frac{1}{n} \sum_{i=1}^{n} (O_i - N_i)^2}}{\sqrt{\frac{1}{n} \sum_{i=1}^{n} N_i^2} + \sqrt{\frac{1}{n} \sum_{i=1}^{n} O_i^2}} \tag{31}$$

$$WI = 1 - \frac{\sum_{i=1}^{n} (N_i \ - N_i\ )^2}{\sum_{i=1}^{n} (|O_i \ - \bar{O}| + |N_i \ - \bar{O}|)^2} \tag{32}$$

$$U_{95} = 1.96\sqrt{(SD^2 + RMSE^2)} \tag{33}$$

$$SI = \frac{\sqrt{\left(\frac{1}{n}\right) \sum_{i=1}^{n} ((N_i - \bar{N}) - (O_i - \bar{O}))^2}}{\left(\frac{1}{n}\right) \sum_{n=1}^{i} O_i} \tag{34}$$

where:
N_i : The measured V_e.
$\bar{N}$: The means of the measured V_e.
O_i : The expected V_e.
$\bar{O}$: The mean of the anticipated V_e.
n : The total number of observations.

FINDINGS AND COMPARISON

Step-by-step Development

An adaptive and consistent ML approach capable of addressing both classification and regression challenges with remarkable endurance and accuracy has been implemented utilizing the ETR model. Enhancing feature relevance, scalability, and flexibility are other objectives of this model. The hyperparameters of the ETR framework that significantly influence effectiveness may be modified via trial and error or optimization techniques. This methodology seeks to improve predictive precision and address missing data issues.

Optimizing an ETR model demands the meticulous adjustment of essential hyperparameters, including $n\_estimators$, max_depth, $min\_samples\_split$, $min\_samples\_leaf$, and $max\_features$, to achieve equilibrium among model intricacy and generalizability, as demonstrated in Table 2. The procedure is optimized by first partitioning the dataset into 75% for learning and 25% for assessment. Innovative optimization approaches, including the $RTHA$ and the $EEFA$, are used to investigate various hyperparameter mixtures and minimize the $RMSE$ on the validation set. The ideal hyperparameter set is determined after comprehensive training and assessment of many models, taking into account the unique efficacy of each model. Table-based diagram for the research program and the tested models and the adopted variables is supplied in Table 3.

Tab. 2 - The related parameters and hyperparameters of models

Optimization algorithms	Initial Parameters	Value	Coupled models		Named	Hyperparameters	Optimal Value
EEFA	Total of iterations	200	ETR+EEFA	⋙	ETR(E)	$n\_estimators$	105
	Total of tries	5				max_depth	18
	Total of population	30				$min\_samples\_split$	2
	Parameter free	-				$min\_samples\_leaf$	3
						$max\_features$	0.76
RTHA	Total of iterations	200	ETR+ RTHA	⋙	ETR(R)	$n\_estimators$	153
	Total of tries	5				max_depth	28
	Total of population	50				$min\_samples\_split$	3
	A	15				$min\_samples\_leaf$	3
	$R0$	0.5				$max\_features$	0.58
	r	1.5					
	N	30					

Tab. 3 - Table-based diagram for the research program and the tested models and the adopted variables

Aspect	Details
Research Objective	"Predicting Volume Expansion of Cement Paste"
Key Phases	Data Collection and Preprocessing. Model Development and Optimization. Model Evaluation and Analysis.
Models Tested	Extra Tree Regression (ETR) optimized with RTHA (ETR (R)) and EEFA (ETR (E))
Optimization Methods	Red-Tailed Hawk Algorithm (RTHA), Electric Eel Foraging Algorithm (EEFA)
Input Variables	Fly Ash (FA), Portland Cement (PC), MgO Expansive Addition (MEA), Sample Age (Age)
Dataset Size	170 samples
Performance Metrics	PI, R^2, $RMSE$, $SMAPE$, $MASE$, U, WI, $U_{95}\%$, and SI
Best Performing Model	ETR (R) (with RTHA tuning)
Key Findings	ETR (R) achieved RMSE values of 0.0053 (training) and 0.01 (testing), outperforming ETR (E) by 28% and 14% respectively.
Recommendations	Expand dataset, incorporate additional parameters, test hybrid models.

Comparison and Justification

This research demonstrates the results of integrating hybridized ETR approaches with the $EEFA$ and $RTHA$ methodologies. The determination of the V_e of cement paste, consisting of FA and MEA, was performed using these techniques. Figure 4 depicts the projected and actual values of V_e during the training and assessment stages of the $ETR\ (E)$ and $ETR\ (R)$ methodologies, which were developed. Furthermore, the figure illustrates the distribution of the residual %. The accuracy of methods for predicting V_e was assessed using several metrics, including PI, R^2, $RMSE$, $SMAPE$, $MASE$, U, WI, $U_{95\%}$, and SI. Furthermore, the rating-based methodology has been established to allocate a score to each index associated with each strategy, with the greatest score awarded to the best suitable value. Table 4 presents the measurement results for the designs, highlighting the optimal scenario and the corresponding scores attained during both the learning and evaluation phases.

The results indicate that the $ETR\ (E)$ and $ETR\ (R)$ methodologies have significant potential for accurately forecasting the V_e. During the training and assessment phase, the $ETR\ (R)$ approach exhibited R^2 values of 0.986 and 0.9603, signifying exceptional precision. The findings for $ETR\ (E)$ were notably lower than those for $ETR\ (R)$, with R^2 values of 0.9787 and 0.9469, respectively. The optimal model was combined with WI, and the results exhibited a performance trend akin to one of the expected measures. Supplementary error-based indicators are also useful in evaluating the validity of the methodology. In the present study, numerous indicators, including PI, $RMSE$, $SMAPE$, $MASE$, U, $U_{95\%}$, and SI were calculated. It is essential to recognize that decreased values signify superior performance for these metrics. The variation percentages of the two models developed for these measures are a minimum of 13%; in some cases, this variation decreases by 53%, illustrating the $ETR\ (R)$'s predictive reliability and efficacy. For instance, for the $RMSE$ index, $ETR\ (R)$ achieved values of 0.0053 and 0.01 during the training and testing phases, which are about 28% and 14% lower than the corresponding values of $ETR\ (E)$ at 0.0068 and 0.0114, correspondingly.

An uncertainty interval, also known as a confidence interval, is a range of numbers that expresses predicting uncertainty. It signifies the dependability of the estimate. Confidence intervals typically denote 95% or 99% confidence levels. It assesses projected dependability. Numerous confidence intervals are linked to 95% or 99% certainty. This research used a 95% confidence interval (lower numbers imply more reliability). The $U_{95\%}$ index values for the evaluation and learning phases were 0.0147 and 0.0275, respectively, based on the $ETR\ (R)$. The corresponding $U_{95\%}$ values for the $ETR\ (E)$ were 0.0187 and 0.0316. The specs stayed consistent during the project. After evaluating evaluation factors, logical inference, and rating levels, it has been concluded that all models are deemed credible and trustworthy. The $ETR\ (R)$ model is somewhat superior to the alternative model regarding its purpose.

The residual values of the V_e denotes the discrepancy between the model's anticipated value and the actual value derived from experiments. The residual is essential for evaluating the precision of the forecasting model, as it signifies the deviation between the expected and actual volume expansion of cement paste. A positive residual signifies that the model has underestimated the volume expansion of cement paste, whereas a negative residual implies an overestimation. Assessing these residual values enhances model accuracy, augments material evaluation, and guarantees that the volume expansion of cement paste adheres to requisite building criteria. Fig. 4(b) indicates that the mean values of $ETR\ (E)$ are 0.002 in the process of learning and 0.001 in the assessment stage. The $ETR\ (R)$ values are 0.002 in the learning phase and 0.001 in the assessment stage. The residual amount clearly demonstrates that the $ETR\ (R)$ surpasses the $ETR\ (E)$ in both the assessment and procurement phases.

Tab. 4 - The coupled and tunned $ETRs$' results

Trees	Workability indicators								
	PI	R^2	$RMSE$	$SMAPE$	$MASE$	U	WI	$U95\%$	SI
	"Training stage"								
ETR(E)	0.0672	0.9787	0.0068	23.607	0.1111	0.0502	0.994	0.0187	0.1337
Grade	B	B	B	B	B	B	B	B	B
ETR(R)	0.0525	0.986	0.0053	18.934	0.0885	0.0393	0.9964	0.0147	0.1046
Grade	A	A	A	A	A	A	A	A	A
Variance %	-28	0.74	-28.30	-24.67	-25.53	-27.73	0.241	-27.21	-27.82
	"Testing stage"								
ETR(E)	0.121	0.9469	0.0114	41.912	0.1209	0.0843	0.9858	0.0316	0.2387
Grade	B	B	B	B	B	B	B	B	B
ETR(R)	0.1062	0.9603	0.01	27.343	0.0833	0.0743	0.9894	0.0275	0.2102
Grade	A	A	A	A	A	A	A	A	A
Variance %	-13.93	1.395	-14	-53.28	-45.13	-13.45	0.364	-14.90	-13.55

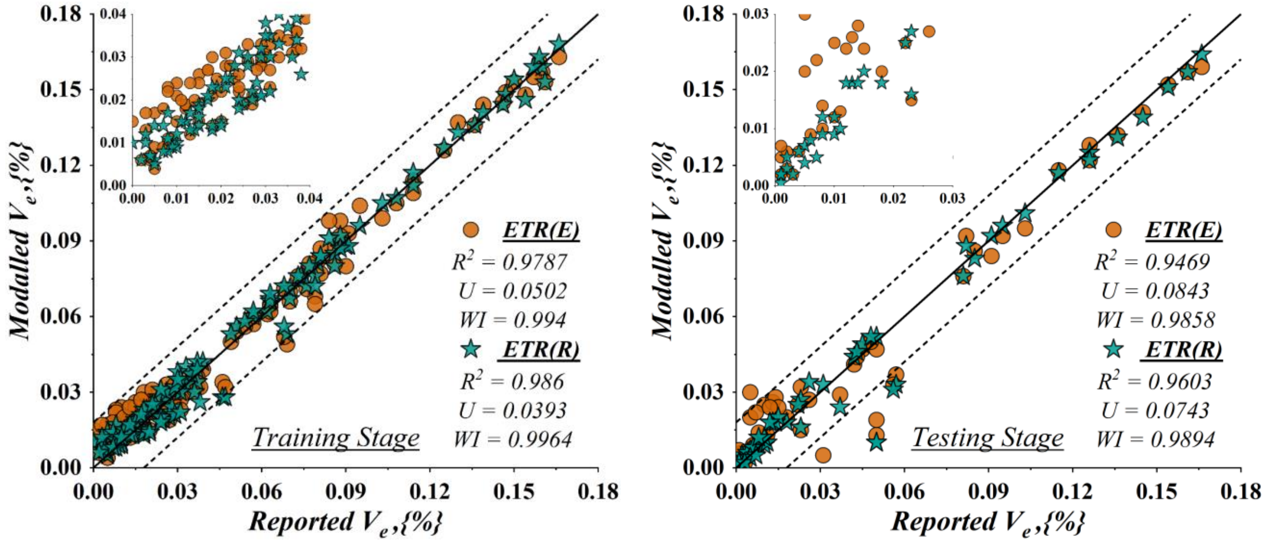

a

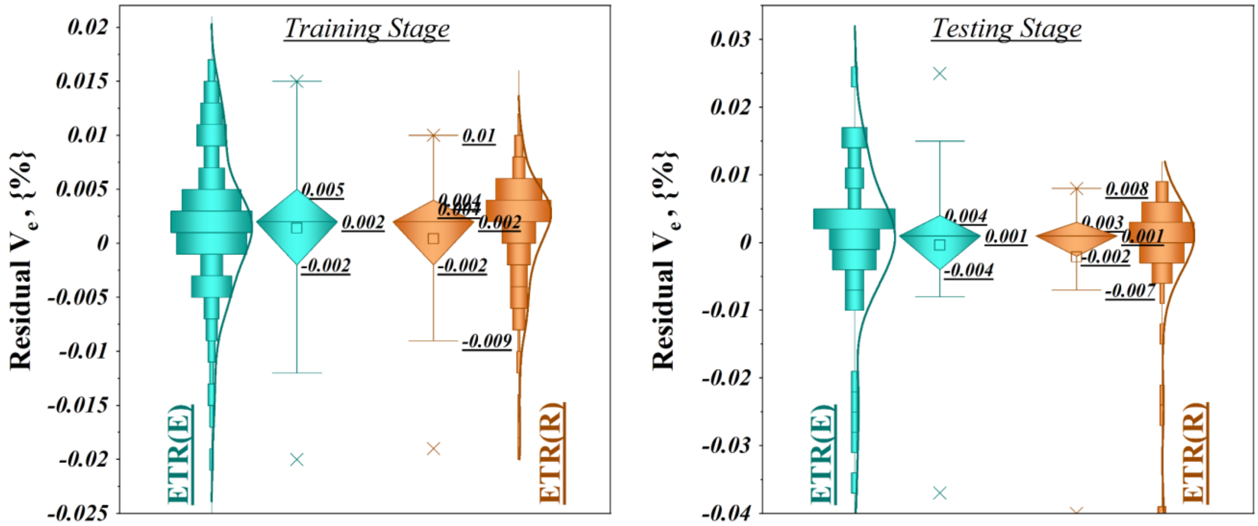

b

Fig. 4 - The coupled and tunned ETRs' results

This has very strong practical implications for construction materials, cement formulation, and quality control. By allowing the model to predict the V_e accurately, in a cement paste with FA and MgO expansive additives, MEA, it helps engineers to optimize material selection by reducing costs and improving structural integrity, as it prevents cracks and deformation. The infrastructure, therefore, lasts longer with minimal maintenance needs. It also currently contributes to quality control, ensuring consistent product performance while contributing to sustainability by efficient use of FA, reducing carbon footprint, and the optimization of MEA applications. Furthermore, it enables customized cement formulation according to project requirements in new construction and rehabilitation of existing ones. This model will improve risk assessments and the follow-through of standards on safety, adding more solidity to the general safety and durability of the project, thus fitting well into current construction practice.

Following suggestions can be considered as recommendations for future works. Exploring combination of the ETR with other algorithms (e.g., stacking or ensemble methods) to enhance prediction accuracy. Including other potentially relevant parameters, such as curing temperature, water content, or admixture type, to improve the model's comprehensiveness. And testing the models against noisy or incomplete data to simulate real-world scenarios and evaluate their resilience.

CONCLUSION

This investigation aimed to develop and evaluate ML techniques for assessing the volume expansion of cement paste (V_e) using FA and magnesium oxide (MgO) expansive additives (MEA). An algorithm known as ETR has been devised to achieve this objective. The present work utilized advanced optimizers, namely the EEFA and the RTHA, for optimization purposes.

The results of the Morris analysis of the data set showed which input parameter would have the greatest impact on the result of the model. For instance, in part c, PC and FA parameters have the highest sensibility values (0.1417), which shows that they have the most influence on the model result. Bar graphs allow a visual comparison of how each parameter contributes to the variability of the outcomes.

The presented correlation matrix shows the Spearman correlation coefficients among the different variables associated with a particular data set. For instance, the correlation coefficient among Age and V_e parameters are significant and are high at 0.69, which indicates a robust positive correlation, as the correlation among MEA variable and V_e has an acceptable correlation with a number of 0.6.

The results indicate that the $ETR\ (E)$ and $ETR\ (R)$ methodologies have significant potential for accurately forecasting the V_e. During the training and assessment, the $ETR\ (R)$ exhibited R^2 of 0.986 and 0.9603, signifying exceptional precision. The findings for $ETR\ (E)$ were notably lower than those for $ETR\ (R)$, with R^2 of 0.9787 and 0.9469. The optimal model was combined with WI, and the results exhibited a performance trend akin to one of the expected measures.

It is essential to recognize that decreased values signify superior performance for workability indicators. The variation percentages of the two models developed for these measures are a minimum of 13%; in some cases, this variation decreases by 53%, illustrating the $ETR\ (R)$'s predictive reliability and efficacy. For instance, for the $RMSE$ index, $ETR\ (R)$ achieved values of 0.0053 and 0.01 during the training and testing phases, which are about 28% and 14% lower than the corresponding values of $ETR\ (E)$ at 0.0068 and 0.0114, correspondingly.

The $U_{95\%}$ values for the evaluation and learning were 0.0147 and 0.0275, based on the $ETR\ (R)$. The corresponding $U_{95\%}$ for the $ETR\ (E)$ were 0.0187 and 0.0316. The specs stayed consistent during the project. After evaluating evaluation factors, logical inference, and rating levels, it has been concluded that all models are deemed credible and trustworthy. The $ETR\ (R)$ model is somewhat superior to the alternative model regarding its purpose.

The impact of this research allows practical applications: cement formulation optimization, structural integrity, and enhanced quality control in the building and construction industry. An example could be an exact prediction of volume expansion V_e by the model, which gives very valuable cost reductions by preventing cracks and material performance consistency in cement paste with FA and MgO additives MEA. In this respect, it also optimizes the use of FA and MEA for sustainability purposes apart from customized cement mixes based on project-specific requirements.

REFERENCES

[1] Bofang Z (2013) Thermal stresses and temperature control of mass concrete. Butterworth-Heinemann

[2] Benemaran RS, Esmaeili-Falak M, Kordlar MS (2024) Improvement of recycled aggregate concrete using glass fiber and silica fume. Multiscale and Multidisciplinary Modeling, Experiments and Design 7:1895–1914. https://doi.org/10.1007/s41939-023-00313-2

[3] Ulm F-J, Coussy O (1995) Modeling of thermochemomechanical couplings of concrete at early ages. J Eng Mech 121:785–794

[4] Esmaeili-Falak M, Sarkhani Benemaran R (2024) Application of optimization-based regression analysis for evaluation of frost durability of recycled aggregate concrete. Structural Concrete 25:716–737. https://doi.org/https://doi.org/10.1002/suco.202300566

[5] Liu X, Zhang C, Chang X, et al (2015) Precise simulation analysis of the thermal field in mass concrete with a pipe water cooling system. Appl Therm Eng 78:449–459

[6] Hassankhani E, Esmaeili-Falak M (2024) Soil–Structure Interaction for Buried Conduits Influenced by the Coupled Effect of the Protective Layer and Trench Installation. J Pipeline Syst Eng Pract 15:. https://doi.org/10.1061/JPSEA2.PSENG-1547

[7] Mo L, Deng M, Wang A (2012) Effects of MgO-based expansive additive on compensating the shrinkage of cement paste under non-wet curing conditions. Cem Concr Compos 34:377–383

[8] Min D, Mingshu T (1994) Formation and expansion of ettringite crystals. Cem Concr Res 24:119–126

[9] Mo L, Deng M, Tang M, Al-Tabbaa A (2014) MgO expansive cement and concrete in China: Past, present and future. Cem Concr Res 57:1–12

[10] Gao P, Xu S, Chen X, et al (2013) Research on autogenous volume deformation of concrete with MgO. Constr Build Mater 40:998–1001

[11] Nobre J, Ahmed H, Bravo M, et al (2020) Magnesia (MgO) production and characterization, and its influence on the performance of cementitious materials: A review. Materials 13:4752

[12] Esmaeili-Falak M, Benemaran RS (2023) Ensemble deep learning-based models to predict the resilient modulus of modified base materials subjected to wet-dry cycles. Geomechanics and Engineering 32:583–600

[13] Liang S, Shen Y, Gao X, et al (2023) Symbolic machine learning improved MCFT model for punching shear resistance of FRP-reinforced concrete slabs. Journal of Building Engineering 69:106257. https://doi.org/https://doi.org/10.1016/j.jobe.2023.106257

[14] Esmaeili-Falak M, Katebi H, Vadiati M, Adamowski J (2019) Predicting triaxial compressive strength and Young's modulus of frozen sand using artificial intelligence methods. Journal of Cold Regions Engineering 33:4019007. https://doi.org/https://doi.org/10.1061/(ASCE)CR.1943-5495.0000188

[15] Esmaeili-Falak M, Benemaran RS (2024) Ensemble Extreme Gradient Boosting based models to predict the bearing capacity of micropile group. Applied Ocean Research 151:104149. https://doi.org/10.1016/j.apor.2024.104149

[16] Zhang K, Zhang Y, Razzaghzadeh B (2024) Application of the optimal fuzzy-based system on bearing capacity of concrete pile. Steel and Composite Structures 51:25

[17] Nobre J, Ahmed H, Bravo M, et al (2020) Magnesia (MgO) production and characterization, and its influence on the performance of cementitious materials: A review. Materials 13:4752

[18] Yang Y, Li C (1999) Study on long term autogenous volume deformation of MgO concrete. J Hydraul Eng 65:54–58

[19] Zhu B (2003) Incremental type of computing model for the volume expansion of concrete with gentle volume expansion. Hydroelec Eng 29:20–23

[20] Zhu B (2002) Computational model and experimental method for bulk expansion of gentle expansive concrete. J Hydraul Eng 33:18–21

[21] Yang G, Yuan M (2004) The hyperbola model for autogenous expansion volume deformation of MgO concrete. J Hydroel Eng 4:38–44

[22] Zhang G, Chen X, Du LH (2005) Analysis of expansion effect of magnesium oxide (MgO) in mass concrete. J Hydraul Eng 2:185–189

[23] Zhang G (2002) MgO micro-expansion thermal integral model considering temperature process effect. Water Power 11:28–32

[24] Feng C, Zhao C, Yu X, et al (2021) A Mathematical Model of the Expansion Evolution of Magnesium Oxide in Mass Concrete Based on Hydration Characteristics. Materials 14:3162

[25] Liu SH, Fang KH (2005) Study on autogenous deformation of concrete incorporating MgO as expansive agent. Key Eng Mater 302:155–161

[26] Xu P, Zhu Y, Ben N (2008) Computing model for autogenous volume deformation of MgO concrete based on degree of hy-dration. Water Resour Hydrop Eng 2:22–25

[27] Zhao W, Wang L, Zhang Z, et al (2024) Electric eel foraging optimization: A new bio-inspired optimizer for engineering applications. Expert Syst Appl 238:122200

[28] Ferahtia S, Houari A, Rezk H, et al (2023) Red-tailed hawk algorithm for numerical optimization and real-world problems. Sci Rep 13:12950. https://doi.org/10.1038/s41598-023-38778-3

[29] Simm J, De Abril IM, Sugiyama M (2014) Tree-based ensemble multi-task learning method for classification and regression. IEICE Trans Inf Syst 97:1677–1681

[30] Zhang J, Lv T, Hou D, Dong B (2023) Synergistic effects of fly ash and MgO expansive additive on cement paste: Microstructure and performance. Constr Build Mater 371:130740

[31] Dawei Y, Bing Z, Bingbing G, et al (2023) Predicting the CPT-based pile set-up parameters using HHO-RF and PSO-RF hybrid models. Structural Engineering and Mechanics 86:673–686

[32] Yaychi BM, Esmaeili-Falak M (2024) Estimating Axial Bearing Capacity of Driven Piles Using Tuned Random Forest Frameworks. Geotechnical and Geological Engineering. https://doi.org/10.1007/s10706-024-02952-9

[33] Li D, Zhang X, Kang Q, Tavakkol E (2023) Estimation of unconfined compressive strength of marine clay modified with recycled tiles using hybridized extreme gradient boosting method. Constr Build Mater 393:131992. https://doi.org/https://doi.org/10.1016/j.conbuildmat.2023.131992

[34] Sun X, Dong X, Teng W, et al (2024) Creation of regression analysis for estimation of carbon fiber reinforced polymer-steel bond strength. Steel and Composite Structures 51:509–527

[35] Akinola OA, Ezugwu AE, Oyelade ON, Agushaka JO (2022) A hybrid binary dwarf mongoose optimization algorithm with simulated annealing for feature selection on high dimensional multi-class datasets. Sci Rep 12:14945. https://doi.org/10.1038/s41598-022-18993-0

[36] Simm J, De Abril IM, Sugiyama M (2014) Tree-based ensemble multi-task learning method for classification and regression. IEICE Trans Inf Syst 97:1677–1681

Article no. 26

THE CIVIL ENGINEERING JOURNAL 3-2025

ANALYSIS OF HISTORIC (80+) CONCRETE STRUCTURE EXPOSED TO WEATHERING

Petr Lukáš[1], David Hes[1], Jiří Pazderka[1], Pavel Reiterman[2], Martin Jiránek[1] and Martina Záleská[3]

1. *Czech Technical University in Prague, Faculty of Civil Engineering, Department of Architectural Engineering, 166 29 Prague, Thákurova 7, Czech Republic; petr.lukas@fsv.cvut.cz, david.hes@fsv.cvut.cz, jiri.pazderka@fsv.cvut.cz, jiranek@fsv.cvut.cz*
2. *Czech Technical University in Prague, Faculty of Civil Engineering, Experimental Centre, 166 29 Prague, Thákurova 7, Czech Republic; pavel.reiterman@fsv.cvut.cz*
3. *Czech Technical University in Prague, Faculty of Civil Engineering, Department of Materials Engineering and Chemistry, 166 29 Prague, Thákurova 7, Czech Republic; martina.zaleska@fsv.cvut.cz*

Received: *08.02.2025*
Received in revised form: *24.07.2025*
Accepted: *30.08.2025*

ABSTRACT

The aim of the study was to analyze historic concrete structures from the 1930s and then to analyze the failures caused by water action on the structures. As part of the study, long-term moisture measurements were taken on a selected structure along with boundary conditions (temperature and relative humidity). By taking measurements at multiple locations on the structure using depth brush probes, it was confirmed that massive historic concrete structures exposed to external boundary conditions contain relatively high amounts of water (typically around 4%). This is mainly due to the large voids and porosity of the old concrete structure. The action of water in historic concrete structures leads to chemical reactions. Their products are chemical leachates which penetrate the surface of the structure. The analysis revealed that calcium is the dominant element, with measured values ranging from 92.42 % to 95.32 %. Although the structure studied is located in an agricultural area subjected to fertilization, the nitrate content was measured at only 0.031 %. Microscopic analysis confirmed potential calcium compounds recrystallization, which could jeopardize the durability of the remediation. This factor should therefore be carefully considered in the remediation design. Samples of historic concrete were produced according to the original 1930s recipe. These samples were subjected to diffusion permeability measurements. The average diffusion coefficient D = $8{,}4.10^{-9}$ (m^2/s) was measured. Such diffusion permeability corresponds to poor quality concrete, even for the newly formed samples. Thus, the structure had these properties at the time of construction 80 years ago and subsequent degradation has had little effect.

KEYWORDS

Historical concrete structures, Structure moisture, Chemical leachates, Remediation of concrete structures

INTRODUCTION

In the 1930s, concrete was considered a relatively new material whose potential had not yet been fully exploited. As World War II approached and progressed, concrete began to be used extensively, including for military purposes [1]. Many buildings have survived that have been exposed to weather conditions for decades without any maintenance [2]. Since then, the properties and behavior of concrete (depending on the concrete mix composition, environment, production technology, processing, protection etc.) have been analyzed worldwide and today it is one of the most used building materials in construction industry [3, 4].

Historical concrete structures are very specific not only in terms of material properties but also in terms of causes of failure [5-9]. Thanks to the preserved structures located in different types of environments around the world, it is now possible to analyze the quality of 85-year-old concrete structures with respect to the different boundary conditions that have significantly changed the original parameters of these structures. Some of the basic boundary conditions affecting the quality of concrete include air temperature, relative humidity, location (which influences airflow velocity and the presence of biological degradation factors) and, of course, the maintenance of the structure [10-12].

The requirement for these concrete structures was to achieve a high durability, ensured by their dimensions, the strength of the concrete and the appropriate design of the steel reinforcement. Although production process was simpler compared to today's, the compressive strength of concrete reached least 450 kg/cm^2 (approximately 44,1 MPa). The original recipe was progressively developed and finally was composed of the following components:

- Aggregate – different types and quantities, depending on the location
- Cement – Portland cement with a higher content of gypsum (up to 4%) and silicon dioxide
- Water – with a very low water-cement (w/c) ratio

Concrete compositions based on the type of aggregate are shown in Table 1 [13].

Tab. 1 - Concrete recipe from 1930s depending on the type of aggregate

Composition	River aggregate	River and crushed aggregate
Sand 0-10	390 l	440 l
River gravel 20-40	300 l	300 l
River gravel 40-60	300 l	300 l
Cement (type A)	400 kg	400 kg
Water	100 l	100 l

Typical types of structures that have been exposed to weathering for long periods without any maintenance are reinforced concrete fortresses built in the 1930s across Europe (France, Germany, Czechoslovakia, Italy, UK, Switzerland, Yugoslavia, Belgium, Poland and other countries). In this study, objects of light fortifications Model 37, built between 1937 and 1938, were used to analyze the properties and behavior of historic concrete. One of these objects can be seen in Figure 1. Although these are fortification objects located in the territory of former Czechoslovakia, the research results can serve as a solid basis for further studies and remediations in other locations.

The long-term degradation processes to which concrete structures have been subjected must be considered in any remediation. The aim of this study is to assess the current state of 85-year-old structures in terms of possible sustainable remediation [14-18].

The most common failures of historic concrete structures are:

- Excessive moisture in the structure followed by the degradation of the cement paste (freezing, biodegradation, etc.)
- Effects of water flow within the structure, resulting in chemical degradation (leaching of chemicals, etc.)
- Loss of adhesion of the covering layer
- Insufficient surface integrity – cracks, etc.

– Partial mechanical destruction of the structure

Fig. 1 – Object of light fortifications Model 37 in Czechia

Today, the remediation of historic concrete structures dating back to the 1930s is a significant topic for professionals and the public. Experts are trying to develop a functional and sustainable remediation system that is universal for all types of historic concrete structures (with possible modifications based on the boundary conditions of the environment where the structure is located). It is believed that a functional remediation system for these structures can be achieved using new technologies and materials [19-23]. In the process of development, most emphasis is placed on research into the effect of crystallization mixtures applied to remediated structures [24-28].

METHODS

For this study, the object of light fortification Model 37 (built in 1937) near the village of Mradice in the Czechia was selected (see Figure 2). This object was intentionally chosen because the structures have not been maintained since 1938 (Munich Agreement). In addition, these objects were not seriously damaged (e.g. a broken machine-gun column, a missing part of the covering ear, etc.), thus the object has been preserved in its original state.

DOI 10.14311/CEJ.2025.03.0026

CIVIL ENGINEERING JOURNAL

Article no. 26

THE CIVIL ENGINEERING JOURNAL 3-2025

Fig. 2 – Overview map of the location of the object (Source: www.mapy.cz)

Research layout

As part of the analysis, the measurement of moisture in concrete structures was conducted using a resistance moisture meter to observe the behavior of structures based on the environmental boundary conditions.

Additionally, lime leachate samples were extracted from the structure and subjected to laboratory tests. The tests performed included the following:

- Chemical analysis of lime leachates using calorimetry
- ED-XDR spectroscopy
- Microscopic analysis

Moisture measurements of the structure

The aim of the in-situ measurements was, on the one hand, to determine the environmental boundary conditions in which the concrete structures are located in the long term and, on the other hand, to determine the behavior of moisture in relation to these conditions or to identify the main source of moisture.

For the resistance moisture meter measurements, it was first necessary to drill holes in the interior of the structure into which brush probes were inserted. Figure 3 shows the location of four points in the building plan that were selected for these holes. At these points, holes were drilled at three height levels (0.1 m, 0.7 m and 1.3 m above the floor) to obtain the moisture profile of the structure at the measured point. Given the technological procedure, pairs of holes were drilled, each with a diameter of 8 mm, approximately 300 mm long and spaced 80-100 mm apart depending on the location of the reinforcement.

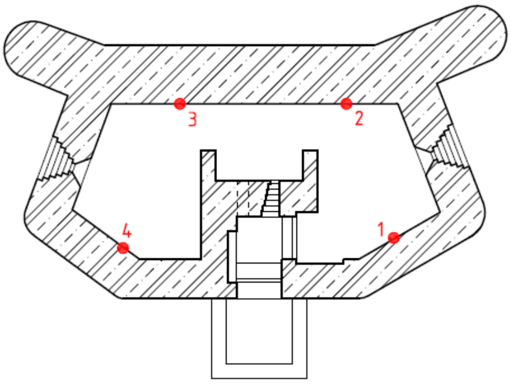

Fig. 3 – Diagram of moisture profile locations measured with resistance moisture meter

From October 25, 2019, to June 3, 2021, resistance moisture measurements in the structures were conducted at approximately weekly intervals to monitor the moisture behavior of the vertical structures over time (see Figure 4).

Fig. 4 – In-situ moisture measurement using electrical resistive hygrometer

To obtain accurate results, due to the imperfections of the analyzed structure, calibration was performed by gravimetric laboratory examination of the collected damaged samples. Based on the values from in-situ moisture measurements and gravimetric laboratory examination, the calibration coefficient K [-] was determined, which in this case has a value of 1.557. Moisture damage, as well as visible cavities and reinforcement corrosion in the concrete structure, can be seen in Figure 5 and Figure 6.

Fig. 5 – Moisture damage and visible cavities in the concrete structure

Fig. 6 – Visible cavities and reinforcement corrosion in the concrete structure

Analysis of chemical efflorescence

A laboratory measurement of the chemical content of the lime leachate sample (salinity measurement) was carried out. For salinity testing, the sample marked in Figure 7 was taken from fortification Model 37 (from 1937) number C-27/52a/A-140Z, located near the village of Mradice.

During the laboratory testing, the pH value of the sample (acidity/alkalinity) was examined and the presence of the following chemicals in addition to calcium was detected:

- Chlorides
- Nitrates
- Sulphates
- Ammonia

The tested sample was crushed to a finer fraction and 2 g of the sample was measured out for further testing. The sample was then placed in an Erlenmeyer flask and 100 ml of water was added. This flask containing the sample was then sealed and subjected to ultrasound to ensure thorough mixing and dissolution of chemicals in the water. After ten minutes, the flask was removed from ultrasound and heated to a temperature of 100 °C. Once the boiling point was reached, the flask was removed and left to allow the sample to settle until the following day. The next day, the prepared solution, free of solid particles, was decanted using a pipette into a clean bottle. Approximately 30 ml of the solution was collected. This purified solution was then used to measure the pH and to test the content of water-soluble chemicals. Testing of the samples was first carried out by qualitative analysis and later by quantitative analysis (see below).

Fig. 7 – Location of leachate sample taken away from the object C27/56a/A-140Z near to Mradice

Qualitative (calorimetric) analysis

Qualitative analysis was used to preliminarily determine both the presence and approximate concentration of specific chemicals in the sample (mg/l). During the analysis, the test strips were immersed in the prepared solution, resulting in a change of their color (see Figure 8). These colors were compared with a calorimetric scale, which indicates the approximate concentration of salt in the sample. Using qualitative analysis, the solution was tested for the presence of nitrates. There was no color change after immersing the test strip in the solution. This indicates that there are no nitrates in the sample. This finding was later confirmed by quantitative analysis.

DOI 10.14311/CEJ.2025.03.0026

Fig. 8 – Calorimetric measurement of pH

Quantitative (photometric) analysis

For quantitative analysis, a Spectroquant® Pharo300 UV-VIS photometric device was used. The device measures the absorption of light rays passing through the modified solution (sample). It is necessary to modify the solution by adding chemical substances that cause a color change. The choice of these substances depends on the type of chemical being analyzed, and the absorption depends on the concentration of the solution. If a high concentration is found or if the photometer is unable to determine the exact chemical content, the sample must be diluted with distilled water in a ratio of 1:10 or 1:100. A cuvette containing the mixed solution is then inserted into the apparatus. Immediately thereafter, the instrument begins to emit light beams of different wavelengths in the visible light spectrum. It is therefore important to close the device quickly to prevent the entry of external light which could affect the measured values. Part of the spectrum passes through the sample while another part is absorbed. The device measures the absorption and then calculates the concentration of the substance in the sample.

The output of the spectrometer measurement is the concentration of the measured substance in the sample (mg/l). For salinity classification in Table 2, it is necessary to recalculate the concentration to mg/g using the sample density.

Tab. 2 - Classification of masonry salinity due to ČSN P 73 0610

The degree of salinity of the masonry	Salt amount (mg/g) of a sample as a percentage of weight					
	Chlorides		Nitrates		Sulphates	
	mg/g	% weight	mg/g	% weight	mg/g	% weight
Low	< 0,75	< 0,075	< 1,0	< 0,1	< 5,0	< 0,5
Increased	0,75 - 2,0	0,075 - 0,20	1,0 - 2,5	0,1 - 0,25	5,0 – 20	0,5 - 2,0
High	2,0 - 5,0	0,20 - 0,50	2,5 - 5,0	0,25 - 0,50	20 – 50	2,0 - 5,0
Very high	> 5,0	> 0,50	> 5,0	> 0,50	> 50	> 5,0

ED-XRF Spectroscopy

ED-XRF spectroscopy is a suitable and reliable method to determine the chemical composition of lime leachate samples. This method performs a rapid, non-destructive, multi-element analysis of the sample. The analysis can measure substances ranging from fluoride (F) to uranium (U) across a wide range of concentrations, from tenths of ppm to one hundred percent. Using ED-XRF, it is possible to analyze homogeneous low-viscosity materials, solid samples, slags, powders, plastics, and thin layers. For this measurement, the original leachate sample from the object in Mradice was used (S1).

Microscopic analysis

A sample of crushed lime efflorescence, taken from the solution prepared for the quantitative analysis of sample S1, was used to examine the microscopic structure of the efflorescence.

The sample collected was applied to a microscope slide, which was then labelled according to the corresponding sample. The slide with the prepared sample was then placed under a microscope. Figure 9 shows its structure before crystallization was examined. In the next step, the sample was exposed to a constant temperature of 60 °C for 14 days, during which the sample crystallized due to water evaporation, as shown in Figure 10. From the figures, it is clear that the solution contained a significant amount of dissolved substances. These substances crystallized after the evaporation of the solution.

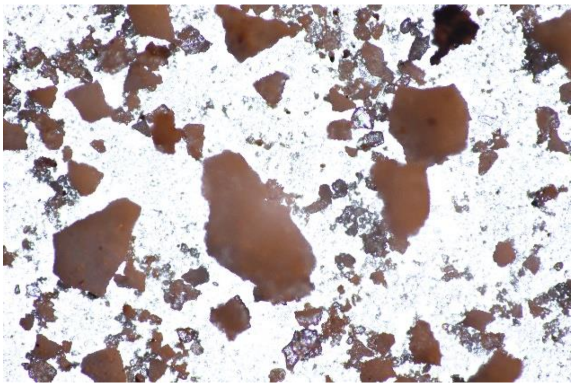

Fig. 9 – The lime efflorescence sample S1 (before crystallization)

Fig. 10 – The lime efflorescence sample S1 (after crystallization)

Diffusion permeability

As part of the analysis, the diffusion permeability of high strength concrete used for development of fortifications in the 1937 – 1938 was determined.

Three test specimens were prepared based on extant concrete recipes from the 1930s. The production of the specimens aimed to replicate the properties of the original concrete as closely as possible. Due to the nature of the test and the size of the samples, it was necessary to adjust the gravel fraction used. Subsequently, measurements of all three samples were performed, and the results were recorded.

For laboratory purposes, three specimens were prepared (see Figure 11), with dimensions ranging from 37.0 mm to 39.3 mm. The effective area (the area through which radon diffuses into the accumulation chamber) of all specimens was 140.10^{-4} m^2 (140 cm^2). A gravel fraction of 4/16 mm was used as aggregate.

Fig. 11 – Preparation of the samples for measurement

DOI 10.14311/CEJ.2025.03.0026

CIVIL ENGINEERING JOURNAL

According to the test methodology A specified in ISO/TS 11665-13, samples of the tested material were placed between the source chamber and three accumulation chambers, as can be seen in Figure 12. Radon diffuses through the tested samples from the source chamber, which is connected to the RF 100 radon source, into the accumulation chambers. Radon concentrations on both sides of the samples are continuously measured by TSR-4 TERA detectors (in the accumulation chambers) and continuous ionization chambers (in the source chamber). The radon diffusion coefficient is determined from the time-dependent radon concentrations in the chambers, as shown in Figure 13. The calculation is based on an iterative numerical solution of the one-dimensional time-dependent radon diffusion equation. The final value of the radon diffusion coefficient is obtained when the solution has a minimal deviation from the measured radon concentration in the accumulation chamber [29, 30].

Fig. 12 – The samples ready for measurement

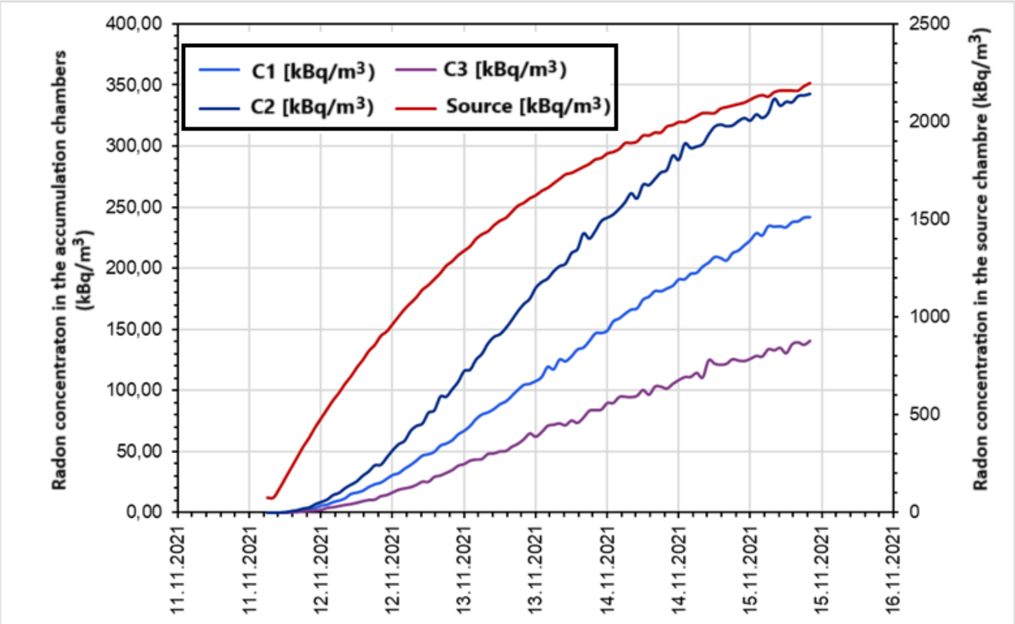

Fig. 13 – The time course of radon concentration in the accumulation chambers and in the source chamber (output of the measuring system of radon concentration RM-2)

RESULTS

Structure moisture measurement

The long-term analysis was used to determine the moisture behavior of the concrete structure during the model year. The moisture measured from September 2, 2019 to July 23, 2021 depends on the position of the structure (whether it was exposed or covered by an earth mound) and the boundary conditions (weathering). Moisture ranged from 3.5% to 4.6% at Point 1, 1.7% to 3.0% at Point 2, 3.0% to 4.5% at Point 3, and 3.5% to 5.0% at Point 4. Values with an extreme deviation indicate the effect of boundary conditions. The lowest humidity values were measured in winter, indicating water freezing in the structure and drier air. Extremely high moisture values were measured during autumn when the structures were exposed to heavy rainfall and during winter due to snow melt. Higher moisture on the exposed side of the structure is likely due to the retention effect of the earth embankment, which was constructed using stone fill.

The analysis further revealed that moisture levels within the height profile of the structure vary significantly. This suggests that the dominant source of water in the structure is not rising groundwater, but weathering water. Another cause of variability in the measured values is the porous and voided structure of the concrete structures caused by manual compaction during construction.

Analysis of chemical leachates

A sample of lime leachate, taken from the fortification near Mradice, was subjected to chemical analysis using both qualitative and quantitative analysis. The analysis determined that the chemical content in the lime leachate was low. The sample was found to contain 0.0124 % chloride, 0.031 % nitrate and 0.209 % sulphate. No ammonia was detected in the sample, as shown in Figure 14.

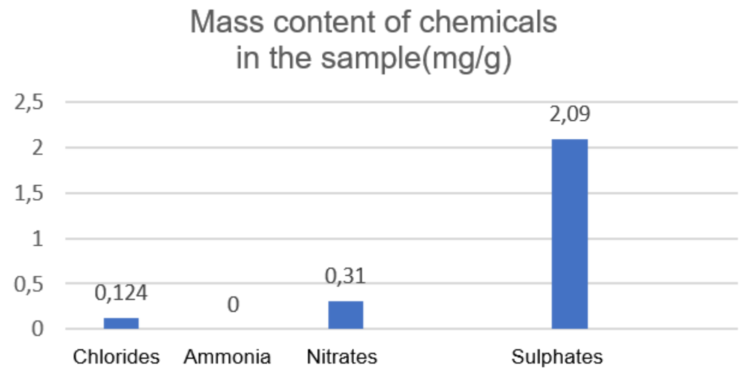

Fig. 14 – Photometric result of lime leachate of sample S1

Although the structure is situated in the middle of the field, the salinity classification of the measurements determined that the sample contained trace amounts of sulfate, nitrate, and chloride.

As a result of this finding, it is not necessary to include any chemical protection measures in the remediation. This conclusion applies only to the analyzed structure and cannot be generalized to all structures. In such cases, a new analysis should be carried out.

ED-XRF Spectroscopy

As part of the ED-XRF Spectroscopy analysis, the composition of the sample extract taken from the structure was analyzed. According to the measured results, presented in Table 2, ED-XRF Spectroscopy revealed that the calcium component accounted for 92.42% and 95.32% of the total composition of the samples. Other elements detected in the sample were aluminum, silicon, strontium, magnesium, barium, and iron; however, all were present only in trace amounts, confirming the results of the analysis in previous chapter. Additionally, a very low presence of titanium, potassium, zinc, and manganese were detected in the composition.

The results obtained from the ED-XRF analysis, together with the long-term study of these structures, indicate that the efflorescence is the result of the carbonation of Portlandite ($Ca(OH)_2$) caused by its exposure to the air near structural cracks. The potential presence of chloride salts, such as calcium chloride, was considered but excluded due to the absence of plausible source. The other elements, particularly those present in trace amounts, depend mainly on the type of aggregate used in the concrete.

Tab. 3 - Composition of the sample according to the ED-XRF spectroscopy method

Sample	Locality	Composition	Chemical symbol	Content (%)
S1	Mradice	Calcium	Ca	92,42
		Aluminium	Al	2,45
		Silicon	Si	1,38
		Strontium	Sr	1,15
		Barium	Ba	0,982
		Iron	Fe	0,665
		Magnesium	Mg	0,606
		Titanium	Ti	0,149
		Potassium	K	0,097
		Zinc	Zn	0,0856
		Manganese	Mn	0,0062

Microscopic analysis

Microscopic analysis was performed on the samples intended for quantitative analysis. From the aforementioned procedure and figures, it is clear that the lime leachates can recrystallise, which has a significant impact on the remediation design, as lime leachates cannot be removed by dissolution. A suitable solution to eliminate the formation of lime leachate is likely to be the application of a crystalline waterproofing, which will create an impermeable zone in the structure at a depth of approximately 50 mm and prevent further spread of the calcite solution through the porous structure. Due to the structure of historical concrete structures, it is probably not possible to completely eliminate the formation of leachates throughout the structure, but it is possible to eliminate their presence on the surface. However, the question remains as to the effect of the leachates within the structure on the structure itself in terms of the pressures generated. This should be the subject of further study.

Permeability

As part of the analysis, the diffusion permeability of the concrete was measured on three specimens. The following parameters were determined: average diffusion coefficient D = $8{,}4.10^{-9}$ (m^2/s), diffusion length l = $63{,}2.10^{-3}$ m and average radon resistance R_{Rn} = 5.1 (Ms/m) with the mentioned tolerances in Table 3.

Since the diffusion coefficient D and the diffusion length l are material constants, the radon resistance depends on the thickness. Thus, for concrete 0,5 m thick, the radon resistance is approximately 10 212 Ms/m. This is of course only valid if there are no cracks in the concrete structure.

The measured values correspond to concrete of lower quality. This is probably due to the aggregate fraction used in the samples. In the case of a real structure from the 1930s, the measured results would likely be even worse due to large voids (imperfect compaction in 1938) and large aggregate fraction.

Tab. 3 - Average measured diffusion parameters of the samples

Material		Concrete
Diffusion coefficient *D* (m^2/s)	Average	$8{,}4.10^{-9}$
	±U	$\pm 1{,}0.10^{-9}$
Diffusion length *l* (m)	Average	$63{,}2.10^{-3}$
	±U	$\pm 7{,}5.10^{-3}$
Radon resistance R_{Rn} (Ms/m)	Average	5,1
	±U	± 0,6

RESULTING OPTIONS FOR REMEDIATION OF HISTORIC CONCRETE STRUCTURES

The study determined that the concrete structures from the 1930s have been exposed to long-term degradation due to high moisture within the structure. A dominant result of this moisture is the frequent and repeated formation of efflorescence on the surface of the structure, which is visually very noticeable.

For the design of durable and functional remediation measures, the formation of lime leachates is a major factor that must be systematically addressed to make the remediation as efficient as possible. It is also necessary to ensure that the surface layer has the same or similar thermal expansion as the concrete structure to prevent cracking and subsequent loss of adhesion.

The conclusions of the study confirmed the need for a complex approach to the remediation of the surface layers of historic concrete buildings. To eliminate all the negative effects analysed above, it is clearly necessary to design a multi-layered remediation system, the basis of which must be measures to prevent the penetration of calcite water on the surface and to ensure the durability of the surface layer, especially in terms of thermal expansion and cohesion with the original surface of the structure. Based on these findings, the authors of the paper have started the development of a 4-layer remediation system designed for the reconstruction of 80+ old concrete structures. The remediation system is based on a combination of the use of a crystallization coating with a crystallization mortar, using a reinforcement layer and a special final remediation plaster. This complex remediation system will be presented in the next publication.

CONCLUSION

The analyses carried out confirmed that one of the biggest problems in terms of damage to the surfaces of historical concrete structures is lime leaching, which is closely related to the mechanism of water transport in concrete. Although the concrete structure in this study is located in the field where fertilizers are commonly used, the analysis of lime leachate revealed that other chemicals (chlorides, nitrates, sulphates and ammonia) were present in the sample only in trace amounts. ED-XRF spectrometry performed on the lime leachate samples showed that the dominant element in the leachate was calcium as expected and the minor elements that were only present in trace amounts in the sample were aluminium, silicon, strontium, magnesium, barium and iron. Examination of the microscopic structure of both samples confirmed the ability of calcium compounds to recrystallize, which is quite important in the formation of leachates by flow through the pore system of the structures. To design a durable and functional remediation measure, it is essential to prevent the flow of calcium-rich water and the recrystallization of calcium compounds within the pore system and on the structure's surface. This can be effectively avoided by the surface application of crystallisation coatings, which will prevent the penetration of liquid water into the structure, but at the same time keep the structure diffusely open.

In particular, the aim of the study was to obtain important data for the subsequent development of a special comprehensive remediation measure for 80+ year old concrete structures. This comprehensive remediation system will be presented in a future.

ACKNOWLEDGEMENTS

This work was supported by the project SGS22/138/OHK1/3T/11.

REFERENCES

[1] Sutherland R.J.M., 1996. Understanding historical concrete. ICE Proceedings Structures and Buildings, vol. 116(3), p. 255-263. ISSN 0965-0911, https://doi.org/10.1680/istbu.1996.28741

[2] Holcapek O., Reiterman P., Pazderka J., 2020. Properties of Czech WW2 Concrete Fortifications after 80 Years. In: XV International Conference on Durability of Building Materials and Components, edited by Serrat C., Casas J.R, Gibert V, https://doi.org/10.23967/dbmc.2020.115

[3] Trtík T., Chylik R., Fládr J., Vašková J., 2022. Analysis of the Migration Process of Concrete Layers during Compaction. Solid State Phenomena, vol. 336, p. 159-163, https://doi.org/10.4028/p-79aoi5

[4] Pan X., Shi Z., Shi C., Ling T.C., Li, N., 2017. A Review on Surface Treatment for Concrete – Part 2: Performance. Construction and Building Materials, vol. 133, p. 81–90, ISSN 0950-0618, https://doi.org/10.1016/j.conbuildmat.2016.11.128

[5] Lukáš P., Pazderka J., 2021. Analysis of moisture level in concrete structures of WW2 bunker no. 37 in Czechia. In: AIP Conference Proceedings 2322, 020039 (2021), https://doi.org/10.1063/5.0042718

[6] Jedidi M., Benjeddou O., 2018. Chemical causes of concrete degradation. MOJ Civil Engineerig, vol. 4(1), p. 40-46.

[7] Nývlt M., Pazderka J., 2019. ANALYSIS OF CORROSION PRODUCTS FROM WW2 CONCRETE BUNKERS IN CZECHIA. Acta Polytechnica CTU Proceedings, vol. 22, p. 77-82, ISSN 2336-5382, https://doi.org/10.14311/APP.2019.22.0077

[8] Pazderka J.; Reiterman P., 2019. CZECH WW2 CONCRETE FORTIFICATIONS: CORROSION PROCESSES AND REMEDIATION METHOD BASED ON CRYSTALLIZING COATING, Acta Polytechnica, vol. 59(4), p. 359-371, ISSN 1210-2709, https://doi.org/10.14311/AP.2019.59.0359

[9] Pazderka J., Purkrtová M., Reiterman P., 2016. Moisture-Related Problems of Historic Concrete Structure. Materials Science Forum , vol. 865, p. 219-223, https://doi.org/10.4028/www.scientific.net/MSF.865.219

[10] Zatloukalová J., Pazderka J., Lukáš P., Reiterman P., 2021. Study on Permeability of Concrete Fortifications from WW2 Based on Mercury Intrusion Porosimetry. Solid State Phenomena, vol. 325, p. 162-167, https://doi.org/10.4028/www.scientific.net/SSP.325.162

[11] Liang M.-T., Lin S.-M., 2003. Modeling the transport of multiple corrosive chemicals in concrete structures: Synergetic effect study. Cement and Concrete Research, vol. 33(12), p. 1917-1924, https://doi.org/10.1016/S0008-8846(03)00081-4

[12] Bochen J., 2015. Weathering effects on physical–chemical properties of external plaster mortars exposed to different environments. Construction and Building Materials, vol. 79, p. 192–206, https://doi.org/10.1016/j.conbuildmat.2014.12.079

[13] Pazderka J., Reiterman P., Ženíšek M. et al., 2022. Stavebně technické průzkumy pevností z 30. let 20. století a technická řešení jejich obnovy. Praha: CTU. Faculty of Civil Engineering, p. 9-12, ISBN 978-80-01-07070-3

[14] Kim J., Kitagaki R., 2020. Chemical properties and mass transfer resistance of mortar surface modified with silicate-based surface impregnant. Construction and Building Materials, vol. 262, 120806, https://doi.org/10.1016/j.conbuildmat.2020.120806

[15] Pavlů T., Fořtová K., Mariaková D., Řepka, J., Pazderka J., 2020. Improvement of the Durability of Recycled Masonry Aggregate Concrete. Materials, vol. 13(23), 5486, https://doi.org/10.3390/ma13235486

[16] Nývlt M., Pazderka J., Reiterman P., 2021. Comparative Study of Different Types of Waterproofing Screeds with a Focus on Cohesion with Selected Building Materials after the Freeze-Thaw Exposure. Applied Sciences, vol. 11(23), 11256. https://doi.org/10.3390/app112311256

[17] Pavlů T., Pazderka J., Fořtová K., Řepka J., Mariaková D., Vlach T., 2022. The Structural Use of Recycled Aggregate Concrete for Renovation of Massive External Walls of Czech Fortification. Buildings, 12(5), 671, https://doi.org/10.3390/buildings12050671

[18] Chew M.Y.L., De Silva, N., 2003. Benchmarks to Minimize Water Leakages in Basements. Structural Survey, vol. 21(4), p. 131-145, https://doi.org/10.1108/02630800310507140

[19] Song Z., Xue X., Li Y., Yang J., He Z. et al., 2016. Experimental exploration of the waterproofing mechanism of inorganic sodium silicate-based concrete sealers. Construction and Building Materials, vol. 104, p. 276-283, https://doi.org/10.1016/j.conbuildmat.2015.12.069

[20] Bader T., Waldner B.J., Unterberger S.H., Lackner R., 2019. On the Performance of Film Formers Versus Penetrants as Water-repellent Treatment of High-performance Concrete (HPC) Surfaces. Construction and Building Materials, vol. 203, 481-490, https://doi.org/10.1016/j.conbuildmat.2019.01.089

[21] Chang J., Li W.Z., Wang D., Zhang Y.Y., 2020. Effect of silicate modulus on tensile properties and microstructure of waterproof coating based on polymer and sodium silicate-activated GGBS. Construction and Building Materials, vol. 252, 119056, https://doi.org/10.1016/j.conbuildmat.2020.119056

[22] Almusallam A., Khan F., Dulaijan S., Al-Amoudi O., 2003. Effectiveness of surface coatings in improving concrete durability. Cement and Concrete Composites, vol. 25(4-5), 473–481, https://doi.org/10.1016/S0958-9465(02)00087-2

[23] Chang S.H., Kang T.H., Choi S.W., Lee C., Hwang G.S., Choi M.S.,2016. An Experimental Study on Fundamental Properties of A Sprayable Waterproofing Membrane. Tunnel and Underground Space, 26(3), https://doi.org/10.7474/TUS.2016.26.3.220

[24] Žáková H., Pazderka J., Reiterman P., 2020. Textile Reinforced Concrete in Combination with Improved Self-Healing Ability Caused by Crystalline Admixture. Materials, vol. 13(24), 5787, https://doi.org/10.3390/ma13245787

[25] Lim S., Kawashima S., 2019. Mechanisms Underlying Crystalline Waterproofing Through Microstructural and Phase Characterization. Journal of Materials in Civil Engineering, 31(9), https://doi.org/10.1061/(ASCE)MT.1943-5533.000275

[26] Rahman M., Chamberlain D., 2017. Performance of Crystalline Hydrophobic in Wet Concrete Protection. Journal of Materials in Civil Engineering, 29(6), https://doi.org/10.1061/(ASCE)MT.1943-5533.000177

[27] Scancella R.J., 1996. Use of Xypex Admixture to Concrete as an Inhibitor to Reinforcement Steel Corrosion. Materials for the New Millennium, p. 1276–1280, ISBN: 0-7844-0210-8

[28] Reiterman P., Davidová V., Pazderka J., Kubissa W., 2020. Reduction of Concrete Surface Permeability by Using Crystalline Treatment. Romanian Journal of Materials, vol. 50(1), p. 69-74

[29] Jiránek M., Kačmaříková V., 2019. Radon diffusion coefficients and radon resistances of waterproofing materials available on the building market. Journal of Environmental Radioactivity, vol. 208-209, 106019, https://doi.org/10.1016/j.jenvrad.2019.106019

[30] Rogers V.C., Nielson K.K., Holt R.B., Snoddy R., 1994. Radon Diffusion Coefficients for Residential Concretes. Health Physics, vol. 67(3), p. 261-265, https://doi.org/10.1097/00004032-199409000-00006

CIVIL ENGINEERING JOURNAL

Article no. 27

THE CIVIL ENGINEERING JOURNAL 3-2025

STATIC PERFORMANCE ANALYSIS OF CABLE-STAYED BRIDGE WITH CABLE DAMAGE CAUSED BY FIRE

Hudandan[1], Baozhen Yan [2], Yiqi Wang[3]

1. *School of Civil and Architectural Engineering, Harbin University, No.109 Zhongxing Road, Harbin, Heilongjiang Province, China; Hardandan@163.com*
2. *Heilongjiang Province Highway Bridge Survey Design Co. Ltd., No. 90 Qingbin Road, Harbin 150040, China*
3. *College of Civil and architectural engineering, Heilongjiang Institute of Technology, No.999 Hongqi Street, Harbin, Heilongjiang Province, China*

Received: 08.02.2025
Received in revised form: 27.07.2025
Accepted: 30.08.2025

ABSTRACT

The stay cable is usually close to the carriageway. Once the fire occurs, it will inevitably cause different degrees of damage to the cable of the bridge. Rapid and accurate mechanical analysis and evaluation of fire-damaged cable-stayed bridges is very important to provide accurate basis for decision makers. Taking fire accident as the engineering background, this paper uses damage theory and finite element theory to simulate the fire damage of different cable-stayed cables and different fire damage degrees of the same cable, and analyzes the change characteristics of the static parameters of the main beam and cable force caused by fire damage of the cable-stayed bridge. The results show that the fire damage of back cable and mid-span cable has a global effect on the alignment and cable force of the whole bridge. Under the melting condition of the outermost two pairs of back cables S13+N13 on the main span, the mid span deflection is 362 mm, an increase of 28.53%. Under the melting condition of two pairs of medium length cables SC7+NC7 on the main span, the increase in mid span deflection is 5 mm, and the percentage change in mid span deflection is 3%. The fire induced fusing damage occurred on the outermost back cable, which caused the cable force of the nearby cable not to reach the warning value, but the surplus was very small. The results of the study can provide implications for similar projects.

KEYWORDS

Cable-stayed bridge, Stay cable, Fire, Static property

INTRODUCTION

Since the dawn of the 21st century, the rapid economic development has led to significant advancements in bridge construction globally [1,2]. Consequently, there has been a gradual increase in the number of vehicles transporting flammable and explosive materials. In the event of a fire, these vehicles pose a significant threat to the bridges they traverse, potentially resulting in substantial loss of life and property, as well as causing traffic paralysis. Notably, large cable-stayed bridges, which serve as vital transportation hubs, would face even greater losses in the occurrence of a fire accident [3-6].

According to incomplete statistics, 11 domestic bridge fire accidents have occurred in the United States in the past 10 years, and the annual loss caused by bridge fire in the United States is 139 million US dollars [7]. In April 2007, a tanker truck explosion occurred at the MacArthur Maze overpass on the highway connecting the two major cities of San Francisco and Oakland in the United States. The raging fire caused the collapse of an approach bridge leading to the cross-sea bridge, which could have had a serious impact on traffic between San Francisco and Oakland [8].

In recent years, bridge fire accidents have frequently occurred in China. Due to the increasing traffic volume, the probability of vehicle traffic accidents on Bridges has greatly increased, which is the main cause of bridge fire [9-11]. In some cities, the clearance under Bridges is limited, and flammable materials such as garbage and firewood are piled up at the bottom of Bridges, resulting in more and more bridge fire accidents [12-15]. According to incomplete statistics, there have been 31 bridge fire accidents in China in the past 10 years, of which 19 were bridge floor fire accidents, 12 were caused by rear-end collision, explosion, rollover and spontaneous combustion of fuel and chemical transport vehicles, 14 were fire accidents under the bridge, and 3 were caused by traffic accidents caused by fuel and chemical transport vehicles under the bridge. 9 cases of fire caused by spontaneous combustion of flammable materials such as firewood and garbage piled up under Bridges and negligence of residents [16, 17].

Bridge fires result in immense losses to both human lives and property, with large cable-stayed bridges—serving as crucial traffic bottlenecks—being particularly vulnerable. In the event of a fire, the use of these bridges is halted temporarily while inspections, tests, and safety assessments are conducted [18-20]. Currently, the cables of cable-stayed bridges are typically composed of high-strength steel wires or strands encapsulated in a high-density polyethylene sheath. However, due to the low melting point of the polyethylene sheath, the protective sleeve of the cables exhibits poor high-temperature performance [21, 22]. Even for protected steel cables, using ultra-thin insulation fiber materials can ensure the structural integrity of the system in the most severe fire scenarios, prior to implementing effective fire resistance measures. Fires on the deck of cable-stayed bridges are inevitable, and in the event of a cable fire caused by such deck fires, conducting prompt and effective assessments of the affected bridge becomes critically important [23, 24].

Currently, there remains a notable gap in research regarding cable damage, particularly in scenarios involving cable fire damage, where the impact and assessment on the overall bridge performance are even more pronounced. Ensuring the reliability and cost-effectiveness of fire-damaged cable repair projects, minimizing losses, and promptly and accurately detecting and evaluating the static performance of the bridge after a fire are practical challenges that need to be addressed.

ENGINEERING BACKGROUND

This paper is based on the cable-stayed bridge. In 2011, a traffic accident occurred on the bridge, and the car involved in the accident burned the nearby cable-stayed cables. Two cable-stayed cables were damaged in this accident, including two back cables N13 and N12 in the upper reaches of the North bank. The PE protective materials of the two cable cables were partially burned, and the stay cables showed obvious signs of fire damage. The phenomenon of steel wire exposure appeared in both cables, and the phenomenon of protrusion deformation and broken wire was not found in the high-strength steel wire of the stay cable. The burn length of the upstream N12 stay cable PE protection material is 16.5 m, and the burn length of the upstream N13 stay cable PE protection material is 5 m. The burnt material is removed to reveal the stay cable wire, and the surface color of the wire is discolored to a certain extent. Cable damage is shown in Figure 1.

(a) - N12 cable fire damage diagram

(b) - N13 cable fire damage diagram

Fig. 1 - Fire damage diagram of two back ropes on the downstream side of the north bank

The main bridge employs a double-tower, double-cable-plane semi-floating system in conjunction with a beam cable-stayed design, while the approach bridge utilizes a prestressed concrete continuous box girder structure. The total length of the bridge spans 1,268.86 m, with the main bridge measuring 696 m and the approach bridge extending 572.86 m. The main bridge features a span arrangement of 44 m (transition span) + 136 m (side span) + 336 m (main span) + 136 m (side span) + 44 m (transition span), and is designed to carry a load of over 20 t for cars and 120 t for trailers. The bridge accommodates four lanes in both directions. Figures 2 and 3 depict the overall and panoramic layouts of the entire bridge, respectively.

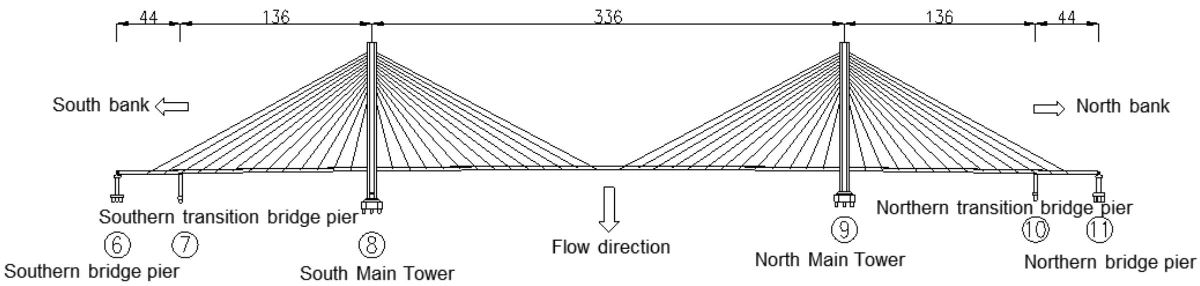

(a) Elevation view

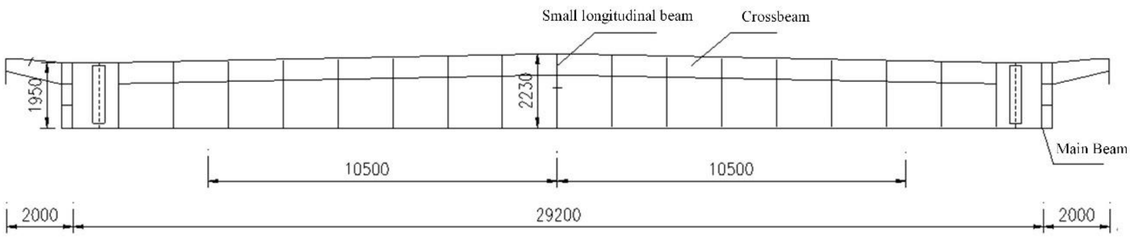

(b) Cross section

Fig. 2 - Overall layout of the main bridge (Unit: m)

DOI 10.14311/CEJ.2025.03.0027

Fig. 3 - Bridge Panoramic View

(1) Bridge tower

The tower is designed as a portal tower comprising two beams: an upper beam positioned above the bridge deck and a lower beam situated below it. These beams divide the bridge tower into three sections: the upper, middle, and lower tower columns. The south tower stands at a height of 110.80 m, while the north tower reaches 106.10 m. The crossbeam, which is a hollow box girder, features an enlarged section at its junction with the tower column, reinforced with chamfers for added strength. A rigid framework is incorporated into the cable tower's wall. Inside the tower, a pedestrian ladder provides direct access to the tower's summit. The pedestrian entrance is conveniently located at the top of the lower beam, adjacent to the tower wall on the bridge deck.

(2) Main bridge main beam

The main beam section consists of two I-beam side ribs, a crossbeam, and a small longitudinal beam positioned centrally. These elements are integrated with the concrete bridge deck to form a composite section. The spacing between the two I-beams is 29.2 m. At the cableway, the main beam has a height of 2.2 m, while at the bridge centerline, it measures 2.47 m. The ratio of the main beam’s height to its main span is 1/136, and the section's aspect ratio is 1/13.4. The steel beam adopts type Q20E, with an elastic modulus of 2.06×10^5 MPa and a strength design value of 360 MPa.

(3) Stay cable

The bridge utilizes hot-extruded polyethylene semi-parallel cables, which are composed of φ7 low-relaxation prestressed galvanized high-strength steel wires. These wires are twisted concentrically in the same direction by 2° to 4° and are enclosed with PE protective materials. Across the entire bridge, there are a total of 52 pairs of cables, with wire counts ranging from 163 to 367. The designed cable force varies between 3,940 kN and 8,870 kN. A diagram depicting the cable numbers is provided in Figure 4.

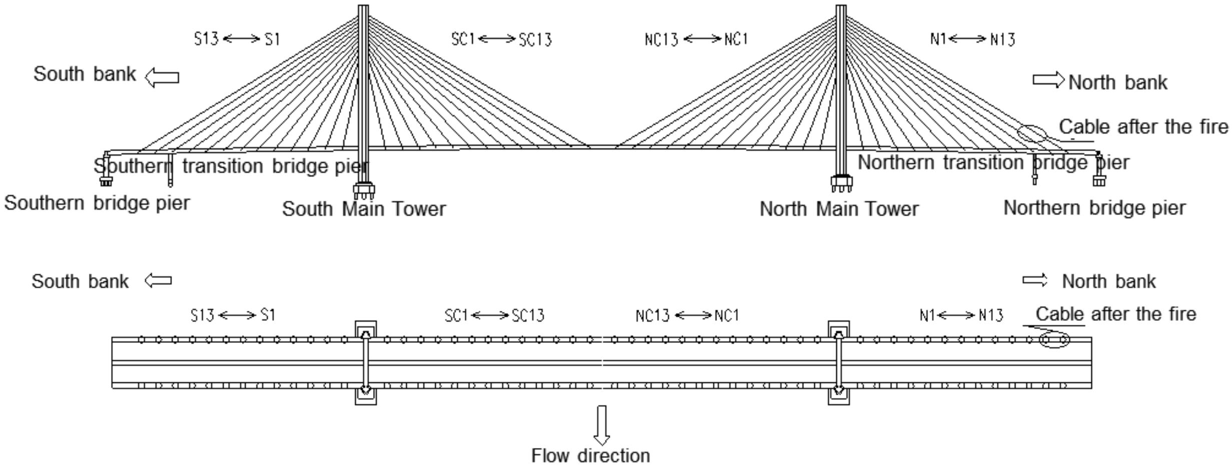

Fig. 4 - South shore north shore cable layout

DAMAGE MECHANISM OF THE STAY CABLE

The cable is a metal material, and the main unidirectional axial force, then a concentrated force P is applied to the cable. Due to the void, the effective cross-sectional area decreases and the net stress per unit area increases. The stress on the straight bar during uniaxial tensile is

$$P = \sigma A = \tilde{\sigma}\tilde{A} \tag{1}$$

Where σ is the Cauchy stress and $\tilde{\sigma}$ is the net stress, that is, the ratio of the external force P applied by the member to the net cross-section area $\tilde{\sigma}$. Then it is easy to get the relationship between effective stress and damage variable.

$$\tilde{\sigma} = \frac{P}{\tilde{A}} = \frac{\sigma}{\varphi} = \frac{\sigma}{1-D} \tag{2}$$

The strain exhibited by damaged material (D ≠ 0) under the influence of net stress is comparable to that of the same material in an undamaged state (D = 0). Based on this principle, the constitutive equation for damaged material (D ≠ 0) can be derived from the constitutive equation for non-damaged material (D = 0).

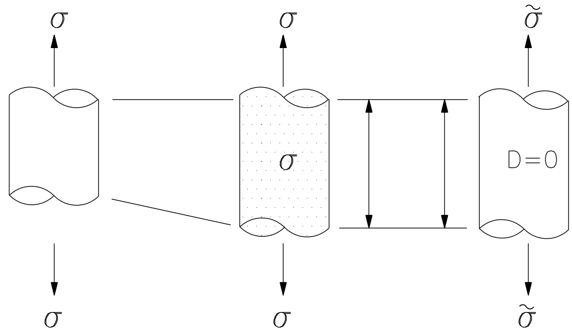

Fig. 5 - Strain equivalence diagram

The net stress after damage replaces the Cauchy stress in the constitutive relation of the lossless material, as shown in Figure 5.

In the absence of damage, the one-dimensional elastic constitutive equation is $\varepsilon = \frac{\sigma}{E}$. By replacing the Cauchy stress in the formula with the effective stress, we can get the one-dimensional elastic constitutive equation after damage:

$$\varepsilon_e = \frac{\tilde{\sigma}}{E} = \frac{\sigma}{E(1-D)} \tag{3}$$

Considering the hole (defective part) as the second-phase component within the composite material, we can utilize the calculation method for the elastic modulus of composite materials to determine the elastic modulus of the damaged material.

$$E_D = E(1-D) + E_K D \tag{4}$$

In the figure: E_D—Elastic modulus of damaged material

E—Nondestructive material elastic modulus

E_K—Hole part modulus of elasticity

If the elastic modulus of the hole E_K=0, so

$$D = 1 - \frac{E_D}{E} \tag{5}$$

Comparing with the previous formula, we will find that $E_D/\mathrm{E} = \tilde{A}/\mathrm{A}$, that is $E_D\mathrm{A} = \tilde{A}\mathrm{E}$, this is consistent with the strain equivalence principle, so that the damage of the material can be expressed as a change in the elastic modulus.

The stay cable consists of multiple high-strength steel wires. When disregarding the impact of high temperatures on the mechanical properties of these wires, damage to the steel wires can be likened to the fusing of the wires. The cable damage is studied from a statistical point of view, and the strength of the cable after damage is determined by the number of remaining wire bundles. That is, the effective area mentioned above is determined by$\tilde{A}$. If the entire cross-section of the stay cable is considered as a continuous medium, the damage variable can be defined as the ratio of the area of the melted steel wire$(\mathrm{A} - \tilde{A})$ to the area of the steel wire in the initial state. Then the damage variable is $\mathrm{D} = \frac{(\mathrm{A}-\tilde{A})}{A} = 1 - \tilde{A}/A$. So the damage in the one-dimensional parallel beam model can be simulated using the decrease in elastic modulus.

FINITE ELEMENT ANALYSIS

Model Building

The cable-stayed bridge's finite element model is constructed using Midas/Civil software. In this model, the main beam, small longitudinal beam, and cross beam are simulated with beam elements, with steel main beam ribs, small longitudinal beams, and cross beams on both sides represented accordingly. The steel main beam rib serves as the primary load-bearing component and connects with the intermediate small longitudinal beam through a steel beam to form a spatial beam structure. This steel beam joins the main beam and small longitudinal beam via common nodes. The concrete bridge deck is modelled as a uniformly distributed force. The reinforcement of the bridge tower is simulated using beam elements, while the stay cables are represented by truss elements. The upper end of each cable attaches to the bridge tower's outer edge, and the lower end connects to the steel main beam's outer edge. Both ends of the cable are anchored to the bridge tower and main beam through rigid arms. The bridge model comprises a total of 1933 nodes and 2272 elements across the entire bridge. There are 10^4 stay cables in total, simulated using truss elements. The main tower and main beam, which endure bending and compression forces, are modelled with beam elements. The finite element discretization diagram of the structure is illustrated in Figure 6.

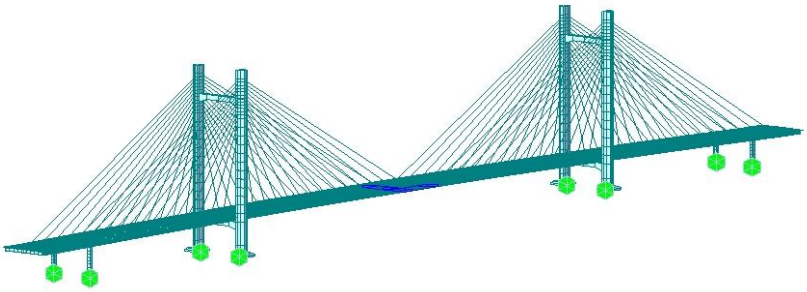

Fig. 6 - Structure finite element discrete diagram

STATIC PROPERTIES OF CABLE-STAYED BRIDGES WITH CABLE DAMAGE

Linear Changes of the Main Beam Under the Melting of Different Stay Cables

The Linear Change of the Main Beam Under the Symmetrical Fusing of the Cable

Firstly, we discuss the impact of various longitudinal cable fire damages on the main beam's characteristics. For simplicity in analysis, we consider pairs of cables that are symmetrical along the main beam's axis and the bridge's span as our subjects of study. The degree of damage is represented by the fused state of the cables, and we analyze how each pair of cables affects the bridge's main beam line when fused due to fire. The scenarios of side span cable fusing damage are presented in Table 1. The changes in the main beam's deflection under different side span cable fuse damages caused by fire are illustrated in Figure 7.

Tab. 1 - Side span cable fusing damage condition description

Working condition	Description of working condition	Midspan deflection increment（mm）	Percentage change in mid span deflection(%)
Lossless	Comparison between the undamaged condition of the cable and the following conditions	0	0
S13 +N13	The outer two pairs of back cable S13+N13 fuse condition	185	14.62
S11+N11	Transition pier top two pairs of back cables S11+N11 fuse condition, compared with S13+N13 condition	119	8.19
S8 +N8	Two pairs of cable fusing conditions near the middle of the side span are compared with S6+N6 conditions	27	1.92
S6 +N6	Melting failure condition of two pairs of stay cables S6+N6 at the midspan of the side span	2	0.02
S1 +N1	Side span tower root two pairs of cable S1+N1 fuse condition	-3	-0.03

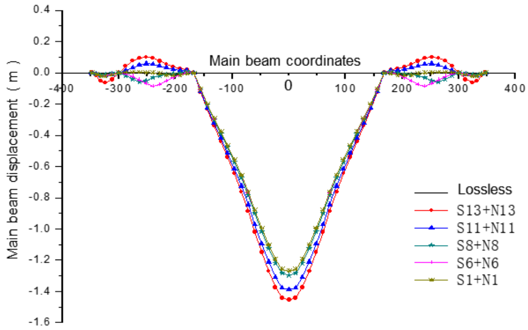

Fig. 7 - Diagram of the deflection change of the main beam under different cable fire induced fuse damage on the side span

As can be seen from Figure 7, the back cable has a great influence on the linear shape of the main beam, and the deflection of the main span, the reverse arch of the side span and the transition span increase significantly. Especially the outermost back cable has the greatest impact, and compared to the outermost back cable, the melting of the inner back cable has a decreasing trend on the linearity of the main beam.

It can be seen by comparing S13+N13 and S11+N11. The influence of other cable fusing on the linear shape of the main beam changes greatly only when the cable is anchored at the position of the main beam. It can be seen from S8+N8 and S6+N6 that due to the fire fusing effect of the cable, its anchorage loses elastic support and is subjected to constant load force, resulting in down torsion near the anchorage position.

The linear shape of the main beam near the main tower is almost the same under the fusing condition as that under the non-destructive condition, indicating that the fusing of the cable near the main tower has very little effect on the linear shape of the main beam, which can be clearly seen from S1+N1 and the non-destructive condition.

For the fire-induced fusing of the main span cable, three groups of main span long cable, middle long cable and short cable at the tower root were selected for fire induced fusing analysis. Cable fusing conditions are shown in Table 2. The deflection variation curve of the main beam under different typical cable melting of the main span is shown in Figure 8.

Tab. 2 - Main span cable fusing condition description

Working condition	Description of working condition	Mid span deflection increment（mm）	Percentage change in mid span deflection(%)
Lossless	Comparison between the undamaged condition of the cable and the following conditions	0	0
SC13+NC13	The outermost two pairs of back cable S13+N13 fuse condition of the main span	362	28.53
SC7+NC7	Main span two pairs of medium long cable SC7+NC7 fusing condition	5	-0.30
SC1 +NC1	Main span tower root two pairs of cables SC1+NC1 fuse condition	1	-0.05

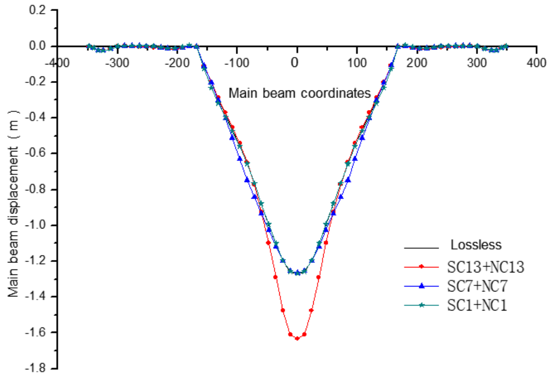

Fig. 8 - Diagram of the deflection change of the main beam under different cable fire induced fuse damage on the main span

From Figure 8, it can be seen that the melting of the cables in the span has a very small impact on the linearity of the main beams in the side span and transition span. Compared with the undamaged state, only when the cables in the middle span are melted, the deflection of the main beam is significantly reduced. In other cable melting situations, the deflection change of the main span is relatively gentle. Under the melting condition of the outermost two pairs of back cables S13+N13 on the main span, the mid span deflection is 362 mm, an increase of 28.53%. Under the melting condition of two pairs of medium length cables SC7+NC7 on the main span, the increase in mid span deflection is 5 mm, and the percentage change in mid span deflection is 3%. Under the condition of two pairs of cables SC1+NC1 melting across the tower root, the increment of mid span deflection is 1 mm, and the percentage change of mid span deflection is -0.05%.

The Linear Change of the Main Beam Under the Asymmetric Fusing of the Cable

In the preceding section, we analyzed the impact on the main beam's shape when both the cables at the symmetrical main beam axis and the mid-span of the main span were in a fused state. According to our analysis, damage to the outer back cables and the mid-span cables of the main span significantly alters the main beam's shape, particularly exemplified by the back cables S13 and N13, as well as the mid-span cables SC13 and NC13. Now, we will discuss the influence of asymmetric cable fusing on the bridge's alignment, where the back cables represent those in the side span affected by fire damage, and the mid-span cables represent those in the main span similarly affected. The specific operating conditions are outlined in Tables 3 and 4.

Tab. 3 - Description of asymmetric fusing damage condition of side span cable

Working condition	Description of working condition
Lossless	Comparison between the undamaged condition of the cable and the following conditions
SU13	The single back cable SU13 on the upstream side of the south bank is used to represent the fused condition of the asymmetric main span and the asymmetric axis in the span
SU13+SD13	Use the south bank edge to span the upstream and downstream side cables SU13+SD13, indicating the asymmetric mid span fuse condition

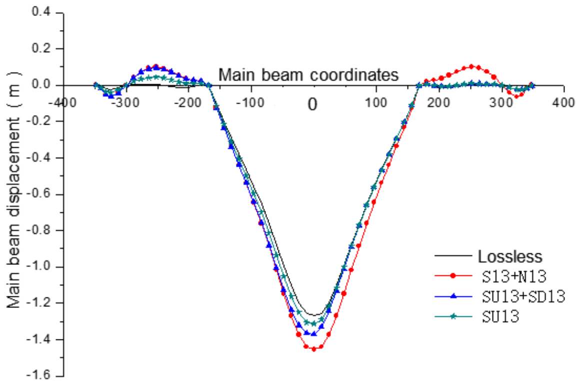

Fig. 9 - Deflection variation diagram of main beam under asymmetric fire fuse of side span back cable

Figure 9 shows the linear changes of the main beam under the asymmetric melting condition of the south bank side span back cable S13, and compares and analyzes them with the non-destructive state and the symmetrical melting state.

Tab. 4 - Main span cable fusing condition description

Working condition	Description of working condition
Lossless	Comparison between the undamaged condition of the cable and the following conditions
SCU13	The single back cable SCU13 on the upstream side of the south bank main span is used to represent the fused condition of the asymmetric main span and the asymmetric axis in the span
SCU13+SCD13	Use the south bank main span edge to span the upstream and downstream side cables SCU13+SCD13, indicating the asymmetric mid span fuse condition

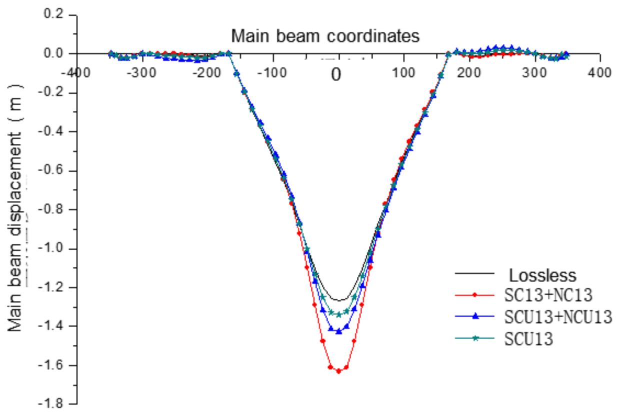

Fig. 10 - Diagram of the deflection change of the main beam under asymmetric fire induced fuse damage in the mid span cable of the main span

Figure 10 shows the linear changes of the main beam under the asymmetric melting damage condition of the main span middle cable SC13, and compares and analyzes them with the undamaged state and the symmetrical melting state.

From Figures 9 and 10, it is evident that the asymmetric fusing of the side span cable primarily influences the alignment of the same side span and the adjacent transition span, while it exhibits minimal impact on the opposite side span and transition span. In the event of asymmetric damage to the side span or transition span, the peak deflection in the main span shifts towards the side that has undergone more severe damage

T The asymmetric fusing damage of the main span cable affects the overall contour of the bridge's main beam, creating an antisymmetric trend across the mid-span of both the side span and the main span. When asymmetric damage occurs in the main span, the peak deflection at its mid-span shifts away from the heavily damaged side. It is not possible to analyze the substantial difference between symmetrical and asymmetrical failure along the axis of the main beam from the figure, as deflection is selected as the analysis variable. In fact, asymmetric failure of the cable along the axis of the main beam can cause a change in the torsion angle of the main beam, which is also an unfavorable form of failure.

Changes in Cable Force Under Different Stay Cable Fusing

The stay cable is subjected to a significant initial stress. In scenarios where the stay cable undergoes fire-induced melting damage, the stress in the main beam undergoes redistribution due to the force of gravity, thereby influencing the tension in other cables. The subsequent discussion delves into the variations in cable tension that arise when the stay cable itself melts due to fire.

Figure 11 illustrates the changes in cable tension for typical cables (SU13, SU11, SU8, SU6, SU1) located on the upstream side of the south bank, following fire-induced fusing damage. This damage is asymmetrical along the bridge's longitudinal axis, resulting in differing upper and lower cable forces. Therefore, the upper and lower cable forces are presented separately and compared to their non-destructive state cable forces. For a detailed description of each operating condition, please refer to Table 5.

Tab. 5 - Description of asymmetric fusing damage condition of main span cable

Working condition	Description of working condition
Lossless	Comparison between the undamaged condition of the cable and the following conditions
U-SU13	Transition span on the upstream side of the south bank, single back cable SU13 melted, and the tension of each cable on the upstream side
D-SU13	Transition span on the upstream side of the south bank, single back cable SU13 melted, and the tension of each cable on the downstream side
U-SU11	After the single back cable SU11 on the upstream side of the south bank is melted, the cable force of each cable on the upstream side
D-SU11	After the single back cable SU11 on the upstream side of the south bank is melted, the cable force of each cable on the downstream side.
U-SU8	After the single cable SU8 near the midspan of the side span on the upstream side of the south bank is melted, the cable forces of various cables on the upstream side
D-SU8	After the single cable SU8 near the midspan of the side span on the upstream side of the south bank is melted, the cable forces of various cables on the downstream side
U-SU6	After the single cable SU6 in the middle of the side span on the upstream side of the south bank is broken, the cable forces of all cables on the upstream side
D-SU6	After the single cable SU6 in the middle of the side span on the upstream side of the south bank is broken, the cable forces of all cables on the downstream side
U-SU1	After the single cable SU1 at the base of the tower on the upstream side of the south bank is broken, the cable forces of all cables on the upstream side
D-SU1	After the single cable SU1 at the base of the tower on the upstream side of the south bank is broken, the cable forces of all cables on the downstream side

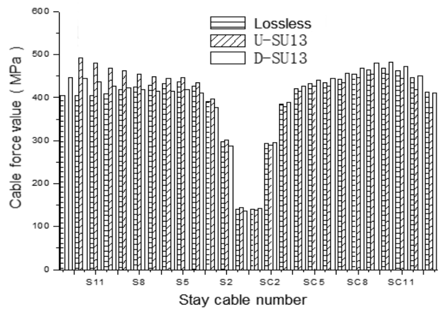

（a）- SU-13

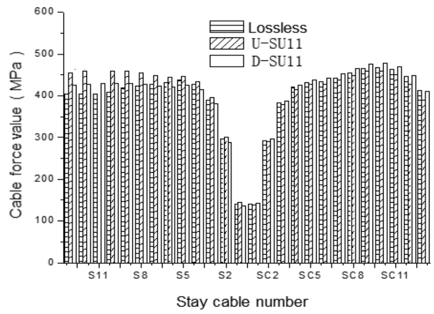

（b）- SU11

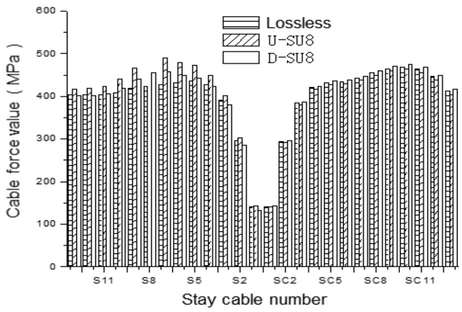

（c）- SU8

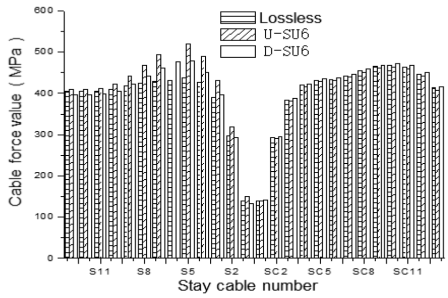

（d）- SU6

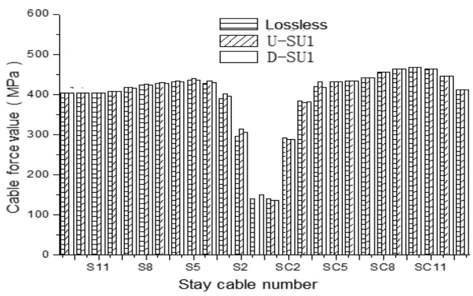

(e) - SU1

Fig .11 - Diagram of the influence of cable force under single cable fire induced fuse damage in transition span and edge span

An analysis of Figure 11 reveals that the fire-induced fusing of the back cable exerts a substantial influence on other stay cables. Besides affecting the cable forces in proximity to the bridge itself (where the cable force on the same side of the bridge's longitudinal axis increases, while the force on the opposite side decreases), it also impacts the cable forces across the span (where the cable force on the same side of the longitudinal axis decreases, while the force on the opposite side increases). Based on this characteristic, the initial extent of fire damage to the cable can be assessed.

The fire-induced fusing of other cables affects approximately 3 to 4 cables in its vicinity, but has minimal impact on cables further away. Damage to the cable at the base of the tower has little effect on nearby cables. When a single cable undergoes fire damage, the change in cable force on the same side is more significant than that on the opposite side.

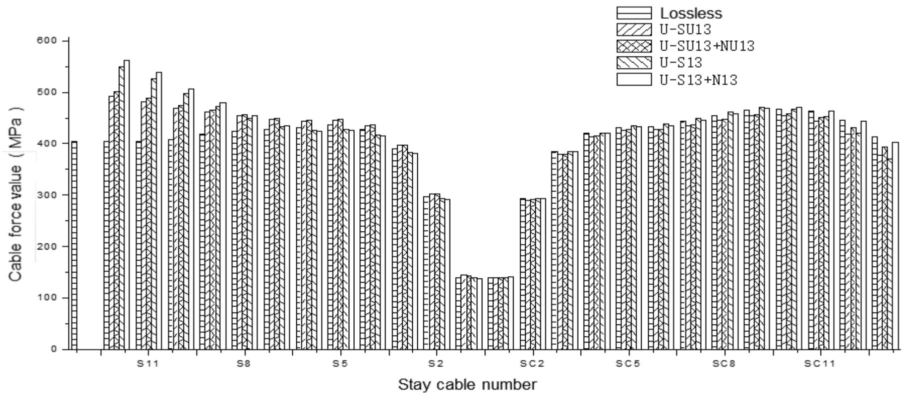

Fig. 12 - Diagram of cable force effect under different fire induced fuse damage of back cable

Figure 12 takes the back cable as an example to analyze the changes of other cable forces under different fire-induced fusing damage conditions. That is, the upstream cable force (U-SU13) when a single cable is damaged on the upstream side of the south bank, and the upstream cable force (U-SU13+NU13) when two cable cables are damaged on the upstream side of the span. The upstream side cable force (U-S13) when a pair of cables are damaged on the south bank, and the upstream side cable force (U-S13+U13) when two pairs of cables are damaged in the middle span are compared with that when there is no damage. Figure 13 shows the amplitude of other cable forces under different back cable injuries, which is used to indicate the degree of cable force changes.

$$\text{Cable force amplitude variation} = \frac{\text{Cable force value after damage} - \text{Non destructive cable force value}}{\text{Non destructive cable force value}}$$

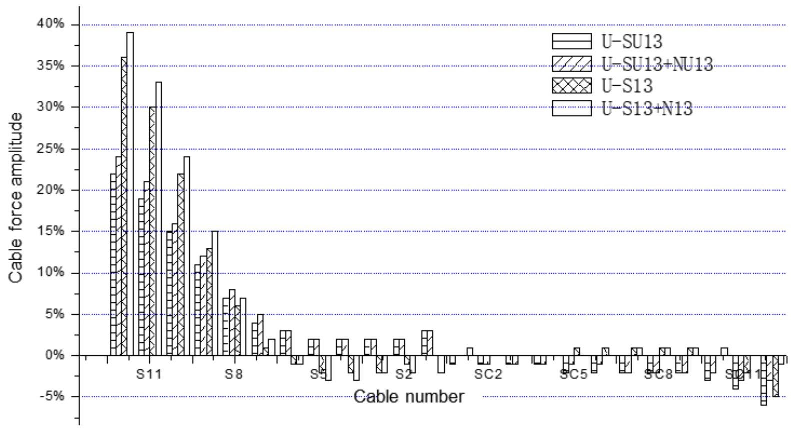

Fig. 13 - Variation of cable force under different fire induced fusing damage of back cable

As can be seen from Figure 13, the mid-span cable force decreases significantly in the case of mid-span asymmetric fire damage along the main span, which can be easily seen by the comparison of U-SU13, U-S13, U-SU13+NU13, U-S13+N13. In scenarios where both paired back cables suffer simultaneous fire damage, the cable force of the three adjacent cables increases markedly, with a variation exceeding 20%. This can be clearly observed by comparing the cases of U-S13, U-S13+N13, U-SU13, and U-SU13+NU13

The design strength of the stay cable is set at 1750 MPa. Taking into account a safety factor of 2.5 times, the maximum service strength of the stay cable should not exceed 628 MPa. In the event of fire damage to the outermost back cable S13, while the cable force of the adjacent cable

S12 did not reach the warning threshold, the margin was already quite small. Therefore, special attention should be given to the outer back cables during the operation of the bridge.

Static Force Analysis of the Entire Bridge Structure Under Different Degrees of Cable Fire Damage

From the variations in the main beam alignment observed under different cable damage scenarios mentioned above, it is evident that damage to the back cables and mid-span cables has a significant impact on the overall performance of the cable-stayed bridge. Conversely, damage to other cables primarily affects the local performance of the bridge and underscores the specific effects of damage on its characteristics. Therefore, considering the common damage scenarios involving back cables S13 and S12, as well as SC13 and SC12, an analysis is conducted to assess the impact of varying degrees of fire damage to side span cables on the bridge alignment and total cable force of the bridge.

According to the two factors of the fire temperature and the fuse amount of the cable, the macro-physical index of the cable after the fire is simulated, and the cable force damage is simulated by the reduction of the elastic modulus. It is assumed that the elastic modulus of the bridge after the damage simulation is reduced to 25%, 50% and 75%, and the mechanical characteristics are compared with those in the non-destructive and fire-induced fuse state. The elastic modulus after fire damage simulation is shown in Table 6.

Tab. 6 - Elastic modulus after fire damage

Damage degree	Damage elastic modulus (MPa)
Lossless	1.9500×10^5
Damage 25%	1.4625×10^5
Damage 50%	0.9750×10^5
Damage 75%	0.4875×10^5
Fire causes fusing	0

Table 7 and Table 8 describe the working conditions of back cable and mid-span cable with different degrees of fire damage respectively. In order to facilitate analysis, simultaneous damage of two pairs of back cables (S13 and S12) was adopted to represent different damage conditions of side span and transition span, and simultaneous damage of mid-span cable (SC13 and SC12) was adopted to represent different damage conditions of main span.

Tab. 7 - Description of different fire damage degree of back cord

Working condition	Description of working condition	Mid span deflection increment （mm）	Percentage change in mid span deflection(%)	λ
Lossless	Cable no state condition, compared with the following conditions	0	—	—
S13+S12-25%	S13 and S12 two pairs of cables with 25% damage condition	38.9	3.1	0.124
S13+S12-50%	S13 and S12 two pairs of cables with 50% damage condition	90.6	7.1	0.142
S13+S12-75%	S13 and S12 two pairs of cables with 75% damage condition	162.7	12.2	0.162
Fire causes fusing	S13 and S12 two pairs of cables with 100% damage condition	270.0	21.3	0.213

Tab. 8 - Explanation of working conditions with different degrees of fire damage to the main span mid span cable

Working condition	Description of working condition	Mid span deflection increment （mm）	Percentage change in mid span deflection(%)	λ
Lossless	Cable no state condition, compared with the following conditions	0	—	—
SC13+SC12-25%	SC13 and SC12 two pairs of cables with 25% damage condition	58.9	4.6	0.184
SC13+SC12-50%	SC13 and SC12 two pairs of cables with 50% damage condition	136.0	10.7	0.214
SC13+SC12-75%	SC13 and SC12 two pairs of cables with 75% damage condition	241.5	19.0	0.253
Fire causes fusing	SC13 and SC12 two pairs of cables with 100% damage condition	394.6	31.1	0.311

The change of deflection of main beam under different fire damage degree of back cable (S13, S12) is shown in Figure 14. The variation of the deflection of the main beam under different fire damage degrees of the middle span cables (SC13, SC12) of the main span is shown in Figure 15.

As illustrated in Figures 14 and 15, within the elastic working range, the impact trend of different levels of damage caused by cable fire on the bridge deflection remains consistent, manifested as quantitative changes. With the increase of damage degree, the deflection has a tendency to accelerate and increase. This can be seen by the λ values in Table 7 and Table 8.

Simultaneously, the aforementioned conclusion regarding asymmetric cable damage is verified. Specifically, when fire-induced damage occurs in the side span, the deflection peak of the main span tends to align closely with the severely damaged side. Conversely, when the fire damage occurs in the main span, the deflection peak shifts away from the severely damaged side.

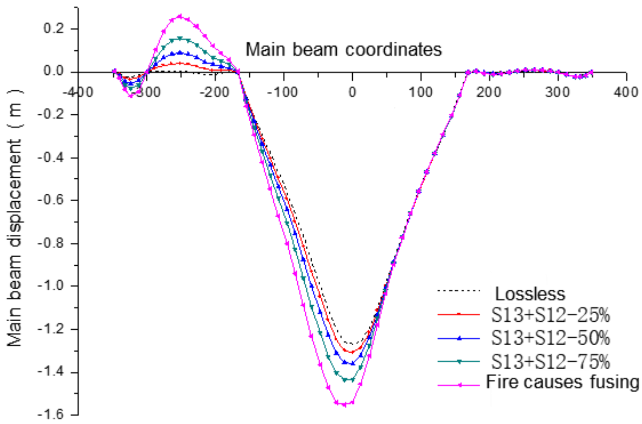

Fig. 14 - Deflection change of back cable (S13, S12) under different fire damage degree

DOI 10.14311/CEJ.2025.03.0027

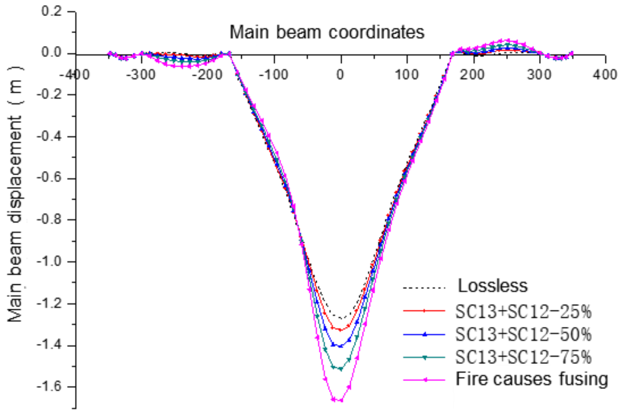

Fig. 15 - Deflection change of main span middle cable (SC13, SC12) under different fire damage degree

Figures 14 and 15 depict the magnitude of cable force variations for two pairs of back cables (S13 and S12) and two pairs of mid-span cables (SC13 and SC12) when subjected to varying degrees of fire-induced damage to other cables. Additionally, Figure 16 illustrates the changes in tension observed in other cables at different levels of fire damage to the mid-span cables (SC13, SC12) of the main span. In the case of different fire damage degrees of the main span middle cable (SC13, SC12), the change rates of other cable forces are shown in Figure 17. Back cable and mid-span cable damage affect each other's cable force, but the effect is less than that of the cable force near themselves. When the fire damage is more than 50%, the change amplitude of several cable forces near the cable is more than 10%. When fire damage occurs to a mid-span cable, the amplitude of change in cable force is greater in the adjacent long cable compared to the short cable.

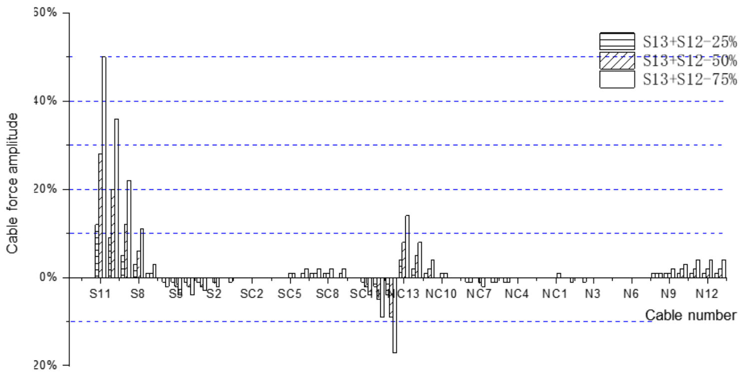

Fig. 16 - The variation range of cable forces in other cables under different levels of fire damage to the mid-span cables (SC13, SC12) of the main span.

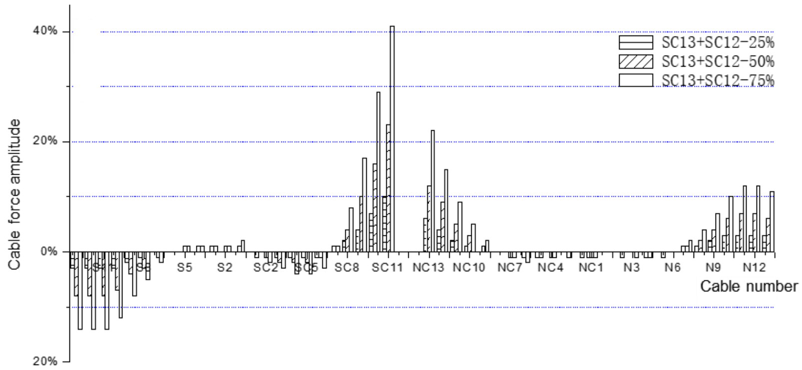

Fig. 17 - The rate of change in cable forces of other cables under different degrees of fire damage to the mid-span cables (SC13, SC12) of the main span.

CONCLUSION

1. The fire-induced damage of other cable is localized, and only the deflection near the main beam of the cable itself and the cable force of 3 to 4 nearby cable have a greater influence, which is similar to the support stiffness change or support failure of the multi-point elastic supported continuous beam. The fire damage of the tower root cable has almost no effect on the line shape and other cables.

2. Under the melting condition of the outermost two pairs of back cables S13+N13 on the main span, the mid span deflection is 362 mm, an increase of 28.53%. Under the melting condition of two pairs of medium length cables SC7+NC7 on the main span, the increase in mid span deflection is 5 mm, and the percentage change in mid span deflection is 3%. When the fire damage is more than 50%, the change amplitude of several cable forces near the cable is more than 10%. When fire damage occurs to a mid-span cable, the amplitude of change in cable force is greater in the adjacent long cable compared to the short cable.

3. In the case of simultaneous fire damage of paired back cables, the cable force of the three nearby cables increases obviously, and the variation amplitude of cable force reaches more than 20%. When the outermost back cable S13 is damaged by fire, the cable force of the adjacent cable S12 does not reach the warning value, but the margin is already quite small. Therefore, special attention should be given to the outer back cables during the operation of the bridge.

REFERENCE:

[1] ZHU, H., JI, J., NIE, J. Early fire evolution and alarm characteristics of cable fires in long and narrow spaces. Fire Safety Journal, 2022, 131, 103627. DOI: https://doi.org/10.1016/j.firesaf.2022.103627

[2] KEREKES, Z., RESTA, Á., LUBLOY, É. The effects causing the burning of plastic coatings of fire-resistant cables and its consequences. Journal of Thermal Analysis and Calorimetry, 2020, 139, 775-787. DOI: https://doi.org/10.1007/s10973-019-08526-9

[3] Lee, J. I., HA, K. C. A study for the fire analysis and igniting cause of freezing protection heating cables. Journal of the Korean Society of Safety, 2018, 33(3), 15-20. DOI: https://doi.org/10.14346/JKOSOS.2018.33.3.15

[4] KOTSOVINOS, P., Judge, R., Walker, G. Fire performance of structural cables: Current understanding, knowledge gaps, and proposed research agenda. Journal of Structural Engineering, 2020, 146(8), 03120002. DOI: https://doi.org/10.1061/(ASCE)ST.1943-541X.0002703

[5] WEINSCHENK, C., MADRZYKOWSK, D. Impact of flashover fire conditions on exposed energized electrical cords/cables. Fire Technology, 2020, 56(3), 959-991. DOI: https://doi.org/10.1007/s10694-019-00915-8

[6] HE, L., MA, G., HU, Q., et al. A novel method for risk assessment of cable fires in utility tunnel. Mathematical Problems in Engineering, 2019, 2019(1), 2563012. DOI: https://doi.org/10.1155/2019/2563012
[7] ALVARES, N., FERNANDEZ-PELLO, A., C. Fire initiation and spread in overloaded communication system cable trays. Experimental Thermal and Fluid Science, 2000, 21(1-3), 51-57. DOI: https://doi.org/10.1016/S0894-1777(99)00053-9
[8] FENG, J., GAO, K., GAO, W., et al. Machine learning-based bridge cable damage detection under stochastic effects of corrosion and fire. Engineering Structures, 2022, 264, 114421. DOI: https://doi.org/10.1016/j.engstruct.2022.114421
[9] KIM, M. O., KIM, K., YUN, J. H., et al. Fire risk assessment of cable bridges for installation of firefighting facilities. Fire Safety Journal, 2020, 115, 103146. DOI: https://doi.org/10.1016/j.firesaf.2020.103146
[10] KOTSOVINOS, P., ATALIOTI, A., MCSWINEY, N., et al. Analysis of the thermomechanical response of structural cables subject to fire. Fire Technology, 2020, 56, 515-543. DOI: https://doi.org/10.1007/s10694-019-00889-7
[11] FISHER, R. P., STOLIAROV, S. I., KELLER, M. R. A criterion for thermally-induced failure of electrical cable. Fire Safety Journal, 2015, 72, 33-39. DOI: https://doi.org/10.1016/j.firesaf.2015.02.002
[12] ZHENG, X., JIAN, J., LIU, L., et al. Static and dynamic performance analysis of cable-stayed bridges with cables damaged fire. Buildings, 2024, 14(4), 884. DOI: https://doi.org/10.3390/buildings14040884
[13] KOTSOVINOS, P., PANEV, Y., LILJA, H., et al. Reliability-based fire protection of structural cables due to deck fires on cable supported bridges. Structural Engineering International, 2023, 33(4), 576-585. DOI: https://doi.org/10.1080/10168664.2023.22132
[14] MI, H., ZHANG, X., WANG, W., et al. A risk analysis method of cable fire in utility tunnel based on a Bayesian network. Mathematical Problems in Engineering, 2022, 2022(1), 1952263. DOI: DOI: https://doi.org/10.1155/2022/1952263
[15] BENNETT, I., MOINUDDIN, K. Evaluation of the impact of potential fire scenarios on structural elements of a cable-stayed bridge. Journal of Fire Protection Engineering, 2009, 19(2), 85-106.
[16] GONG, X., AGRAWAL, A. K. Safety of cable-supported bridges during fire hazards. Journal of Bridge Engineering, 2016, 21(4), 04015082. DOI: https://doi.org/10.1061/(ASCE)BE.1943-5592.000087
[17] CHEN, C., CHEN, J., ZHAO, X., et al. Experimental investigation on combustion characteristics of steel cable for cable-stayed bridge. Journal of Thermal Analysis and Calorimetry, 2018, 134, 2317-2327. DOI: https://doi.org/10.1007/s10973-018-7689-6
[18] KIM, M., O, KIM, K., YUN, J. H., et al. Fire risk assessment of cable bridges for installation of firefighting facilities. Fire Safety Journal, 2020, 115, 103146. DOI: https://doi.org/10.1016/j.firesaf.2020.103146
[19] LIU, Y. J., NING, B., WANG, Y. Study on thermal and structural behavior of a cable-stayed bridge under potential tanker truck fires. Applied Mechanics and Materials, 2012, 238, 684-688. DOI: https://doi.org/10.4028/www.scientific.net/AMM.238.684
[20] LEE, J., CHOI, K., YOON, J., et al. Numerical analysis-based structural behavior assessment of a cable-stayed bridge under tanker fire. Structure and Infrastructure Engineering, 2023, 19(12), 1761-1778. DOI: https://doi.org/10.1080/15732479.2022.2053553
[21] ZHANG, Y., FANG, Z., JIANG, R., et al. Static performance of a long-span concrete cable-stayed bridge subjected to multiple-cable loss during construction. Journal of Bridge Engineering, 2020, 25(3): 04020002. DOI: https://doi.org/10.1061/(ASCE)BE.1943-5592.0001529
[22] LIU, Z., LOU, G., HOU, J., et al. Designing a two-level steel cable-stayed bridge against fires. Structural Engineering International, 2023, 33(4), 569-575. DOI: https://doi.org/10.1080/10168664.2023.2171331
[23] CHEN, W., CHEN, X., SHEN, R., et al. Fire resistance analysis and protection measures for cable components of suspension bridges. Journal of Constructional Steel Research, 2024, 220, 108852. DOI: https://doi.org/10.1016/j.jcsr.2024.108852
[24] KOTSOVINOS, P., JUDGE, R., WALKER, G., et al. Fire performance of structural cables: Current understanding, knowledge gaps, and proposed research agenda. Journal of Structural Engineering, 2020, 146(8), 03120002. DOI: https://doi.org/10.1061/(ASCE)ST.1943-541X.0002703

Article no. 28

THE CIVIL ENGINEERING JOURNAL 3-2025

STUDY ON THE COMBINED IMPACT ABOUT JOINT DIP ANGLE AND ROCK THICKNESS ON THE EXCAVATION STABILITIES OF TUNNELS WITH LARGE-SPAN BASED ON NUMERICAL EXPERIMENT

Wen Wang[1], Yiqiao Liu[2], Jikang Yang[1], Jichun Hu[1], Huijian Zhang[2] and Lichuan Wang[3]

1. *CCCC Third Highway Engineering Bureau, Anding Wai Street, Dongcheng District, Beijing, 100010, China*
2. *Southwest Jiaotong University, School of Civil Engineering, Key Laboratory of Transportation Tunnel Engineering, Ministry of Education, No. 111, North Section, Second Ring Road, Jinniu District, Chengdu, Sichuan Province, 610031, China*
3. *China Railway 18th Bureau Group Co., Ltd., Tianjin, 300222, China; huijianz@163.com*

Received: *13.12.2024*
Received in revised form: *15.07.2025*
Accepted: *01.09.2025*

ABSTRACT

The stability of the surrounding rock is intricately linked to joint characteristics, particularly when a tunnel traverses layered, jointed rock masses. However, existing research has predominantly concentrated on tunnel stability within single-jointed rock formations, considering large-span tunnels situated under complex geological conditions. Therefore, drawing upon the Chongqing Guobo Station Tunnel Project as a case study, this paper employs a numerical experimental approach to conduct an in-depth exploration of the relationship between joint dip angles, the thickness of jointed rock layers, and the stability of the tunnel's surrounding rock. The research findings reveal that variations in both joint dip angle and the thickness of jointed layers exert a substantial influence on the stability of the surrounding rock. Under different conditions, the maximum increase in tunnel deformation approaches 400 mm. As the dip angle changes, the deformation of the surrounding rock initially decreases and then increases. The disparity between displacement perpendicular to the joint surface and displacement along the bedding plane initially narrows and subsequently widens, eventually becoming predominantly governed by displacement along the bedding direction. Moreover, the location of maximum displacement gradually shifts from the arch shoulder to the tunnel crown. For large joint dip angles, the surrounding rock primarily undergoes tensile yield failure along the direction of the joint surface and shear yield failure perpendicular to it. When the thickness of the joint layer increases, both the displacement of the surrounding rock and the distribution range of the plastic zone diminish, which enhances the overall integrity and bolsters the stability of the surrounding rock.

KEYWORDS

Tunnel with large span, Numerical test, Influence rule, Surrounding rock stability

INTRODUCTION

In the Chongqing-Guizhou region, the geological setting is exceedingly intricate, characterized by a diverse array of adverse geological conditions. Among these, the layered jointed rock mass stands as a quintessential example. Guaranteeing the stability of the surrounding rock is of paramount importance for the safety of tunnel construction activities [1-3]. Notably, the existence of joints exerts a profound impact on the stability of the surrounding rock [4]. Owing to the cutting action within the joints, construction operations in certain soft rock masses may trigger a series of disasters. These include substantial displacement of the surrounding rock, block-falls from the tunnel crown, and cracking of the preliminary lining [5, 6]. Consequently, it becomes imperative to conduct in-depth research on the stability of tunnel excavation in laminated jointed rock masses. Such research is essential to fully ensure not only the safety but also the efficiency of tunnel construction endeavors.

Several studies have primarily centered on the failure mechanisms inherent in jointed rock masses [7, 8], highlighting that the dip angle of rock strata exerts a substantial influence on the mechanical behavior and failure patterns of rock specimens. In addition, scholars have also conducted a certain degree of research on the stability challenges associated with tunnels constructed in jointed rock masses [9]. Luo et al [10] found that for the steep dip angle of the joint, the stability of surrounding rocks was mainly affected by the nature of the rock mass, while for a slow dip angle, the joints are the key factors leading to damage to the surrounding rock. Suo et al [11] pointed out that the surrounding rock was the most stable if the dip angle of joints was in the range 45° ~ 60°. Zhou et al [12] found that the maximum extrusion deformation of the excavation face of a nodular rock tunnel was distributed in an ‘M’ curve centered at 90°, and the deformation was largest when the inclination angle was 60° and 120°. If the inclination angle increases, the damage form of the palm face was circular, triangular, and inverted triangular in that order. Li et al [13] analyzed the impact of inclination angles as well as the spacings of surrounding rock joints on tunnel deformation, and concluded that the tunnel displacement with the change of inclination angle shows a decrease and then an increase, and the lining control effect is positively correlated with the inclination angle. Zheng et al [14] found that the size and distribution density of joint inclination are negatively correlated with tunnel stability, in which joint inclination is the most critical factor affecting the stability of the surrounding rock. Tang et al [15] investigated the impact of laminated rock body on the stabilities of surrounding rock, and found that the displacement of surrounding rocks caused by the joint surface was the greatest in the direction of vertical joint surface, and the failure zone of surrounding rocks was also largely distributed along the directions in vertical joint surface. An in-depth analysis was conducted on the influence of dip direction on the main deformation zones of layered rock masses [16]. The findings revealed that the main deformation zones were prone to developing in areas where the normal direction of the rock layers is oriented towards the interior of the tunnel. Wang et al [17] delved into the impact of columnar joints on the stability of surrounding rock. Their study demonstrated that, in terms of the self-bearing capacity of the rock mass under various dip angles, the order from the weakest to the strongest is 45°, 60°, 75°, 90°, 30°, 0°, and 15°. Jiang et al [18] explored the failure characteristics of jointed rock in deep-buried tunnels at different inclination angles. They discovered that when the inclination angle of the fracture surface is either less than 70° or greater than 77°, stress-controlled failure serves as the primary failure mode. Conversely, stress-structural control failure occurs under other circumstances. Jia et al [19] investigated the effects of different dip angles of layered joints and lateral pressure coefficients on the stability of tunnels within jointed rock masses. Numerical analyses carried out in their study indicated that both the joint dip angle and the lateral pressure coefficient exert significant influences on the failure modes and deformation characteristics of tunnels. Jayakumar et al [20] analyzed the failure characteristics of tunnels under different fault dip angles. Their research found that when the dip angle is 60°, the structural force generated in the tunnel lining is greater.

In conclusion, while research into the influence of joints on the stability of tunnel surrounding rocks has yielded some notable achievements, a significant portion of the existing findings primarily pertains to medium and large-span tunnels. In contrast, relevant research on super - large - span tunnels remains relatively scarce. On the flip side, current studies have predominantly concentrated on a single type of jointed rock mass. Consequently, the applicability of these existing research results to large-span tunnels with a complex composition of jointed rock masses, as well as the impact of geologic compliant bias, remains uncertain. In light of these gaps, this paper undertakes a systematic investigation into the effects of varying joint inclinations and rock thickness on the excavation stability of large-span tunnels. The study is based on the Chongqing East Ring Road Guobo Center Station project. Such research is instrumental in ensuring the safety and stability of the construction process and serves as a valuable reference for similar projects in the future.

PROJECT OVERVIEW

The Guobo Center Station of Chongqing East Ring Railway has a total length of 284m, with a burial depth ranging from approximately 23m to 55m, and an excavation width and height of 24m and 22m, respectively. The tunnel section area is approximately 449.6m^2, which belongs to the super large-span tunnel. The location of Guobo Station was displayed in Figure 1.

The tunnel is covered with miscellaneous fill at the top and passes through a stratified, jointed rock body, which is mainly composed of sandstone and mudstone. The rock stratum occurrence is S-N/38~40ºNW, with rock dip angles varying between 38° and 40°. The surrounding rock is fragmented and exhibits poor stability, primarily rated as Grade V. The exposed surrounding rock at the excavation faces of the tunnel is displayed in Figure 2.

Fig. 1 – Location of the Guobo Station

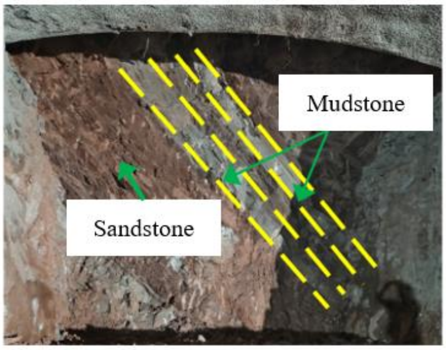

Fig. 2 – Joint Condition of rock mass in the on-site tunnel

NUMERICAL TEST MODEL AND CALCULATION INSTRUCTIONS

Drawing on the tunnel dimensions of the project under consideration, along with the stratigraphic distribution features and the objective of minimizing boundary-effect impacts, the ultimately adopted and established computational model is presented in Figure 3. The computational model has dimensions of length × width × height = 243 m × 60 m × 190 m. There is a

DOI 10.14311/CEJ.2025.03.0028

vertical distance of 110 m between the tunnel bottom and the base of the model. Normal constraints [21] have been applied to the front, back, left, right, and base surfaces surrounding the model. In contrast, the top surfaces are designated as free surfaces, allowing for unrestricted deformation. Regarding the initial stress conditions, only the gravitational stress field has been taken into account.

The mesh generation strategy has a huge impact on the calculation results. Therefore, a large number of mesh division trials were conducted before the start of this study. Considering the computational efficiency and accuracy, a local densification of the mesh was ultimately adopted in the area close to the tunnel, while a sparser mesh was used in the area far from the tunnel. Due to page limitations, the final adopted mesh division diagram is placed in this section, as shown in Figure 3.

The surrounding rock is simulated using solid zones, while joints were modeled with thinner solid zones and reduced mechanical parameters compared to the surrounding rock [22, 23]. Considering that the Mohr-Coulomb constitutive model can well characterize the shear failure of rock masses with high calculation efficiency, and the calculated parameters are convenient and accurate to obtain [24, 25]. Therefore, both the surrounding rock and the joints follow the Mohr-Coulomb ideal elastoplastic constitutive relation. Referring to the field geological survey of Guobo tunnel project and the data in *Code for Design of Railway Tunnels* [26], the computation parameter for the surrounding rock adopted in this paper is shown in Table 1.

Tab. 1 - Mechanically computation parameters of the surrounding rock

Surrounding rock	Elastic modulus E (MPa)	Poisson's ratio μ	Internal friction angle φ (°)	Cohesion c (kPa)	Density ρ (kg/m^3)
Miscellaneous fill soil	13	0.28	5	50	1800
Sandstone	1800	0.35	35	400	2200
Mudstone	130	0.38	24	65	2200

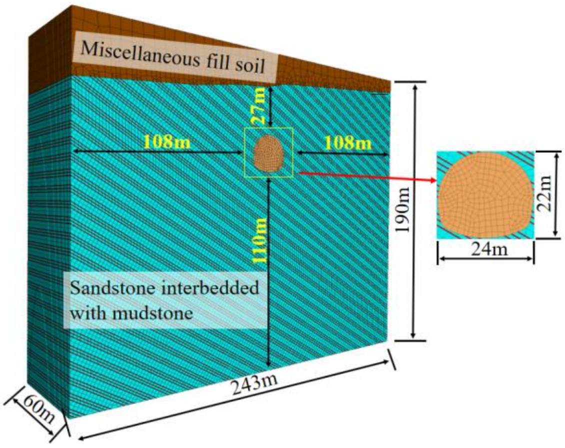

Fig. 3 – Calculation Model

To investigate the combined impact of jointed dip angles and variation in rock layer thickness on the stability of tunnels with large-span sections, the relevant calculated condition is displayed in Table 2.

Tab. 2 - Calculation condition

Variable name	Variable value			Remarks
Joint dip angle	30°	45°	55°	Fixed rock layer thicknesses of 1m
Rock layer thicknesses	1m	2m	3m	Fixed joint dip angle 45°

The tunnel is excavated by the full-face excavation method, with a cycle footage of 2 meters. No support is provided until the tunnel is excavated through. That is to say, the focus is on studying the impact of laws of jointed dip angles as well as rock layer thickness on the construction stability of super-large span tunnels without support, to offer a reference basis for the selection of tunnel lining methods in the subsequent dependent projects. The middle section (y = 30m) of the model is used as the monitored section, and the schematic diagram of the layout of monitored positions is displayed in Figure 4.

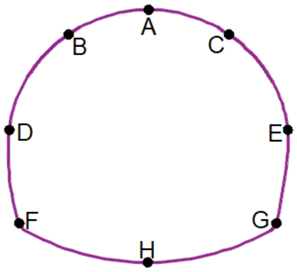

Fig. 4 – Layout of the monitoring point

ANALYSIS OF THE CALCULATION RESULTS

Discussion about tunnel stability under various joint dip angles

The cloud diagrams of surrounding rock displacement under various jointed dip angles are displayed in Figure 5. In Figure 5, the changes in jointed dip angles have very significant impacts on the displacement of the surrounding rock. For the jointed dip angle at 30°, the displacement of the surrounding rock in both the direction perpendicular to the jointed plane and the bedding direction is relatively large. Still, the displacement in the former direction is greater than that in the latter, and the maximum displacement is located near point B at the arch shoulder. For the jointed dip angle at 45°, the displacement of the surrounding rock in the bedding direction and the direction perpendicular to the joint plane are relatively close, and the maximum displacement appears between points A and B. For the jointed dip angle at 55°, the displacement of the surrounding rock in the bedding direction dominates, and the displacement perpendicular to the jointed plane is relatively small, with the maximum displacement appearing near point A. It indicates that during the addition of the jointed dip angle, the difference in displacement in the two directions first decreases and then increases. Eventually, the displacement in the bedding direction becomes dominant, and the location of maximum deformation of the surrounding rock moves from point B at the arch shoulder to point A at the crown, with the maximum displacement increasing from 43.2 mm to 437 mm.

DOI 10.14311/CEJ.2025.03.0028

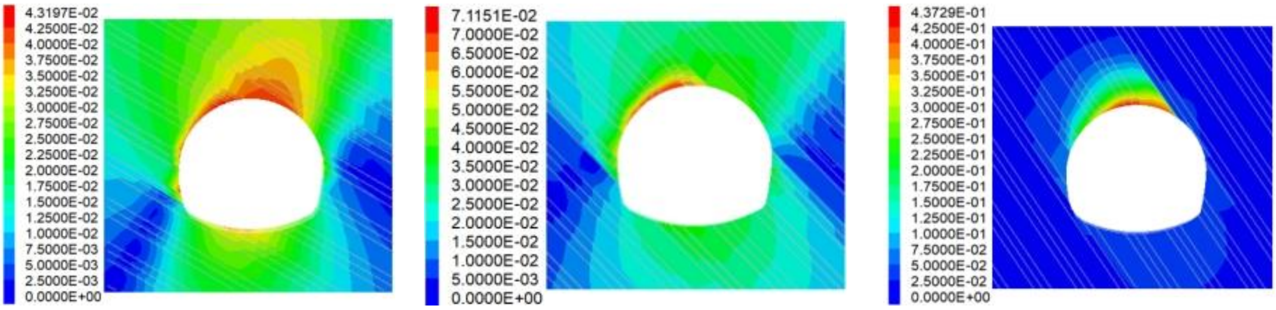

(a) 30° *(b) 45°* *(c) 55°*

Fig. 5 – Cloud diagrams of surrounding rock displacement under various jointed dip angles

The variation curves of surrounding rock displacement with the joint dip angles are displayed in Figure 6.

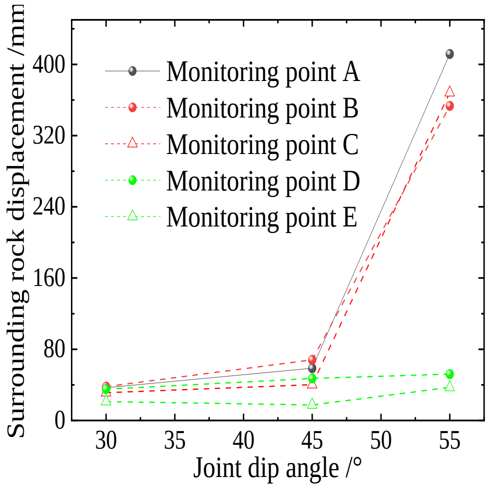

Fig. 6 – Diagram of the relationship between the displacement of tunnel surrounding rocks and jointed dip angles

In Figure 6, for the dip angle at 30° ~ 45°, although the surrounding rock displacement increases, the change is relatively slow. Nevertheless, when the dip angles varied within the range of 45° to 55°, notable increases in displacement are recorded at the vault and both arch shoulders. In comparison to the preceding angular variation range, monitoring points A, B, and C demonstrate growth rates of 600%, 360%, and 700%, respectively. As the dip angle changes, the characteristics of the stratum bias pressure also evolve, as evidenced by the fact that the displacement difference between the surrounding rocks on either side initially decreases and subsequently increases, reaching a maximum difference of 36 mm. Ultimately, the displacement observed at monitoring point C surpasses that at monitoring point B.

Figure 7 displays the cloud diagrams of the distributed state of the plastic area of the surrounding rock under various dip angles. Among them, the red part represents shear failure, and the black part represents tensile failure. The relationship diagram between the area ratio of the plastic zone of the surrounding rock to the tunnel sectional area (abbreviated as "R_{pt}") at various jointed dip angles is displayed in Figure 8.

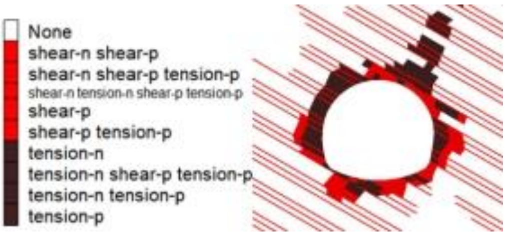

(a) 30°

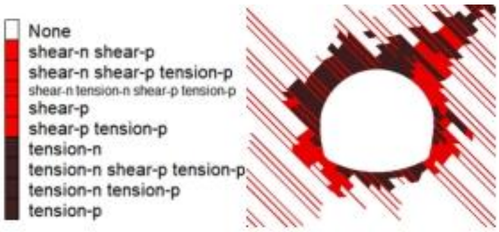

(b) 45°

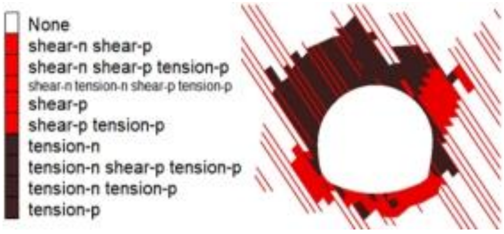

(c) 55°

Fig. 7 – Cloud diagrams of the plastic zone of the surrounding rock under various joint dip angles

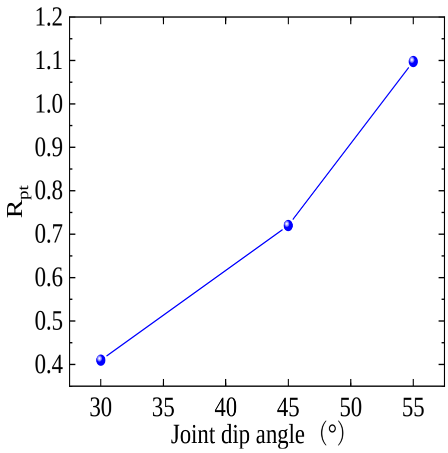

Fig. 8 – Diagram of the relationships between the R_{pt} and the jointed dip angles

In Figure 7, the weak interlayer is mainly subject to shear slip failure, and the distribution range of surrounding rock failure is mainly in the two directions perpendicular to the joints and along the joints. At little dip angles, shear failure predominates as the primary failure mode. If jointed dip angles increase, the distribution ranges of plastic zones in the two directions also change accordingly. The range along the joint plane direction gradually increases, while the range in the directions perpendicular to the joint plane slowly decreases. Finally, the failure mode along the joint plane direction is mainly tensile yield, and the failure in the directions perpendicular to the jointed plane is mainly shear yield. As the dip angle increases, the main failure mode of the rock mass changes from shear failure to shear-tension failure, which is consistent with the results of the model test [27]. Overall, the plastic area of the surrounding rock mostly appears above the center line of the tunnel, while yield zones on the left and right sides show an asymmetric distribution.

It can be seen from Figure 8 that R_{pt} also presents a nonlinear growth tendency with the increase of the dip angles, indicating that the jointed dip angle has a large influence on the failure of tunnel surrounding rocks, and the maximum increase rate of R_{pt} even reaches 0.7.

CIVIL ENGINEERING JOURNAL

Article no. 28

THE CIVIL ENGINEERING JOURNAL 3-2025

Discussion about the surrounding rock stability in a tunnel under different rock layer thicknesses

The cloud diagrams of the deformation of the tunnel surrounding rock under various rock layer thicknesses are displayed in Figure 9. The curve diagram of relationships between the displacement in the surrounding rock and variation of the rock layer thickness is shown in Figure 10.

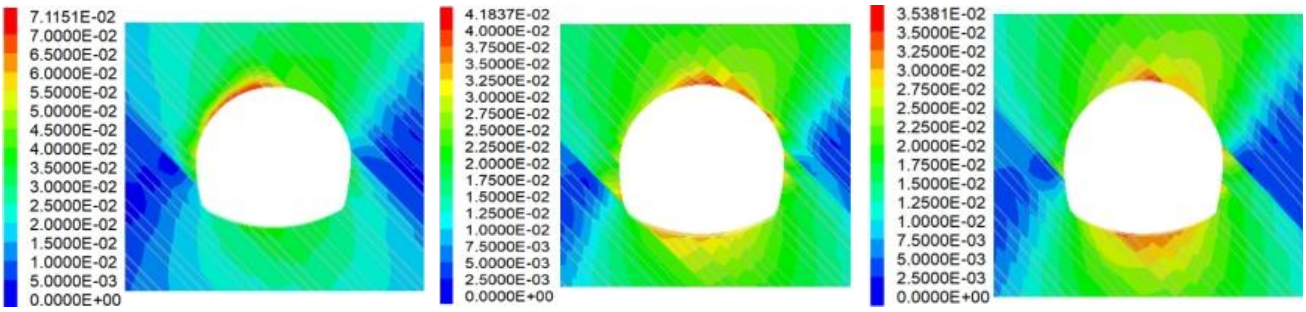

(a) 1m *(b) 2m* *(c) 3m*

Fig. 9 – The relationship between rock layer thickness and displacement diagram of the tunnel surrounding rocks

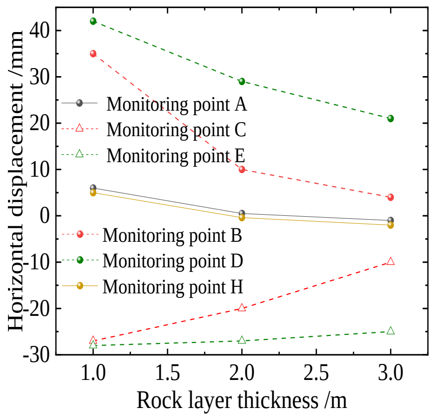

Fig. 10 – The relationships between the displacement of tunnel surrounding rocks and the variation of rock layer thickness

In Figures 9 and 10, for rock layer thickness at 1m, the displacement of the surrounding rock in the bedding direction and the direction perpendicular to the joint plane is relatively close. If the layer thicknesses increase, the deformation of the surrounding rock in the two directions basically remains consistent. This indicates that if joint dip angles remain constant, the changes in layer thickness hardly influence the difference in the distribution of surrounding rock deformation in different directions but have a relatively large impact on the magnitude of surrounding rock displacement. When the layer thickness increases, the displacement of the surrounding rocks at each monitoring position gradually decreases. Especially at the monitoring points B, C, and D, E, which are symmetrically distributed along the tunnel centerline, the variation in horizontal displacement of surrounding rocks gradually decreases; that is, the integrity of the rock mass becomes better. Since the increase in layer thickness brings about a reduction in the proportion of joints around the tunnel, thereby weakening the unbalanced pressure effect on the layer, as well as enhancing the stability of the surrounding rock. It is important to note that the horizontal displacement observed at vault point A and invert point H is nearly equal in magnitude and gradually converges towards 0 mm. This phenomenon can be attributed to the fact that these two points are vertical measurement locations, where horizontal displacement tends not to be significant.

The distribution of the plastic zone of the surrounding rock under various rock layer thicknesses is displayed in Figure 11. The variation of the R_{pt} of the tunnel with rock layer thicknesses is shown in Figure 12.

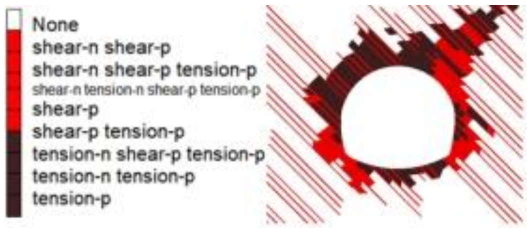

(a) 1m

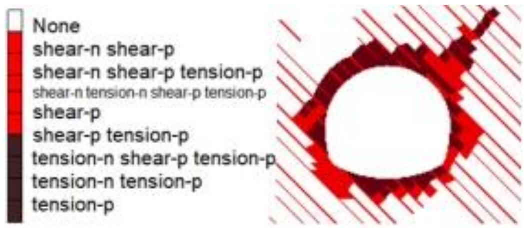

(b) 2m

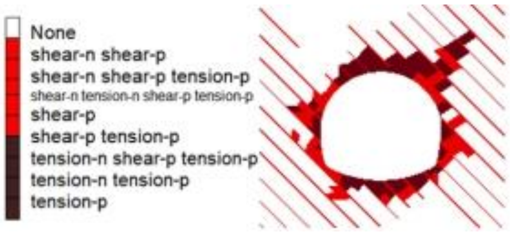

(c) 3m

Fig. 11 – Diagram of relationships between the cloud diagram of the surrounding rock plastic area and the rock layer thickness

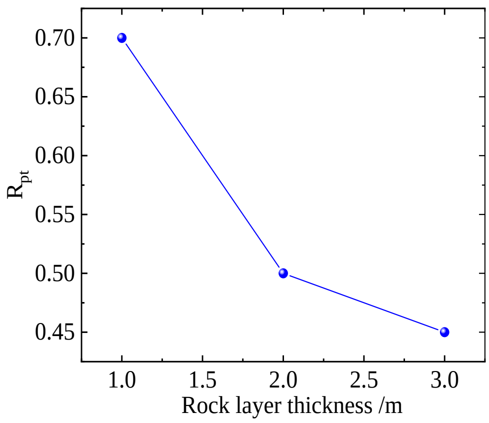

Fig. 12 – The relation curves between R_{pt} and rock layer thickness

It can be seen from Figures 11 and 12 that the failures range of the surrounding rock in the directions perpendicular to the joint and in the bedding direction are basically the same, and it is found that the thickness of the layer has a great influence on the distribution area of plastic area of the surrounding rock. When the layer thickness is 1m, the joints are distributed relatively densely, and the integrity of the rock mass is poor, resulting in a relatively large distribution area of the plastic zone, which is mainly distributed at arch waists. When the layer thicknesses increase, the spacing between joints gradually widens, the integrity of the rock masses improves, making them less susceptible to damage. Concurrently, the distribution area of plastic zones diminishes accordingly. As the layer thickness increases, the R_{pt} gradually decreases, the fragmentation degree of the surrounding rocks is reduced, and stability is enhanced. The maximum reduction rate of the R_{pt} reaches 0.25. Generally speaking, the thicknesses of the jointed layer have a direct effect on the stability of tunnel excavation. The smaller the joint spacing and the denser the distribution, the poorer the stability of the surrounding rock [14].

CONCLUSION

The main findings of this paper are listed below:

(1) The variation in dip angles exerts a profound impact on the displacement of the surrounding rock. When the dip angle is set at 30°, the displacement occurring in directions perpendicular to the joint plane surpasses that in the bedding direction. At a dip angle of 45°, the displacement of the surrounding rock in both the bedding direction and the direction perpendicular to the joint plane is relatively similar. Once the dip angle reaches 55°, the deformation of the surrounding rocks in the bedding direction becomes dominant. As the dip angles continue to increase, the growth rate of the surrounding rock's displacement initially exhibits a slow-paced trend, which then accelerates. The location of the maximum displacement gradually shifts from the arch shoulder towards the crown. Simultaneously, the difference in displacement between the two sides of the surrounding rock gradually widens, and the characteristics of unbalanced stratum pressure become increasingly prominent.

(2) Under varying joint dip angle scenarios, the plastic zone of the surrounding rock predominantly concentrates in two key directions: perpendicular to the joints and along the joints. Nevertheless, the extent of the plastic zone's distribution undergoes alterations in response to changes in the joint dip angle. As the dip angles gradually increase, the area encompassed by the plastic zone expands in a nonlinear fashion. In the case of large dip angles, the surrounding rocks are primarily subject to tensile yield failure along the direction parallel to the joint plane. Conversely, they mainly encounter shear yield failures in the direction perpendicular to the joint plane.

(3) When the dip angles are held constant, alterations in layer thickness exert minimal influence on the distribution pattern of surrounding rock deformation, whether in the direction perpendicular to the joint planes or along the jointed plane. However, they have a relatively significant impact on the magnitude of surrounding rock displacement. In scenarios where the layer thickness is small, the displacement of the surrounding rocks tends to be relatively substantial. As the layer thickness gradually increases, the displacement of the surrounding rock exhibits a corresponding decrease. Simultaneously, the disparity in displacement between the surrounding rocks on both sides of the tunnel diminishes. Consequently, the characteristics of unbalanced stratum pressure are mitigated, and the stability of the surrounding rocks is enhanced.

ACKNOWLEDGMENTS

This research was supported by the National Natural Science Foundation of China (Grant number: 52178395).

REFERENCES

[1] Kong W.Y., Zhou L.X., Wang J.L., 2024. Key technologies for quality control of tunnel lining construction of Xi'an-Kunming high speed railway. Railway Engineering, vol. 64, p. 96-100. http://doi.org/10.3969/j.issn.1003-1995.2024.07.17

[2] Yang Q.L., Li X., Wang Y.L., 2024. Discrete element numerical test of tunnel structure failure in fault fracture zones. Experimental Technology and Management, vol. 41, p. 136-142. http://doi.org/10.16791/j.cnki.sjg.2024.08.018

[3] Rong W., Su X.L., Zhao C.J., et al, 2024. Design of an experimental platform for investigating the structural response law of tunnel models crossing unfavorable geological zones. Experimental Technology and Management, vol. 41, p. 119-127. http://doi.org/10.16791/j.cnki.sjg.2024.07.016

[4] Lin C.B., Yu J., Chang F.Q., et al, 2023. Influence of three-dimensional persistent joints on surrounding rock stability of large-span tunnel. Journal of Central South University (Science and Technology), vol. 54, p. 1141-1152. http://doi.org/10.11817/j.issn.1672-7207.2023.03.030

[5] Liu X.Z., Liu W.Y., Suo C.F., 2014. Effects of the joint dip angle on the collapsed arch of surrounding rock around a highway tunnel. Modern Tunnelling Technology, vol. 51, p. 73-77. http://doi.org/10.13807/j.cnki.mtt.2014.06.012

[6] Pan W.T., He C., Wu F.Y., et al, 2023. Effect of bedding angle of layered soft rock tunnels with different large deformation grades. Journal of Civil and Environmental Engineering, vol. 45, p. 94-105. http://doi.org/10.11835/j.issn.2096-6717.2021.198

[7] Zhang Z.L., Wang, T., 2023. Failure modes of weak interlayers with different dip angles in red mudstone strata, Northwest China. Bulletin of Engineering Geology and the Environment, vol. 82, 156. https://doi.org/10.1007/s10064-023-03165-9

[8] Li Y.Z., Yuan L., Zhang Q.H., 2024. Brittle rock mass failure in deep tunnels: The role of infilled structural plane with varying dip angles. International Journal of Rock Mechanics and Mining Sciences, vol. 176, 105721. https://doi.org/10.1016/j.ijrmms.2024.105721

[9] Nikadat N., Marji M.F., 2016. Analysis of stress distribution around tunnels by hybridized FSM and DDM considering the influences of joints parameters. Geomechanics and Engineering, vol. 11, p. 269-288. https://doi.org/10.12989/gae.2016.11.2.269

[10] Luo S.L., Wu R.B., Zhang Z.Q., 2023. The influence of joint inclination angle and set number on stability of railway tunnel surrounding rock. Railway Investigation and Surveying, vol. 49, p. 48-53. http://doi.org/10.19630/j.cnki.tdkc.202302100001

[11] Suo C.F., Shi Y.D., Li J., 2013. Model test of effect of joint characteristics on stability of broken rock mass. Journal of Highway and Transportation Research and Development, vol. 30, p. 82-87. http://doi.org/10.3969/j.issn.1002-0268.2013.04.015

[12] Zhou J., Zhou Y., Chen L., et al, 2022. Influence of joint dip angle on deformation and instability mode of soft rock tunnel face. Subgrade Engineering, vol. 6, p. 196-200. http://doi.org/10.13379/j.issn.1003-8825.202205100

[13] Li J., Wu H.Q., Wang Y.J., et al, 2013. Analysis of the influence of joints characteristics and surrounding rock supporting on tunnel deformation. Construction Technology, vol. 42, p. 82-86. http://doi.org/10.7672/sgjs2013030082

[14] Zheng Y.C., Zhang W.S., Sun K.G., et al, 2020. Study on the stability of large-span tunnel by distinct element based strength reduction method. Modern Tunnelling Technology, vol. 57, p. 18-25. http://doi.org/10.13807/j.cnki.mtt.2020.01.00

[15] Tang R., An J.J., Xiang L., et al, 2019. Analysis of the impact of layered rock mass on stability of a highway tunnel. Modern Tunnelling Technology, vol. 56, p. 216-224. http://doi.org/10.13807/j.cnki.mtt.2019.S2.032

[16] Cui Z.D., Liu D.A., Wu, F.Q., et al, 2014. Influence of dip directions on the main deformation region of layered rock around tunnels. Bulletin of Engineering Geology and the Environment, vol. 73, p. 441-450. http://doi.org/10.1007/s10064-013-0511-6

[17] Wang L.X., Zhu Z.D., Zhu S., et al, 2023. A case study on tunnel excavation stability of columnar jointed rock masses with different dip angles in the Baihetan diversion tunnel. Symmetry, vol. 15, 1232. https://doi.org/10.3390/sym15061232

[18] Jiang, M.F., Feng, X.T., Zhao, J., et al, 2024. Time-dependent failure characteristics of natural jointed granite of deep tunnel under different dip angles conditions. Acta Geotechnica, vol. 19, p. 3075-3093. https://doi.org/10.1007/s11440-023-02201-y

[19] Jia P., Tang C.A., 2008. Numerical study on failure mechanism of tunnel in jointed rock mass. Tunnelling and Underground Space Technology, vol. 23, p. 500-507. https://doi.org/10.1016/j.tust.2013.07.017

[20] Jayakumar V., Visuvasam J.A., 2024. Numerical investigation on failure mechanism of tunnel lining with different fault dip angles and Geological Strength Index under geohazard of fault movement and seismic action. Geomatics Natural Hazards and Risk, vol. 15, 2363425. https://doi.org/10.1080/19475705.2024.2363425

[21] Xia Z.Y., Zhang C., Cao P., et al, 2023. Mechanical characteristics of large-section tunnel in soft rock based on various rock conditions and excavation footages. Stavební obzor-Civil Engineering Journal, vol. 32, p. 490-503. https://doi.org/10.14311/CEJ.2023.04.0037

[22] Zheng Y.R., Wang Y.F., Wang C., et al, 2011. Stability analysis and exploration of failure law of jointed rock tunnel-seminor on tunnel stability analysis. Chinese Journal of Underground Space and Engineering, vol. 7, p. 649-656. http://doi.org/10.3969/j.issn.1673-0836.2011.04.006

[23] Chen Q.C., Xu Q.F., Xie P.H., et al, 2023. Application of antisliding pile-key combination structure in gently inclined bedding rock slope with soft interlayer. Safety and Environmental Engineering, vol. 30, p. 131-140. http://doi.org/10.13578/j.cnki.issn.1671-1556.20221386

[24] Chai S.B., Hu J., Zhou Y.Q., et al, 2024. Influence of interface inclination angle of soft-hard strata on longitudinal mechanical properties of shield tunnel. China Railway Science, vol. 45, p. 135-146. http://doi.org/10.3969/j.issn.1001-4632.2024.05.13

[25] Pan H.W., Wu Y.C., Duan Y.X., et al, 2024. Optimization analysis of treatment scheme for metro tunnel base waterlogged collapsible loess formation. Urban Mass Transit, vol. 27, p. 261-265. http://doi.org/10.16037/j.1007-869x.2024.07.044

[26] National Railway Administration of the People's Republic of China, 2016. Code for Design of Railway Tunnels (TB 10003-2016). China Railway Publishing House, Beijing, p. 22.

[27] Song Z.P., Liu H.K., Zheng F., et al., 2023. Mechanical behavior and failure response characteristics of hard sandstones considering bedding dip angles. Coal Geology & Exploration, vol. 51, p. 167-175. http://doi.org/10.12363/issn.1001-1986.23.05.0227

Article no. 29

THE CIVIL ENGINEERING JOURNAL 3-2025

RESEARCH ON LONG-TERM STRAINS FOR BEAMS WRAPPED WITH SELF-COMPACTED CONCRETE

Hajdar Sadiku[1], Mazllum Kamberi[1], Hakim Abdelgader[2], Gazmend Nafezi [1], Durim Sadiku [1]

1. *University of Prishtina, Faculty of Civil Engineering, Department of Construction, Prishtina, str. Agim Ramadani, Kosovo; mazllum.ing@gmail.com, fin@uni-pr.edu*
2. *University of Tripoli, Faculty of Civil Engineering, Department of Construction, Tripoli, Libya; h.abdelgader@uot.edu.ly*

Received:	*29.04.2025*
Received in revised form:	*09.07.2025*
Accepted:	*07.08.2025*

ABSTRACT

Many objects built in the past do not meet the new construction standards and may be at risk from the action of special loads. Therefore, there is a need for their structural elements to be reinforced by increasing the moment of inertia, and with this, there is a need to increase the cross-sectional dimensions.

The realization of reinforcing structural elements, particularly columns and beams, can be easily achieved by increasing their dimensions using self-compacting concrete, which benefits from its excellent workability properties as fresh concrete, enabling easy filling of formworks.

In this case, the reinforced elements of reinforced concrete structures will be subjected to a new process of strains, whether elastic or more importantly, they are also subjected to strains in the long-term process such as shrinkage strains and creep strains.

For the analysis of strains in structural elements reinforced with self-compacting concrete both at the moment of load action and in the long-term process of load action, an experiment was carried out for a period of two years.

During this experiment, the mechanical and deformable characteristics of elements (laboratory samples and beams) from normal concrete and from self-compacting concrete were analysed. The research of these characteristics was carried out both at the time t0=40 days, of the load action, and in the long-term process up to the time t∞=400 days

This paper presents the results obtained for shrinkage strains and creep strains during the analysis of beams made of ordinary concrete, self-compacting concrete, as well as repaired beams, whose core is made of ordinary concrete and after hardening, at the age of 40 days they are wrapped with a layer of self-compacting concrete on three sides of the beam. Results for the modulus of elasticity, compressive strength, breaking toughness, and water permeability results obtained from laboratory sample testing will also be provided.

KEYWORDS

Self-Compaction concrete, Conventional concrete, Creep, Shrinkage, Strains

INTRODUCTION

Self-compacting concrete (SCC) in addition to aggregate, cement, water also contains special chemical additives such as new generation plasticizers called hyper plasticizers, which greatly reduce the water/cement ratio (W/C) as well as the special content of fly ash make self-compacting concrete special in its workability properties in the phase when the concrete is fresh. The higher content of granular aggregate affects the reduction of tensile strength, in particular reduces the modulus of elasticity and in this case also increases the deformable characteristics of concrete after hardening (shrinkage strains, creep strains, settlements, etc.) both in the short-term process and especially in the long-term process of load action.

One of the ways to ensure the stability of the mixture is to increase the content of binding materials such as fly ash. Another alternative is the use of chemical additives, such as viscosity modifying agents (VMA), which help maintain the stability of the mix and are particularly suitable for self-compacting concrete [1].

The long-term performance and durability of concrete structures depend not only on the composition of the mix, but also on the curing conditions during the very early stage, which plays a key role in the formation of the microstructure of the material [1].

The formation of cracks in the early hardening of concrete is a critical factor in the deterioration of structures, as it allows the penetration of aggressive agents and accelerates the corrosion of the reinforcement. The gradual development of damage, if not controlled, significantly reduces the stability and load-bearing capacity of the structure in the long-term process of load action. Drying shrinkage strains cause a reduction in the shear capacity due to the segregation of aggregate from the cement paste[2] .

Long-term strains generated by drying shrinkage and creep in reinforced concrete (RC) beams represent a significant problem and need to be accurately determined. The four main types of shrinkage are autogenous shrinkage (caused by self-drying during hydration of concrete), plastic shrinkage (caused by moisture loss from concrete before hardening), carbonation shrinkage (caused by chemical reactions between hydrated concrete and atmospheric CO_2), and drying shrinkage (as a result of long-term dehydration of concrete over a long period). Shrinkage and creep are essential for long-term serviceability [3].

Rehabilitation of structural concrete elements and their repair are important for their use not only today but also in a longer period of their use[4].

Proper repair of beams with self-compacting concrete improves some of the properties of the beams and in particular increases the stiffness and thus the rigidity of the beams, improves the appearance, limits water permeability to the maximum, closing the cracks protects the reinforcement from corrosion and will be more acceptable for environmental conditions[4].

For proper filling of the formwork of the repaired beams, we have used three-fraction self-compacting concrete since the thickness of the layer for wrapping the beams is small and the reinforcement bars and rods prevent proper distribution of the concrete throughout the length of the beam. In these cases, the self-compacting concrete must be pumped with a pressure pump or lightly spread through a rod.

The action of some dynamic loads leads to defects and then the appearance of cracks, subjecting concrete structures to a possible failure [5]. Self-compacting concrete fills the spaces where the old concrete meets the new and leaves no gaps inside the cut, therefore it is one of the most suitable materials for increasing the performance of beams in the case of repair [6].
The creep strains are very similar for the same maintenance conditions of beams made of self-compacting concrete and beams made of ordinary concrete[7].

In Kosovo, since 2008, the rehabilitation of structural elements with self-compacting concrete has begun. The reinforcement of the bridge piers in the Han i Elezit-Kaqanik segment was made with self-compacting concrete.

Self-compacting concrete has been used both in the renovation of some existing business buildings and in new buildings for the construction of basements where it has played the role of waterproof concrete in order to eliminate the use of special insulation.
In this paper, we aim to provide experimental results for some of the characteristics of concrete elements that have been made with self-compacting concrete, and which results have been compared with those made with ordinary concrete.

But the main goal is to provide an overview of the behaviour of reinforced concrete elements repaired with self-compacting concrete to short-term and long-term loads. It is important to understand the impact of the cooperation between the two types of concrete (SCC and OC) both in shrinkage strains and in creep strains.

The results presented in this paper will help civil engineering professionals, both in the design and construction phases, to apply new methods for the rehabilitation of damaged structural elements.

MATERIALS AND METHODS

Experimental program

Preparation of equipment - To carry out the experiment, it was necessary to prepare equipment in advance to carry out the load with which the beams that were investigated for

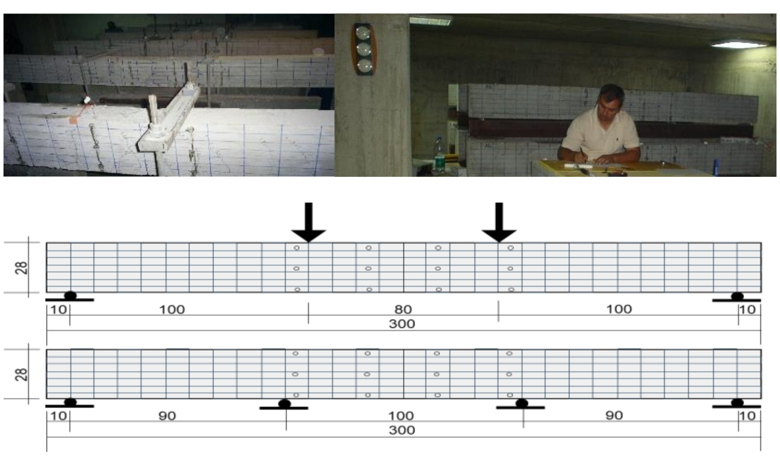

Fig. 1- Real appearance and schematic representation of beams treated in creep and shrinkage [11]

determining the creep strains were loaded. Supports with metal profiles and rods were made which were then loaded with concrete sides. This metal support was hung at two points on the beams where in this way the beam was loaded with two concentric gravitational forces. The beams were placed on concrete pillars with dimensions of 40x40cm. The beams that were used to carry out the research on shrinkage strains were placed on metal beams supported on four points with unhindered possibility for small displacements in the longitudinal direction. During the entire time, the temperature and relative humidity of the air were measured.

For the research of the creep coefficient, a device was prepared to realize the load which must be constant throughout the research process [1], [8], [9].

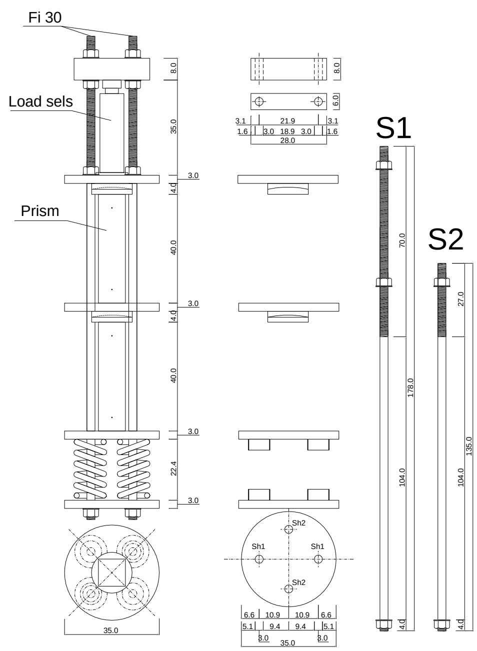

Fig. 2 - Equipment for the research of the creep coefficient [11]

The measurement of strains in the long-term process was carried out with a mechanical deform meter, while in the process of testing the beams at break in the short-term process, measuring tapes and a data logger were also used for direct reading of strains using the Watson bridge. The force was carried out with a hydraulic pump where the force was read in the data logger for reading the force.

The measurement of the size of cracks with a special microscope was carried out both in the long-term process and during the process of breaking the beams, and verification of new cracks and their distribution under the influence of increasing forces was also carried out.

DOI 10.14311/CEJ.2025.03.0029

Fig. 3 - Measurement and verification of cracks [11]

Measurement of the settlements with mechanical settlement gauge during testing in the short-time process and in the long-time process are shown in the figure 4.

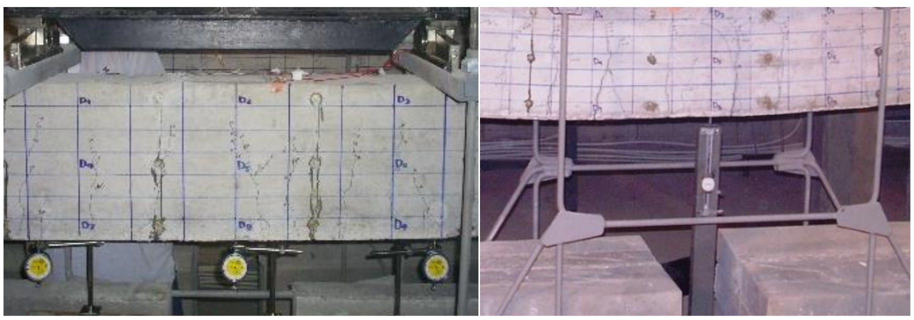

Fig. 4 - Measuring deflections [11]

Preparation of the room for the experiment

Considering the fact that the research of strains in the long-term process requires constant hydrometric conditions and temperature conditions, we were forced to prepare a space where the temperature throughout the experiment was constant (20+-20C) and the air humidity was also approximately constant (60-70%). The surface area of the room for the long-term research was S=150m^2.

But previously, for the preparation of the beams, a space of 500m^2 and a considerable number of people were used, both for the preparation of the samples and for the realization of the breaking tests [10].The process of concrete work and filling the samples - The concrete was worked in the experimental space where the mixing was carried out with a mixer with a capacity of 1m^3.

Two concrete mixtures were carried out, initially the ordinary concrete mixture was carried out, while after forty days the self-compacting concrete mixture was carried out. This was done so that the cores of the beams repaired from ordinary concrete would go through the hardening phase and then be covered with self-compacting concrete.

DOI 10.14311/CEJ.2025.03.0029

The used materials

Considering that self-compacted concrete has specific characteristics, the choice of materials is also of particular importance. The use of stone fly ash to homogenize the concrete mix as well as the application of special chemical admixtures to enable easy processing and placing of the concrete without vibration make the difference between ordinary concrete and self-compacting concrete [8].

The beams are made of concrete class C 30/37, to produce concrete, crouched aggregate divided into three fractions produced from limestone rocks is used. Maximum aggregate grain 16 mm, PC 45 15p USJE cement is used to produce ordinary concrete and self-compacting concrete, while to produce self-compacting concrete, a hyper plasticizer chemical additive (superfluid 21) is applied and stone fly ash from the same aggregate is used as powder. The beams are reinforced with steel reinforcement of B500B quality [12][13].

The concrete mix design for ordinary concrete and for self-compacting concrete are shown in Table 1.

Tab. 1 - Concrete mix design for ordinary concrete and for self-compacting concrete

	Ordinary concrete kg/m3	Self-compacting concrete kg/m3
Fraction (0-4)	710	750
Fraction (4-8)	430	470
Fraction (8-16)	735	473
Cement	325	320
Water	210	200
Stone powder	x	104
Admixture(hyperplasticizer)	x	3

Preparation of elements and testing methods

For determining the quality of concrete, a significant number of cylindrical, cubic and prismatic samples were prepared, through which the following were determined: compressive strength EN 12930-3[14], Flexural Strength EN 12930-5 [15], Tensile Splitting Strength 12930-6 [16], modulus of elasticity ASTM 469[17], waterproofing EN 12930-8[18] , sound conductivity, pore content, shrinkage EN 12930-16[19] and creep coefficient [20].

This paper also provides a comparison of the results of mechanical characteristics between regular concrete and self-compacting concrete [21].

Fig. 6 - Laboratory testing process of samples [11]

Compressive strength EN 12930-3

The compressive strength was determined on cubic samples with dimensions of 15x15x15cm. A digital hydraulic press was used for testing, where the speed of the load was 500 Kpa, and the sensitivity during testing of the sample was 5Mpa.

Tensile Splitting Strength 12930-6

Cubic samples were also used to determine the tensile Splitting Strength. For testing, a metal mechanism was used to transmit the linear force from the press to the sample and a hydraulic press, where in this case the speed of the load was 50Kpa, while the sensitivity for the tear strength was 0.5Mpa.

The secant modulus of elasticity was determined using cylindrical samples with a diameter of 150mm and a height of 300mm.

A metal mechanism was used to measure strains at three points and a deform meter with an accuracy of 0.001mm, where the sample was subjected to the loading-unloading process until two consecutive equal results were achieved.

A sample was previously tested to determine the compressive strength and a value of 40% of this result was used to load the samples during the elastic modulus testing for OC and SCC.

Water permeability EN 12930-8

To carry out the water permeability testing, cubic samples from OC and SCC with dimensions of 15x150x150mm were used, which were previously processed by removing the thin layer of cement past in the place where water will act at a pressure of 5bar for a period of 72 hours.

The determination of the depth of water penetration is determined after the sample is removed from the device for carrying out the action of water under pressure, is inserted into the press and divided into two parts by splitting the sample, where then with a metal ruler the distance from the end of the sample to the knee where the water has penetrated is measured.

Creep coefficient

Eurocode EN 1992-1-1 and ACI 209 provide methods for calculating and understanding the creep coefficient- To determine the coefficient of creep, prismatic samples of OC and SCC with dimensions 100x100x400mm and the special frame, which is presented in Figure 2, a deform meter with a measuring step of 300mm and an accuracy of 0.001mm was also used. References for measuring strains on the four sides of the prismatic samples were placed on the prism.

The creep coefficient testing process consists of two types of deformation measurements at the same time:

In the device where we have placed two prisms under the action of the load, the creep and shrinkage strains were measured together (creep & shrinkage), in order to know the result only from creep, we used three samples from the same concrete where we measured the shrinkage strains which we have subtracted from the previous result (creep & shrinkage-shrinkage) and thus we have only extracted the results from creep.

For testing self-compacted concrete in the fresh phase, the following methods were used: J ring, V funnel and U box with the test results [22]: J ring, h=7.4cm, d=59cm; V funnel, t1=8.2s, t2 =9.5 s; U box, h=37 mm. The j-ring and V-funnel testing is shown in Figure 11.

Fig. 3 - J-ring and V-funnel test [22]

To analyse the impact of short-term and long-term loads on concrete beams, eighteen concrete beams with a cross-section of (15x28) cm and a length of 3m were made. Three series of beams are made with two types of concrete, with ordinary concrete and with self-compacting concrete. The beams are reinforced with B 500B reinforcement, placed two Φ12 bars in the lower and two bars Φ 8 on the top of the cross-section, Figure 7.

The cooperation of normal concrete with self-compacting concrete is a very important characteristic for the rehabilitation of concrete elements. To investigate this cooperation, beams with ordinary concrete cores with cross-section dimensions of (7x20) cm were made, the same after reinforcement were wrapped with self-compacting concrete[13][20].

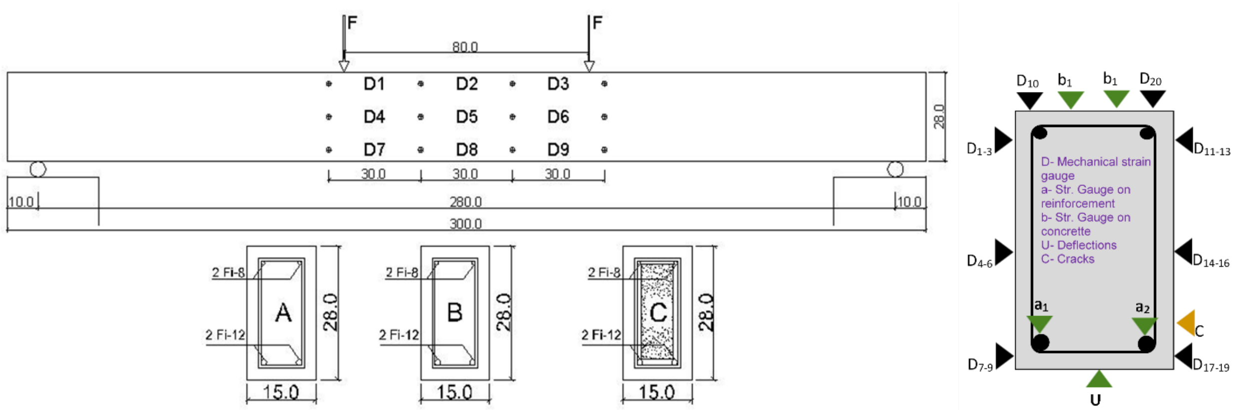

Fig. 7 - Beam, beam cross-sections and positioning of measuring points [11]

Applying strain gauge to concrete and reinforcement as well as measuring strains with a mechanical strain gauge and measuring of porosity are presented in Figure 8.

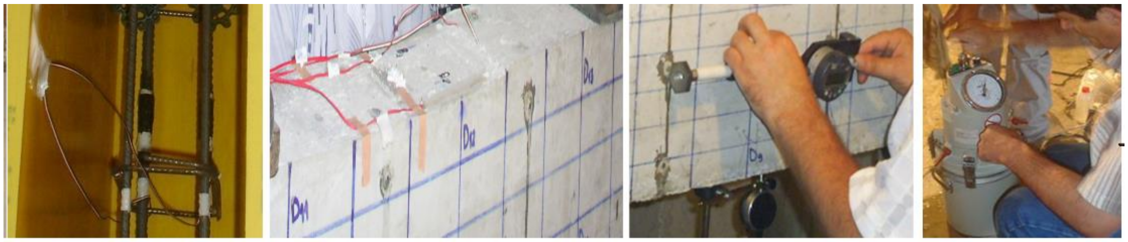

Fig. 8 - Application of measuring tapes, mechanical deformation and porosity measurement [11]

RESULTS

The test results for compressive strength, fracture toughness and modulus of elasticity are presented through the diagrams shown in Figure 9. These results were obtained from testing samples from OC and SCC under completely identical conditions.

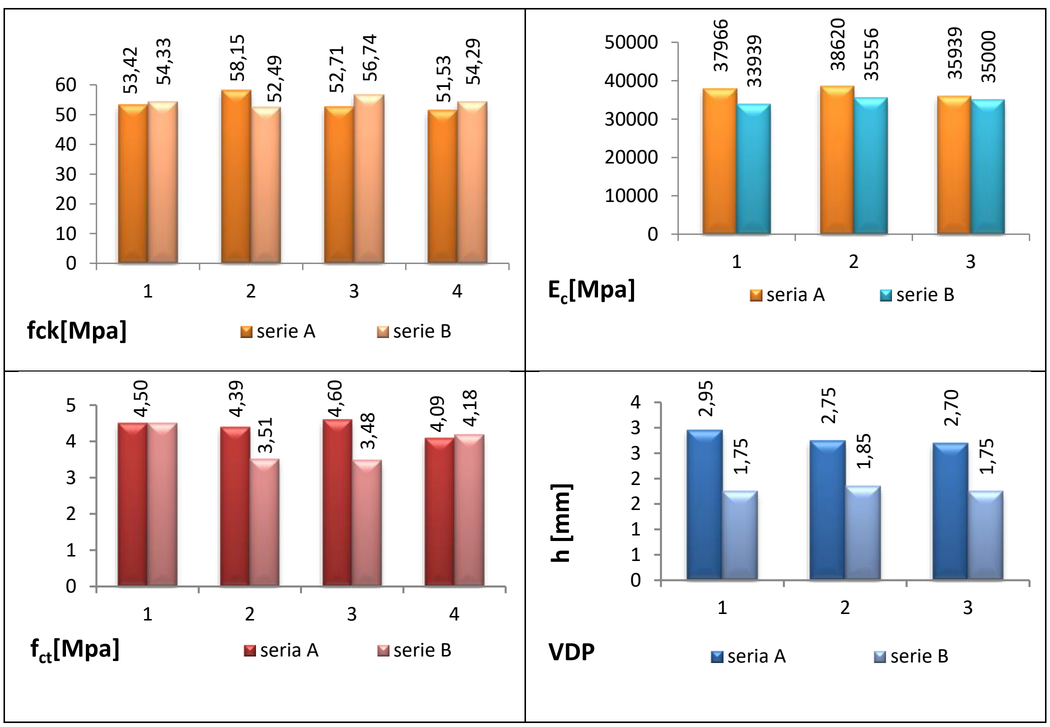

Fig. 9 - Comparison of the: Compressive strength(fck), Modulus of elasticity(E), Tensile Splitting Strength and Flexural Strength (fct), waterproofing (VDP)

The results for the creep coefficient for the OC samples, for the SCC samples and the calculated results according to Eurocode 2 (EC-2) are presented graphically in Figure 10.

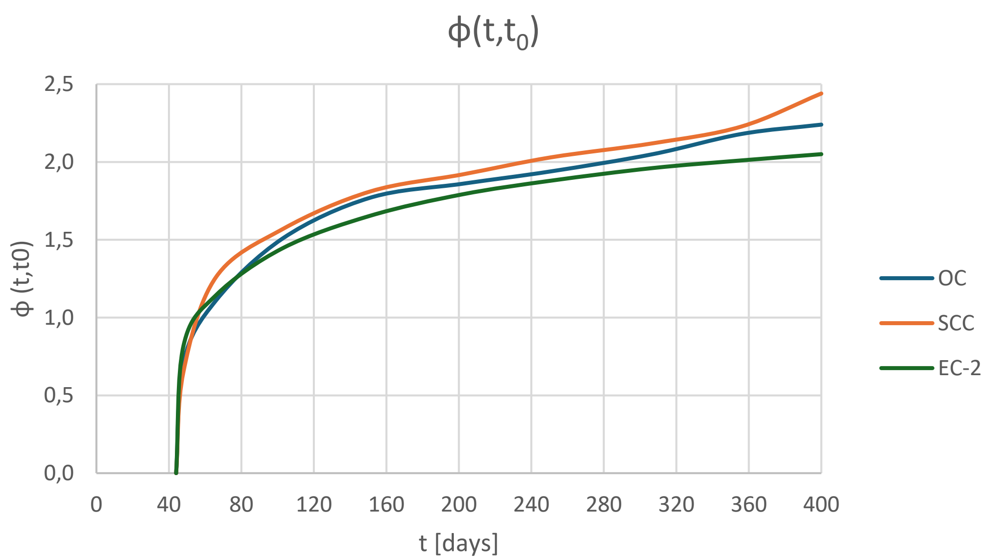

Fig. 10 - Creep coefficient results (OC, SCC, EC-2)

All the results for strains in the long-term process (shrinkage strains and creep strains) will be presented in graphically form for beams of series A, B and C.

During the experiment, measurements for shrinkage strains and creep strains were measured at twenty points, but we will present the diagrams of concrete strains in the compressed zone and in the tensile zone between the beams [23].

To analyse the shrinkage strains for ordinary concrete beams, AI-2 and AII-2 beams were analysed, for self-compacting concrete beams, B-3 and B-4 beams were analysed, while for beams covered with self-compacting concrete, there were treated beams C-3 and C-4.

Shrinkage strains result for ordinary concrete beams (A-series beams), shrinkage strains results for self-compacting concrete beams (B-series beams) and shrinkage strains results for self-compacting concrete clad beams (beams of series C) as well as the comparison of these results are shown in Fig. 11.

DOI 10.14311/CEJ.2025.03.0029

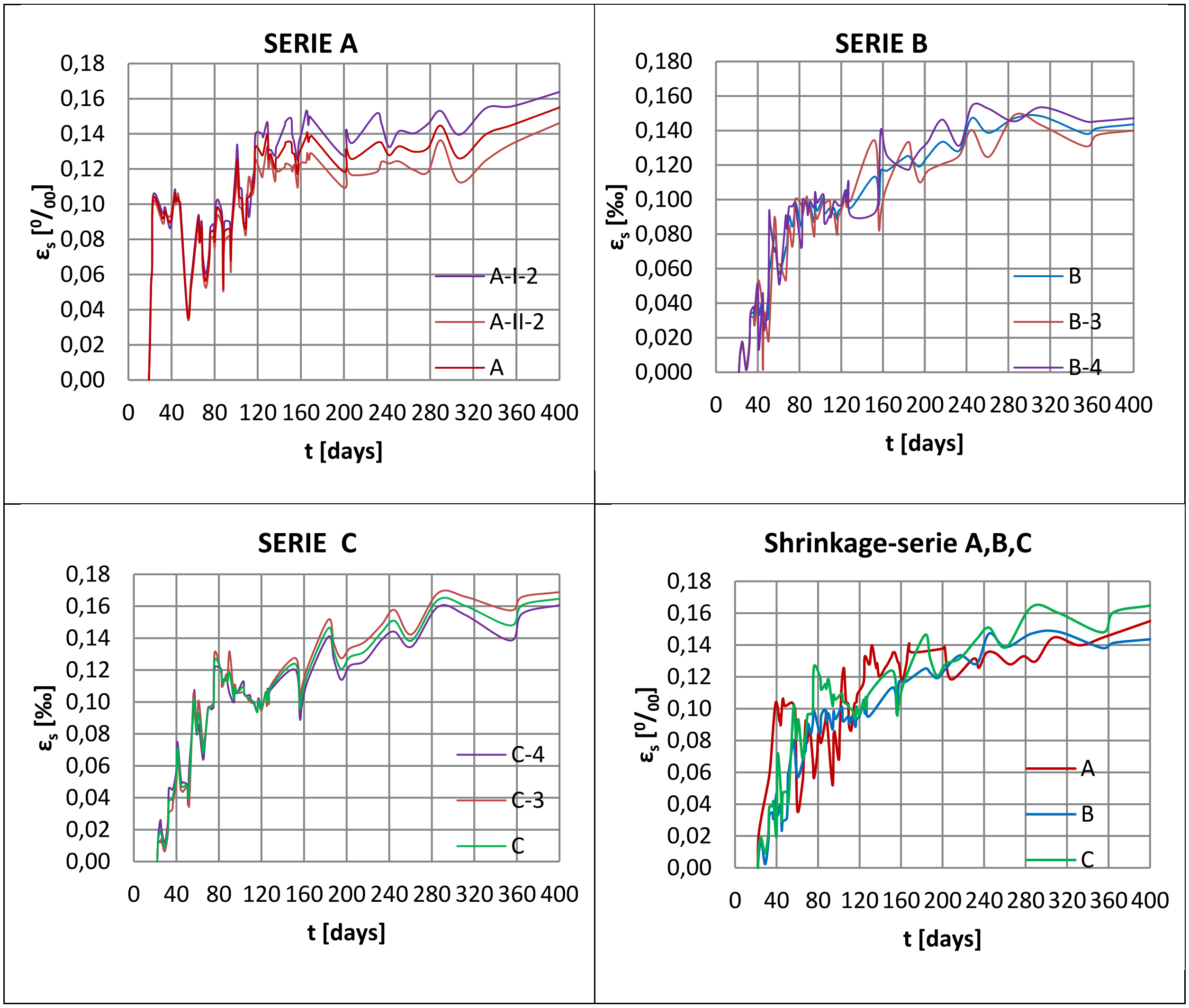

Fig. 11 - The results of shrinkage strains and their comparison for beams from ordinary concrete (series A), for beams from self-compacting concrete (series B) and beams covered with self-compacting concrete (series C).

From the diagrams we see that movement results in three months are more pronounced but after that time they begin to be stabilized. Finally note that the largest strain of shrinkage has in the repaired beams (series C). At time t = 400 days difference between the normally concrete beams and self-compacted concrete beams results is 7% (A-B), A-C is 14% while for self-compacted concrete beams and repaired beams (BC) results differ for 6%.

Creep strains on compression and tensile zone of the beams and the neutral axis position are presented in Figure 12. These diagrams are presented for different time, starting from time t=40 day until the time t=400 days.

DOI 10.14311/CEJ.2025.03.0029

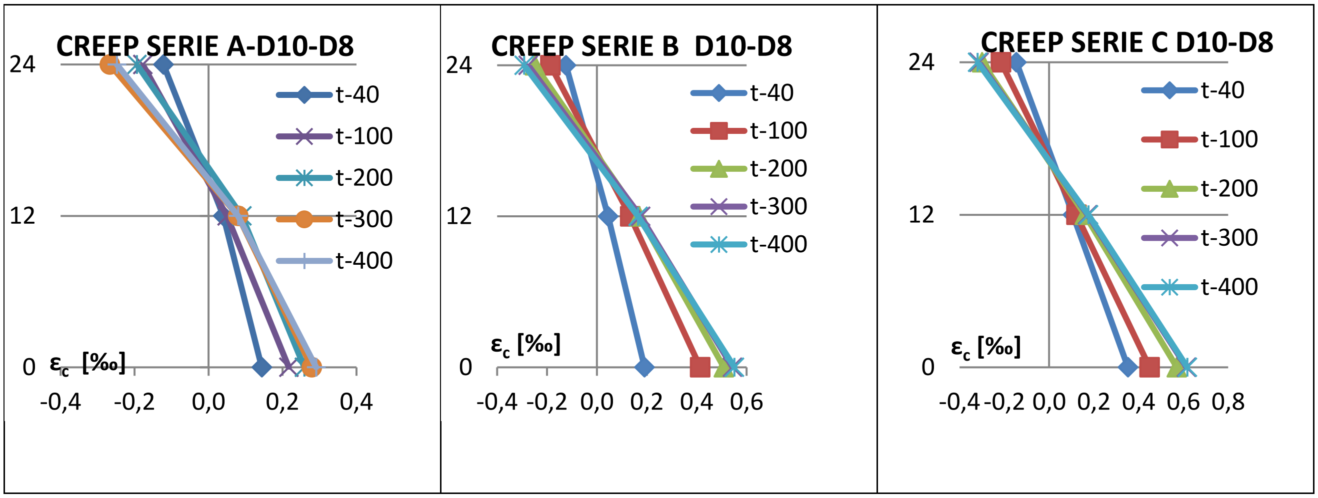

Fig. 12 - Creep strains on compression and tensile zone of the beams and the neutral axis

The results of the creep strains together with the shrinkage strains (C+S) and the results of the creep strains (C) in the compression zone (D-10) and in the tensile zone (D-8) for ordinary concrete beams (series A), self-compacting concrete beams (series B) and beams covered with self-compacting concrete (series C) are shown in Figure 13.

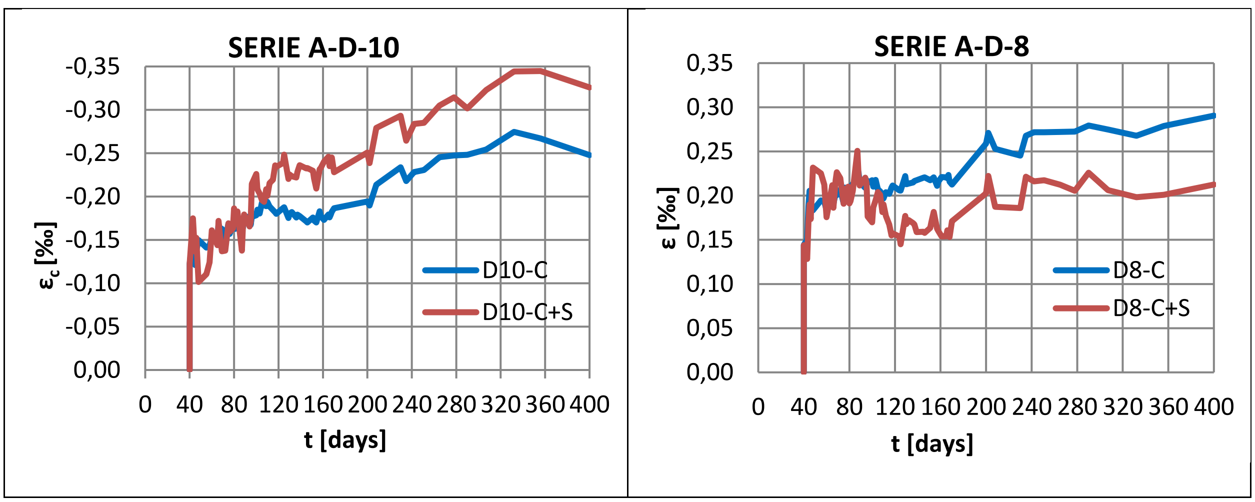

DOI 10.14311/CEJ.2025.03.0029

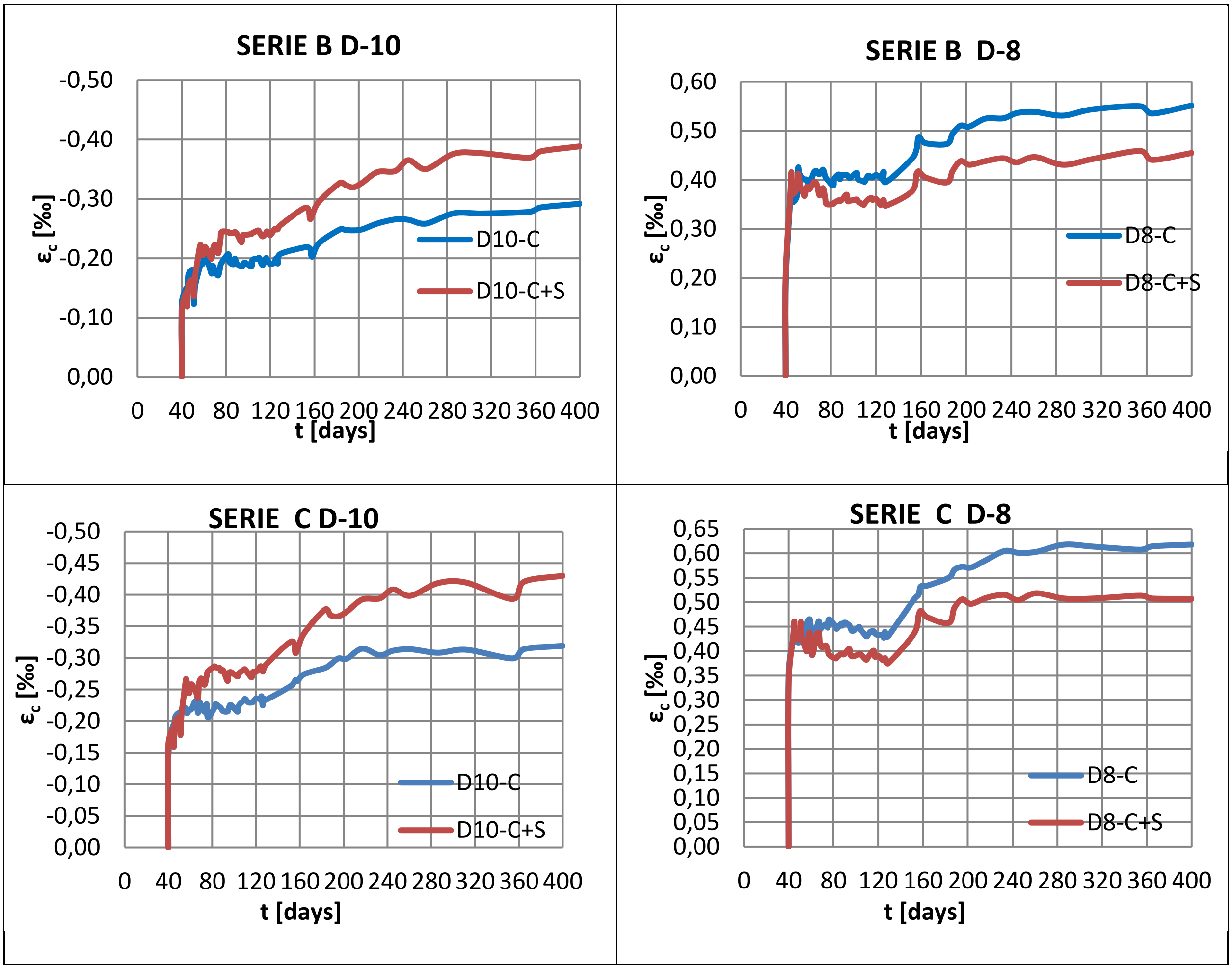

Fig. 13 - The results of the creep strains together with the shrinkage strains (C+S) and the results of the creep strains (C) in the compression zone (D-10) and in the tension zone (D-8).

Comparison of the results of creep strains in the compression zone and in the tensile zone of beams from ordinary concrete (series A), beams from self-compacting concrete (series B) and beams covered with self-compacting concrete (series C) as and neutral axis position are shown in Figure 14.

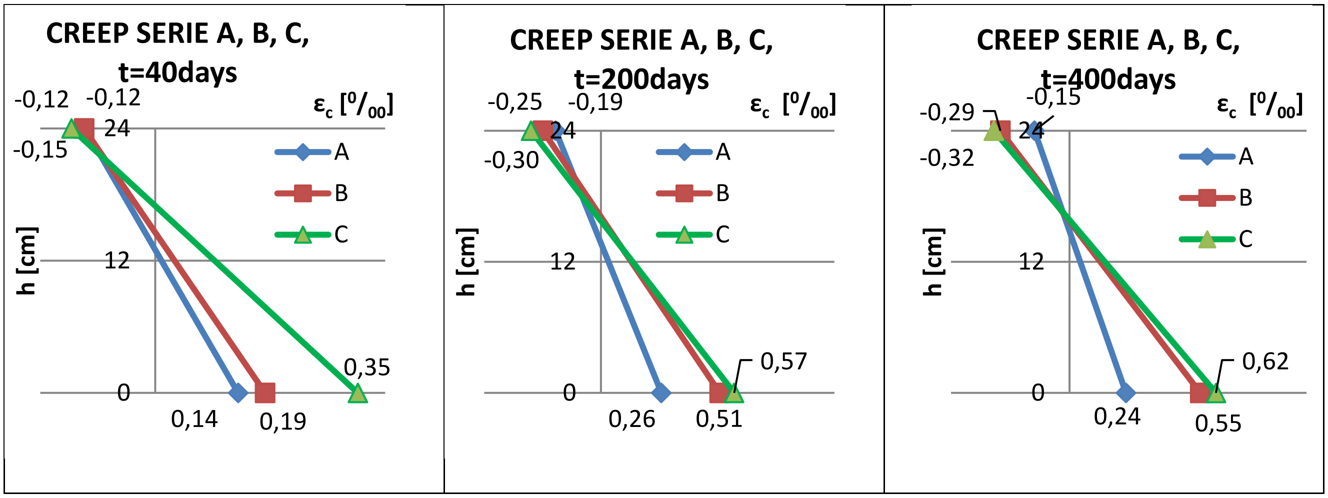

Fig. 14 - Comparison of the results of creep strains in the compressive zone and in the tensile zone for the three types of beams.

In Figure 15 there are presented comparisons of results of creep strains together with shrinkage strains (C+S) and results of creep strains (C) for beams of series A, B and C on compression (D-10) zone and on tensile zone (D-8).

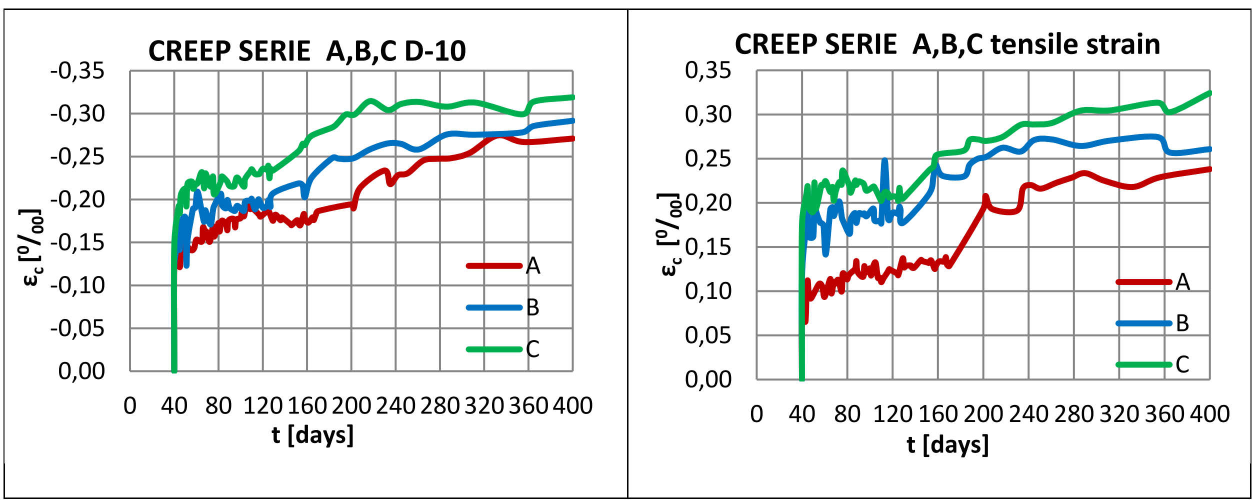

Fig. 15 - Comparison of results of creep strains together with shrinkage strains (C+S) and results of creep strains (C) for beams of series A, B and C.

After time t = 400 day of creep strain in concrete in compression zone for beams of ordinary concrete (series A), beams from self-compacting concrete (series B) differ for 7.2%, strain in tensile zone differ for 47%. For beams of ordinary concrete and beams covered with self-compacting concrete (series C) strains in compression zone differ for 13.7%, strain in tensile zone differ for 53%. The beams from self-compacting concrete (series B) and beams covered with self-compacting concrete (series C) series have these differences in results: Strain in compression zone differ by 7%, strain in tensile zone differ for 10.7% [9] [31].

CONCLUSION

The speed of sound permeability in self-compacting concrete samples is lower than in regular concrete samples.

Self-compacting concrete has better waterproofing results than ordinary concrete.

Analysing the results of testing samples in splitting tensile strength and testing samples in bending, we conclude that self-compacting concrete has lower tensile strength results than ordinary concrete.

From the comparison of experimental results for the modulus of elasticity, we conclude that the results of samples from self-compacting concrete have lower results compared to conventional concrete.

Comparing the diagrams of the results of the coefficient of creep, we notice the same phenomenon as in the case of the results of the tensile strength and the results of the modulus of elasticity, where the samples from self-compacting concrete have a higher coefficient of creep, which is related to the use of aggregates and fly ash for the realization of the self-compacting concrete mix, which content reduces the properties of the tensile strength of concrete. We can say that the experimental results are close to the theoretical results calculated with EC-2.

Strains from shrinkage in self-compacting concrete beams up to the first six months are greater, but with time they approximate, after 300 days, according to the experiment, strains from shrinkage in beams from ordinary concrete are greater. This phenomenon can be explained by the fact of the better cooperation of the reinforcement with the self-compacting concrete (better adhesion).

The results of strains from shrinkage in beams from self-compacting concrete up to the first six months are greater than in beams from ordinary concrete, but over time they approximate, after 300 days according to the experiment the results of strains from shrinkage in beams from ordinary concrete are bigger. This phenomenon can be explained by the fact of the better cooperation of the reinforcement with the self-compacting concrete (better adhesion).

The difference in the results of shrinkage strains for beams from ordinary concrete, beams from self-compacting concrete and for repaired beams is small and after the time t = 400 days the difference is about 7%.

REFERENCES

[1] K. Kovler. Drying Creep of Concrete in terms of Age-Adjusted efective moduls method. https://tudresden.de/bu/bauingenieurwesen/ifb/ressourcen/dateien/studium/BoxAccess/BoxAccessReadings/Creep-Kovler.pdf?lang=en

[2] Yang Song, Qier Wu. Concrete shrinkage and creep under drying_wetting cycles. DOI: 10.1016/j.cemconres.2020.106308

[3] I. Faridmehr, M. Shariq, V. Plevris, and N. Aalimahmoody. Novel hybrid informational model for predicting the creep and shrinkage deflection of reinforced concrete beams containing GGBFS. Neural Comput Appl, vol. 34, no. 15, pp. 13107–13123, Aug. 2022, DOI: 10.1007/s00521-022-07150-3.

[4] M. H. Kabir, M. Z. Jumaat, and M. Obaydullah. A Review of the Repair of Reinforced Concrete Beams, 2006. https://www.researchgate.net/publication/234083515_A_review_of_the_repair_of_reinforced_concrete_beams/citations

[5] Z. Jin. Strategies to improve the impact resistance of self-compacting concrete (SCC) after freeze-thaw cycles Author links open overlay panel.
DOI: 10.1016/j.jobe.2023.105854Get.
[6] J. N. Kansara. Experimental Investigations on Self Compactin Concrete using polymeric waste. https://www.researchgate.net/publication/374478031
[7] X. J. Liu, Z. W. Yu, and L. Z. Jiang. Long term behavior of self-compacting reinforced concrete beams," Journal of Central South University of Technology (English Edition), vol. 15, no. 3, pp. 423–428, Jun. 2008, DOI: 10.1007/s11771-008-0079-7.
[8] Y. L. Bhirud and K. K. Sangle. Comparison of Shrinkage, Creep and Elastic Shortening of VMA and Powder Type Self-Compacting Concrete and Normal Vibrated Concrete. Open Journal of Civil Engineering, vol. 07, no. 01, pp. 130–140, 2017. DOI:10.4236/ojce.2017.71008.
[9] European Commission. *EUROCODE 2 – Worked Examples*. Available online: https://eurocodes.jrc.ec.europa.eu/showpublication.php?id=124 (accessed on 10 July 2025).
[10] H. Sadiku and D. Sadiku. Strains in the short-term process on Self-Compacting Concrete for repaired beams. International Journal of Advanced Research in Engineering and Technology (IJARET), vol. 11, no. 6, pp. 1–9, 2020, DOI:10.34218/IJARET.11.6.2020.001.
[11] Sadiku, H. E. (2010). Determination of impact load of self-compacting concrete elements in long-term process (Doctoral dissertation). University of Skopje, Skopje, Macedonia.
[12] Prakash, N. Rational Mixture Design of Self-Compacting Concrete. Ph.D. Thesis, Division of Building Technology and Construction Management (Doctoral dissertation). Indian institute of Technology Madras
[13] European Committee for Standardization (CEN). *EN 206-1: Concrete – Part 1: Specification, performance, production and conformity*. Brussels, 2000.
[14] SIST. SIST EN 12390-3:2019 - Testing of Concrete: Part 3: Compressive Strength of Test Specimens. Standards Institution of the Republic of Slovenia, 2019.
[15] SIST EN 12390-3:2019. *Testing hardened concrete – Part 3: Compressive strength of test specimens*. Slovenian Institute for Standardization, Ljubljana, 2019.
[16] SIST EN 12390-6:2010. *Testing hardened concrete – Part 6: Tensile splitting strength of test specimens*. Slovenian Institute for Standardization, Ljubljana, 2010.
[17] ASTM C469/C469M-14. *Standard Test Method for Static Modulus of Elasticity and Poisson's Ratio of Concrete in Compression*. ASTM International, West Conshohocken, PA, USA, 2014. Available online: https://www.astm.org (accessed on 10 July 2025).
[18] SIST EN 12390-8:2019. *Testing hardened concrete – Part 8: Depth of penetration of water under pressure*. Slovenian Institute for Standardization, Ljubljana, 2019.
[19] SIST EN 12390-16:2019. *Testing hardened concrete – Part 16: Determination of the shrinkage of concrete*. Slovenian Institute for Standardization, Ljubljana, 2019.
[20] SIST EN 12390-1:2001. *Testing hardened concrete – Part 1: Shape, dimensions and other requirements for specimens and moulds*. Slovenian Institute for Standardization, Ljubljana, 2001.
[21] T. Y. Lo, P. W. C. Tang, H. Z. Cui, and A. Nadeem. Comparison of workability and mechanical properties of self-compacting lightweight concrete and normal self-compacting concrete. Materials Research Innovations, vol. 11, no. 1, pp. 16–17, Mar. 2007, DOI: 10.1179/143307507X196239.
[22] EFNARC. *The European Guidelines for Self-Compacting Concrete: Specification, Production and Use*. European Federation of National Associations Representing for Concrete, May 2005. Available online: https://www.efnarc.org/pdf/SCCGuidelinesMay2005.pdf (accessed on 10 July 2025).

[23] H. E. Sadiku, E. Gashi, and M. Misini. Crack Calculation of Beams from Self-Compacted Concrete," International Journal of Advanced Engineering Research and Science, vol. 4, no. 5, pp. 161–166, 2017, DOI: 10.22161/ijaers.4.5.25.

Article no. 30

THE CIVIL ENGINEERING JOURNAL 3-2025

CONSTRUCTION PROCESS ANALYSIS OF THE COMBINATION SYSTEM BRIDGE OF CABLE-STAYED BRIDGE AND SHAPED ARCH BRIDGE

Jianwei Li, Hongjian Lu and Wentao Xu

Puyang Institute of Technology, Henan University, West Section of Yellow River Road, Puyang, Henan Province, China; pygxyljw@163.com

Received: *30.01.2025*
Received in revised form: *14.07.2025*
Accepted: *30.08.2025*

ABSTRACT

The combination system bridges of cable-stayed and shaped arch bridges feature innovative structures and complex force distributions, necessitating intricate construction processes. Monitoring these processes ensures that the bridge's stress state aligns with designed internal forces. Measured stress values on the main girder's edges align with theoretical trends but are slightly lower. Throughout construction, the middle span experiences compression, with maximum stresses of -5.1 MPa on both edges. Full support during construction minimizes the impact of stay cable and derrick tension on main girder stress. After support removal, compressive stress increases on the upper edge and decreases on the lower. The tower's elevation is slightly above design, aiding in reducing prestress loss and deflection in later stages. At 16.5 m above the bridge girder, the tower's left side experiences tension and the right compression, with a tensile stress of only 1.0 MPa, indicating sound design and effective construction control.

KEYWORDS

Combination system bridges of cable-stayed bridge and shaped arch bridge, Construction monitoring, Stress, Elevation

INTRODUCTION

The primary load-bearing components of a cable-stayed bridge comprise the stay cables, bridge tower, and stiffened girder [1]. During the early 20th century, significant advancements in the development, refinement, and manufacturing of high-strength, high-elastic steel wire, along with its corresponding anchor system, combined with enhancements in orthotropic steel deck panels, fuelled the rapid evolution of cable-stayed bridges [2,3]. However, as the spans of cable-stayed bridges have widened, ensuring the stability of the cantilever section of the stiffened girder prior to closure has grown increasingly complex. Notably, the axial force within the stiffened girder has surged, leading to an elevated proportion of dead weight. Consequently, the height of the bridge tower has increased, and the sag effect of the stay cables has become more pronounced [4].

The arch bridge, as one of the foundational types of bridges, boasts a historical legacy stretching over 3,000 years. Over this extended period, continuous innovations in construction materials, technology, and design theory have evolved arch bridges from ancient stone structures dating back to pre-Christian times, through the concrete and simple steel arch bridges of the 19th century, to the advanced truss arch and concrete-filled steel tube (CFST) arch bridges of the 20th century [5-7]. Presently, significant breakthroughs have been achieved in both the span and structural configurations of arch bridges. However, as spans increase, so do the dead loads of traditional arch bridges, thereby escalating the challenges associated with cable construction. Additionally, CFST arch bridges face issues such as susceptibility to corrosion and void formation within the concrete fill. Steel arch bridges, on the other hand, are marked by high construction costs, substantial maintenance expenses, and prominent stability concerns [8-10].

Cable-stayed bridges and arch bridges are currently utilized extensively worldwide; however, their inherent limitations hinder further advancements in bridge span capabilities [11-14]. In recent years, due to the escalating demand for aesthetic appeal in bridge design, the engineering community has proposed a hybrid system that combines cable-stayed and shaped arch bridges. This innovative bridge type capitalizes on the strengths of both cable-stayed and arch bridges while compensating for their respective shortcomings [15,16].

The composite system bridge not only enhances the spanning capacity and structural rigidity but also boasts a more visually appealing design. It improves the stability of the bridge structure, enhances safety during construction and operation, and reduces the height of the bridge tower. This bridge exhibits exceptional cooperative performance, mitigating tensile forces in stay cables or slings, facilitating a more uniform distribution of internal forces, minimizing local stresses, and offering superior structural performance along with substantial economic benefits [17-20].

The construction control technology of cable-stayed bridge, arch bridge, suspension bridge and continuous beam bridge has developed rapidly in China, but the research on the construction control of cable-stayed arch cooperative system bridge is relatively few, and the development of construction control is not very mature. On the basis of previous studies, this paper adopts adaptive control method to control the bridge construction.

PROJECT OVERVIEW

A combination system bridge of cable-stayed bridge and shaped arch bridge, with span arrangement of 40 m+90.5 m. The carriageway has a 1.5% transverse slope in both directions, and the sidewalk has a 1% transverse slope in one direction (inward). The main beam is a prestressed concrete cast-in-place box beam with a height of 2.7 m~3.8 m. The tower has a concrete section and is 59.5 m above the bridge girder. The distance of the stay cables is 8.5m, and there are 8 pairs of stay cables. The two arch ribs are constructed using a steel box structure, with concrete being poured only at the arch foot. The distance of the sling is 4.25 m, and there are 38 slings in the whole bridge. The bridge layout diagram is shown in Figure 1.

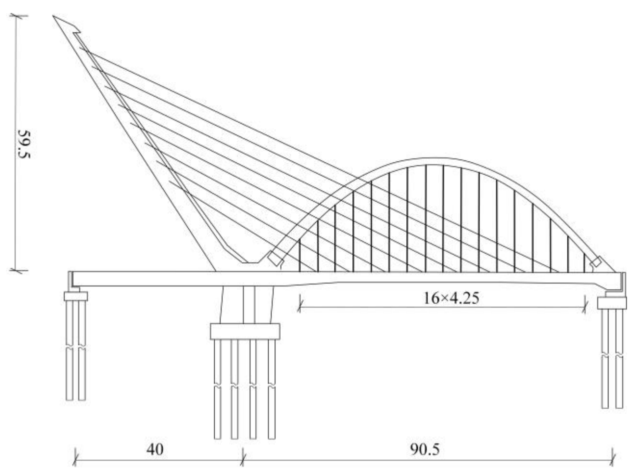

Fig.1- Schematic diagram of bridge layout （Unite: m）

DOI 10.14311/CEJ.2025.03.0030

Main girder

The main girder consists of a prestressed concrete cast-in-place box beam with a height of 2.7 m. Within a range of 21 m, the top of the pier transitions from 2.7 m in height on the left and right sides to 3.8 m. The main girder is provided with an end beam at 0# abutment with a width of 1.5 m. The top of 1# pier is provided with a middle beam, which is a box-type structure with a total width of 16.4 m, a middle web width of 3 m, and a web width of 0.8 m on both sides. An end beam is set at the 2# abutment. The beam retains its box-type structure, featuring an overall width of 5.5 m, a web width of 0.7 m, and a girder height of 3.8 m. A cross-sectional view of the bridge is depicted in Figure 2.

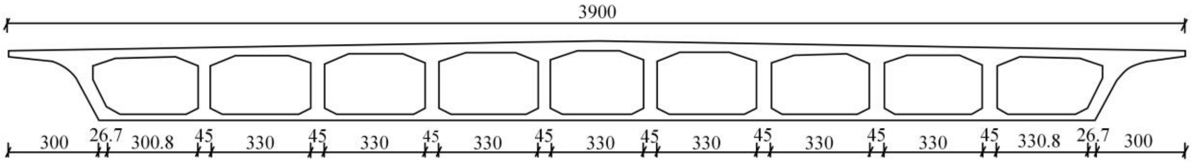

Fig. 2 - Cross section of the bridge (cm)

Tower

The bridge tower is constructed from reinforced concrete utilizing C50 concrete material. The portion of the tower situated above the bridge girder stands at a height of 59.5 m, with a horizontal inclination angle of 56° and a rear inclination angle of 34°. The tower section is rectangular in shape, featuring a transverse width of 3.5 m. The longitudinal width tapers from wider at the base to narrower at the top, with the longitudinal width at the tower top measuring 2.2 m. The base of the tower is widened to 6 m and is integrated with the main beam, arch, and pier for added stability.

Arch rib

The arch rib is constructed as a steel box structure, comprising two separate arch ribs, with concrete poured only in the vicinity of the arch foot. The span of each arch rib measures 84 m, and the ratio of the rise (vector) to the span is 1/3. Both ends of the arch rib feature concrete arch feet that are integrated with the main girder, tower, and pier. The arch rib extends deeply into the length of the concrete arch foot, and the interface between the arch foot and the concrete is connected using a pressure plate. To ensure seamless force transmission within the structure, the pressure plate is designed with a thickness of 60 mm.

Arch rib transverse wind bracing

Transverse steel arch rib is provided with 3 wind braces, wind braces into a "K" shape. The section forms of each main pole and strut are square. The main rod section size of the first two wind bracings is 60 mm×60 mm, and the section thickness is 10mm. The section size of the main rod of the third wind bracing is 80 mm × 80 mm, and the section thickness is 16mm. The section size of the strut of the wind bracing is 40 mm×40 mm, and the section thickness is 10mm.

Cable and sling

A total of 8 cables are arranged longitude wise, and the cable layout spacing is 8.5m. They are stretched on the tower and anchored on the girder. A total of 19 slings are arranged longitudinally in the arch rib slings, and the arrangement distance of the slings is 4.25 m. The slings are stretched on the bottom plate of the box girder, and the upper anchorage point is arranged outside the arch rib of the steel box with ear plates. Both the cable and the boom are made of steel strand cables, and the standard tensile strength is 1860MPa. The cable specifications are GJ15-25 and GJ15-31, which are tensioned on the tower and anchored on the girder. The suspender specifications are GJ15-12, GJ15-17 and GJ15-19, which are stretched on the bottom plate of the box girder, and the upper anchorage point is arranged on the outer side of the arch rib of the steel box with ear plates.

BRIDGE CONSTRUCTION PROCESS AND SIMULATION

Construction process

The construction process of cable-stayed arch bridge is mainly divided into substructure construction, main girder construction, cable tower construction and stay cable tension, arch rib construction and suspender tension.

Main girder construction

The main girder was poured for the full support. The support was set up and pre-pressed to eliminate the inelastic compression of the support. The main concrete beam is poured in layers, the bottom plate is poured first, then the web is poured, and the roof is poured finally. The concrete parts of the two arch feet were poured together with the main beams.

Tower construction and cable tensioning

The portion of the tower situated above the bridge girder reaches a height of 59.5 m. The bridge tower boasts a tilt angle of 34°, and its cross-section is solid, with a transverse width of 3.5 m. The longitudinal width tapers from wider at the base to narrower at the top. The cable tower section below the main beam is poured together with the side pier. The cable tower section above the main beam is divided into two sections from the bottom up: rectangular solid prestressed section B and cable section A with large inclination rectangular section. The section A is divided into A1~A16 sections every 4m along the direction of the cable tower. Section B (0 m~6.6 m above the bridge girder) adopts the cast-in-place construction technology, section A1~A3 (6.6 m~20 m above the bridge girder) adopts the inverted mold construction method, and A4~A16 (20 m~59.5 m) adopts the inverted mold construction technology, as shown in Figures 3 and 4.

The cable-free area of the bridge tower is constructed by cast-in-place construction with supports, while the cable-supported area is constructed with climbing formwork. During the construction of the climbing formwork, when the bridge tower sections are anchored by the tension cables, the tension cables are initially tensioned to ensure that the initial tension force of the tension cables can balance the weight of the bridge tower.

All the sections of the tower are divided horizontally, and the construction phase is divided as shown in Figure 5. After the construction of the cable tower in section A6, the initial tension of the cable S01 is started. Then every construction of 1 to 2 sections of the tower will be initially stretched a cable. The cable is tensioned three times. After the tower is completed and the initial tensioning of the cable is completed, the cable is tensioned a third time.

Fig. 3 - Cable tower and arch rib support

Fig. 4- Tower turning mold construction

DOI 10.14311/CEJ.2025.03.0030

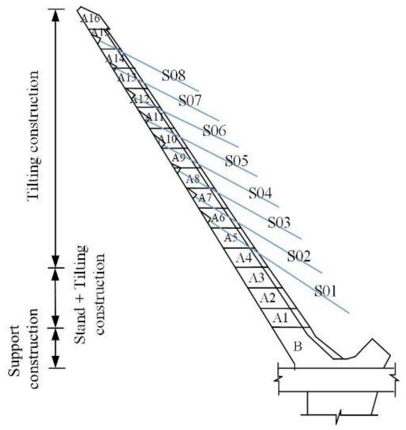

Fig.5 - Schematic diagram of tower construction phase division

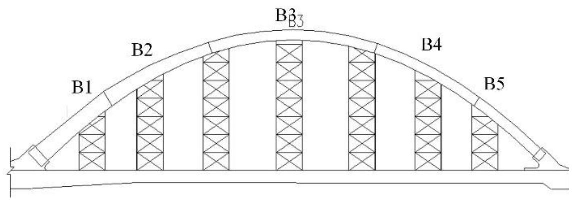

Fig.6 - Segment division of arch rib and support layout diagram

Arch rib construction and sling tension

Concrete arch foot is poured (poured together with the main girder concrete) and steel box arch is embedded in the arch foot section. Install the boom, stretch the boom in sections, and the tension sequence is as follows: D5, D9, D13, D8, D10, D4, D14, D1~D3, D6, D7, D11, D12 and D15~D17.

Construction simulation

The spatial model of the cable-stayed arch bridge was established by using Midas/Civil finite element software. The construction state of cable-stayed arch bridge is simulated, and the results of calculation and analysis are used to guide the construction control. The structure of the main bridge is divided into a spatial beam lattice system by static calculation. Beam elements are utilized for the main girder, main tower, and arch rib, while truss elements are employed for the stay cables and suspenders. The piers, towers, beams and arches are consolidated together, and the bottom of the piers is consolidated and constrained. Stay cables share nodes with towers and beams, and hangers share nodes with arches and beams. A diagram illustrating the structural dispersion is depicted in Figure 7.

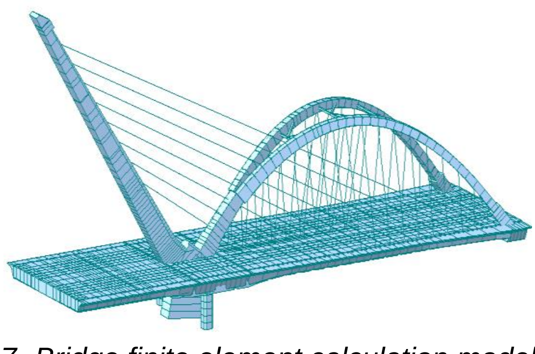

Fig. 7- Bridge finite element calculation model

BRIDGE CONSTRUCTION CONTROL CONTENT

The construction monitoring of cable-stayed arch bridge mainly adopts the adaptive control method, and the correction end point control method is adopted in some sections. According to the principle of controlling the linear shape and cable force value of the main girder, tower and arch rib, the stress control of the main girder, arch rib and tower is supplemented, the control section of the whole bridge is comprehensively monitored. The stress state of bridge structure in each construction

DOI 10.14311/CEJ.2025.03.0030

process should be mastered, and the stress, linear shape, displacement and reaction of each control part in each construction stage should be strictly controlled to ensure the structural safety in the construction process.

Structural stress and temperature field monitoring

The stress control section should be identified as the most disadvantageous (the most critical or disadvantageous point) of the main girder, crossbar beam, tower, arch rib, and cross brace during each construction stage or upon completion of the bridge. The precise arrangement of the monitoring sections is illustrated in Figure 8.

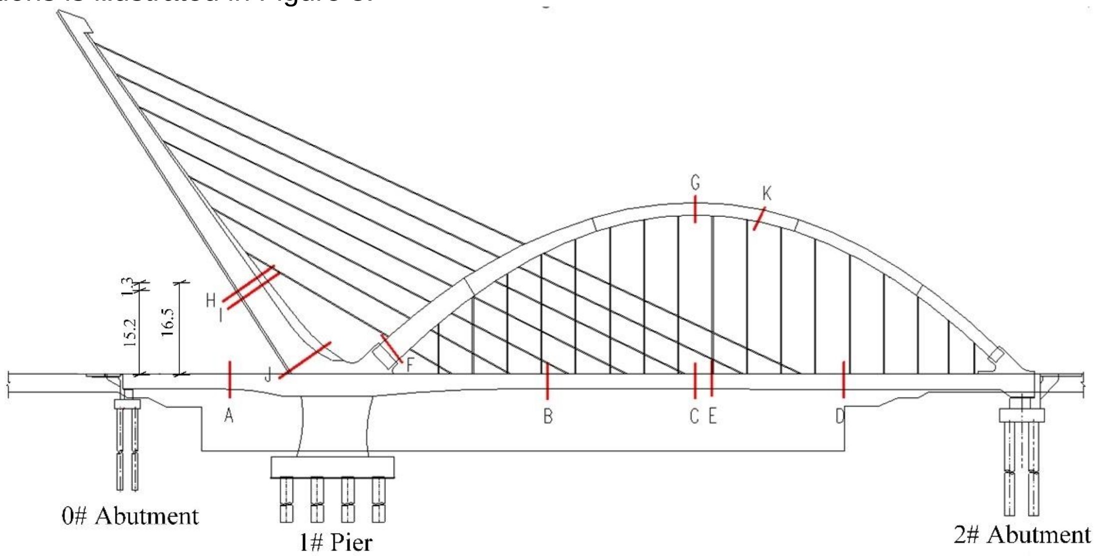

Fig.8 - Stress and temperature monitoring section layout (m)

Main girder and transverse spacer beam

Strain and temperature measurement points are strategically placed in various sections of the bridge, including the middle of the first span, the L/4 section of the second span, the L/2 section of the second span, and the 3L/4 section of the second span. Sections A, B, C, and E depicted in the figure correspond to the strain and temperature testing sections of the main beam. The strain sensors for the main beam should be installed along the longitudinal axis of the bridge. Specifically, a total of 16 strain gauges and 3 temperature sensors are installed on the main beam, while an additional 4 strain gauges bring the total to 20 strain gauges along with 3 temperature sensors on both the main girders and transverse beams. The arrangement of these measurement points is clearly shown in Figure 9.

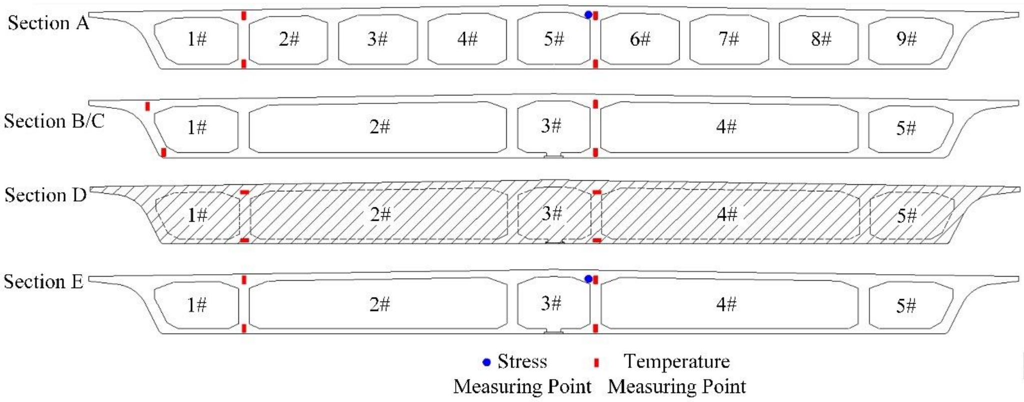

Fig.9 - Layout of stress and temperature measuring points of the main girder

Tower

The strain measuring points for the main tower are strategically positioned in three sections: at the base of the tower, 15.2 m above the main girder, and 16.5 m above the main girder. Sections H, I, and J represent the strain test sections of the main tower. The strain sensors for the main tower should be installed along the axis of the bridge tower. The arrangement of these measurement points is illustrated in Figure 10.

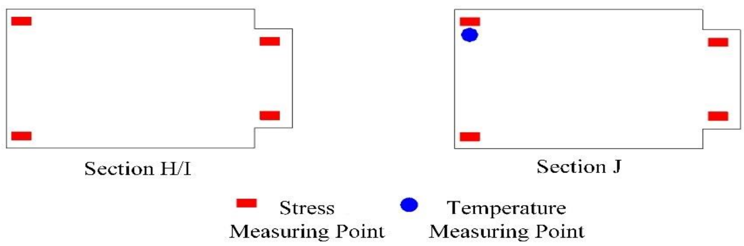

Fig.10 - Layout of tower stress and temperature measuring points

Arch rib

The steel box arch rib strain measurement points are arranged at the arch foot and mid-span position of 1# pier, and there are 2 sections in total. Sections F and G are designated as the strain test sections for the steel box arch rib. The strain sensors for the steel box arch rib should be installed along the length of the arch rib. The arrangement of the measurement points is depicted in Figure 11.

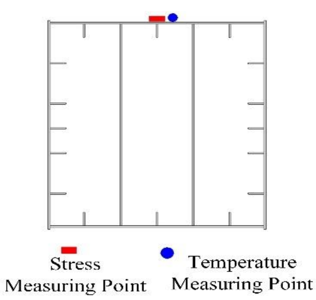

Fig.11- Layout of arch rib stress and temperature measurement points

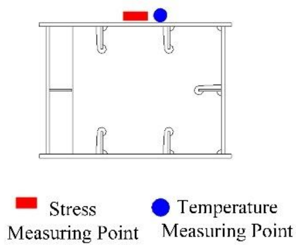

Fig.12 - Transverse brace stress and temperature measuring point layout

Wind bracing

The strain measuring point for the K-shaped transverse wind brace of the main arch rib is positioned at the 3# wind brace, comprising a total of one section. The strain gauge is installed on the upper surface of the end of the arch rib, in proximity to the K-brace transverse brace. The arrangement of these measurement points is illustrated in Figure 12.

The embedded concrete strain gauge is used to monitor the stress of the main girder and tower, and the measured concrete strain is converted to the corresponding stress value. The JMT-36B temperature sensor was selected for temperature monitoring. In order to make the measurement results more accurate, the JM2X-212AT surface strain gauge is selected for steel structure strain monitoring. The layout and test conditions of field strain gauges and sensors are shown in Figure 13~ Figure 16.

Fig.13 - Main girder strain gauge installation diagram

Fig.14- Strain test diagram of main girder

Fig.15-Strain test diagram of bridge tower

Fig.16- Strain test diagram of arch rib

Structural elevation and cable force monitoring

The main girder, tower and arch rib elevation monitoring section is selected as the key section of construction. There are 13 main girder monitoring sections, 17 tower monitoring sections and 9 arch rib monitoring sections. The specific layout of the monitoring section is shown in Figure 17.

DOI 10.14311/CEJ.2025.03.0030

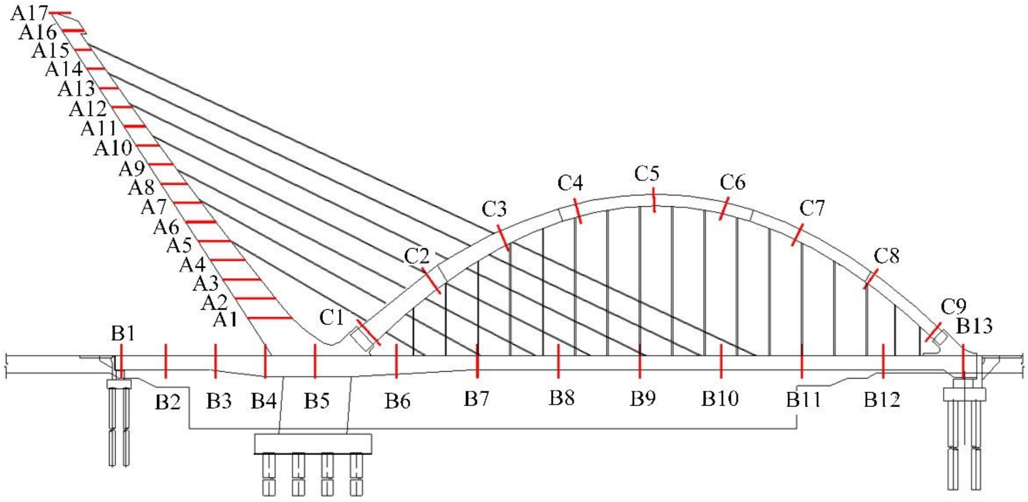

Fig.17- Elevation of linear monitoring section layout

Main girder elevation and center line deviation monitoring

A total of 13 sections of the main beam should be observed for the deviation of elevation and center line. Each section of the elevation observation point is arranged with 4 measuring points, which are corresponding positions on the outside of the anti-collision wall, and the deviation measuring points on the center line are corresponding bridge floor points on the center line of the box girder. The tasks of monitoring are as follows: measuring the elevation of the whole bridge during the main girder pouring, tower construction, triple tensioning of the stay cable, sling tensioning and completion of the bridge.

Main tower elevation monitoring

The measurement of the main tower's displacement involves determining the displacement value in both the longitudinal (along the bridge) and transverse (across the bridge) directions. The measuring points along the longitudinal direction are positioned at the interfaces of each section during the die-turning construction process. Additionally, measuring points are arranged on the side of the cable tower, close to the arch rib. The monitoring task entails measuring all elevations of the tower during various stages, including during the construction of the tower itself, during the three tensioning phases of the stay cables, during the tensioning of the boom, and upon the completion of the bridge. The monitoring tasks are as follows: all the elevations of the tower are measured during tower construction, stay cable tensioning, sling tensioning and bridge formation.

Arch rib elevation monitoring

Elevation observation points are strategically placed at various sections along both sides of the arch rib, including the arch foot, L/8, L/4, 3L/8, L/2, 5L/8, 3L/4, and 7L/8 sections. These measurement points are located on the sides of both the left and right arch ribs. The monitoring tasks associated with these points encompass the following: lifting of the arch rib, removal of arch rib supports, tensioning of slings, and monitoring of arch rib measurement points during the bridge stage. Figures 18 and 19 illustrate the calibration points of the main girder and the elevation of the tower, respectively.

Fig.18 -Main girder elevation measurement anchor point

Fig.19 -Tower elevation measurement diagram

BRIDGE CONSTRUCTION CONTROL EFFECT

Key construction control effect

To gain a comprehensive understanding of the actual stresses experienced by the bridge during construction, real-time monitoring is conducted on the stress and displacement of critical sections of the tower, arch rib, and main beam. Additionally, the stress of key sections of the wind bracing, as well as the internal forces of critical slings and stay cables, are also monitored. The measured data from these key construction stages are then analyzed.

Tower

Tower stress

Since the A1~A16 sections of the cable tower are all constructed by tilting mold, the cable force only balances the dead weight of the cable tower, especially when the cantilever length of the cable tower is long, the stress of the cable tower should be monitored. The comparisons between the measured and theoretical values of the left and right stresses in the tower test sections I, J, and H at each key construction stage are presented in Figures 20, 21 and 22.

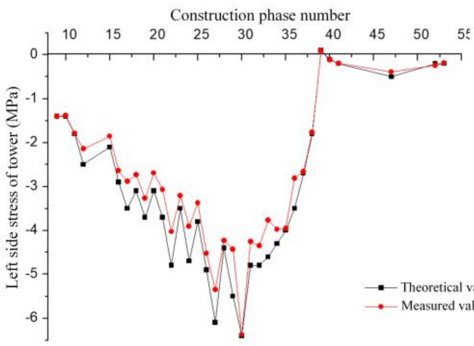

(a) Left side of the bridge tower

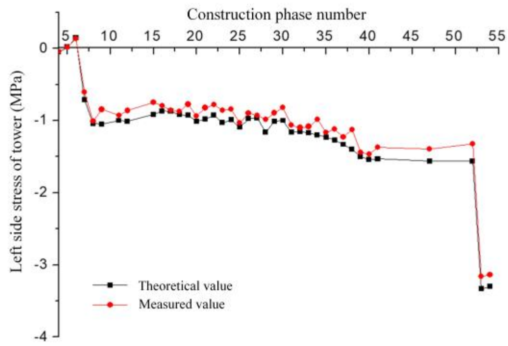

(b) Right side of the tower

Fig.20 - The section I stress comparison during construction

DOI 10.14311/CEJ.2025.03.0030

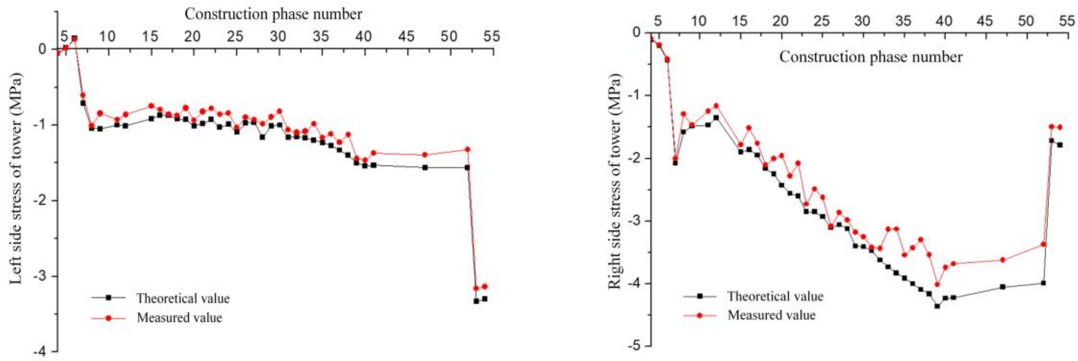

(a) Left side of the tower *(b) Right side of the tower*

Fig.21- Section J stress comparison during construction

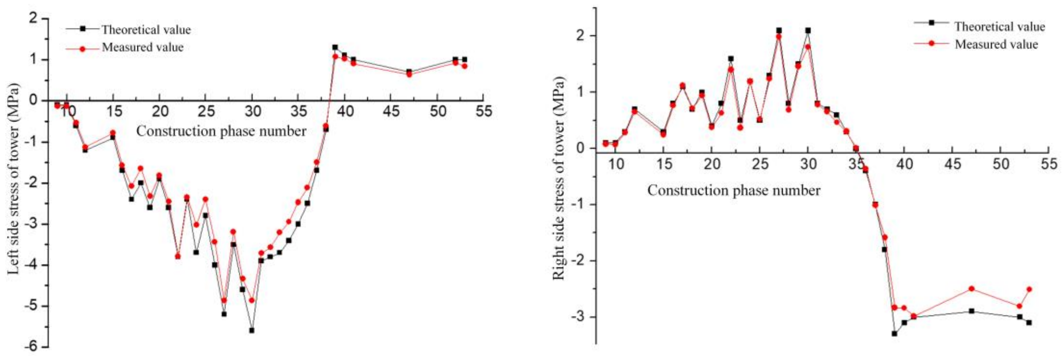

(a) Left side of the tower *(b) Right side of the tower*

Fig.22- The section H stress comparison during construction

As evident from Figures 20 to 22, the overall trend of the measured stress aligns with the theoretical stress. However, the measured stress values are lower than the theoretical ones, primarily due to the finite element model's inability to accurately simulate the behavior of ordinary steel bars. The stress on both the left and right sides of sections I and H gradually increases as construction progresses, peaking upon the completion of section A16 or section A14, respectively. Section I on the left is -5.6 MPa and Section I on the right is 2.3 MPa. The H section on the left is -4.9 MPa, and the H section on the right is 2.0 MPa. As construction progressed, the stress on the left side of section J of the tower girder gradually increased. Conversely, after the unloading of the main girder and tower support, the stress on the right side decreased. The maximum stress recorded on section J was -4.0 MPa. Notably, the stress levels in the tower conformed to the standard requirements.

During the cantilever construction of the tower, the maximum stress in the tower can be mitigated by tensioning the cable once per process. As the tensile force of the cable increases, the compressive stress on the left side of sections I and H gradually diminishes, potentially even transitioning into tensile stress. Meanwhile, the tensile stress on the right side progressively decreases, ultimately transforming into compressive stress. The stay cable plays a pivotal role in enhancing the structural forces during the mold construction process.

The tensile stress on the left side of the tower diminishes, while the compressive stress gradually increases. Conversely, the compressive stress on the right side of the tower decreases progressively. Because after the derrick is stretched, the main girder arches up, the extension of the cable decreases, and its internal force decreases.

Tower displacement

The junction node between S01 and the pylon is selected as the representative. The variables of the horizontal and vertical displacement of the pylon in the construction process are shown in Figure 23.

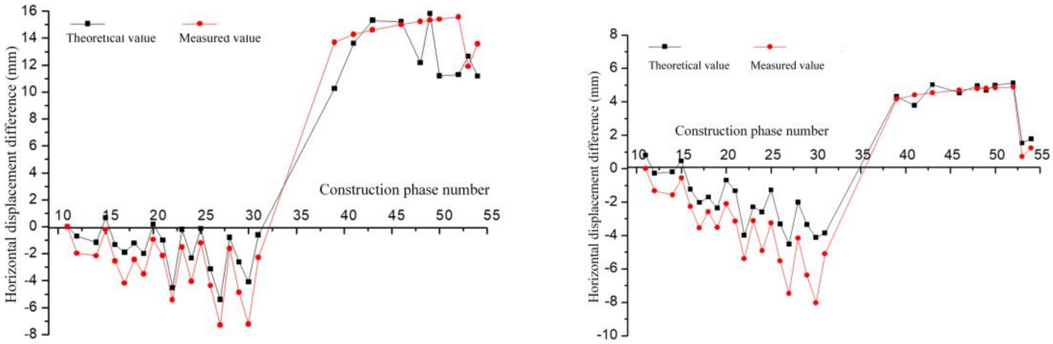

(a) Horizontal displacement difference *(b) Vertical displacement difference*

Fig.23 - The tower displacement difference comparison in each construction stage

As observed in Figure 23, the theoretical and measured values of tower displacement exhibit a similar overall trend. In the early stages, the measured values are smaller than the theoretical ones, although significant discrepancies arise between them in the later construction phases. As the cantilever length increases, both the horizontal and vertical displacements of the cable tower augment. However, the tension cable effectively mitigates these displacements. With an increase in the tension force of the cable, the direction of displacement in the cable tower shifts from the side with the smaller pile number towards the side with the larger pile number, and from downward displacement to upward displacement. Due to the self-balancing construction using tension cables, during the construction process, in order to remove the bottom support of the bridge tower, the tension force of the tension cables is used to balance the self-weight of the bridge tower. Therefore, during the tension stage of the tension cables, the bridge tower will experience significant horizontal and vertical displacements.

Main girder

Figure 24 presents a comparison between the measured and theoretical values of the stress measurement points for test section C, located in the middle span of the main girder, during certain key construction stages.

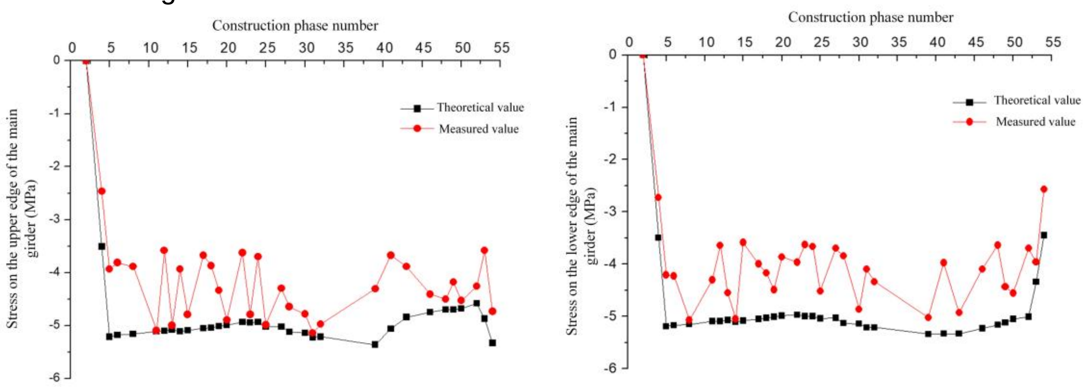

(a) Upper edge of main girder *(b) Lower edge of main girder*

Fig.24 - The section C stress comparison during construction

The measured stress values on both the upper and lower edges of the main beam closely align with the theoretical values, albeit being slightly smaller, as depicted in Figure 24. Throughout the construction process, the main girder span experiences compressive stress consistently. The maximum stress measured on the upper edge is -5.1 MPa, and similarly, the maximum stress measured on the lower edge is also -5.1 MPa; both of these values adhere to the code requirements. Given that the entire main beam is constructed with full support, the tension in the stay cable and derrick has a minimal impact on the stress distribution within the main beam. Upon unloading the main girder support, the compressive stress on the upper edge of the main girder intensifies, whereas the compressive stress on the lower edge decreases.

Arch rib stress

Figure 25 presents a comparison between the measured stress value and the theoretical stress value for test section G, located in the span of the arch rib, during a key construction stage.

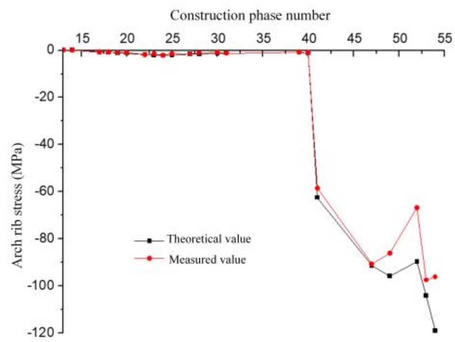

Fig.25 - The section G stress comparison during construction

As shown in Figure 25, the measured stress on the upper edge of the arch rib follows the overall trend of the theoretical value during construction, albeit being slightly smaller. Throughout the construction process, the middle and upper edges of the arch rib span experience compressive stress. Initially, due to the construction of the arch rib support, the stress in the arch rib remains low. However, upon unloading the arch rib support, the stress in the span of the arch rib increases rapidly. After the unloading of the main beam support, the measured stress attains its maximum value of -97.5 MPa, which complies with the code requirements.

Wind bracing stress

Figure 26 displays a comparison between the measured and theoretical stress values for section K during several key construction stages.

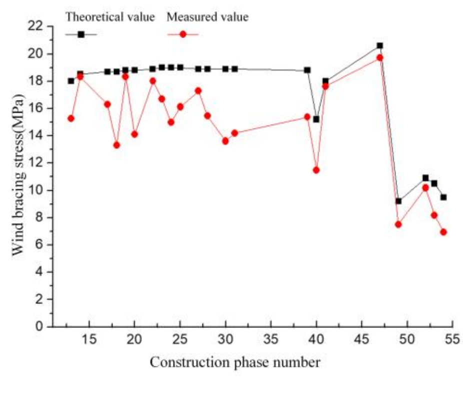

Fig. 26 - The K section stress comparison during construction

As illustrated in Figure 26, the measured stress value at the upper edge of the K brace exhibits an overall trend that is consistent with the theoretical value during construction. However, the measured value is slightly smaller than the theoretical value. The upper edge of the K-type support is in a tension state during the construction process, and the measured stress reaches the maximum value of 19.7 MPa after the tensioning of the derrick LX01, LX02, LX03, RX01, RX02, RX03, which meets the requirements of the specification.

Cable force test

The analysis of the measured cable forces for the stay cable S08 and the sling LD10 during the key construction process is presented in Figures 27 and 28, respectively.

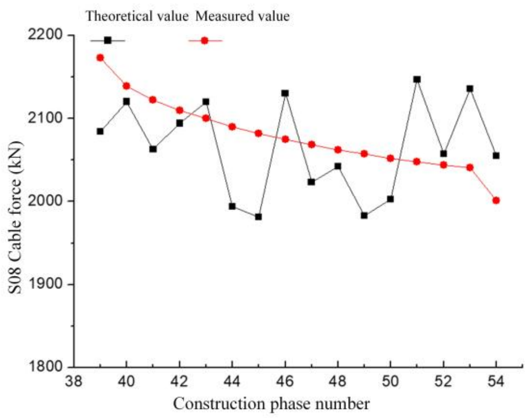

Fig.27 - S08 cable force comparison

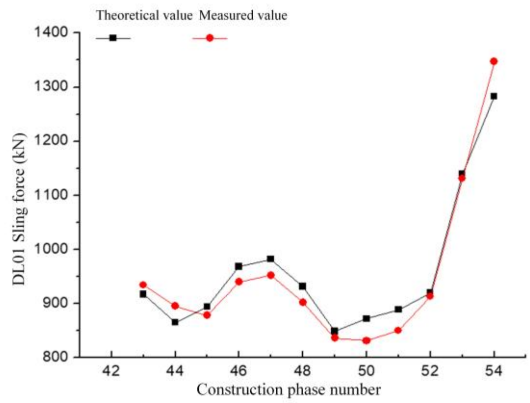

Fig.28 - LD10 cable force comparison

As observed in Figures 27 and 28, the overall trend of the measured cable forces closely aligns with the theoretical values. Specifically, the maximum discrepancies between the measured and theoretical values for the stay cable S08 and the suspension rod LD10 are 4.8% and -4.9%, respectively, both of which satisfy the specification requirements. Furthermore, the cable force of the stay cable S08 gradually diminishes as construction progresses, whereas the cable force of the suspension rod LD10 progressively increases with the advancement of construction.

Bridge state control effect

Elevation control

Based on the design elevations of the main girder, arch rib, and tower, along with the preset pre-arch degree, the corresponding vertical mold elevations are determined. The least squares method is employed to identify and adjust for any parameter errors that arise during the construction process, ensuring that the relevant lines adhere to the code requirements. The elevation errors for each key section of the bridge are depicted in Figure 29.

DOI 10.14311/CEJ.2025.03.0030

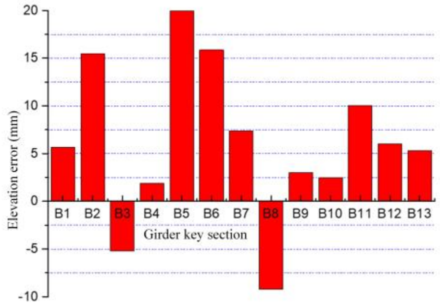

(a) Elevation error diagram of key section of main girder

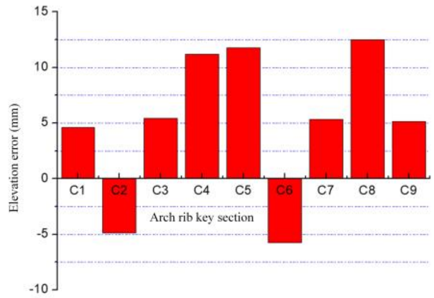

(b) Elevation errors of key sections of arch ribs

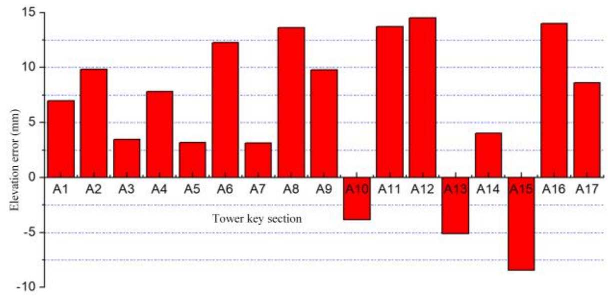

(c) Elevation error diagram of key sections of the main girder

Fig.29- Elevation errors of key sections

As illustrated in Figure 29, following the construction of the bridge deck pavement, railings, and other secondary loads, as well as the removal of the main beam supports, the elevation of the entire bridge falls within the error control range, satisfying both specification and design requirements. Specifically, the overall elevation of the main beam is slightly above the design value, with a maximum deviation of 20.0 mm. Similarly, the overall elevation of the arch rib and the cable tower are also slightly higher than their respective design elevations, with maximum deviations of 12.5 mm and 14.5 mm. These slight elevations are advantageous as they contribute to reducing prestress loss in the main beam and decreasing its deflection.

Stress control

By monitoring the stress value of each key surface in real time, the stress change and the final stress value can be fully controlled. The measured stress value of each stress control section in each construction stage does not exceed the limit, and the stress of the main beam, arch rib and cable tower in the bridge completion stage is shown in Figure 30.

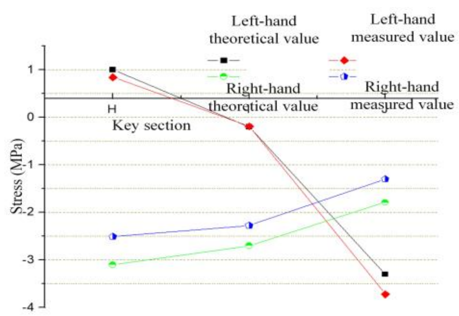

(a) Pylon control cross-section diagram

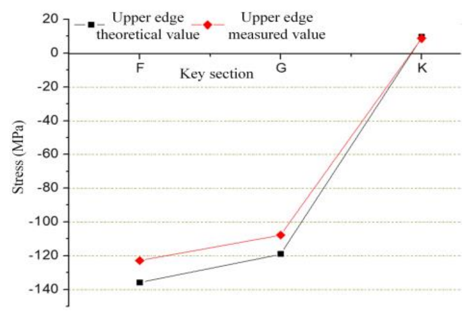

(b) Stress diagram of arch rib and wind support control section

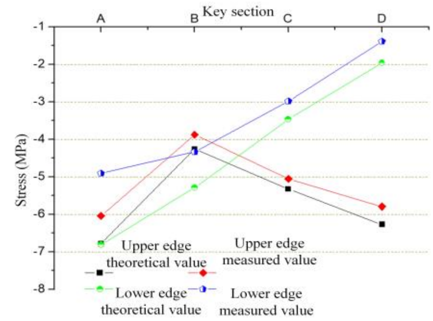

(c) Main girder control section diagram

Fig.30 -Stress diagram of each key section

As shown in Figure 30, the measured stress of each control section at the bridge completion stage is basically consistent with the theoretical stress. The upper edge of the arch rib, the main girder and the tower at the prestressed section are all under pressure, and the upper edge of the wind brace is subject to small tensile stress. At the height of 16.5 m above the bridge girder, the left side of the tower is strained and the right side is compressed, and the tensile stress is only 1.0 MPa, which indicates that the design is reasonable and the construction control measures are appropriate.

Cable force control

Since the cable of the bridge is divided into three tensioning times, the tensioning process is complicated, and the cable plays an important role in the stress of the tower construction process, so the cable force of the cable-stayed cable should be closely monitored, and the cable force of the remaining cable-stayed cable should be measured every time one cable is tensioned. This paper only analyzes the cable forces of the cable-stayed cable and boom when the bridge is completed, and the cable forces during the construction phase when the cable-stayed cable is fully tensioned, as shown in Figure 31 and Figure 32.

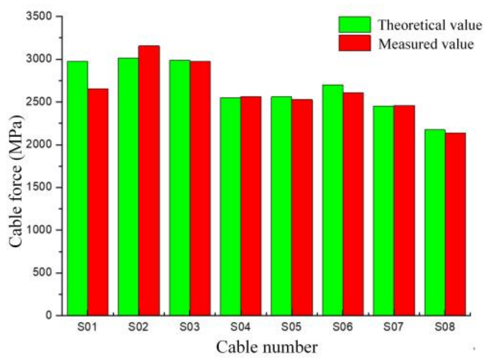

Fig.31- Cable force value of the cable during construction

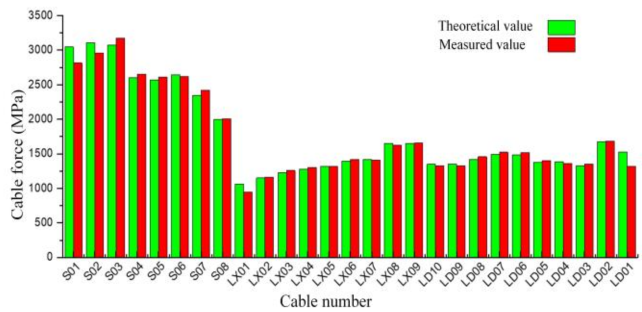

Fig.32- Bridge cable force value

As shown in Figures 31 and 32, the errors of short cable S01, LX01 and LD01 are relatively large, which are 7.6%, 10.9% and 13.4%, respectively. The errors of the remaining cable and derrick force are all within the range required by the specifications. This is because the short cable testing force is more obviously affected by the cable length error.

CONCLUSIONS

(1) The measured stress values on the upper and lower edges of the main girder align with the overall trend of the theoretical values, albeit being slightly smaller. Throughout the entire construction process, the main beam span experiences compressive forces. The measured maximum stress on the upper edge is -5.1 MPa, and similarly, the measured maximum stress on the lower edge is also -5.1 MPa. Both of these values comply with the code requirements.

(2) The elevation of the main girder is marginally higher than the design value, with a maximum deviation of 20.0 mm. Similarly, the overall elevation of the arch rib exceeds the design elevation slightly, with a maximum deviation of 12.5 mm. The tower's overall elevation is also slightly above the design elevation, with a maximum deviation of 14.5 mm. These slight elevations are advantageous as they contribute to minimizing prestress loss in the main girder and reducing its deflection.

(3) The upper edge of the arch rib, the main girder and the prestressed section tower are all under pressure, and the upper edge of the transverse brace is subjected to little tensile stress. At the height of 16.5 m above the bridge girder, the left side of the tower is strained and the right side is compressed, and the tensile stress is only 1.0MPa, which indicates that the design is reasonable and the construction control measures are appropriate.

REFERENCES

[1] Puri N, Turkan Y. Bridge construction progress monitoring using lidar and 4D design models[J]. Automation in Construction, 2020, 109: 102961.

[2] He Z, Li W, Salehi H, et al. Integrated structural health monitoring in bridge engineering[J]. Automation in construction, 2022, 136: 104168.

[3] Jiang Z, Shen X, Ibrahimkhil M H, et al. Scan-vs-BIM for real-time progress monitoring of bridge construction project[J]. ISPRS Annals of the Photogrammetry, Remote Sensing and Spatial Information Sciences, 2022, 10: 97-104.

[4] Tian J, Luo S, Wang X, et al. Crane lifting optimization and construction monitoring in steel bridge construction project based on BIM and UAV[J]. Advances in Civil Engineering, 2021, 2021(1): 5512229.

[5] Lin Y B, Pan C L, Kuo Y H, et al. Online monitoring of highway bridge construction using fiber Bragg grating sensors[J]. Smart Materials and Structures, 2005, 14(5): 1075.

[6] Bai Y, Huan J, Kim S. Measuring bridge construction efficiency using the wireless real-time video monitoring system[J]. Journal of Management in Engineering, 2012, 28(2): 120-126.

[7] Fujino Y, Siringoringo D M. Bridge monitoring in Japan: the needs and strategies[J]. Structure and Infrastructure Engineering, 2011, 7(7-8): 597-611.

[8] Zhou G D, Yi T H, Li W J, et al. Standardization construction and development trend of bridge health monitoring systems in China[J]. Advances in Bridge Engineering, 2020, 1: 1-18.

[9] Butler L J, Lin W, Xu J, et al. Monitoring, modeling, and assessment of a self-sensing railway bridge during construction[J]. Journal of Bridge Engineering, 2018, 23(10): 04018076.

[10] Fu M, Liang Y, Feng Q, et al. Research on the application of multi-source data analysis for bridge safety monitoring in the reconstruction and demolition process[J]. Buildings, 2022, 12(8): 1195.

[11] Kim H, Moon B, Hu X, et al. Construction and performance monitoring of innovative ultra-high-performance concrete bridge[J]. Infrastructures, 2021, 6(9): 121.

[12] Xin J, Wang C, Tang Q, et al. An evaluation framework for construction quality of bridge monitoring system using the DHGF method[J]. Sensors, 2023, 23(16): 7139.

[13] Wan B. Using fiber-reinforced polymer (FRP) composites in bridge construction and monitoring their performance: an overview[J]. Advanced composites in bridge construction and repair, 2014: 3-29.

[14] Gou H, Liu C, Bao Y, et al. Construction monitoring of self-anchored suspension bridge with inclined tower[J]. Journal of Bridge Engineering, 2021, 26(10): 05021011.

[15] Fang Y M, Chou T Y, Hoang T V, et al. Automatic management and monitoring of bridge lifting: a method of changing engineering in real-time[J]. Sensors, 2019, 19(23): 5293.
[16] Yang H, Xia M. Advancing bridge construction monitoring: AI-based building information modeling for intelligent structural damage recognition[J]. Applied Artificial Intelligence, 2023, 37(1): 2224995.
[17] Xin J, Jiang Y, Wu B, et al. Intelligent Bridge Health Monitoring and Assessment[J]. Buildings, 2023, 13(7): 1834.